Cranfield University

Elizabeth M. K. Hillier

The Effect of Zinc-Cobalt Electroplating on the Hydrogen Embrittlement of High Strength Steel

School of Industrial and Manufacturing Science

PhD

Cranfield University

School of Industrial and Manufacturing Science

Ph.D. Thesis

Academic Year 2000/2001

Elizabeth M. K. Hillier

The Effect of Zinc-Cobalt Electroplating on the Hydrogen Embrittlement of High Strength Steel

Supervisor : Dr. M. J. Robinson

July 2001

CONTENTS PAGE

ABSTRACT 10

INTRODUCTION 11

LITERATURE REVIEW 18

HYDROGEN EMBRITTLEMENT 18
HE FAILURE MODES 20
HYDROGEN EVOLUTION AND ENTRY 22
THE MECHANISM OF HYDROGEN EVOLUTION OR ENTRY 23
HYDROGEN ENTRY MECHANISMS 26
ABSORPTION SURFACE EFFECTS 26
Hydrogen permeation measurement 29
TRAPPING OF HYDROGEN IN STEEL 31
Accumulation in Voids 33
Accumulation at High Strain Fields 34
Grain Boundary Traps 35
Dislocation Trapping 35
Impurity Trapping 36
Trap characterisation 36
Trap ranking 37
HYDROGEN EMBRITTLEMENT MECHANISMS 37
Internal Pressure Theory 38
Hydride Induced Cracking Theory 38
Brittle Crack Tip Theory 39
Hydrogen Induced Slip Softening / Enhanced Plastic Flow Model 40
Lattice Decohesion Theory 43
Hydrogen Adsorption / Surface Energy Theory 45
Summary 46
IDENTIFICATION OF HYDROGEN LOCATION 47
Decoration Techniques 47
Hydrogen Probes 48
MEASUREMENT BY HYDROGENPERMEATION 48
MECHANICAL TESTING 54
Constant stress tests 54
Constant load tests 55
Statistical analysis techniques 56
CORROSION 57
Corrosion prediction 57
Corrosion Control 57
Electrochemical Control 59
Corrosion of zinc-alloy coatings 61
Aircraft Requirements 63
Corrosion performance of zinc-alloy coatings 64
Corrosion rate measurements 67
METALLIC COATINGS 71
ELECTROPLATING 73
NORMAL CO-DEPOSITION 74
ANOMALOUS CO-DEPOSITION 74
Development of the Anomalous Co-Deposition Model 75
Cathode Efficiency 79
Underpotential Deposition Model 80
Electrolyte Additives 80
Zinc-cobalt electrolytes 83
Alkaline Cyanide 83
Alkaline Cyanide Free (Zincate) 83

Acid Chloride *83*
Embrittlement Implications *84*
Zinc-cobalt electrolyte composition *84*
Choice of electrolyte *85*
Present study *86*

EXPERIMENTAL *87*
METALLOGRAPHICAL EXAMINATION OF THE TEST MATERIAL 87
ELECTRODEPOSITION PARAMETER VARIATION 88
ELECTRODEPOSIT SURFACE EXAMINATIONS 93
Scanning Electro Microscopy (SEM) / Energy Dispersive Spectrometry (EDAX) *93*
Inductively Coupled Plasma Spectrometry (ICP) *95*
Auger Electron Spectroscopy (AES) *96*
X-Ray Photoelectron Spectroscopy (XPS) *97*
MECHANICAL TESTING 98
Specimen Design *98*
Heat Treatment *99*
Tensile Specimen Preparation *100*
Alloy Plating *101*
Layered electroplated coatings *101*
Cadmium Plating *102*
Baking Treatment *102*
Coating Measurement and Polishing Technique *102*
Slow Strain Rate Test Procedure *104*
PERMEATION STUDIES 105
HYDROGEN DETECTION 109
Hydrogen microprint techique (HMT) *109*
CORROSION MEASUREMENTS 111
Potentiodynamic Polarisation Scans *112*
Linear Polarisation Resistance (LPR) *113*
Weight Loss *114*

RESULTS *116*
MATERIAL TESTING 116
PARAMETER VARIATION 117
Time *118*
Temperature *120*
pH *122*
Current Density *124*
MECHANICAL TESTING *139*
PERMEATION TESTING 158
HYDROGEN DETECTION BY DECORATION TECHNIQUE 162
CORROSION TESTING 167
Polarisation scan results *167*
Linear polarisation resistance results *173*
Weight loss results *181*

DISCUSSION ZINC-COBALT 183
PARAMETER VARIATION 183
ELECTRODEPOSIT EXAMINATION 192
HYDROGEN EMBRITTLEMENT TESTING 194
Control Specimens *194*
Standard Zinc-Cobalt Electroplated Specimens *195*
Modification of the Standard Zinc-Cobalt Electrolyte *196*
Change in pH of Standard Electrolyte *197*
Compositionally Modulated Multi-Layer Deposits *198*
PERMEATION TESTING 200
HYDROGEN DETECTION 214
CORROSION MEASUREMENTS 218

DISCUSSION ZINC-NICKEL 223
PARAMETER VARIATION 223
ELECTRODEPOSIT EXAMINATION 228
HYDROGEN EMBRITTLEMENT TESTING 229
PERMEATION TESTING 231
HYDROGEN DETECTION 234
CORROSION MEASUREMENTS 234

DISCUSSION ZINC-COBALT-IRON 236
PARAMETER INVESTIGATIONS 236
ELECTRODEPOSIT EXAMINATION 239
HYDROGEN EMBRITTLEMENT TESTING 240
PERMEATION TESTING 244
HYDROGEN DETECTION 245
CORROSION MEASUREMENTS 245
SUMMARY 249
LIMITING HYDROGEN EMBRITTLEMENT 249
WHERE THE HYDROGEN GOES 249

CONCLUSIONS 253

FUTURE WORK 256

ACKNOWLEDGEMENTS 257

APPENDICES 258

REFERENCES 259

Table of Figures Page

FIGURE 1: OPEN CIRCUIT POTENTIAL OF SOME METALS AND ALLOYS IN 3.5% NACL SOLUTION AT 25°C. 13
FIGURE 2: ZINC-ALLOY TYPES USED IN JAPAN, USA AND EUROPE IN 1992 15
FIGURE 3: TEMPERING EFFECTS ON THE TENSILE PROPERTIES OF 4340 AND 300M STEELS 19
FIGURE 4: STATIC FATIGUE TESTS ON HYDROGEN CHARGED AISI 4340 STEEL AFTER VARIOUS BAKING TIMES 20
FIGURE 5: MECHANISTIC STEPS DURING THE HYDROGEN EVOLUTION REACTION 25
FIGURE 6: EFFECT OF AN ELECTROPLATED LAYER ON THE OBSERVED PERMEATION TRANSIENT 27
FIGURE 7: PERMEATION TECHNIQUE APPARATUS, CELL AND CIRCUIT 28
FIGURE 8: MODEL SHOWING HYDROGEN ENERGY LEVELS IN THE TRAP VICINITY 32
FIGURE 9: HYDROGEN DECORATION TECHNIQUE 33
FIGURE 10: MICROSCOPIC FRACTURE MODES SHOWN BY BEACHAM 40
FIGURE 11: TEMPERATURE DEPENDENCE OF HE IN STEEL MEASURED BY (%) REDUCTION IN AREA 43
FIGURE 12: ATOMIC MODEL OF A CRACK EDGE 44
FIGURE 13: RELATIONSHIP BETWEEN (A) COHESIVE FORCES AND STRAIN, (B) HYDROGEN CONCENTRATION IN IRON AND STRAIN 45
FIGURE 14: TYPICAL PERMEATION TRANSIENT 51
FIGURE 15: EFFECT OF GRID ELECTROPLATING ON PERMEATION TRANSIENTS 52
FIGURE 16: VARIATION IN HYDROGEN DIFFUSIVITY WITH DEPOSIT THICKNESS 53
FIGURE 17: HYDROGEN CONCENTRATION PROFILE WITH (A) GALVANOSTATIC AND (B) POTENTIOSTATIC CONDITIONS 53
FIGURE 18: POURBAIX DIAGRAM OF IRON IN WATER 59
FIGURE 19: EVANS DIAGRAM OF CATHODIC AND ANODIC POLARIZATION 60
FIGURE 20: VARIATION IN OPEN-CIRCUIT POTENTIAL OF ELECTRODEPOSITED ZINC-NICKEL WITH IMMERSION TIME IN NEUTRAL 5% NACL SOLUTION 68
FIGURE 21: VARIATION IN OPEN-CIRCUIT POTENTIAL OF ELECTRODEPOSITED ZINC-COBALT WITH IMMERSION TIME IN NEUTRAL 5% NACL SOLUTION 69
FIGURE 22: GENERAL RELATIONSHIP OF COMPOSITION AND DEPOSITION CURRENT DENSITY FOR ZINC-IRON GROUP ALLOYS 75
FIGURE 23: INFLUENCE OF 30MM/L ZINC ON THE CATHODE POTENTIAL VERSES CURRENT DENSITY CURVES OF A WATTS NICKEL ELECTROPLATING BATH AT DIFFERENT PH VALUES 78
FIGURE 24: RELATIONSHIP BETWEEN ALLOY CONTENT AND (A) CATHODE PH OR (B) FILM RESISTANCE AT VARIOUS CURRENT DENSITIES 79
FIGURE 25: EFFECT OF METAL ION CONCENTRATION ON DEPOSIT COMPOSITION 85
FIGURE 26: BASIC GALVANOSTATIC ELECTROPLATING SET UP 90
FIGURE 27: SHIM SPECIMEN TO BE ELECTROPLATED 91

FIGURE 28: SCHEMATIC OF COPPER SHIM ELECTROPLATED OVER VARYING TIME 95
FIGURE 29: TENSILE SPECIMEN SPECIFICATIONS 99
FIGURE 30: CROSS SECTION OF POLISHING ARRANGEMENT 103
FIGURE 31: EXPERIMENTAL SET UP FOR THE PERMEATION APPARATUS 106
FIGURE 32: THE HYDROGEN MAPPING TECHNIQUE 109
FIGURE 33: POLARISATION AND LPR MEASUREMENT EXPERIMENTAL SET UP 113
FIGURE 34: WEIGHT LOSS EXPERIMENTAL SET UP 114
FIGURE 35: AS RECEIVED 116
FIGURE 36: QUENCHED AND TEMPERED (QT) 116
FIGURE 37: BAKED AND (QT) 116
FIGURE 38: EFFECT OF TIME ON DEPOSIT COMPOSITION AND CATHODE EFFICIENCY 118
FIGURE 39: EFFECT OF TEMPERATURE ON DEPOSIT COMPOSITION AND CATHODE EFFICIENCY 120
FIGURE 40: EFFECT OF pH VALUE ON DEPOSIT COMPOSITION AND CATHODE EFFICIENCY 122
FIGURE 41: EFFECT OF CURRENT DENSITY ON DEPOSIT COMPOSITION AND CATHODE EFFICIENCY 124
FIGURE 42: ZINC-COBALT DEPOSIT WITH LARGE HOLIDAYS 126
FIGURE 43: ZINC-COBALT DEPOSIT FORMED FOR 1 MINUTE WITH ZINC HYDROXIDE WHISKERS VISIBLE 126
FIGURE 44: ZINC-COBALT DEPOSIT FORMED IN STAGNANT CONDITIONS FOR 30 MINUTES SHOWING ZINC HYDROXIDE WHISKERS 127
FIGURE 45: FULL XPS TRACES FOR ZINC-COBALT ELECTROPLATING 130
FIGURE 46: FULL XPS TRACES FOR ZINC-NICKEL ELECTROPLATING 131
FIGURE 47: FULL XPS TRACES FOR ZINC-COBALT-IRON ELECTROPLATING 132
FIGURE 48: AUGER DEPTH PROFILE OF ZINC-COBALT ELECTROPLATING AT pH4.2 134
FIGURE 49: AUGER DEPTH PROFILE OF ZINC-NICKEL ELECTROPLATING 135
FIGURE 50: AUGER DEPTH PROFILE OF ZINC-COBALT-IRON ELECTROPLATING 136
FIGURE 51: AUGER DEPTH PROFILE OF A ZINC-COBALT SPECIMEN ELECTROPLATED AT pH1 138
FIGURE 52: FRACTURED END OF A PLATED TENSILE SPECIMEN 139
FIGURE 53: A DUCTILE FRACTURE SURFACE 139
FIGURE 54: A BRITTLE FRACTURE SURFACE 139
FIGURE 55: FRACTURED TENSILE SPECIMEN WITH A PARTIALLY DETACHED POROUS COATING 140
FIGURE 56: STRESS STRAIN DIAGRAM FOR BAKED ZINC-COBALT SPECIMENS 141
FIGURE 57: STRESS STRAIN DIAGRAM FOR ZINC-COBALT SPECIMENS PLATED AT ALTERED pH 141
FIGURE 58: WEIBULL GRAPH OF SSRT DATA FOR EACH BATCH OF AIR TEST SPECIMENS 142
FIGURE 59: WEIBULL GRAPH OF ALL THE UNPLATED CONTROL SPECIMENS TOGETHER 143
FIGURE 60: WEIBULL GRAPH OF THE EFFECT OF BAKING CONTROL SPECIMENS 144
FIGURE 61: WEIBULL GRAPH OF THE EFFECT OF CADMIUM ELECTROPLATING 145
FIGURE 62: WEIBULL GRAPH OF THE EFFECT OF ZINC ELECTROPLATING 146
FIGURE 63: WEIBULL GRAPH OF THE EFFECT OF ZINC-NICKEL ELECTROPLATING 147
FIGURE 64: WEIBULL GRAPH OF THE EFFECT OF ZINC-COBALT ELECTROPLATING 148

FIGURE 65: WEIBULL GRAPH OF THE EFFECT BAKING ZINC-COBALT PLATED SPECIMENS 149
FIGURE 66: WEIBULL GRAPH OF THE EFFECT OF BAKING TIME ON ZINC-COBALT SPECIMENS..... 150
FIGURE 67: WEIBULL GRAPH OF THE EFFECT OF DELAYED BAKING ON ZINC-COBALT PLATED SPECIMENS 151
FIGURE 68: WEIBULL GRAPH OF THE EFFECT OF ELECTROLYTE PH ON ZINC-COBALT PLATING 152
FIGURE 69: WEIBULL GRAPH OF UNBAKED AND BAKED ZINC-COBALT-IRON SPECIMENS 153
FIGURE 70: WEIBULL GRAPH OF THE EFFECT OF AN INTERLAYER ON DBT ZINC PLATED SPECIMENS.. 154
FIGURE 71: WEIBULL GRAPH OF THE EFFECT OF AN INTERLAYER ON DBT ZINC-COBALT PLATED SPECIMENS 155
FIGURE 72: WEIBULL GRAPH OF THE EFFECT OF AN INTERLAYER ON DBT ZINC-NICKEL PLATED SPECIMENS 156
FIGURE 73 WEIBULL GRAPH OF THE EFFECT OF BAKING DBT COBALT/ NICKEL THEN ZINC-COBALT PLATED SPECIMENS 157
FIGURE 74: PERMEATION TRANSIENTS FOR ALL THE TYPES OF ELECTROLYTE USED 158
FIGURE 75: PERMEATION TRANSIENTS FOR VARIATION IN PH OF THE ZINC-COBALT ELECTROLYTE.... 159
FIGURE 76: PERMEATION TRANSIENTS FOR ALL THE TYPES OF ELECTROLYTE USED 160
FIGURE 77: PERMEATION TRANSIENTS FORMED AT DIFFERENT CHARGING TEMPERATURES 161
FIGURE 78: PERMEATION TRANSIENTS FROM CHARGING A COBALT PLATED STEEL SHIM 162
FIGURE 79: BAKED ZINC-COBALT COATING TREATED WITH HMT EMULSION..... 163
FIGURE 80: ELECTROPLATED ZINC-COBALT COATING TREATED WITH HMT EMULSION..... 163
FIGURE 81: TYPICAL DBT SPECIMEN AFTER HMT TREATMENT 164
FIGURE 82: RESPONSE OF DELAYED HMT TREATMENT ON DBT SPECIMEN..... 164
FIGURE 83: TYPICAL CHARGED STEEL SPECIMEN SHOWING THE HMT DETECTION BAND AND A CHARGED SPECIMEN SHOWING A COMPLETE RESPONSE..... 164
FIGURE 84: THEORETICAL DEPTH PROFILE FOR HYDROGEN PENETRATION..... 166
FIGURE 85: POLARISATION SCANS FOR STEEL COUPONS..... 167
FIGURE 86: POLARISATION SCANS FOR CADMIUM ELECTROPLATED COUPONS 168
FIGURE 87: POLARISATION SCANS FOR ZINC ELECTROPLATED COUPONS 169
FIGURE 88: POLARISATION SCANS FOR ZINC-COBALT ELECTROPLATED COUPONS 170
FIGURE 89: POLARISATION SCANS FOR ZINC-NICKEL ELECTROPLATED COUPONS 171
FIGURE 90: POLARISATION SCANS FOR TERNARY ELECTROPLATED COUPONS..... 172
FIGURE 91: TYPICAL LINEAR POLARISATION SCAN 173
FIGURE 92: LPR SCANS FOR IMMERSED STEEL COUPONS 174
FIGURE 93: LPR SCANS FOR IMMERSED CADMIUM ELECTROPLATED COUPONS..... 175
FIGURE 94: LPR SCANS FOR IMMERSED ZINC ELECTROPLATED COUPONS..... 176
FIGURE 95: LPR SCANS FOR IMMERSED ZINC-COBALT COUPONS 177
FIGURE 96: LPR SCANS FOR IMMERSED ZINC-NICKEL ELECTROPLATED COUPONS..... 178
FIGURE 97: LPR SCANS FOR IMMERSED ZINC-COBALT-IRON ELECTROPLATED COUPONS..... 179
FIGURE 98: WEIGHT LOSS FOR 3 AND 6 MONTH IMMERSION COUPONS 181

FIGURE 99: VARIATION OF ZINC-COBALT SPECIMEN MORPHOLOGY WITH COATING TIME 184
FIGURE 100: SCHEMATIC OF ANOMALOUS CO-DEPOSITION 185
FIGURE 101: ZINC-COBALT EQUILIBRIUM DIAGRAM 187
FIGURE 102: VARIATION OF VISUAL BRIGHTNESS OF ZINC-COBALT SPECIMENS WITH TEMPERATURE. 189
FIGURE 103: VARIATION OF SPECIMEN MORPHOLOGY WITH PH 191
FIGURE 104: VARIATION IN SPECIMEN MORPHOLOGY WITH CURRENT DENSITY 193
FIGURE 105: BREAKTHROUGH TIME AND POSITION OF CURVE 201
FIGURE 106: RISE TIME AND SHAPE OF CURVE 201
FIGURE 107: AMOUNT OF HYDROGEN PERMEATED AND DECAY OF THE TRANSIENT 202
FIGURE 108: PERMEATION TRANSIENTS FOR ZINC AND ZINC-COBALT ELECTROPLATING 203
FIGURE 109: AMOUNT OF HYDROGEN PERMEATED BY THE TYPE OF ELECTROPLATES 204
FIGURE 110: AMOUNT OF HYDROGEN PERMEATED FOR DIFFERENT TEMPERATURES 207
FIGURE 111: AMOUNT OF HYDROGEN PERMEATED AT DIFFERENT PH VALUES 208
FIGURE 112: EFFECT OF CHARGING CURRENT DENSITY 210
FIGURE 113: INTEGRATION OF THE CURRENT DENSITY TRANSIENTS 211
FIGURE 114: PREDICTED HYDROGEN DIFFUSION PROFILES DURING PERMEATION EXPERIMENTS 213
FIGURE 115: COMPOSITIONAL VARIATION OF BINARY ELECTRODEPOSITS WITH CURRENT DENSITY ... 227
FIGURE 116: TOTAL AMOUNT OF UNCORRECTED HYDROGEN PERMEATED 233
FIGURE 117: TOTAL AMOUNT OF HYDROGEN PERMEATED BY THE TYPE OF ELECTROPLATING 244
FIGURE 118: HYDROGEN DISTRIBUTION DURING ELECTROPLATING 251

This thesis is dedicated to both my grandmothers.

"Ah, that great friend of my youth is dead! I felt that heart, that great soul, in whose presence I seemed to be more than I was, because I was all that I could be. Never shall I forget her, never her firm understanding and her divine tolerance". Johann Wolfgang von Goethe, from 'The sorrows of young Werther', 1774.

ABSTRACT

Electroplated cadmium coatings are widely used in the aerospace industry to provide corrosion protection for components such as fasteners, which are manufactured from high strength steels. Due to environmental and safety concerns with regard to the use of cadmium, there is a requirement to investigate suitable replacements. Any alternate coating, in addition to effective corrosion protection, must not have deleterious effects on the steel substrate. Hydrogen is known to be absorbed during electroplating and there are concerns that this could cause hydrogen embrittlement of high strength steel fasteners. This study has investigated the effect of zinc-cobalt electroplating on the embrittlement of high strength steels used for aerospace applications, due to promising corrosion properties.

Permeation measurements have been used to measure the hydrogen uptake during electroplating, and slow strain rate testing performed to establish the effect of hydrogen on the embrittlement of the steel substrate. The influences of bath composition, temperature and pH have been studied, plus the addition of other iron group elements to the plating bath to minimise the risk of embrittlement. Hydrogen that has passed into the metal substrate has been located by a decorative mapping technique that also showed the high concentration present in the electroplated coatings. Corrosion tests have been executed to assess the performance of the electroplated coatings that have been tested.

The factors that affect the embrittlement of zinc-cobalt electroplated high strength steels and the methods, including modulated multi-layer coatings and baking, that could be used for its control are described.

INTRODUCTION

Steel is used in many widespread environments and while it is a very versatile material, it needs to be protected from corrosion in order to avoid premature failure. This can be achieved in many ways, but the most commonly adopted method is the application of a protective coating. These coatings can be applied in a range of ways including; simple organic methods such as painting and spraying techniques[1], metallic sputtering, plasma vapour deposition [2], chemical vapour deposition, hot dip galvanizing, anodizing, composite coatings[3], organic metal flake coatings (e.g. Dacromet) and electroplating with or without conversion coatings[4].

Electrodeposition is commonly used, because it is generally fast, cheap and effective in many situations. However, an inherent problem with all electroplating is that the electrodeposition of a metallic coating on to high strength steel introduces the risk that the steel will fail by hydrogen embrittlement (HE). Plating processes generally have a current efficiency of less than 100%. A proportion of the current passed during electrodeposition results in the generation of hydrogen, some of which becomes incorporated in the deposit and subsequently diffuses into the steel substrate. This hydrogen can have deleterious effects on the steel substrate and so stringent testing is required to determine the extent of any HE of the steel. The number of listed deaths caused by structural failure, fatigue or HE on aircraft from 1920 - 2000, is 1,488 [5].

Where HE is thought to present a risk, de-embrittlement treatment may be required. Embrittlement effects are often further complicated by slow diffusion rates of hydrogen through the electrodeposit which can effectively "trap" the hydrogen making its elimination much more difficult. For example, steels with an ultimate tensile strength over 1800MPa would require baking for 24 hours at a temperature between 190 and 230°C, following cadmium electroplating [6].

A wide variety of steel components manufactured from non-corrosion resistant alloys are currently protected from corrosion using coatings of electroplated cadmium. Cadmium provides excellent corrosion protection and its sacrificial nature means that if the coating is damaged, cadmium will still protect the steel substrate by corroding

preferentially. Cadmium has excellent galvanic compatibility with aluminium alloys, which is especially useful in aerospace applications. It has a low coefficient of friction, so requires moderate torques to set the loading even without the use of lubricants. This is useful when re-tightening plated nuts and threaded components and due to these properties, cadmium plating is used in many situations for component protection, by both the aircraft and land vehicle industries. Cadmium plating is also particularly effective as a coating for steel in marine environments, being both a barrier and sacrificial coating in chloride bearing media. Its performance can be further improved by the application of a passivation treatment over the electrodeposited layer [7].

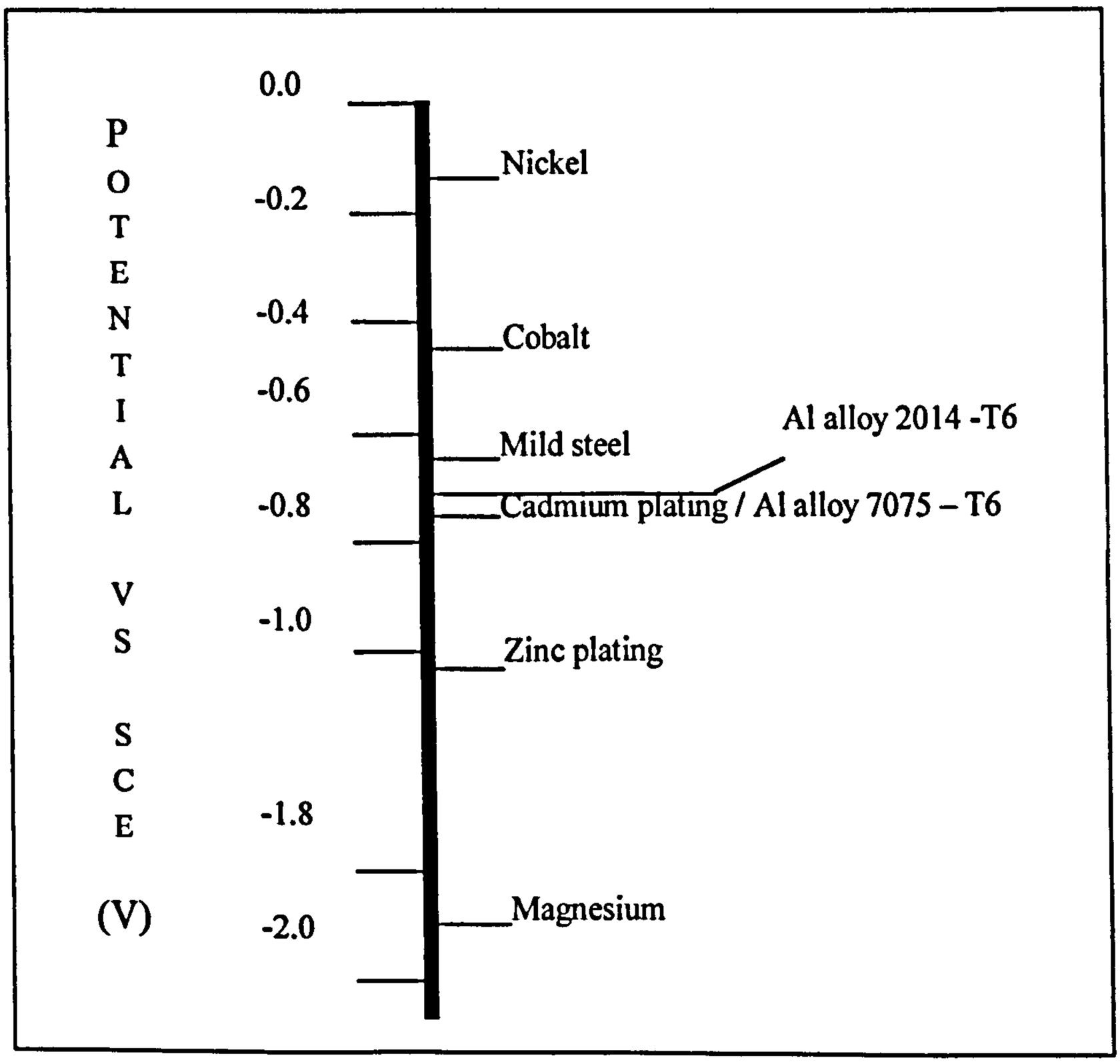
However, cadmium and cadmium containing compounds do have a major disadvantage in that they are toxic. Environmental and safety concerns have caused the industries using them to look for alternative materials. The reason for this are two fold; the cadmium itself is carcinogenic and the electrolytes from which it is deposited are cyanide based which leave dangerous effluent that needs to be treated before disposal. Many aerospace companies e.g. Boeing, spurred on by legislation, have been investigating cadmium replacements for well over a decade [8].

When considering replacements for cadmium several things must be considered. The desirable characteristics the coating must have, the way in which it will be produced and any problems associated with its production or use. One possible replacement for cadmium coatings are zinc or zinc-alloy coatings. As seen in FIGURE 1, zinc is even more electronegative than cadmium and would therefore act as a sacrificial coating for mild steel components. Indeed pure zinc coatings have been used for many years as a sacrificial coating on steel substrates. Zinc provides an excellent protective layer even when slightly damaged but the lifetime of the coating is directly related to the thickness of the zinc [9]. In the maritime atmospheres to which aircraft are often exposed, zinc gives excellent protection, whereas in acidic conditions it is regarded as too active, resulting in rapid loss of the coating. While greater protection could be afforded by increasing the thickness of the zinc layer, this is not always possible as there maybe interference problems on threaded parts, such as nuts and bolts. The corrosion products from zinc plating are also voluminous and can in turn, cause wedging and seizure of threaded

parts. The reaction that can be experienced with aircraft fuel also results in zinc coatings being of limited use in certain aerospace applications.

The use of alloying to increase the corrosion resistance of the zinc, without increase in coating thickness, by additions of a more noble metal has been practised for some years. Both zinc-nickel and zinc-cobalt alloys have been examined along with other transition group metals [10, 11, 12, 13, 14] multi- layer deposits[15] and composites [3]. Corrosion resistance can be significantly improved by the additions, with minimal increase in cost for the coatings and without incurring increased environmental issues [16]. Electrodeposited zinc and zinc-alloys are particularly recommended for applications on aerospace parts, which may experience operating at elevated temperatures during their service [7].

FIGURE 1: Open Circuit Potential of Some Metals and Alloys in 3.5% NaCl Solution at 25°C[17].

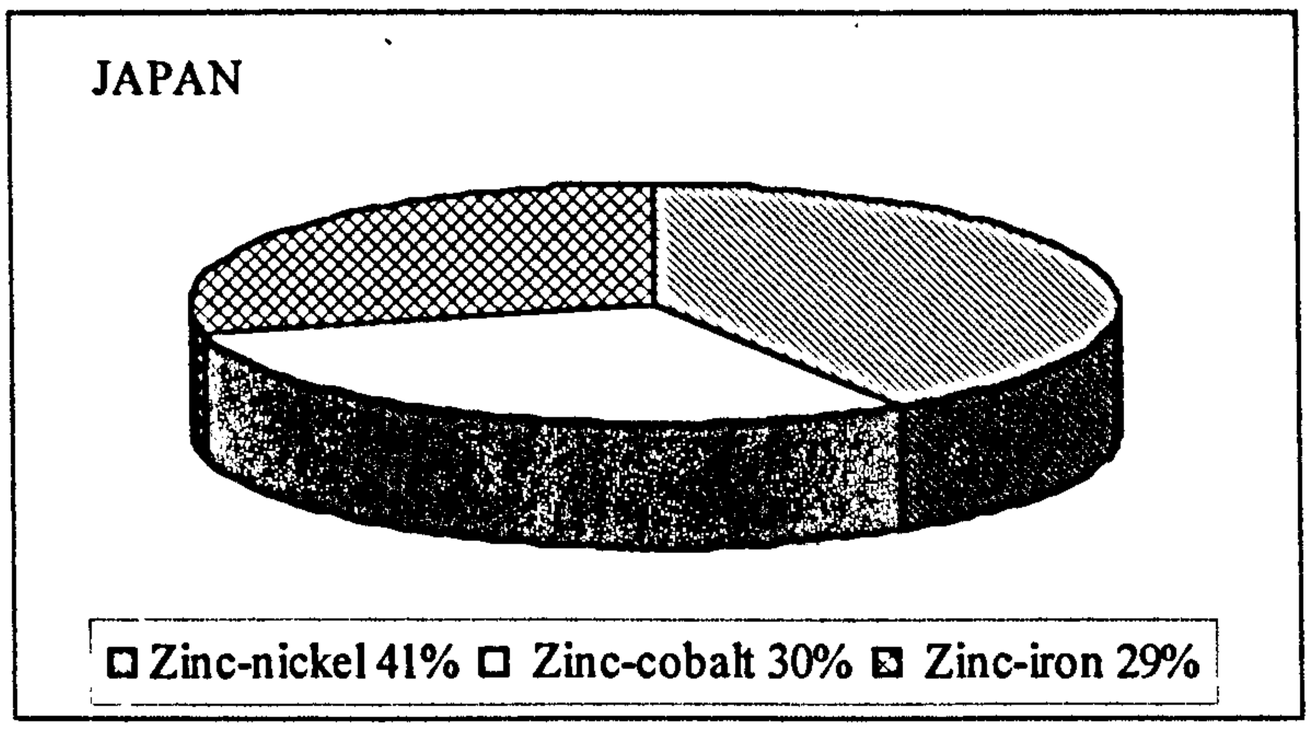


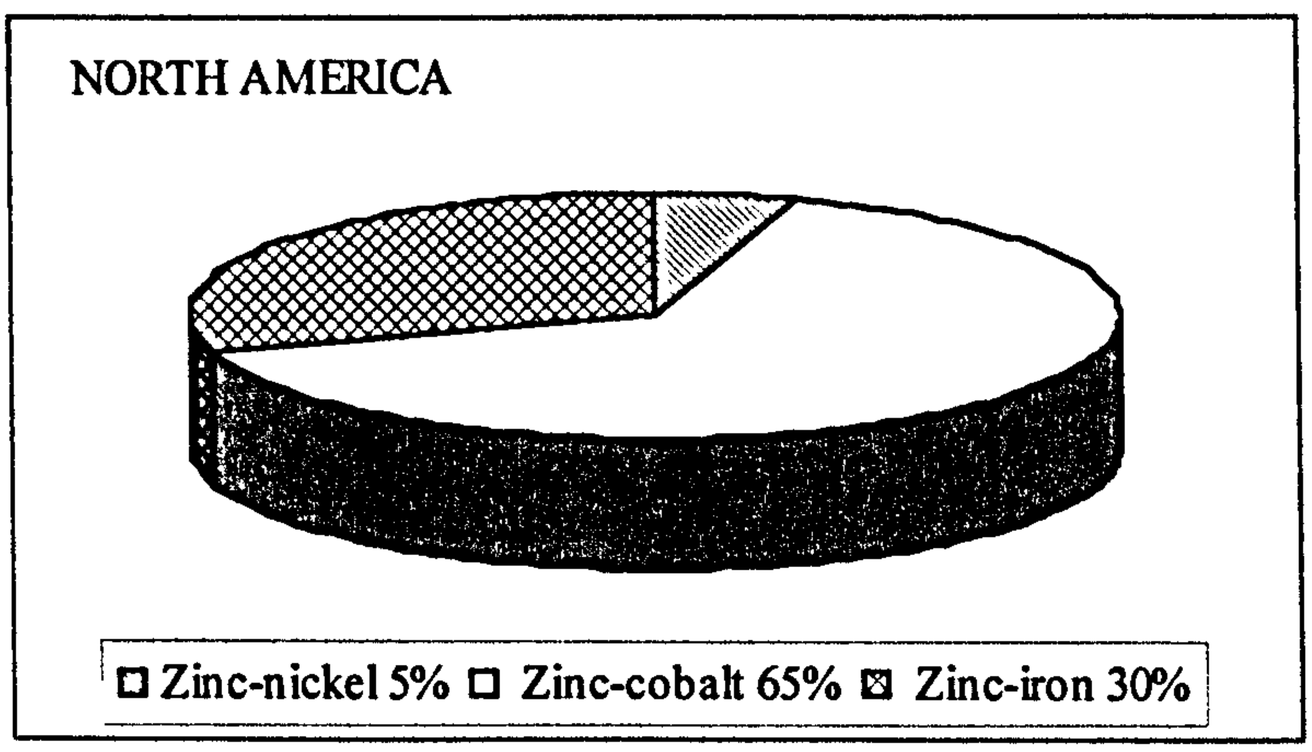
The electrodeposition of zinc-iron group metals can be carried out from a simple aqueous bath using conventional apparatus without the need for complexed electrolytes or extreme experimental conditions. The small quantity of noble metal in the alloyed coating, to provide increased protection, can be partly attributed to the unique type of deposition mechanism it undergoes. The 'Normal' deposition mechanism would produce a coating rich in the noble metal component. However, under certain conditions 'Anomalous co-deposition' can occur, allowing the less noble metal to be preferentially deposited, thus easily producing an unusual electrolytic alloy rich in zinc. The noble component is the first to be deposited which causes a rise in pH, which allows the precipitation of zinc hydroxide that can then be reduced to zinc metal on the surface. Further examination of coatings such as these, indicates the presence of 'an interlayer' of noble metal close to the surface which may provide additional beneficial properties[18].

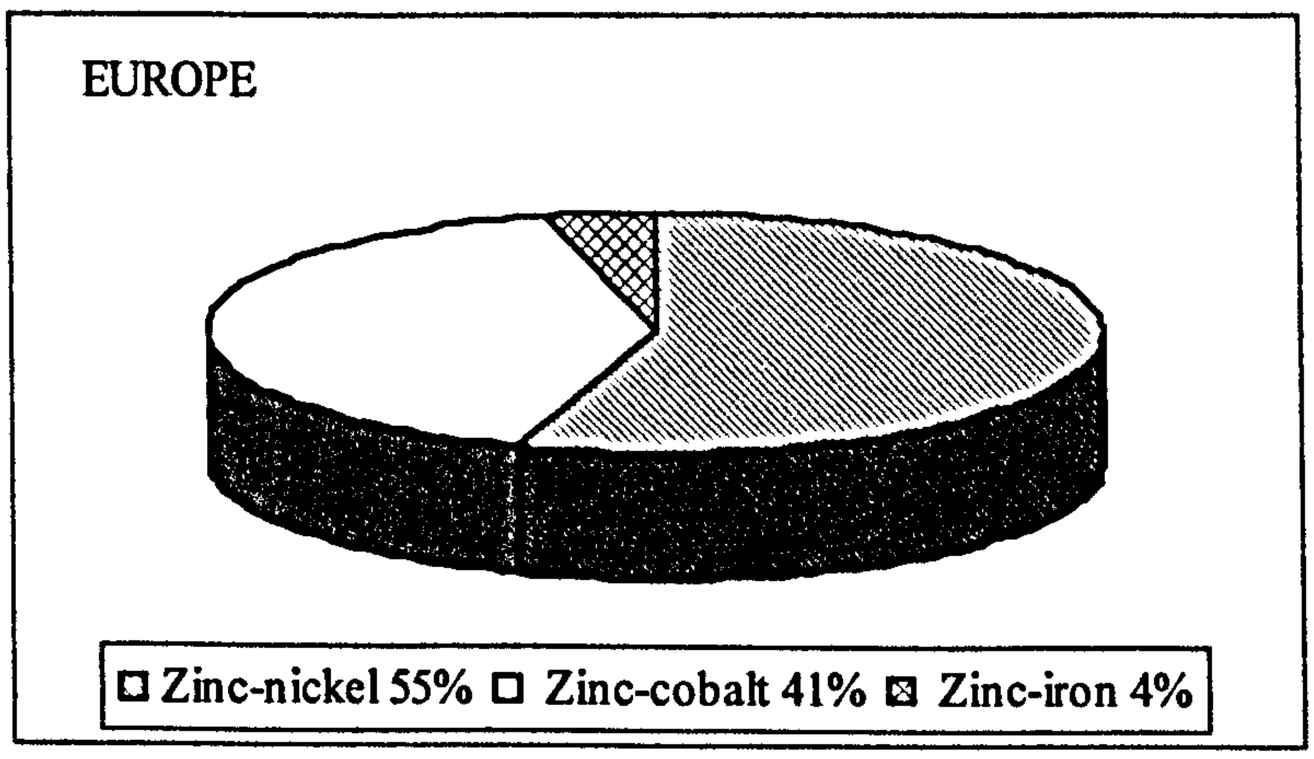
Electrodeposited zinc-cobalt alloys appear to offer very good properties, with the optimum corrosion resistance occurring between 1- 4% Co by weight. This represents a significant saving in cost compared to zinc-nickel alloys, which require approximately 10-14% Ni by weight to give similar corrosion resistance [19]. However, the toxicity of nickel salts is now also believed to be unacceptable.

Currently, in Britain, zinc-cobalt electroplating systems are used in the automotive, motor cycle and electrical fitting industries [20]. In Europe zinc-cobalt plating has been used for protection of ski bindings because of its excellent temperature and scratch resistance properties. Zinc-cobalt plating has, in one circumstance, also replaced zinc-nickel barrel electrodeposition of hydraulic components, as well as being used as a cadmium replacement in North Sea oil and gas extraction equipment. Japan and North America have followed Europe and use considerable quantities of binary zinc-alloy electroplating, including zinc-cobalt, where zinc galvanizing would have been previously used [21]. FIGURE 2 illustrates the percentage of zinc-cobalt electroplating used worldwide in 1992 compared to other binary zinc-alloy types. The figures shown relate to situations where galvanizing would have previously been used, including uses in the water, chemical and energy production industries.

FIGURE 2: Zinc-Alloy Types Used in Japan, USA and Europe in 1992 [21]







The first industrial zinc-cobalt system was introduced in 1982, and it employed an acid based bath which produced coatings for specific motor vehicle components including some machined high strength steel parts [22]. It is particularly useful because it can be used on virtually all ferrous materials including cast iron brake components and mild steel pressings. Ford, Chrysler and Saab have all taken advantage of this system. However, there are concerns over the use of zinc-cobalt electroplating on high strength steels and Saab in particular has restricted its use to steel with a strength below 1400MPa [23]. TABLE 1 shows types of zinc-alloy coatings used in a variety of applications.

TABLE 1: Zinc-Alloy Systems and their Major Appliactions [20, 22, 24]

Zinc-Alloy	Country	Application
Acid zinc-cobalt	France Spain UK UK	Brake callipers Auto parts Electrical fittings Automotive
Alkaline zinc-iron	Benelux Germany/ Spain Scandinavia	Auto fasteners Automotive Automotive
Zinc-cobalt-iron	Germany/ Spain Scandinavia UK	Automotive Aerospace Automotive
Acid zinc-nickel	France Germany	Auto fasteners Automotive
Alkaline zinc-nickel	Germany/ UK	Automotive

Like many other electrodeposited systems a zinc-cobalt electroplated layer can have its properties further enhanced by use of a passivation treatment or conversion coating layer which is applied over it. Although this is not always required for the particular application for which it is being used, it is an advantage that makes zinc-cobalt

electroplating much more versatile [24]. Unsurprisingly the type of passivation treatments that are commonly employed for zinc-cobalt plated systems are very similar to those used for other zinc-alloy electroplated parts. Chromate treatments can be used to further enhance their corrosion performance.

Electroplated zinc-cobalt is being considered as a corrosion coating replacement for cadmium on high strength steels (UTS 1800 MPa) commonly used in the aerospace industry. This is due to promising corrosion performance in salt spray testing and improved physical characteristics compared with pure zinc.

The objectives of the current study are outlined below:

- Hydrogen permeation measurements were used to determine the amount of hydrogen absorbed by a steel specimen during zinc-cobalt electroplating.

- The effect of electrolyte modifications on the quantity of hydrogen absorbed by the steel substrate was investigated. The parameters examined included pH, current density, temperature, deposition time, multiple layering of coatings and bath composition.

- Hydrogen absorption and embrittlement of high strength steels electroplated with nickel, cadmium and zinc-nickel alloys have been the subjects of two recent research programs carried out at Cranfield [18, 25]. These findings were compared with the data for the zinc-cobalt electrodeposits collected during this work.

- Hydrogen embrittlement testing of electroplated high strength steel specimens was used to detect any reduction in mechanical properties that resulted from the coating.

- The effectiveness of post-plating heat treatments in removing absorbed hydrogen and avoiding the risk of hydrogen embrittlement of the steel substrate was also studied.

- Determination of the optimum electroplating conditions and de-embrittlement treatments required for zinc-cobalt coatings was achieved from embrittlement and hydrogen permeation data.

- Examination of the corrosion performance of the various unchromated single layer coatings studied was carried out for comparison with their relative embrittlement performances.

LITERATURE REVIEW

HYDROGEN EMBRITTLEMENT

Hydrogen embrittlement (HE) can be defined as, 'The hydrogen caused reduction of the load bearing and / or the mechanical energy absorption ability of a metallic alloy'[26]. Hydrogen absorption can occur during metal processing and fabrication, in processes such as electroplating, solidification, forging and welding [27]. It may also occur during service in a hydrogen containing environment from corrosion, galvanic interaction between dissimilar metals and cathodic protection, often termed re-embrittlement [28].

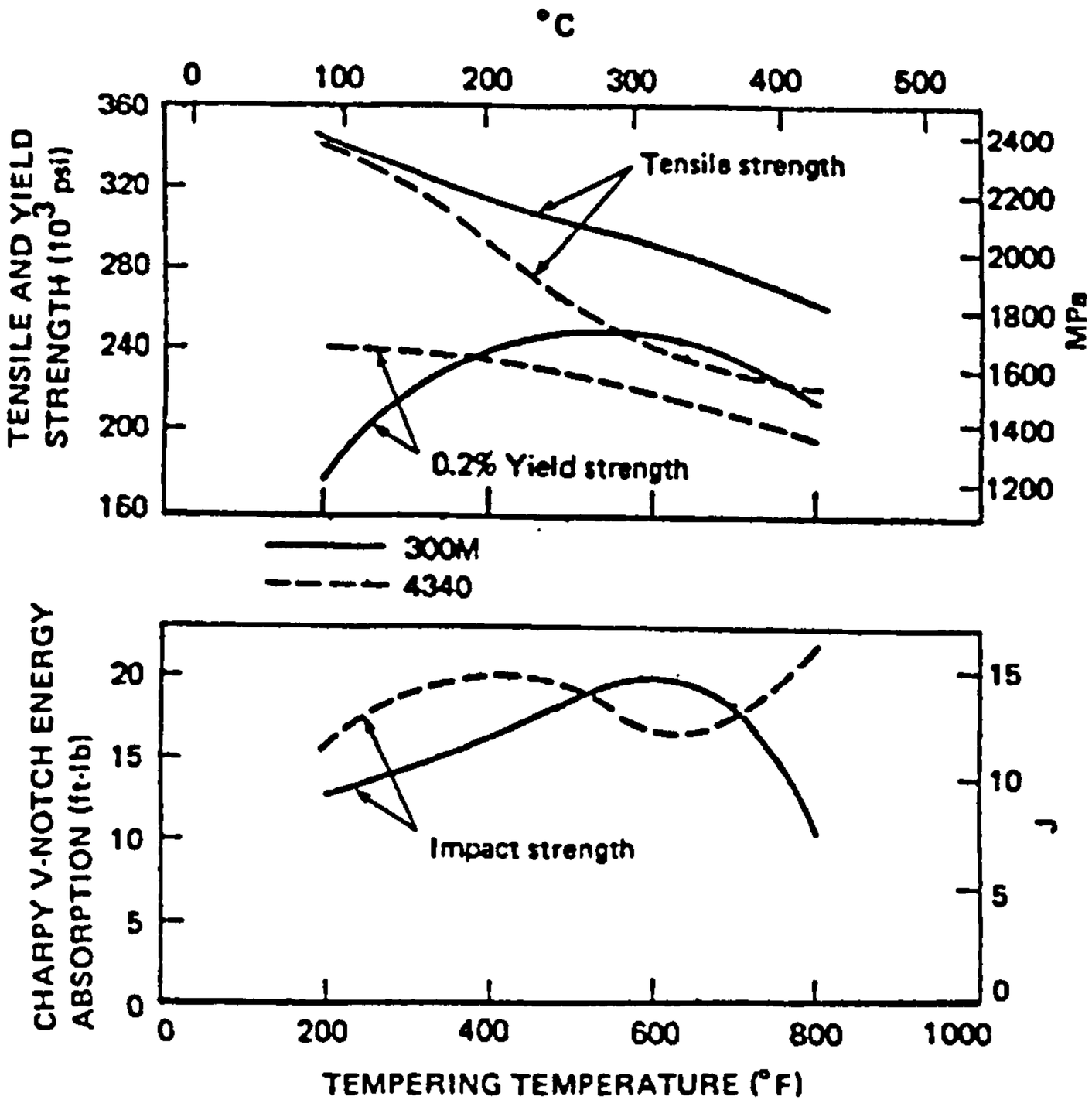
Once the hydrogen has been introduced into the steel substrate, it can then cause an embrittlement effect. Hydrogen embrittlement can have significant integrity consequences for many applications that operate under pressure or load. Hydrogen degradation of steel is well documented and the effect on mechanical properties, such as loss of macroscopic ductility or cracking of the steel is often attributed to HE [29]. Slow strain rate test specimens can show a decrease in tensile strength due to HE. They are generally also accompanied by a reduction in area, but their yield strength is not significantly affected. However, an increase in yield strength usually leads to an increased HE susceptibility, for steels and certain other high strength alloys [30].

The HE susceptibility of a material is temperature dependent, both in the service environment and more importantly during processing because of its influence on the microstructure that is produced. The microstructure HE susceptibility is; lower banite< quenched and tempered martensite< pearlite or spheroidized structures < untempered martensite is the most susceptible [28]. Developments in steel processing allow steels with desirable characteristics e.g. finer ferrite grain sizes, lower carbon content and higher strength and lower HE susceptibilities to be produced, by maintaining strict microstructural control [31].

Steel microstructure and chemical composition have an interrelated effect on the susceptibility to hydrogen degradation. Higher carbon content in steel is regarded as detrimental, increasing the susceptibility to HE. The degree to which this occurs is also dependent on the heat treatment used during manufacture and processing. Steel

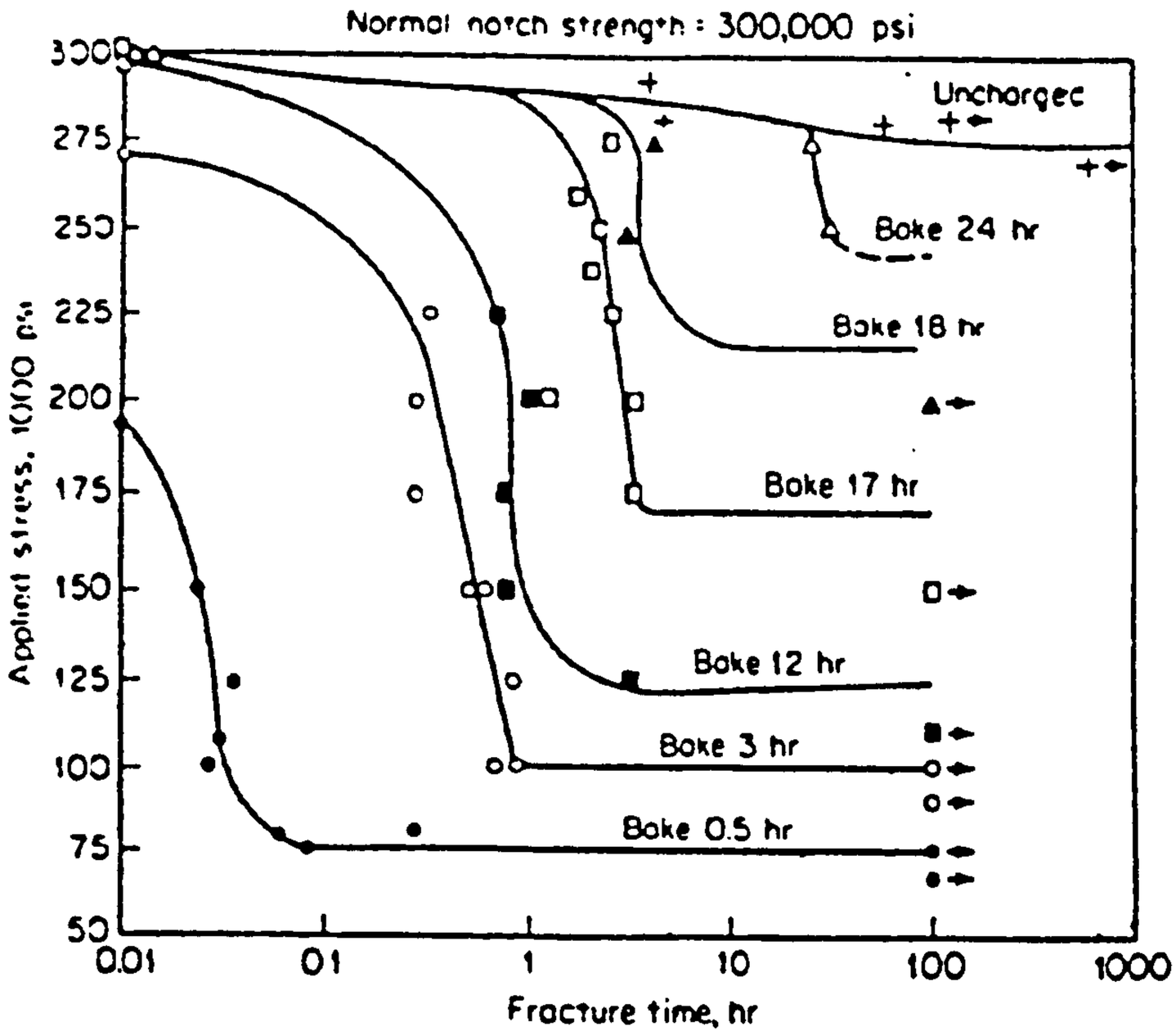
hardening is carried out by heating the steel between recommended values for a set time, followed by quenching in oil or air for thin sections, to produce maximum hardness. Tempering to relieve internal stresses and allow further hardening by precipitation processes can occur between 200 and 650°C. Tempering time is minimised (generally recommended for at least 30 minutes), followed by air cooling. Tempering temperature can have pronounced effects on tensile strength and is also often minimised, as shown in FIGURE 3.

FIGURE 3: Tempering Effects on the Tensile Properties of 4340 and 300M Steels [18]



Steel that contains hydrogen from either deliberate charging or an industrial process, benefits from a post treatment baking cycle. Baking facilitates hydrogen diffusion to microstructural traps within the steel or escape to the atmosphere. The temperature at which it is carried out and the duration of treatment are carefully controlled to avoid loss of strength. FIGURE 4 shows the effect of baking time on charged AISI 4340 fatigue specimens. Despite baking being an effective method of removing hydrogen, it is important to remember that the process is costly and time consuming.

FIGURE 4: Static Fatigue Tests on Hydrogen Charged AISI 4340 Steel after Various Baking Times [18]



When considering whether a steel specimen or component has failed by HE it is necessary to look at the composition and microstructure of the material along with the operating conditions and environment. The way in which specimens fail can vary significantly. It is important to remember that the failure modes that are considered to be due to HE are not always mutually exclusive of one another and there may be more than one mechanism or mode operating at the same time. The failure mechanisms are discussed fully later in the Chapter, but are outlined briefly below.

HE FAILURE MODES

Hydrogen Cracking

Generally, quenched and tempered steels are vulnerable to hydrogen damage that takes the form of cracking. Hydrogen assisted cracking, as it is termed, follows prior austenite grain boundaries if the level is sufficient. Refining the grain boundary size by heat treatment reduces the susceptibility to stress corrosion cracking (a particular form of HAC) in sulphide environments, and reducing it seems to act as a barrier to crack growth [32]. This maybe due to the relationship between grain size and strength, or due to a larger effective grain boundary area that may not deleteriously accumulate hydrogen.

Environmental Embrittlement

Hydrogen environment embrittlement occurs during the plastic deformation of ferritic steels, nickel based alloys, titanium alloys and austenitic stainless steels that are in contact with a hydrogen rich environment. The degradation of their mechanical properties is highest with a low strain rate and high hydrogen concentration [40].

Brittle Fracture

Brittle fracture under sustained load, usually below the yield strength of the material, due to hydrogen can be called hydrogen stress cracking. The hydrogen fugacity, material strength, heat treatment, microstructure, applied stress and temperature all affect the material response. The absorption of hydrogen and a delayed time to failure (incubation time during which hydrogen diffuses to regions of high triaxial stress) are associated with this phenomenon.

High Temperature

Hydrogen damage can occur in carbon and low alloy steels that are subjected to hydrogen at high temperatures for extended periods of time. If sufficient thermal energy is available, (400 - 500°C) combined with high hydrogen pressures, hydrogen may reduce carbide or oxide inclusions at grain boundaries to form methane or water. The resulting loss in strength of the alloy is due to a change in volume in certain areas of the lattice from the hydrogen reaction. The resulting crack and decarburisation of the steel leads to an increased susceptibility to ductile failure.

Blistering

Blistering occurs predominantly in low strength alloys. Atomic hydrogen diffuses into internal defects e.g. laminations or non-metallic inclusions, and then precipitates as molecular hydrogen [33]. This can reach a level that causes localised plastic deformation of the alloy, forming a blister that may rupture. As the stresses build up on neighbouring inclusions, coalescence of the cracks by localised shear can occur and this can be termed step-wise cracking. Exposure to aggressive corrosive environments containing hydrogen sulphide or pickling can induce this form of failure.

Shatter cracks, flakes and fish eyes are comparable to blistering. They can occur during forging, welding and casting. During the melting operation, hydrogen is picked up due to its higher solubility in the liquid metal than in the solid form. When the melt solidifies, hydrogen diffuses to voids or discontinuities and concentrates forming structures similar to blisters. Micro-perforation, also similar to blistering, can occur in steels at extremely high hydrogen pressures at room temperature. A network of small fissures open in the alloy due to hydrogen which can then allow permeation by gases and liquids.

Loss of Ductility

Loss in tensile ductility and reduced elongation and / or reduction in area of specimens can be observed for steels, stainless steels, nickel based alloys, aluminium and titanium alloys that are exposed to hydrogen. Generally, loss of ductility is seen for lower strength alloys, it is more pronounced at low strain rates and the extent of damage is dependent on the hydrogen content of the material. Degradation of flow properties in hydrogen environments has also been found at ambient temperatures for iron and steel and at elevated temperatures for several alloys systems [34].

Hydride Formation

Loss in ductility in many metals and their alloys can be accredited to the precipitation of metal hydride phases, due to hydrogen uptake from welding, heat treatment, charging from corrosion or melting of the alloy. Hydride formation can be enhanced by the application of stress and its effect on ductility is considered to be temperature dependent.

HYDROGEN EVOLUTION AND ENTRY

Corrosion can occur via the oxygen reduction reaction (ORR), which is limited by the availability of oxygen, or via the hydrogen evolution reaction (HER). In neutral or alkaline solutions, hydrogen evolution occurs infinitely slowly, and, in the absence of oxygen, so does corrosion. EQUATIONS 1-4 show the possible reactions undergone by hydrogen under various pH conditions.

EQUATION 1: Hydrogen Formation

$$2\,H^+ + 2e \rightarrow 2\,H \rightarrow H_2$$

EQUATION 2: Oxygen Reduction Reaction

$$\tfrac{1}{2}\,O_2 + 2H_3O^+ + 2e \rightarrow 3H_2O \qquad \text{(acid)}$$

$$\tfrac{1}{2}\,O_2 + H_2O + 2e \rightarrow 2OH^- \qquad \text{(neutral, alkaline)}$$

EQUATION 3: Hydrogen Evolution Reaction

$$H_3O^+ + e \rightarrow \tfrac{1}{2}\,H_2 + H_2O \qquad \text{(acid)}$$

$$H_2O + e \rightarrow \tfrac{1}{2}\,H_2 + OH^- \qquad \text{(neutral, alkaline)}$$

EQUATION 4: Hydrogen Absorption Reaction

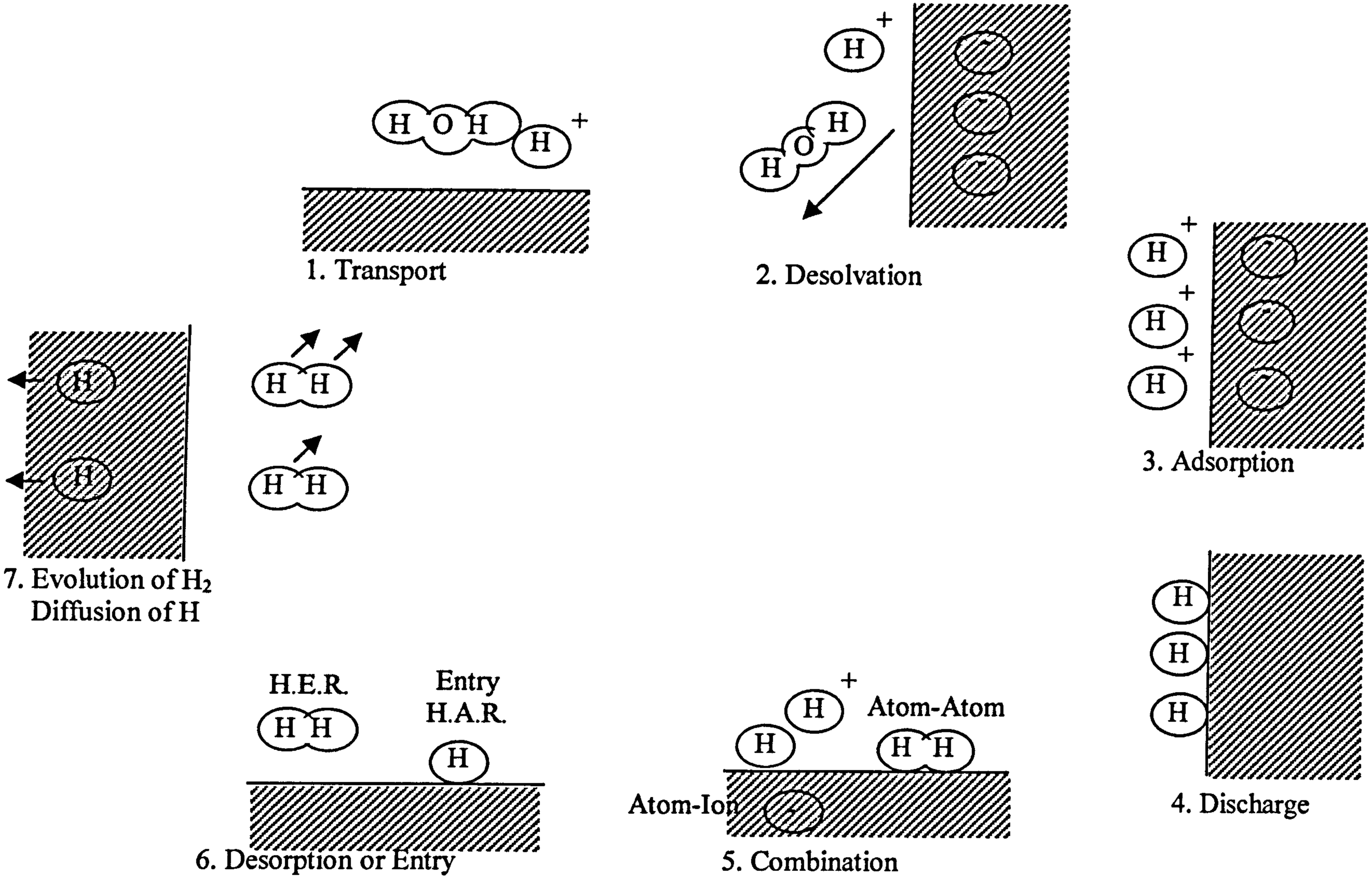
$$H_{adsorbed} \underset{k_{des\ (desorption)}}{\overset{k_{abs\ (permeation)}}{\rightleftarrows}} H_{absorbed}$$

THE MECHANISM OF HYDROGEN EVOLUTION OR ENTRY

It is generally accepted that hydrogen evolution occurs via a two step process. The first step, common to all metals, is reduction of water to form a metal hydride and hydroxyl ions. Due to the high overpotential required to produce hydrogen it is assumed that the oxidation of the adsorbed hydrogen is negligible. The next step depends on the nature of the electrode metal and the cathodic current density. Detachment of hydrogen atoms from the surface of the metal may either be under chemical (recombination) or electrochemical (absorption) control. Metals that can absorb hydrogen undergo the hydrogen evolution and absorption reactions simultaneously. Absorption provides an alternative reaction path to chemically controlled detachment of a hydrogen molecule or atom. The process by which hydrogen enters a substrate can be divided into a stepwise mechanism.

FIGURE 5 illustrates the steps that are necessary for hydrogen diffusion or evolution to occur on a metal surface. Firstly, a hydrated proton (H_3O^+) is transported to the double layer at the metal surface. The desolvation step promotes the loss of the hydration shield next to the double layer. Once the proton has been adsorbed to the metal electrode surface, discharge of electrons can occur, forming a neutral adsorbed hydrogen atom. Combination occurs in two ways. Chemical combination of two adjacent adsorbed hydrogen atoms can occur forming a hydrogen molecule. Migration between the discharge and recombination site can occur, and is termed the coupled discharge mechanism. An adsorbed hydrogen atom can also combine directly with a proton that is simultaneously reduced by an electron, thus forming a hydrogen atom. Next, either desorption of hydrogen molecules (HER), or absorption of hydrogen atoms can occur. In the final stage, either hydrogen molecules evolve as bubbles of H_2, or hydrogen atoms diffuse into the metal substrate.

FIGURE 5: Mechanistic Steps During the Hydrogen Evolution Reaction [35]



HYDROGEN ENTRY MECHANISMS

There are two proposed models for hydrogen entry into a metal [28]. Model A considers hydrogen entering in the atomic state which it exists in on the substrate surface. In this model absorption and chemical desorption (recombination) of hydrogen are competing processes. Therefore, the entry rate should be proportional to the surface coverage of adsorbed hydrogen atoms. Model B proposes that hydrogen enters in the same form in which it is discharged i.e. as protons. This leads to independent evolution and absorption reactions.

These models A and B can also be related to the type of chemisorption that is seen for a system. If the bonding of hydrogen atoms with the metal is considered to be covalent, it is termed r-type. The hydrogen is the negative part of the dipole and it is positioned directly over, but outside, a corresponding metal atom's electronic cloud. Model A is comparable with this type of chemisorption. It has been shown, from resistivity experiments with nickel and platinum, to dominate at low hydrogen surface coverage. However, if the surface coverage is high, model B will operate because s-type adsorption will occur. This higher energy state is seen with lattice defects or surface imperfections. Hydrogen in this case bonds in a more ionic manner, behaving like protons within the metal atoms electronic cloud.

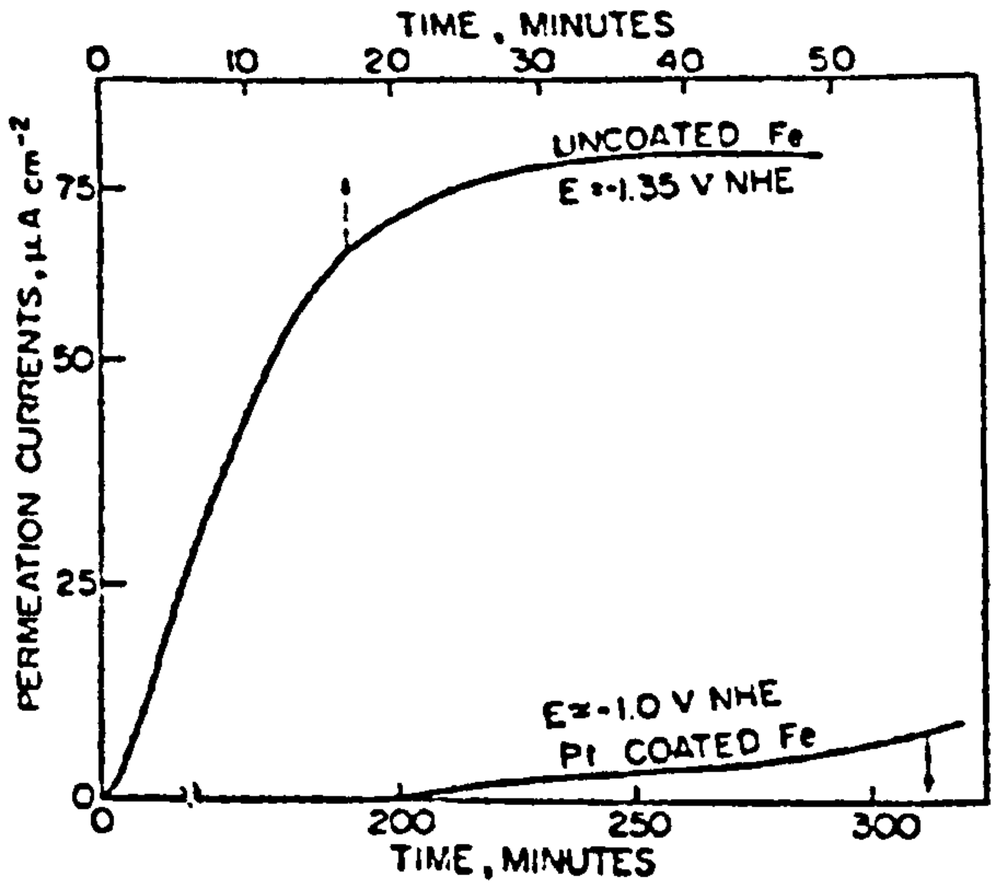
ABSORPTION SURFACE EFFECTS

Usually only a small quantity of hydrogen that is liberated at the cathode enters the metal, but the absorbed hydrogen can diffuse into the steel resulting in embrittlement. Cathodic poisons such as arsenic and thiourea (hydrolysed to hydrogen sulphide) can accelerate the hydrogen absorption reaction by preventing evolution and so promoting absorption. In the laboratory, mineral acids can be used to generate diffusible hydrogen allowing hydrogen embrittlement to be studied.

It has been found that if a metal has a high exchange current density, such as palladium and platinum, it rapidly loses its adsorbed hydrogen and so has low hydrogen surface coverage [18]. This can reduce the amount of hydrogen that is absorbed by a metal substrate, and can result in a lower embrittlement probability. FIGURE 6 shows that discontinuous Pt, Cu or Ni coating on steel substrates can reduce the quantity of

hydrogen entering the substrate. The surface and subsurface of a metal can behave differently with respect to hydrogen diffusivity and result in a discontinuity in the hydrogen concentration gradient. This effect will be discussed later in this Chapter.

FIGURE 6: Effect of an Electroplated Layer on the Observed Permeation Transient [18]



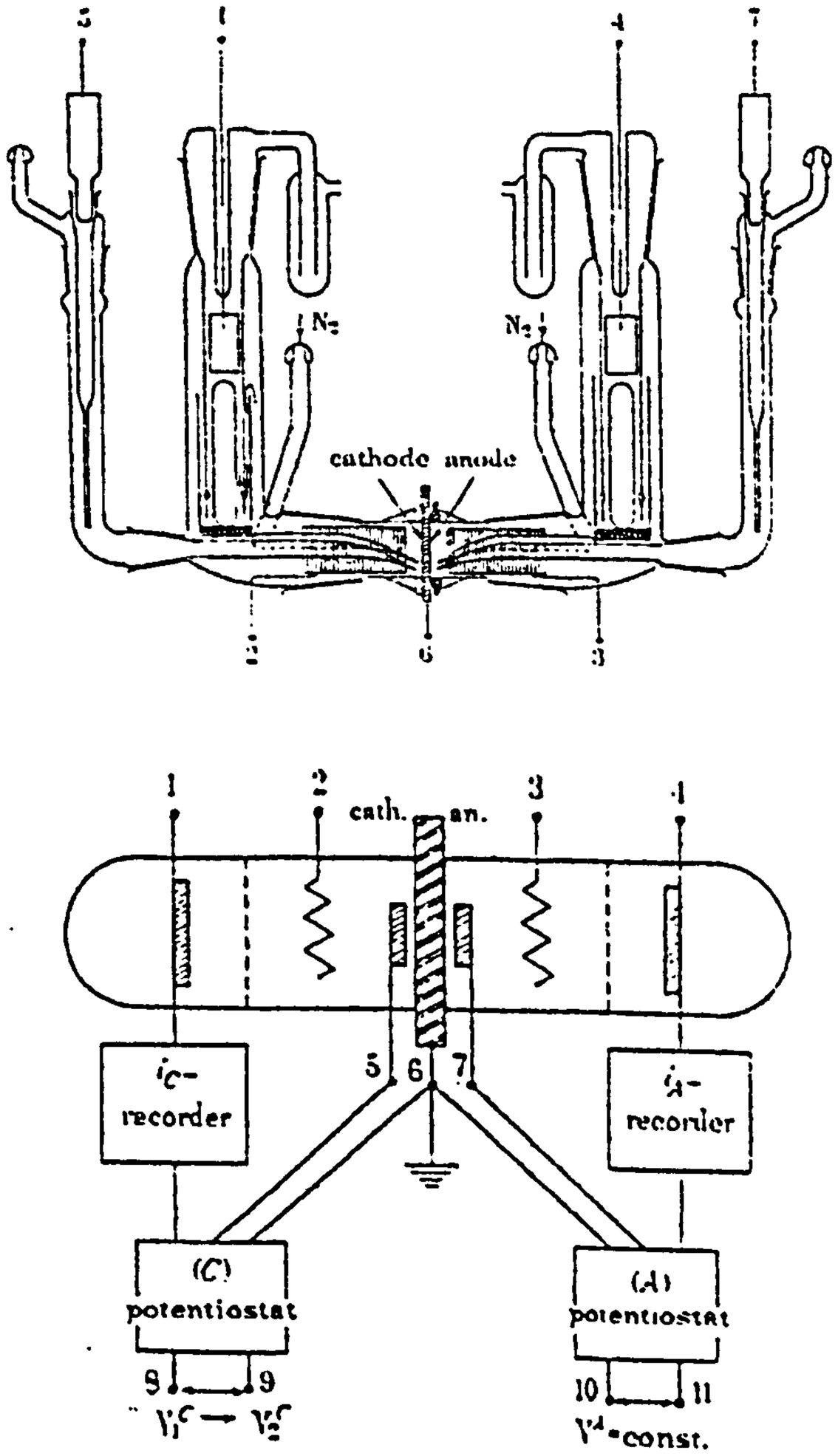
Bockris and Koch [36] studied the hydrogen evolution reaction using hydrogen and deuterium from iron cathodes. They concluded that the rate determining step (RDS) for the reaction was simply the slow discharge of a proton to an adsorbed hydrogen atom, the combination step in FIGURE 5 (step 5).

Several groups have shown that the degree of surface coverage of hydrogen can be used to identify the subsequent steps in the hydrogen evolution mechanism[37, 38]. Mechanistic studies, do not require absolute values, as measurement of variation in coverage as a function of potential can be used to calculate the current density. Measurement of diffusion rates of hydrogen permeating through a steel membrane is an excellent way of carrying this out. Devanathan and Stachurski viewed the RDS in the evolution reaction electrochemically using sensitive laboratory permeation measurements with the double cell technique they pioneered [39].

The double cell apparatus shown in FIGURE 7 allows a metal membrane to be exposed to a source of mobile hydrogen, some of which adsorbs to the metal membrane and diffuses across it under the concentration gradient provided by the opposite side. On the

opposite side of the membrane, the atomic hydrogen that permeates through is oxidised to water, which produces an associated current. This current can be measured giving a direct indication of the amount of hydrogen present, once steady state conditions have been achieved. As the effective surface hydrogen concentration on the emerging (anodic) side of the membrane is zero, the surface hydrogen concentration on the input (cathodic) side can be calculated from the resulting steady state current.

FIGURE 7: Permeation Technique Apparatus, Cell and Circuit



Using their permeation technique, Devanathan and Stachurski determined, that the discharge step (step 4), followed by Tafel recombination at low overpotentials (step 5), and finally electrochemical desorption at overpotentials > 600mV NHE (step 6) were

the rate determining aspects of the model in FIGURE 5. The other mechanistic steps were not considered to limit the rate of reaction.

Hydrogen permeation measurement

Electrochemical methods for monitoring hydrogen permeation through membranes can be carried out under potentiostatic or galvanostatic conditions. Each of these methods provides a different set of boundary conditions at the metal surface. The anodic surface usually has the hydrogen concentration held at a minimum value relative to the background concentration. It has been previously assumed that these two modes of hydrogen charging will produce simple static boundary conditions at the entry surface. Potentiostatic charging was thought to produce boundary conditions that led to an anodic surface concentration of zero, a variable flux but a constant surface hydrogen concentration. It was assumed that galvanostatic charging would produce boundary conditions based on a constant flux at the charging surface.

Both these situations have proved to be incorrect because a transient, intermediate to that which was predicted, is produced [40]. Allcock investigated galvanostatically controlled permeation experiments and compared them with theoretically generated transients. He found that the experimental transient shape was in good agreement with constant surface coverage models, not the predicted constant flux model. The boundary conditions that are established depend on the electrochemical method of hydrogen introduction, the relative rates of the hydrogen evolution steps at the entry side of the membrane and the subsequent diffusion through the membrane[41, 42].

If the mechanism in FIGURE 5 is viewed physically, from a hydrogen absorption perspective, the RDS then is dependent upon the adsorption of the proton, (step 3). Under steady state conditions, (fixed surface coverage or concentration of hydrogen atoms on the surface), this is dependent on a specific rate constant, k_{abs}, shown by EQUATION 4. These constants can be estimated experimentally from the steady state hydrogen permeation current, obtained at various cathodic charging currents, using a series of interrelated equations developed by Iyer, Pickering and Zamanzadeh.

The IPZ model was formulated using experimental data from the Devanathan and Stackurski double cell technique. The hydrogen overvoltage and diffusivity could then be established from experimental cathodic charging values [37,43]. Manipulation of the model's equations can also result in determination of the mechanism undergone. In certain circumstances, the quantitative analysis of hydrogen partitioning between the evolution and absorption reactions can be achieved. Graphical evaluation of partitioning is possible if linear plots are obtained from EQUATION 5.

EQUATION 5a: Relationship Required for Hydrogen Partition Determination

$$i_{\infty} \text{ against } \sqrt{i_r}$$

Where: i_{∞} = steady state current density

i_r = hydrogen recombination current density

i_c = cathodic current density

$(i_r = i_c - i_{\infty})$, also $i_{\infty} = c_s/b$

c_s = surface hydrogen concentration

When a graph of i_{∞} against $\sqrt{i_r}$ is plotted and the relationship is found to be linear then hydrogen partition determination is possible. The alternate relationship shown below can also be used in this determination technique.

EQUATION 5b: Alternative Relationship Required for Hydrogen Partition Determination

$$f_{i\eta} (= i_c e^{a\alpha\eta}) \text{ against } i_{\infty}$$

Where: $b = L/FD_1$, $a = F/RT = 38.94\ V^{-1}$

η = hydrogen overpotential

α = HER transfer coefficient

From the determined values of flux, hydrogen discharge current, recombination and permeation reaction data the surface and near surface kinetics of the reaction can be studied. The important surface properties relating to hydrogen absorption and adsorption rate constants can be evaluated by combining complete polarisation data with the permeation data for different membrane thicknesses. The latter parameters can provide a quantitative description of the surface hydrogen coverage, using EQUATION 6.

EQUATION 6: Rate of Absorption and Adsorption Determination

$$(k'')^{-1} = (k_{ads}/k_{abs}) + (D_l/k_{abs})(L)^{-1}$$

Where:
- k'' = thickness dependant absorption/adsorption coefficient
- k_{ads} = adsorption rate constant
- k_{abs} = absorption rate constant
- D_l = diffusion coefficient
- L = membrane thickness

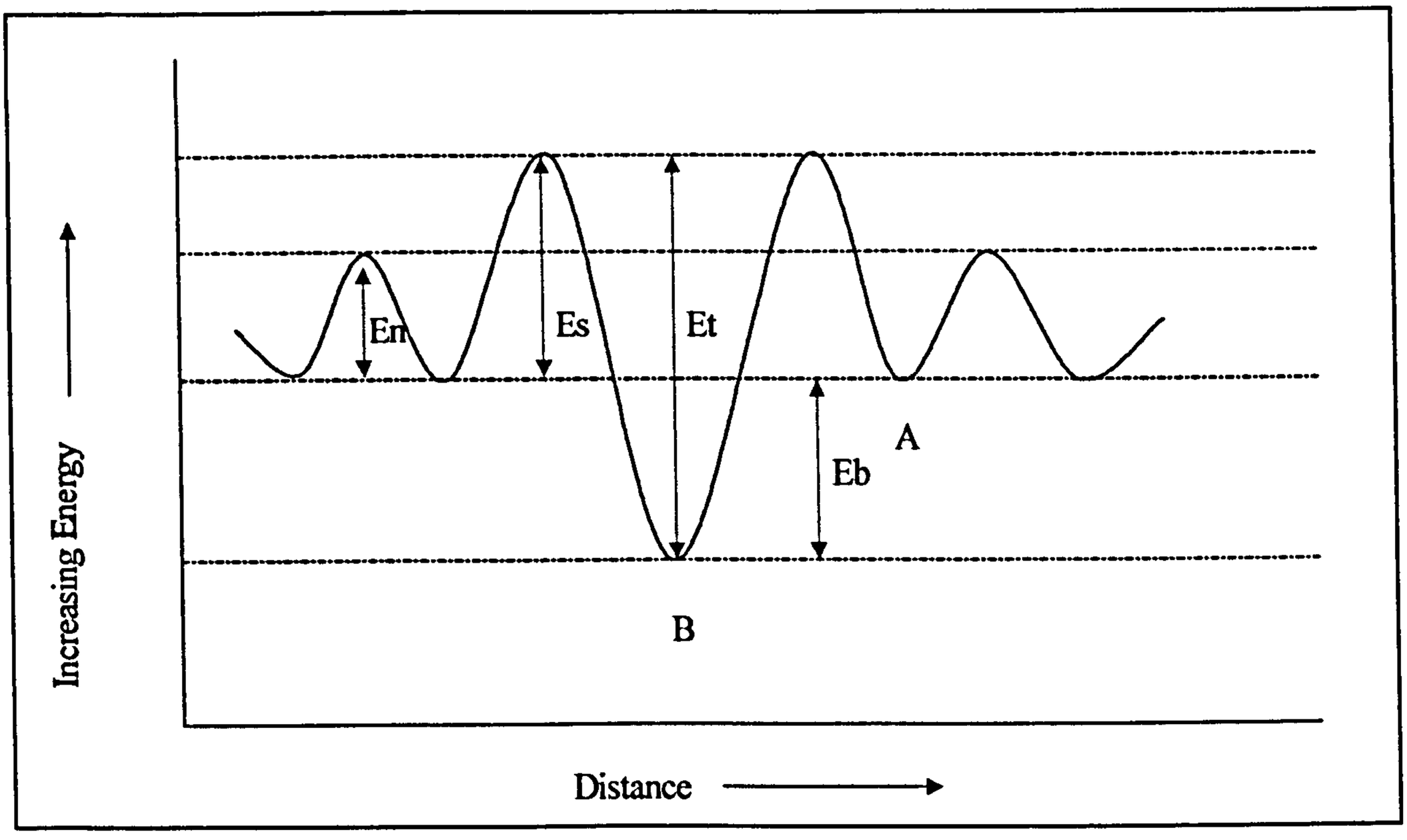
When a graph of 1/k'' is plotted against 1/L and it is shown to be linear, and if D_l is known the rates of absorption and adsorption can be determined.

TRAPPING OF HYDROGEN IN STEEL

Metallic materials are not perfect crystals as they contain defects or voids that can trap hydrogen e.g. crack tips, grain boundaries, carbide interfaces, inclusions and dislocations. The rapid diffusion of hydrogen, even at low temperatures, can result in speedy trapping. Trapped hydrogen in the metal matrix can interact with other dissolved hydrogen atoms to form clusters resulting in high concentration areas. These, in turn, can have deleterious effects on the metals mechanical properties. Once hydrogen is trapped, the hydrogen transport rate decreases, as the time spent in the trap is inevitably longer than the time spent in a normal lattice diffusion site.

There is an associated deepening of the theoretical potential energy well with hydrogen traps, which is shown in FIGURE 8 [44]. There are two distinct types of trap; reversible or irreversible, which can be present in a material in varying quantities. Reversible traps can only contain hydrogen for a limited time, at a given temperature, and have a low interaction energy. Irreversible traps under the same conditions, have a negligible probability of releasing hydrogen.

FIGURE 8: Model Showing Hydrogen Energy Levels in the Trap Vicinity [44]



Where : A = interstitial site

B = trapping site

Et = trap activation energy

En = absorption from surface to bulk energy level

Es = absorption from bulk to trapping site energy level

Eb = potential well of trapping site

The size of Eb determines type of site, if Et>Eb then trap is irreversible.

Traps affect the hydrogen distribution in the matrix, the quantity of hydrogen desorbed from the metal at room temperature and the hydrogen embrittlement susceptibility of the material. All of these factors are important when trying to understand hydrogen transport[40]. The type of trap present in a material can significantly effect the extent of any physiological effect that is seen.

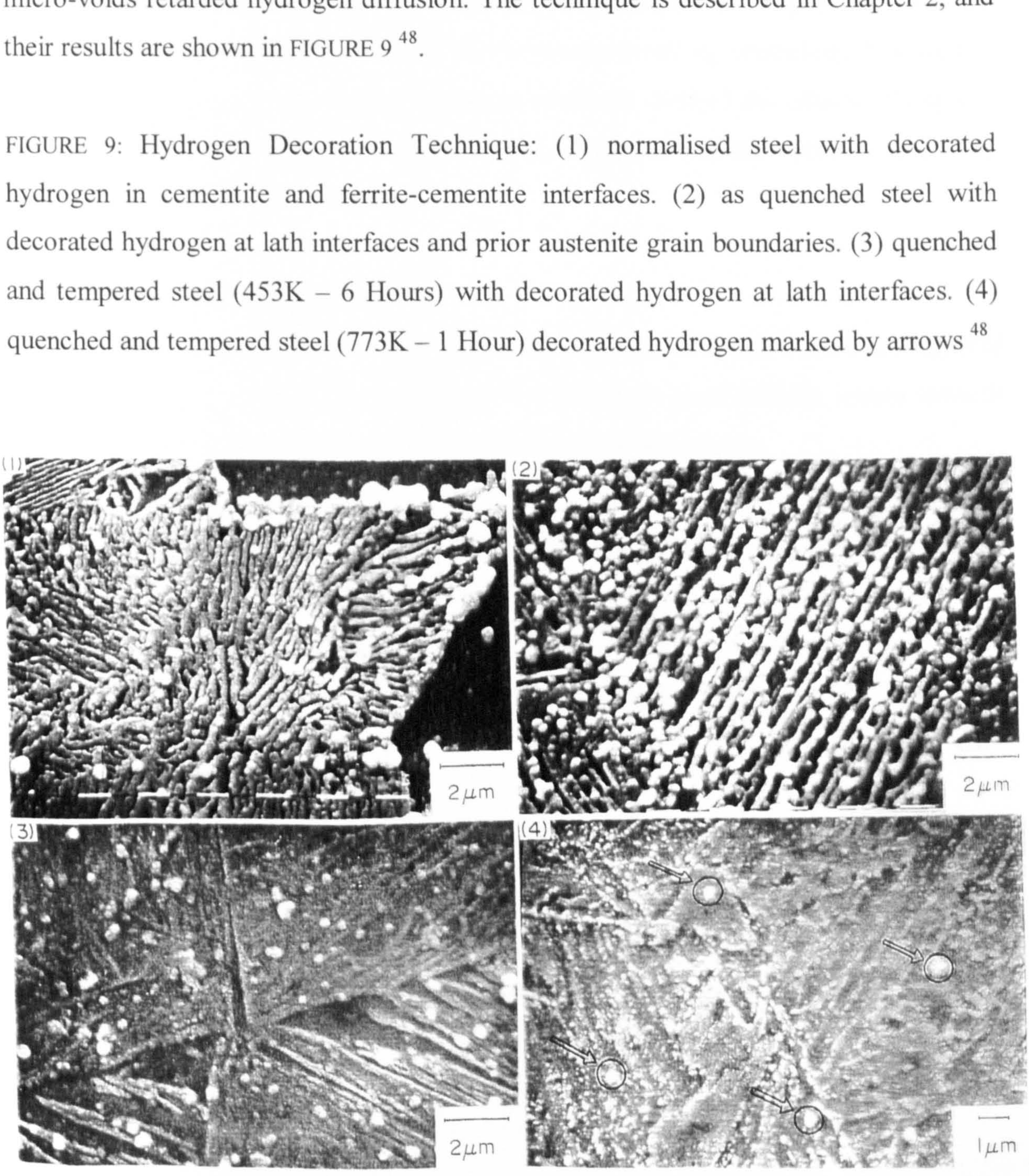
Several groups, undertaking high pressure or low temperature diffusion studies, have examined the effect trapping has on the hydrogen diffusion coefficient. McNabb and Foster [45], Oriani [46] and Koiwa [47] all considered the effect of different trap types, in

different lattice sites would have on steel diffusion coefficients. (It was generally assumed that there were tetrahedral or octahedral site occupancy in a body centred cubic {bcc} lattice structure).

Accumulation in Voids

Observing hydrogen accumulation in deliberately produced quenched vacancies in bcc metals has been difficult to achieve experimentally. However, Luppo and Ovejero-Garcia, used a silver decoration technique (HMT), to demonstrate that trapping in micro-voids retarded hydrogen diffusion. The technique is described in Chapter 2, and their results are shown in FIGURE 9 [48].

FIGURE 9: Hydrogen Decoration Technique: (1) normalised steel with decorated hydrogen in cementite and ferrite-cementite interfaces. (2) as quenched steel with decorated hydrogen at lath interfaces and prior austenite grain boundaries. (3) quenched and tempered steel (453K – 6 Hours) with decorated hydrogen at lath interfaces. (4) quenched and tempered steel (773K – 1 Hour) decorated hydrogen marked by arrows [48]



Von Ellerbrook used published information from outgassing experiments performed at room temperature, to fit experimental data that he obtained by calculating the release rate of hydrogen. He deliberately produced voids that contained hydrogen by annealing or deforming either iron or steel used in his experiments[49]. He proved that the non-Arrhenius behavior of hydrogen diffusion at high temperatures and <150°C seen could be attributed to reversible trapping in microvoids.

Kumnick and Johnson deduced microvoid hydrogen trapping from electrochemical measurements[50]. Armco iron foil was used experimentally to produce hydrogen permeation transients. When the foil used was produced by annealing, followed by rolling, the resulting experimental transients produced showed the effects of trapping. However, if the thin iron foil was produced by chemical reduction prior to annealing, similar transients were not produced.

Accumulation at High Strain Fields

Many theories of hydrogen segregation have been proposed but few have been proved experimentally. Numerous people assume that hydrogen preferentially moves towards the tip of a crack in a strain field and hence assists in crack growth.

Cottrell and Bilby [51] considered the way in which interstitials interacted with strain fields about dislocations and concluded that atmospheres of interstitials could form under the edge of dislocations. The published model was later confirmed by the interpretation of permeation work carried out by Kumnick and Johnson [50] . The trapping efficiency of a dislocation was found to be about 1 or 2 atoms of hydrogen per atom plane of dislocation length.

Cochardt [52] calculated the actual interaction energies of interstitials with strain fields about edge and screw dislocations. However, calculations for larger strain fields near interstitials are extremely difficult. The application of boundary conditions is further complicated by interactions between numbers of parts within the same system, so has not been achieved yet.

Grain Boundary Traps

It has long been established that grain boundaries are sinks for impurities and hydrogen can be absorbed on the interfaces between precipitates and the metal lattice. Podgurski and Oriani used iron-aluminium alloys to demonstrate that hydrogen is absorbed to the surface of the aluminium nitride particles [53]. The interface can reversibly absorb hydrogen at room temperature, but at temperatures >500°C, prior nitrogen absorption at the interface can block sites to later hydrogen absorption. Bernstein and Thompson [32] produced an excellent review of data for hydrogen absorption at iron and metallic carbide interfaces in steels that illustrate this type of trap.

Dislocation Trapping

A standard method for the measurement of dislocation trapping is to observe the absorption and evolution of hydrogen from a gaseous medium. Surface problems that can be encountered, can be overcome in part by coating the exit surface of specimens with a thin layer of palladium. Kumnick and Johnson [50] could not deduce the trapping energy from their permeation studies, because there were two sorts of traps present in their system. The transient deviations were due to deep microvoid traps as described by Von Ellerbrock [49] and also to dislocation traps. The presence of these traps, deduced from annealing studies, were thought not to be isolated.

It is important to remember that the steady state permeation rate of hydrogen through a material is unaffected by the presence of traps, provided that the traps are filled prior to equilibrium. Gonzales [54] reviewed hydrogen permeation in alpha-iron and concluded that, despite the inevitable varying density of traps present, the rates given were consistent. Donovan used tritium, a radioactive tracer, to generate a wide range of information, including the activation energies for tritium as a function of temperature in materials including iron and nickel [55]. He confirmed Gonzales findings, showing that accelerated evolution of hydrogen from metals during plastic flow yields consistent data.

Impurity Trapping

Impurity trapping has a more simply defined geometry than large scale voids, dislocations, boundaries and strained regions. The thermodynamics and kinetics of hydrogen bound to impurities are therefore also easier to specify. Iino [56] thought that precipitates or secondary phases in steels could be the trap sites that were responsible for controlling hydrogen induced embrittlement. He described the relationship in terms of binding energies between hydrogen and substitutional foreign atoms.

Trap characterisation

Hirth [57] produced hydrogen binding energy values associated with; an ideal lattice interaction, a hydrogen trap and deviations from both. Binding energy values can be found from shallow or reversible traps at ambient temperature by permeation, absorption or evolution experiments. However, the thermodynamic equilibrium of hydrogen in normal lattice sites and in abnormal trap sites must be assumed. Hydrogen traps that are not shallow at ambient temperature may behave as heat sinks and therefore high temperature experiments may need to be attempted [40].

Turnbull [58] compared the combined effects of reversible and irreversible trapping, with varying degrees of occupancy, on the hydrogen transport in metals. Coupled with electrochemical permeation measurements, he characterised diffusion and trapping in an oil tubing steel. He concluded that it was not suitable to use an effective diffusion coefficient to characterise hydrogen transport in systems that were dominated by irreversible trapping.

Generally, trap type and its efficiency to contain hydrogen is believed to be primarily a microstructural factor. This is linked to the observed embrittlement for a system, but whether a trap is can irreversibly trap hydrogen is also an important concern. Normalised steels with high carbon content and small carbide particles tend to lead to a large total interfacial area. This would lead to high levels of hydrogen trapping at carbide faces. However, quenched and tempered steels tend to hold high quantities of hydrogen in low energy reversible traps at dislocations.

De-embrittlement of hydrogenated specimens can be undertaken by baking treatments, which can help the steel to regain its non-hydrogenated properties. Standards have been produced from extensive research and are available for a wide range of steels. However, the basic idea is to remove as much potentially mobile hydrogen from the steel, as economically viable in a set time. The hydrogen targeted for removal is located in reversible traps because it may diffuse from here to cause an embrittlement effect. The duration and temperature of baking are economic considerations but the temperature used may also alter the steel microstructure. This can be undesirable as e.g. an austenitic steel microstructure can act as a hydrogen reservoir, causing embrittlement even after baking has been carried out. Both mobile and immobile hydrogen are present in steel because of the inherent trap sites. Manipulation of microstructure to create a fine dispersion of trapping sites within a metal can therefore be a beneficial tool to improve the hydrogen embrittlement performance of a particular steel.

Trap ranking

For the trap types that are mentioned in this section, dislocation and grain boundary traps can be considered to be reversible traps with a similar binding energy and the other types are stronger and can be considered to be irreversible traps[58]. Reversible traps are thought to be more significant because the hydrogen can diffuse to defect sites within the material and cause embrittlement whereas irreversibly trapped hydrogen cannot.

HYDROGEN EMBRITTLEMENT MECHANISMS

There seems to be no universal theory to clarify how hydrogen embrittlement operates in all the situations in which it can be found. Many things must be considered when explaining HE including; hydrogen solute properties, interaction between hydrogen atoms and the metal lattice, hydrogen transport and localisation (trapping) properties of a metal and where hydrogen atoms can surface and recombine. However, there is a consensus on three principals [57]; there maybe more than one mechanism operating at any one time in a specimen, the dominant mechanism may change with different conditions and hydrogen must undergo transport to the metal surface, adsorption, absorption and finally transportation into the metal bulk.

Birnbaum produced a broad classification of hydrogen embrittlement mechanisms by division into the physical effects that are seen within the metal lattice [59].

1. Hydrogen related phase change mechanisms:
   - -Hydride Induced Cracking
2. Hydrogen enhanced local plasticity mechanisms:
   - -Hydrogen Induced Slip Softening
   - -Enhanced Plastic Flow
3. Hydrogen effects on the cohesive energy:
   - -Lattice Decohesion
   - -Hydrogen Adsorption (Surface Energy)

Internal Pressure Theory

The pressure theory of hydrogen embrittlement was initially considered in the 1970's and earlier as a mechanism for hydrogen damage in metals. Embrittlement is attributed to hydrogen concentration in voids or imperfections in the metal lattice, such as interfaces of precipitates and inclusions e.g. MnS [34]. Subsequent recombination to form molecular hydrogen may reach such a level as to enlarge the cavity, causing triaxial stress and resulting in eventual fracture of a metal specimen. In hydrogen charged specimens, hydrogen can diffuse into micro voids or cracks and then reform as molecular hydrogen on their inner surface, possibly stabilising the crack and allowing an increase in crack number, with no need for plastic deformation [60].

Whether the fracture is plastic, biaxial, triaxial or formed by elastic energy release has not been confirmed. Hirth discounts internal pressure theory, as saturation studies show the hydrogen levels in a specimen were too low to account for the mechanism [61]. However, the hydrogen gas that is present in blisters is considered by some to be an example of this mechanism.

Hydride Induced Cracking Theory

Westlake proposed that formation of a metal hydride, at sites of high triaxial stress e.g. a crack tip, maybe responsible for brittle cracking in the lower strength region and hence

crack propagation [62]. The triaxial tensile fields at the crack tip promote hydride formation, when they would otherwise be thermodynamically unstable, due to their increased volume. Once the hydride has contributed to crack propagation, it could dissolve, forming a mobile cracking medium when it is in contact with hydrogen. This is the most common example of hydrogen related phase change and Group (V) metals in the periodic table (including Nb, V, Ta, Zr, Ti, Mg and Pd), are particularly susceptible to hydride formation.

Gilman proposed that it was thermodynamically possible for iron hydride to be formed and stabilised by regions of high stress [63]. Experimentally, iron and steel substrates have failed to demonstrate this, possibly due to the lack of stability at low hydrogen pressures[57]. This may also be due to subsequent decomposition of the hydride when the crack begins to open up. Building on previous theoretical calculations work carried out at lower temperatures may provide more convincing evidence [64].

Brittle Crack Tip Theory

Thompson proposed that the plastic zone in ductile materials, could screen a brittle crack tip from the complete force of the external stress field, while still allowing brittle propagation. Hydrogen present in steel could lower the surface energy sufficiently to prevent the blunting of the sharp crack. If blunting does not also occur due to another competing mechanism, such as rounding out by dislocation interactions, then this form of modified brittle fracture is possible. He demonstrated that lattice decohesion by continuous opening of an atomically sharp crack, termed brittle fracture by many, can occur in ductile materials and may be responsible for a modified form of hydrogen embrittlement [65]. Otherwise Thompson believed that the competing mechanism type of 'ductile hole growth' would occur.

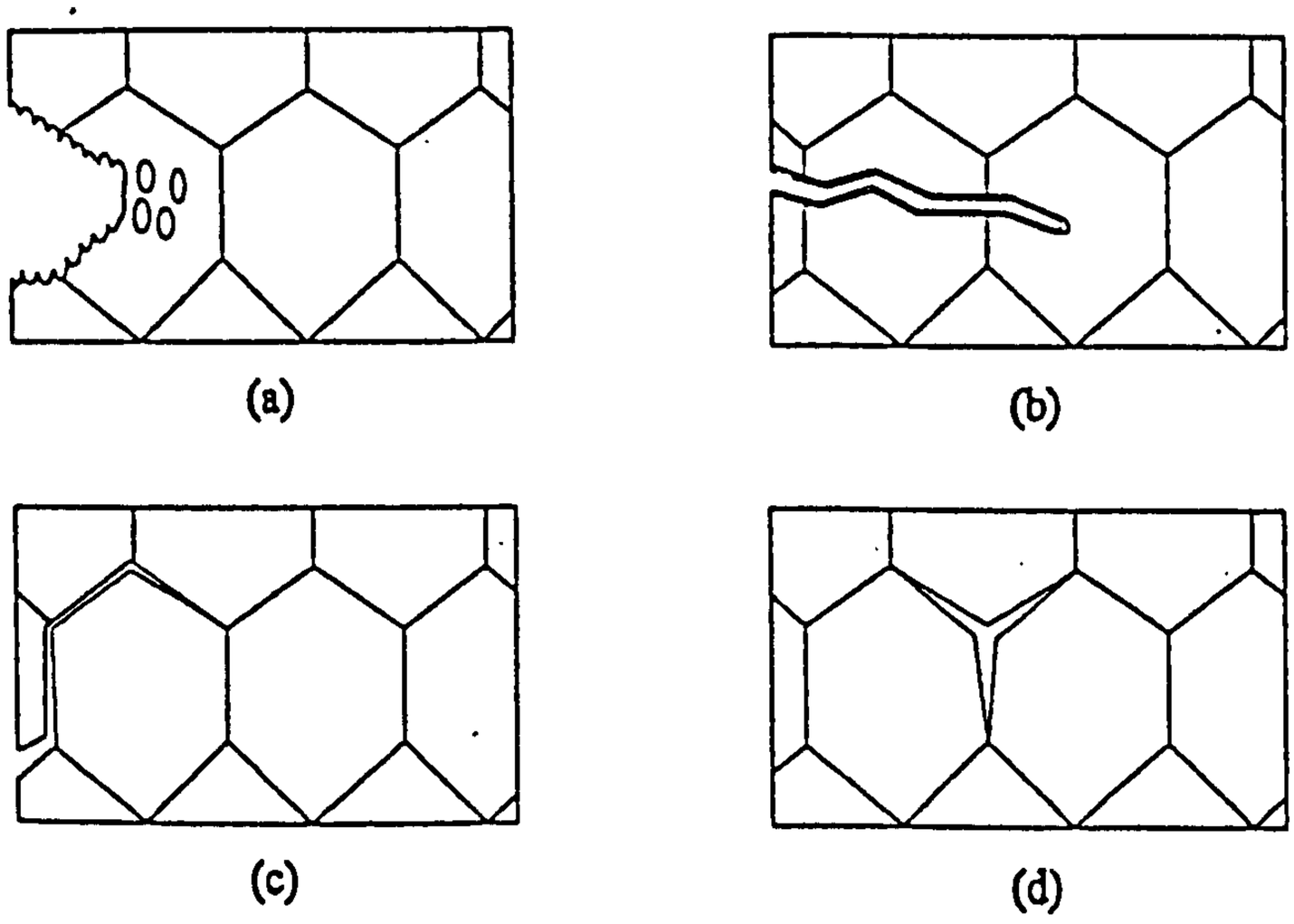
Brittle crack tip theory is generally considered to be a thermodynamic theory, closely linked to hydride cracking. Irreversible brittle cracking may occur athermally or thermally, when screened concentrated stress at a defect site (at a given distance from the crack tip) reaches yield stress at that point. Hirth states that segregation of any element to an interface necessarily embrittles that interface [57]. Gilman also proposed

that strong chemisorption would tend to prevent dislocation emission at crack tips and so favour brittle cracking [63]. Support has been given to aspects of this mechanism, despite no accurate kinetic model being available yet.

Hydrogen Induced Slip Softening / Enhanced Plastic Flow Model

Beachem[66] proposed that if the dissolved hydrogen concentration in the lattice ahead of a crack tip is high enough, plastic deformation is localised, and crack propagation can occur by a variety of microscopic mechanisms. He concluded that the hydrogen-steel interaction would either aid dislocation motion or generate it. FIGURE 10 illustrates Beachem's experimentally determined fracture modes as a function of decreasing stress intensity factor (K), compared with decreasing cracking rate.

FIGURE 10: Microscopic Fracture Modes Shown by Beacham (a) Microvoid Coalescence, (b) Quasi Cleavage, (c) Intergranular Cracking, (d) Intergranular Cracking under High Hydrogen Pressure [66]



Beachem believed that high stress intensity values, combined with high hydrogen concentrations, caused large volumes of material to be plastically deformed at the crack tip. Experimentally he found that where there was a large plastic zone it would contain inclusions. He postulated that these inclusions could act as void nuclei and the fracture process would develop by microvoid coalescence, as shown in FIGURE 10(a). The K value decreased as the crack lengthened because the plastic zone that was formed was

not big enough to incorporate large numbers of inclusions and so microvoid coalescence could not be sustained.

However, the K value in case FIGURE 10(b) is high enough to propagate cracks formed by plastic deformation required in quasi cleavage. Where the crack is even longer and the K value is further reduced, neither microvoid coalescence nor quasi cleavage can be maintained. In this case the lower energy fracture mechanism, intergranular cracking, is seen to occur, as illustrated in FIGURE 10(c). If the K value is insufficient to cause crack growth by any of the mechanism discussed, cracking can only occur if hydrogen diffuses into the metal and collects in the grain boundaries over time FIGURE 10(d). Beachem stated that grain boundaries or weak boundaries with sufficient pressure could provide their own driving force to augment the other forces already present.

It must be remembered that the fracture modes mentioned are dynamic and are also subjected to further physical considerations while cracking occurs. Intergranular cracking is more energetically favourable to either microvoid coalescence or quasi cleavage, but those modes dominate at high K values because they are kinetically faster processes. Slower cracking rates at longer crack lengths allow hydrogen to diffuse ahead of the crack tip, raising the hydrogen concentration at the grain boundaries generating an increased plastic zone and hence possibly altering the prevailing fracture mode.

The interactions that Beachem proposed could account for many of the phenomena encountered in stress corrosion cracking (SCC) and hydrogen assisted cracking (HAC) in quenched and tempered steels. Once hydrogen has been supplied to the matrix, by the steps described by McCright shown in FIGURE 5 [35] it diffuses to regions of high triaxial stress, e.g. just ahead of the crack tip. The dissolved hydrogen in a ferrite matrix will then aid the deformation of that matrix, by whichever process the microstructure will allow. Experimental data supports the supply steps of hydrogen to critical regions in the matrix, however it is this final point that is crucial in determining the crack susceptibility of a material. Beacham concluded that hydrogen unlocks dislocations,

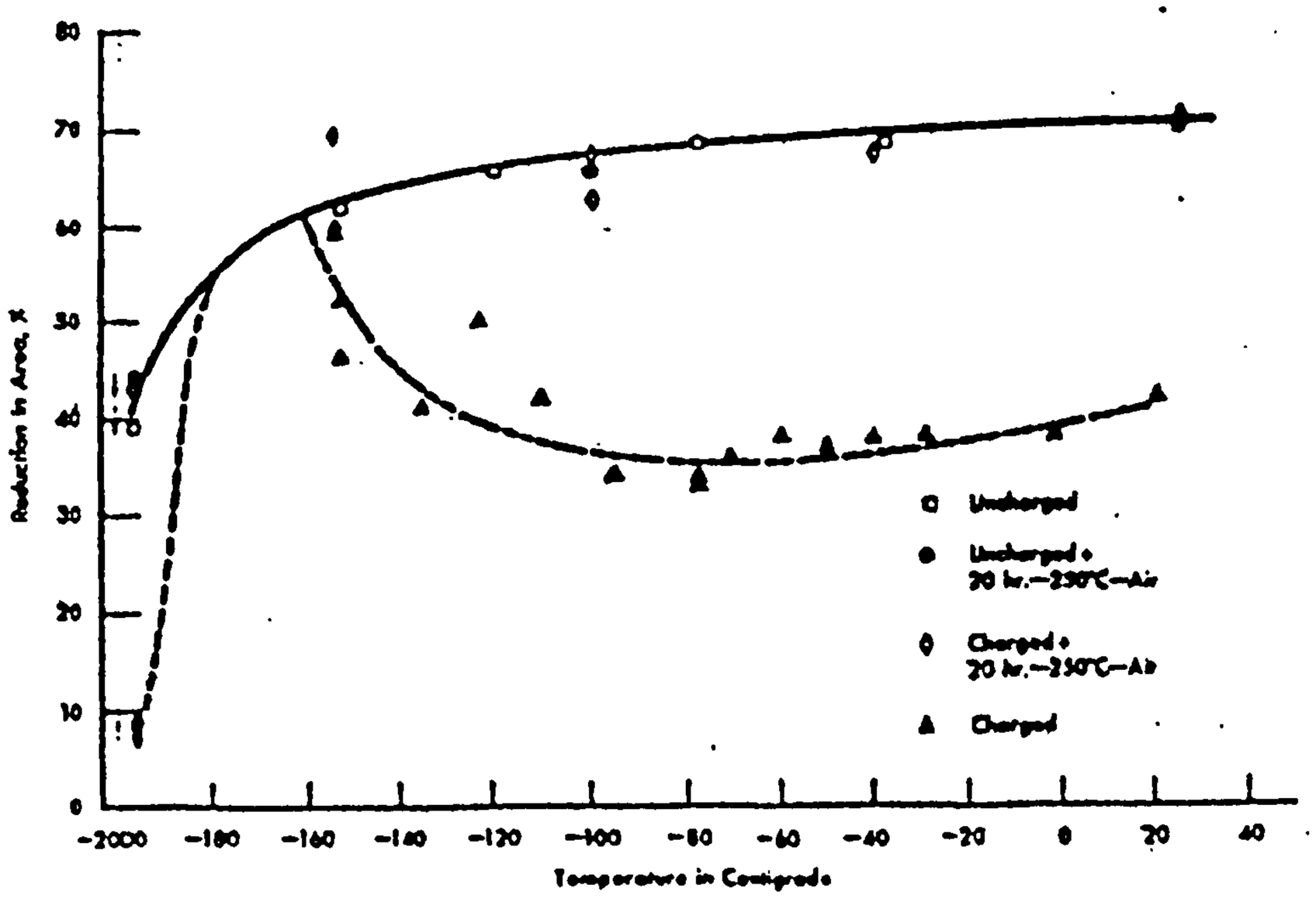
allows their multiplication and increases their movement along slip planes by reducing stresses. He also believed that this was a plastic effect.

Lynch supported this theory fractographically, showing that SSC, HAC and liquid metal embrittlement (LME) failures can be identical and that very small dimples can be found on cleavage surfaces [67,68,69,70]. Lynch believed that LME occurs at a crack tip on the surface of the solid metal. It could be postulated that SCC and HAC must also apply to surface crack tips, as they are so similar in appearance. Lynch considered HE to be a surface effect, but gives no explanation how the hydrogen or liquid metal may appear ahead of the crack tip.

Birnbaum extended the parameters investigated to include the hydrogen already contained in the bulk of the material and produced the 'Hydrogen Enhanced Local Plasticity' model (HELP)[71]. He postulated that internal hydrogen associates around discontinuities in the metal lattice, e.g. inclusions, point defects and dislocations and due to the high diffusivity of hydrogen, the movement of dislocations facilitates its transport. Using transmission electron microscopic (TEM) techniques, he observed failure in thin, hydrogen free specimens and those in which hydrogen had been deliberately introduced [72]. Ductile processes due to localised hydrogen plasticity ahead of the crack tip resulting in embrittlement were observed to occur in both cases.

Hirth [57] gives values for the binding energy of hydrogen of 10-50 $kJmol^{-1}$. Dissociation at high temperatures and low temperature stability of hydrogen would therefore make hydrogen transport along dislocations unlikely to occur. Extremes of temperature would therefore provide an inhospitable environment for HE if dislocation transport of hydrogen were a significant factor. These hypotheses are borne out by the experimental findings of Rogers who compared reduction in area measurements with temperature dependence of HE in steels, as shown in FIGURE 11 [73].

FIGURE 11: Temperature Dependence of HE in Steel Measured By (%) Reduction in Area [73]



If a metal lattice is strained the solubility of hydrogen is increased, as the areas where hydrogen can lodge dilate. However, Zakroczymski found no increase in bulk diffusion during plastic deformation of iron, stainless steels and nickel, which would be expected if dislocation movement was responsible for hydrogen transport [74]. Trapping was seen to increase during plastic deformation, effectively reducing the diffusivity and permeability of hydrogen through the metal. However, this does not completely exclude hydrogen movement by dislocations.

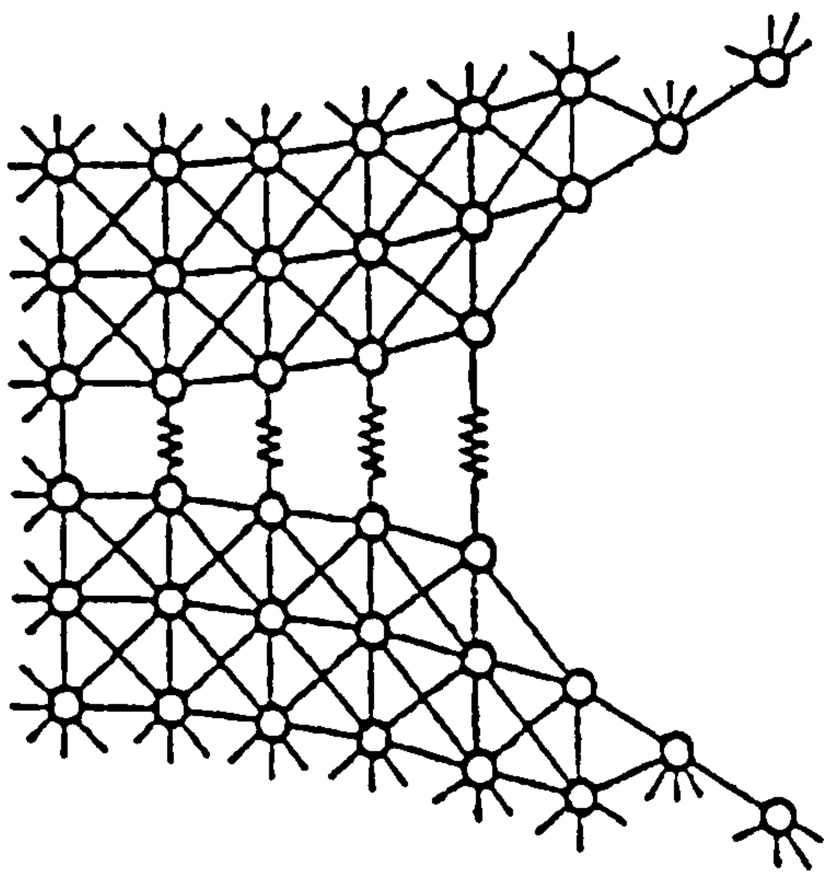
Lattice Decohesion Theory

It has been proposed by several groups, that dissolved hydrogen atoms concentrated locally in certain parts of the metal lattice, may lower the local cohesive force of the metal atoms and be responsible for crack propagation [29,75,76]. However, the increased solubility of hydrogen described by Troiano is insufficient to be solely responsible for the observed metal fracture. He suggested that there were elastic stresses near the crack tip, which would be thermodynamically favourable for hydrogen accumulation and allow a weakening of the Fe-Fe bond. Electrostatic ion interactions between hydrogen atoms and metal atoms in the lattice could cause an increase in repulsive forces between metallic cores or an effective reduction in cohesive strength of the lattice. The crack,

once brittle nucleated, could propagate to a region of lower hydrogen concentration and eventually be arrested by plastic deformation. The accumulation of hydrogen in this form of discontinuous propagation has been observed experimentally using tritium tracer studies [77].

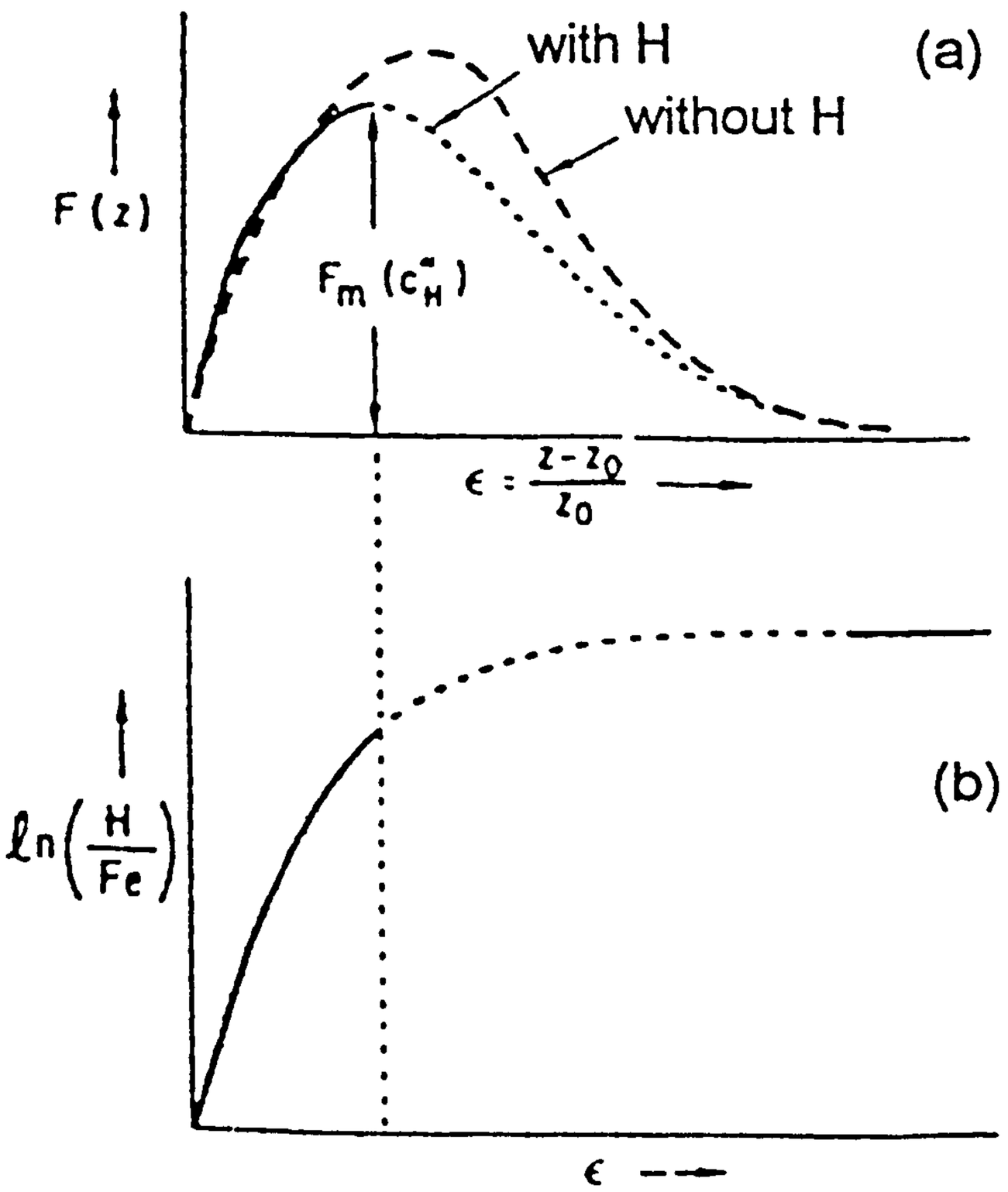
Development of this theory by Oriani [78], led to work into the type of site which could allow the hydrogen concentration to be high enough to account for the proposed behaviour. He suggested that two areas 'within a few atomic distances' of the surface fulfil the criteria; a few angstroms ahead of a sharp crack subjected to opening forces and an interface, which could be a surface, inclusion, grain boundary or dislocation. Hydrogen diffuses to sites of high triaxial stress and once in these sites, just ahead of the crack tip, the hydrogen interacts with the atoms of the metal lattice reducing the cohesive forces. When the local stress equals the cohesive force between the atoms in the lattice, at the tip, the crack will then propagate, as shown in FIGURE 12. Oriani assumed that there was a critical hydrogen concentration for the mechanism to operate and work carried out by Vehoff and Rothe showed that the mechanism could operate via micro-cleavage[79].

FIGURE 12: Atomic Model of a Crack Edge [18]



The stress required for a given extension is also affected by the presence of hydrogen. If hydrogen is present in a lattice, the required stress and the work done to cause fracture is reduced. This relationship is shown in FIGURE 13, increases with added strain and hydrogen concentration but eventually levels off to a maximum [26].

FIGURE 13: Relationship between (a) Cohesive Forces and Strain, (b) Hydrogen Concentration in Iron and Strain [26]



Hydrogen Adsorption / Surface Energy Theory

Surface energy theory is closely associated with lattice decohesion theory. It is based on the Griffith proposal that some of the energy from the applied strain is released during crack propagation and is converted to surface energy [80]. When a crack initiates, a fresh surface is invariably formed. Crack propagation and growth will occur when the strain energy released is greater than the new surface energy. Hydrogen adsorbs to the crack surface reducing the surface energy and promoting crack propagation at a rate limited by supply of hydrogen to the crack tip [81]. Pugh expressed a view that for slow crack propagation situations it would seem unlikely that a sharp crack would remain stable in a ductile (fcc) alloy [82]. He therefore highlighted that hydrogen adsorption (or surface energy theory), is only based on energy considerations and any plasticity or microstructural effects are not accounted for.

Uhlig considered that adsorbing a monolayer of chemical species would reduce the surface energy and cracking resistance of a lattice and referred to it as 'stress sorption cracking'[83]. He proposed controversially, that the adsorption occurs at dislocations or mobile imperfections near the crack tip, and that there was a critical potential below which it does not occur.

Hancock showed that oxygen could reduce surface energy more readily than hydrogen, due to a more exothermic heat of adsorption. However, it has been found experimentally not to promote cracking in specimens, and reduces the effect any hydrogen present may have [84].

The adsorption model, which suggests that hydrogen assisted cracking, is a surface or near sub-surface effect is in direct contradiction to the localised slip theory. However, Hirth [57] suggested, based on the fracture work of Lynch [68], that adsorption could still occur as a complicated crack tip mechanism. A mechanism for the way hydrogen may facilitate new surface formation or how its effects maybe reversed by stress removal, is however, still unclear from this model.

Summary

As can be seen from the previous sections, there is no single mechanism that gives a satisfactory explanation for all of the observed hydrogen embrittlement phenomena. Decohesion and the surface energy models offer established explanations for how hydrogen embrittlement operates. They assume hydrogen reduces the cohesive forces in iron but they differ on where the embrittlement takes place. However, no experimental data has been produced to support the decohesion model. Despite limited corroborating data for this mechanism, it has been stated that the requirement of substrate dislocations to result in hydrogen embrittlement is not a mechanism but merely a contributing factor[57]. Electrochemical determinations of kinetic parameters yield information about the slowest step of the hydrogen reaction process, but they cannot provide mechanistic information. Hydrogen embrittlement is therefore, a result of a complex mixture of metallurgical and environmental factors and has yet to be fully understood in every situation in which it is found to operate.

IDENTIFICATION OF HYDROGEN LOCATION

Due to the significant role hydrogen embrittlement plays in many failure situations, it would be useful to pinpoint precisely where a specimen contains hydrogen, to help identify how or why it failed. Originally destructive techniques were used to remove and analyse the gas in a failed specimen. Later methods such as ionic bombardment and vacuum extraction were developed. Nielsen's in situ methods developed over thirty years ago, were the next major advancement, which were used to decorate local corrosion sites on austenitic stainless steels [85]. Despite the application and experimental procedure being relatively simple, the examination and preparation of the specimens were very complicated.

Decoration Techniques

Twenty years on, the hydrogen microprint technique (HMT) had been developed [86] and later the technique was extended and modified [48]. This is much simpler method and allows the hydrogen position in a charged specimen to be identified by means of a standard reduction reaction. Hydrogen charged specimens are covered with a monolayer of warm liquid nuclear emulsion containing silver bromide crystals. Any hydrogen on the surface of the steel reduce the silver bromide molecules to metallic silver, via the reaction shown in EQUATION 7, which can then be detected as white particles when viewed under a scanning electron microscope (SEM). These particles should correlate to where the hydrogen had been situated on the specimen surface.

EQUATION 7: Silver Reduction Reaction

$$Ag^{+} + H_{ad} \rightarrow Ag\downarrow + H^{+}$$

Once the emulsion has been applied there is no need to use a developer as hydrogen reacts directly with the silver ions in the bromide emulsion. However, fixing is required to allow the removal of any unreacted emulsion, while not interfering with the reduced silver on the metal surface. A modified sodium thiosulphate solution is used to form a complex with the free silver ions in the emulsion and aid the dissolution of the remaining silver bromide. Sodium sulphite and bisulphate are added to this solution to preserve the fixer, and allow shorter rinse times and the addition of 5% sodium nitrite

inhibits corrosion of the specimen. The next process stage is rinsing, which removes any excess chemicals on the specimen surface, before final viewing on the SEM.

Hydrogen Probes

Hydrogen that is present in a material may be detected by use of a hydrogen probe[40]. There are three basic types; pressure, vacuum and electrochemical hydrogen probes. The pressure variety works by monitoring the pressure of hydrogen diffusing through an internal wall in the probe. The vacuum types measure hydrogen that is liberated as an ion current formed by laser action when it enters a vacuum detector. Electrochemical probes work via a glass or Teflon cell that allows hydrogen to permeate into it, generating a concentration gradient which can then be detected. The type of probe that is used for a particular situation depends on the requirements, and each of the probes has advantages in particular locations and environments.

Measurement by Hydrogen Permeation

Devanathan and Stachurski introduced an electrochemical double cell arrangement, which allowed easy measurement of the hydrogen that entered and permeated a metal electrode [39]. The two cells are separated by a thin membrane test electrode, one side of which acts as a cathode in one cell and an anode in the other. The hydrogen that is absorbed at the membrane surface diffuses through the steel to the anodic cell (exit side) where electrochemical conditions are set to oxidise the emerging hydrogen atoms, generating a current which will be recorded as a function of time. Due to the oxidation process in the anodic cell, the surface concentration remains zero and so a constant profile through the membrane can be established. It is a sensitive technique that can detect very low hydrogen concentrations. The environmental conditions of the set-up can be easily manipulated to provide information on effects of temperature, potential and applied current density. It has also been used to elucidate kinetic information on the hydrogen evolution and reduction reactions, which were mentioned earlier in Chapter 1.

Diffusion is a random process of particle motion from an area of high concentration to a region of lower concentration at a given temperature. The permeation technique described uses a deliberately produced concentration gradient and Fick's First law to

equate each electron of the anodic current to a hydrogen atom permeating the electrode. The assumption, using Fick's second law, that the unidirectional diffusion of hydrogen from the entry to the exit side is greater than the hydrogen escaping from the entry side is also often made and leads to EQUATION 8.

EQUATION 8: Hydrogen Flux

$$J = - DF \, \delta c / \delta x$$

Where:

J	=	hydrogen flux/ permeation rate ($\mu A \, cm^{-2}$)
D	=	hydrogen diffusion coefficient of the material ($cm^2 \, s^{-1}$)
F	=	Faraday constant (96500 coulombs mol^{-1})
δc	=	change in current
δx	=	change in distance (membrane thickness)

During permeation experiments, initially there is a delay as the first hydrogen atoms diffuse through the membrane to the exit surface (breakthrough time). The current then steadily increases until a steady equilibrium current or plateau value is reached (J_∞) which allows the surface hydrogen concentration to be calculated from a combination of Fick's first law and Faradays laws. It is sometimes more convenient to avoid solving the complex equations that can be derived by Laplace or Fourier transform methods. The technique has been used extensively for hydrogen permeation measurements to determine D and C_0 values in steel and other alloys, using EQUATION 9.

EQUATION 9: Steady State Permeation Rate

$$C_0 = J_\infty \, L \, / \, F \, D$$

Where:

J_∞	=	steady state hydrogen flux/ permeation rate ($\mu A \, cm^{-2}$)
C_0	=	hydrogen concentration (10^{-6} gm H / gm Fe)
L	=	thickness of membrane (cm)
F and D	=	as previously defined

Measurement of the breakthrough time for a specimen also enables calculation of the diffusion coefficient of the material, if the thickness of the electrode is known. This relationship is shown in EQUATION 10.

EQUATION 10: Breakthrough Time

$$t_b = L^2 / 15.3\ D$$

Where: t_b = breakthrough time (s)

L and D = as previously defined

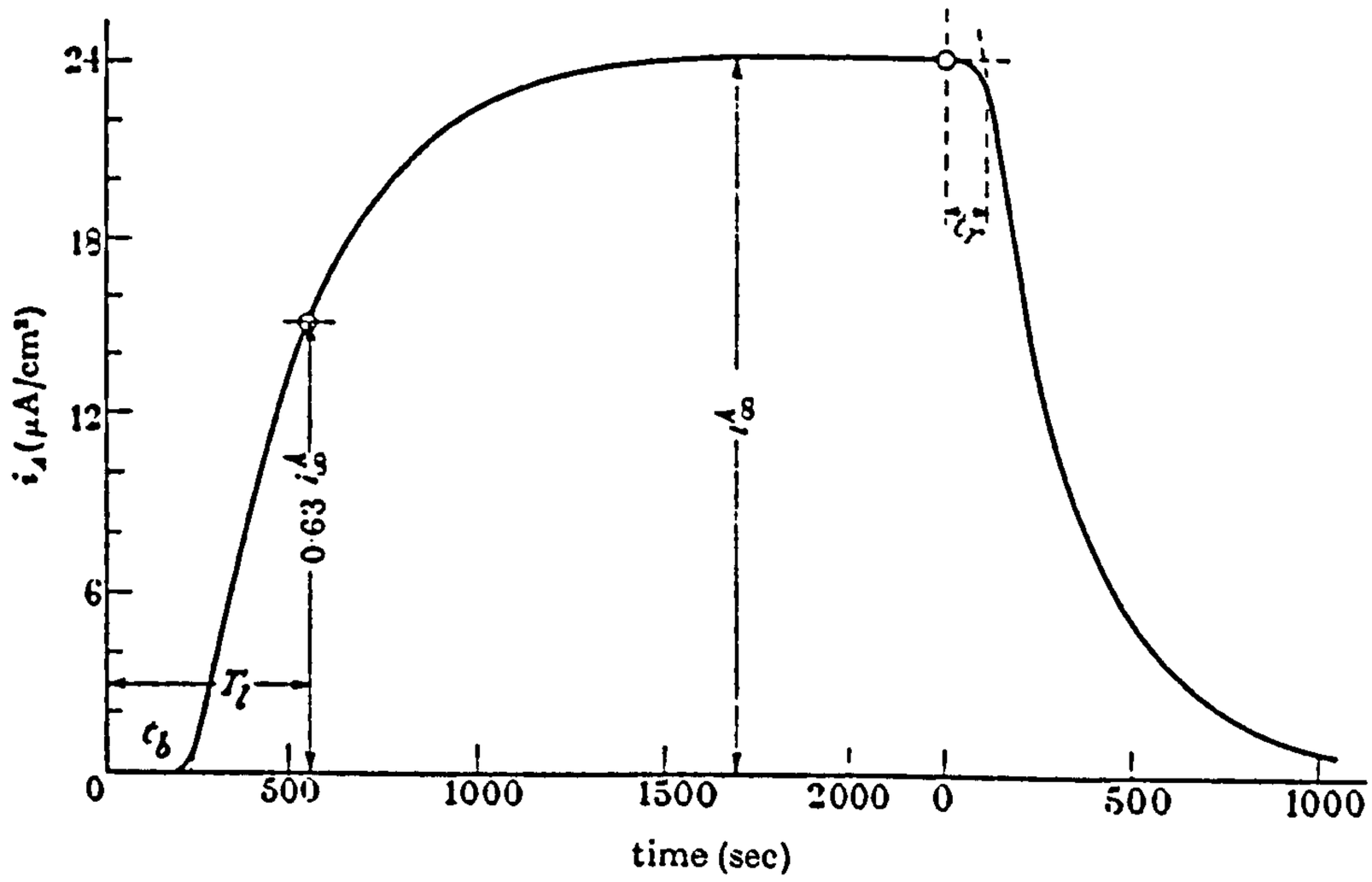
The hydrogen diffusion coefficient (D) is dependent on the microstructure and trapping capability of a material, surface properties that effect the adsorbed hydrogen concentration, the membrane thickness and the experimental temperature [87]. Reduction in experimental temperature reduces the hydrogen flux diffusing through a membrane. The calculated hydrogen concentration values will reflect the lower diffusion coefficient values.

D is independent of applied stress, but the hydrogen permeability is increased with higher applied stress [87]. The magnitude of the diffusion coefficient varies significantly with the type of steel used [88] and examples are given in TABLE 2. A more useful comparison would be obtained from the material microstructure, rather than the material grade. Microstructural effects were mentioned earlier in this Chapter.

TABLE 2: Literature Diffusion Coefficients

STEEL TYPE	DIFFUSION COEFFICIENT ($Cm^2\ s^{-1}$)	REFERENCE
77	7.2×10^{-6}	89
D2	4.9×10^{-7}	89
LCMS (0.17% C)	10×10^{-8}	90
1018 (0.15-0.2% C)	8.3×10^{-5}	91
4340 (0.4% C)	4.0×10^{-7}	92

FIGURE 14: Typical Permeation Transient



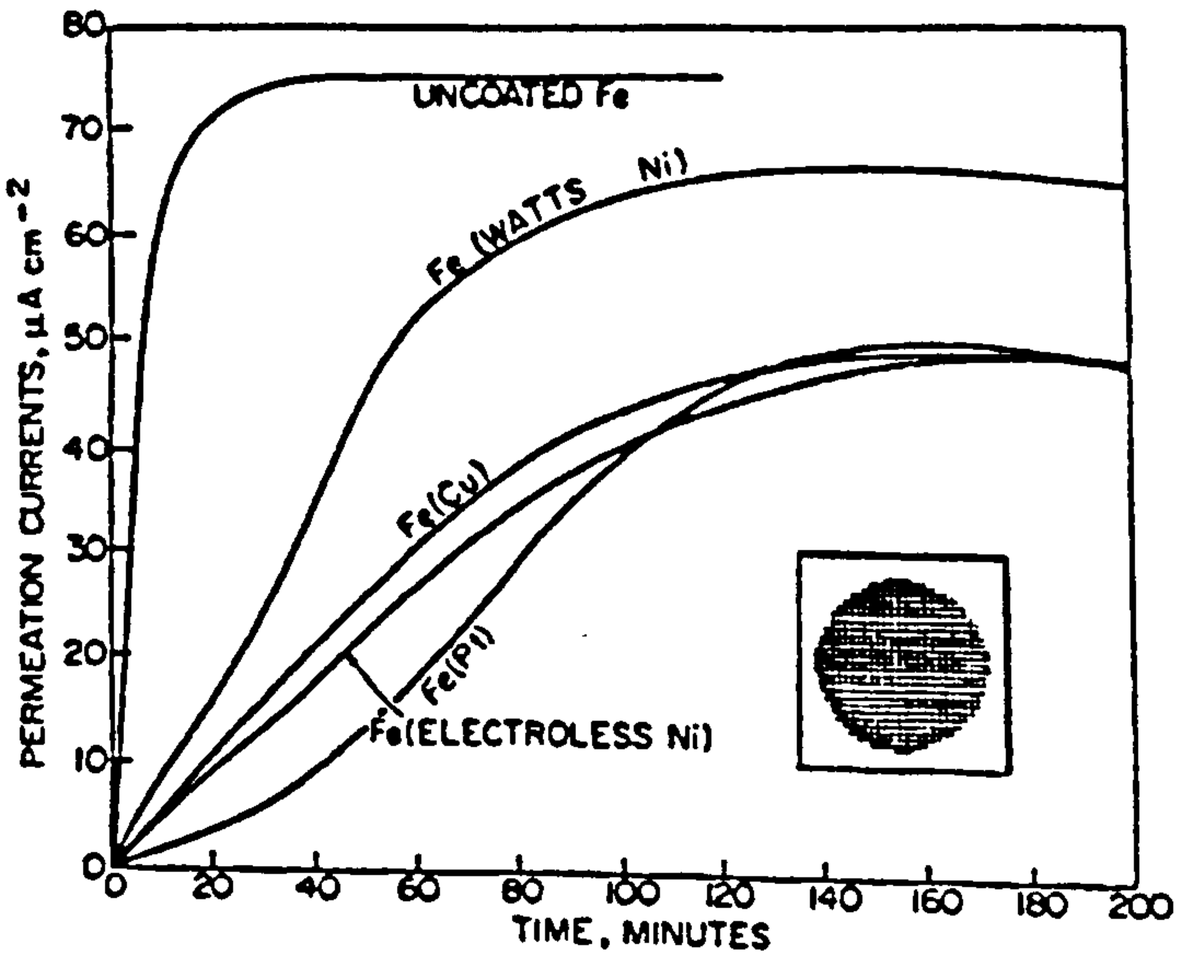
A typical permeation transient is given in FIGURE 14. Starting at zero, the time to reach the point t_b represents the breakthrough time. The time required for the permeation transient to reach the steady state value is termed t_∞, which also corresponds to the highest flux of hydrogen passing through the membrane. After the initial steep rise to reach the maximum flux, a plateau region is attained for a time, after which it will decay relatively quickly back towards zero.

During an electroplating experiment the thickness of the permeation membrane varies as the electrodeposit is formed. The diffusion mathematics are further complicated by the nature of the fresh material that is deposited. If the hydrogen supplied to the surface is now assumed to be from the electrodeposit, approximations of hydrogen concentration can be made over short periods of time, using the final total thickness. This simplification can then allow estimation of the hydrogen concentration at the electrodeposit-steel interface.

Permeation of hydrogen through an electrodeposited coating has been studied for pure metals deposited on the charging side of a double cell arrangement. A bilayer comprising electrodeposited Pt, Cu or Ni and a steel substrate has been shown in FIGURE 6, to delay hydrogen absorption [93]. Pronounced effects were clearly observed at the shorter time range and were dependent on the nature and thickness of the

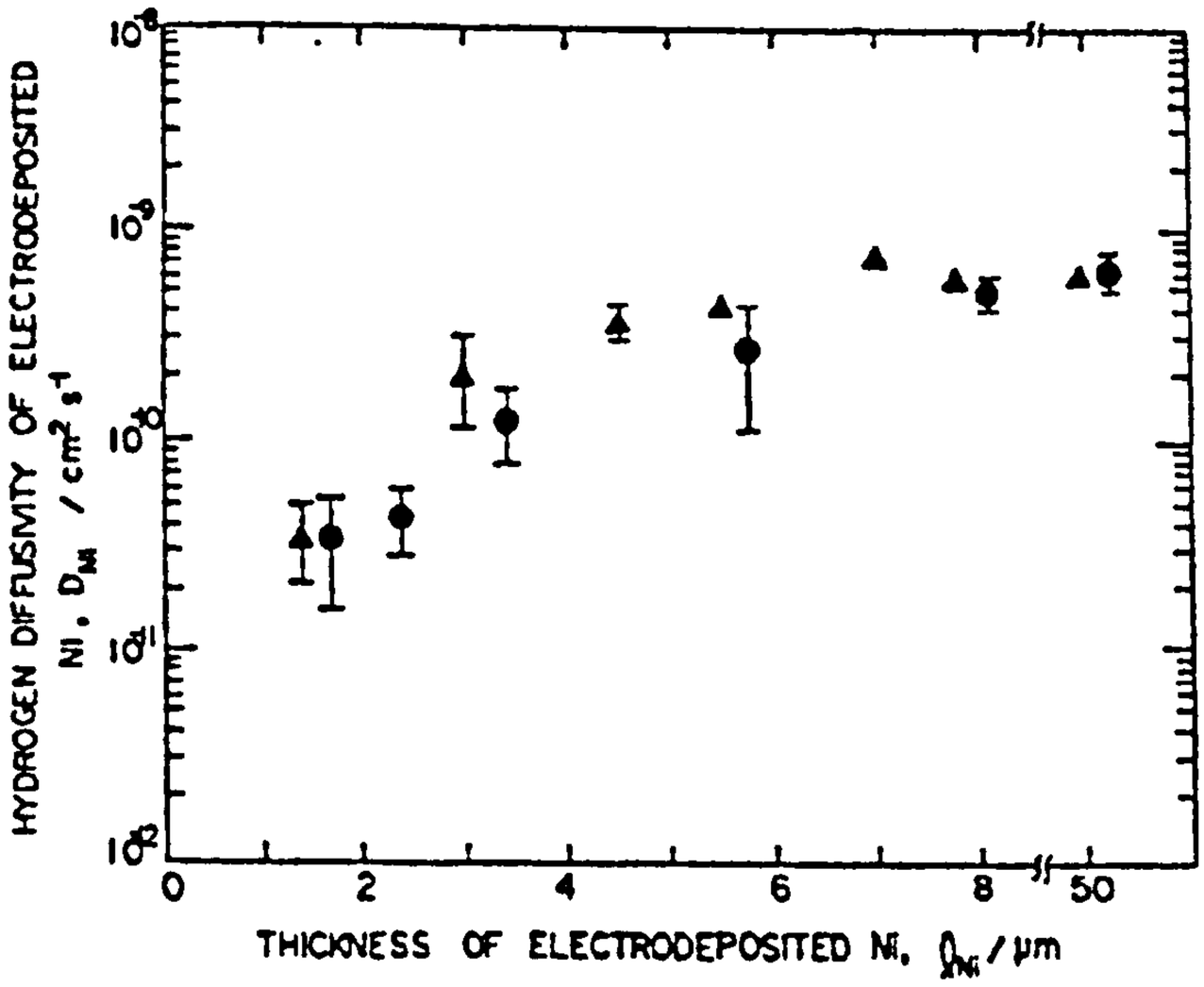
electrodeposit. The largest effect was seen for Pt, followed by Cu and Ni having the least predominant effect. Further experiments were performed on specimens that been electroplated over 20% of their surface. The results shown in FIGURE 15, illustrate a reduction of greater than 20% in the hydrogen permeated compared with bare steel. It was concluded that hydrogen was being produced catalytically at the more noble cathodic sites (electroplated areas), reducing the hydrogen overpotentials of the composite electrode. More rapid hydrogen recombination reduced the hydrogen surface coverage and further reduced the quantity of permeating hydrogen.

FIGURE 15: Effect of Grid Electroplating on Permeation Transients [93]



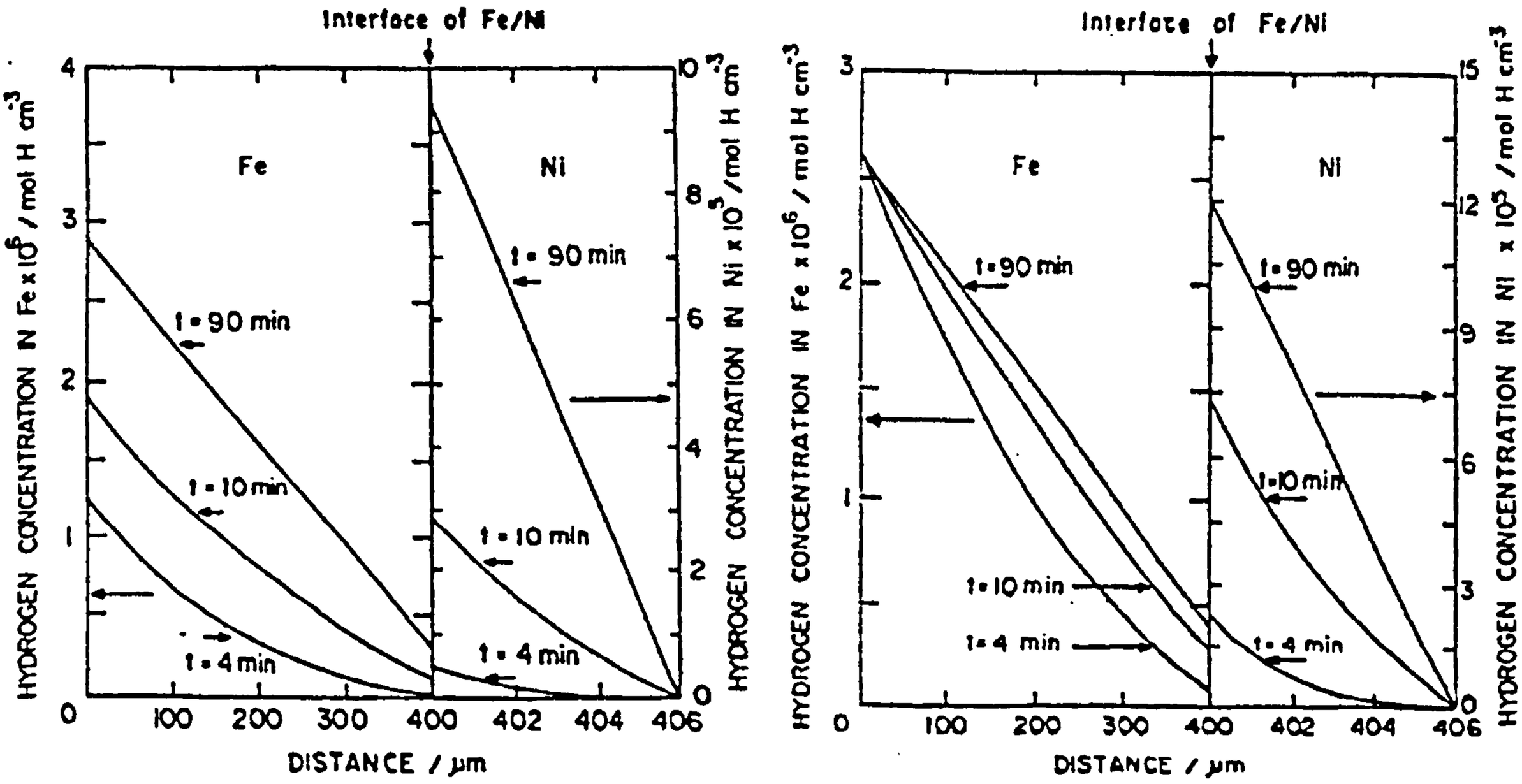
Song and Pyun investigated the barrier effect of nickel and developed a computer based numerical solution with which to compare their experimental findings [94]. In an attempt to counteract any catalytic effects on the entry surface they electroplated the electrode exit surface. They determined that there was no major advantage to the barrier system of a thicker coating as the diffusion coefficient seemed to increase with increasing thickness of electrodeposit, as shown in FIGURE 16. They concluded that a thin coating of nickel could be as effective barrier to hydrogen absorption as a thick coating.

FIGURE 16: Variation in Hydrogen Diffusivity with Deposit Thickness [94]



The hydrogen profiles across the bilayer as a function of time under galvaonstatic and potentiostatic boundary conditions, were also estimated and are shown in FIGURE 17.

FIGURE 17: Hydrogen Concentration Profile with (a) Galvanostatic and (b) Potentiostatic Conditions [94]



It is important to remember that traps in the substrate, electrodeposit and the interface of the two systems can influence the diffusion parameters for a composite system. Hydrogen diffusion can be influenced by environmental conditions including pH and chemical contacts as well as by boundary conditions at the membrane surface to which hydrogen adsorbs. The hydrogen uptake of the membrane is a small proportion of the adsorbed hydrogen and so is also directly affected by the surface state of the membrane.

The diffusion characteristics of hydrogen are not fully understood for passive layers that may form on permeation membranes in aqueous media. It is believed that unsteady boundary conditions can result. Researchers have used a 60nm thick Pd layer as a surface coating to prevent oxide layer formation and it provides a zero hydrogen surface concentration on the exit side of the membrane. The layer also prevents anodic dissolution because none of the hydrogen is used for reduction of the coating layer [95]. A thin Pd layer is believed not to affect hydrogen permeability or diffusivity, or delay onset of the observed transient, because the steel membrane has the dominating control on the process. Pd can also be applied to the entry surface to prevent passive film build up. However, 0.2N sodium hydroxide solution is also thought to keep steel in the passive condition and prevent an iron oxidation current from increasing the measured current [95].

MECHANICAL TESTING

Observation of the change in physical or mechanical properties that are influenced by hydrogen absorption can be used to establish a measure of the hydrogen absorption of a system. This involves charging the specimen with hydrogen and measuring a change in properties such as: ductility, elongation, tensile strength, reduction in area, shear strength, fracture toughness or electrical resisivity.

Constant stress tests

Hydrogen cracking has been shown to proceed in four distinct stages: incubation, initiation, propagation and arrest. However, the initiation and propagation stages are difficult to separate. Reproducibility of fracture mechanics experimental data has generally been low. Pre-cracked specimens were introduced as a method of controlling

crack growth and limiting experimental scatter [96]. Specimen geometry can be used to derive critical combinations of crack length and external applied stress using a single threshold stress intensity factor, K_{ISCC} or K_{th}. Crack initiation induced by hydrogen will only occur above the threshold intensity value. This value can be used to establish limiting loads that ensure structures containing possible undetectable defects will operate safely during their service life. Experimental specimens can also be sectioned to show the effects of pitting that may also aid cracking.

Constant K tests are of little use if the K_{th} value is not known before the experiment is undertaken. K_{th} can be obtained with few replicate specimens using double cantilever beam (DCB) or wedge opening load (WOL) specimens. They both operate as decreasing K value tests and offer the best method of obtaining the ultimate K_{th} value in an environment that may increase in severity with time. The stress intensity factor fluctuates with many experimental variables. Lucas and Robinson established a significant reduction in K_{th} with a lower concentration of hydrogen in the metal lattice by hydrogen probe measurements [97].

Constant load tests

Constant load and slow strain rate testing (SSRT) are two of the most popular stress corrosion cracking and hydrogen embrittlement tests. The techniques allow time for the mobile hydrogen within a specimen to diffuse, and so will detect the effect of embrittling hydrogen present in the sample structure.

Constant load specimens are commonly in the form of a cylindrical bar, wire or C-ring supporting a load equivalent to a fixed percentage of the breaking load of the specimen (50 or 90%). A variety of specimen sizes and shapes including notched or smooth can be used along with wire, plate, rod, tubing or welded parts.

Slow strain rate testing, employed extensively over the last three decades, uses ideal strain rates in the range 10^{-7} to $10^{-5}ms^{-1}$. It is a quick, comparative technique based on time to failure after elongation, and can quantitatively measure the extent of hydrogen embrittlement for many specimen types. The advantage of strain rate testing compared

to constant load testing is that failure of a specimen is guaranteed. Tensile strength information and the shape of a stress-strain diagram produced for specimens can be useful when comparing embrittled with non-embrittled specimens.

As with all techniques, care must be taken to avoid certain problems that can be associated with it. Crack progression during testing can result in partial relaxation of the specimen, and specimen necking can cause the strain rate to locally increase by up to two orders of magnitude. This change in strain rate can be particularly important, as hydrogen embrittlement is dependent on the strain rate and so a specimen may be removed from the hydrogen sensitive region. The critical strain rate for a specimen within the range mentioned before can be determined before commencing testing either experimentally or from the literature[98]. Tensile machine frame stiffness can also affect the time to failure measurements. However, when dealing with a ranking system for groups of data, this should present no real data interference, providing the parameters are unaltered.

Statistical analysis techniques

As with all testing, scatter of the time to failure data from slow strain rate experiments makes quantification of the hydrogen effects difficult. The scatter can arise from changes in charging conditions, defect size or location in a specimen, and surface imperfections. Many evaluation techniques have been used to aid the analysis of experimental data. Weibull developed a statistical approach to evaluate the scatter seen with brittle fracture in ceramics fifty years ago.

Pollock collected slow strain rate data for cadmium electroplated AISI 4340 steel specimens that had been baked and those that had been exposed to paint stripper. He used the Weibull technique to illustrate that steel susceptible to hydrogen embrittlement must be limited in the pre-treatment cycles it undergoes and care must also be taken in the de-embrittlement treatment not to alter the microstructure of the steel. Notched specimens were used and compared to each other against a control group using a student T-test [99].

A modified version of this time to failure based technique has been successfully applied to embrittlement seen in charged steel specimens and those that have been nickel electroplated [18,25]. Comparison of permeation results, proved that hydrogen was co-deposited with nickel during electroplating. Static load tests showed that hydrogen could be held in the electrodeposit. The mobile hydrogen could slowly diffuse from the electrodeposit that acted as a hydrogen reservoir, into the metal substrate long after electroplating had ceased. These findings illustrate the importance of using information from a number of techniques in conjunction with each other to form an overall picture of what is happening to a specimen.

CORROSION

Corrosion is a spontaneous electrochemical reaction. In aqueous environments it can be described as the oxidation of the metal (anodic reaction) and the reduction of water (cathodic reaction). When metals with dissimilar electrochemical potentials are in direct contact in a suitable environment, galvanic corrosion may occur, as one will act as the anode and the other the cathode.

EQUATION 11: Anodic Reaction

$$Fe \rightarrow Fe^{2+} + 2e$$

EQUATION 12: Cathodic Reaction

$$O_2+2H_2O+4e \rightarrow 4OH\text{-} \text{ (aerated only)}$$

$$2H_2O+2e \rightarrow H_2 + 4OH^-$$

CORROSION PREDICTION

Corrosion can be defined in a variety of ways, and thermodynamic, kinetic and physical considerations must all be included. The electromotive force (emf) of a cell expresses the tendency for a metal to corrode and is based on the thermodynamic quantity, Gibbs free energy, shown in EQUATION 13.

EQUATION 13: Gibbs Free Energy

$$\Delta G = -n\ F\ E$$

Where: G = Gibbs free energy
n = number of electrons
F = Faraday constant
E = electrode potential

While this can show the tendency for a reaction to occur, it does not include any physical properties or kinetic parameters of a system. A more complete equation can be used to define the emf of a cell in terms of activities of reactants and products. The Nernst equation, given in EQUATION 14, includes the kinetic parameters of reactant concentration and temperature dependence of the system[100].

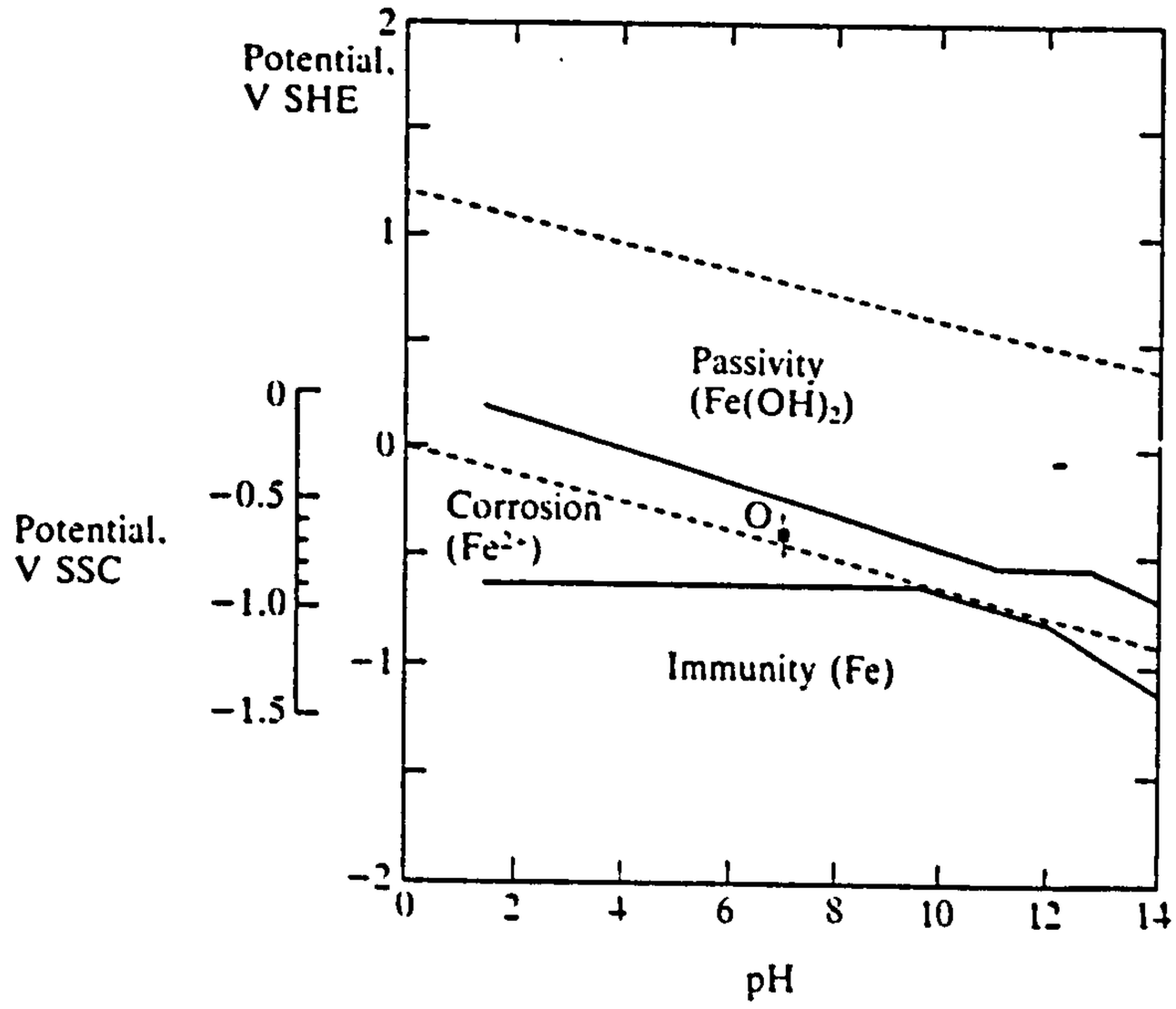
EQUATION 14: Nernst Equation

$$E = E^0 - (RT / nF) \ln [a/b]$$

Where: E = electrode potential
E^0 = standard electrode potential
R = gas constant
T = temperature (K)
n = number of electrons
F = Faraday constant
a = chemical activity of products
b = chemical activity of reactants

Pourbaix developed a straightforward visual summary of thermodynamic data in the form of a potential-pH diagram. These diagrams relate the electrochemical and corrosion behaviour of a metal in water and show the reaction state of a metal at a particular pH/potential. They do not give any idea of reaction rate. The Pourbaix diagram for iron is given in FIGURE 18 [101].

FIGURE 18: Pourbaix Diagram of Iron in Water



The most commonly used corrosion guide is probably the Galvanic series, shown in FIGURE 1 in the introduction. It is the open-circuit potential of a substance in the particular environment in which it is being used and is useful because it can take account of a substance that appears in several states. Comparison of metals in a particular environment can then lead to the correct material selection for a particular task.

Corrosion Control

When the corrosion risk associated with a system is high and corrosion prevention is required, several basic types of protection systems are used:

- Metal alloying to resist its working environment e.g. Stainless steel
- Coating or cladding, either fully or partly with a reactive material that will preferentially corrode e.g. zinc on iron (shown from the Galvanic series)
- Covering with an impermeable layer e.g. enamel, ceramic, rubber or paint (red lead).

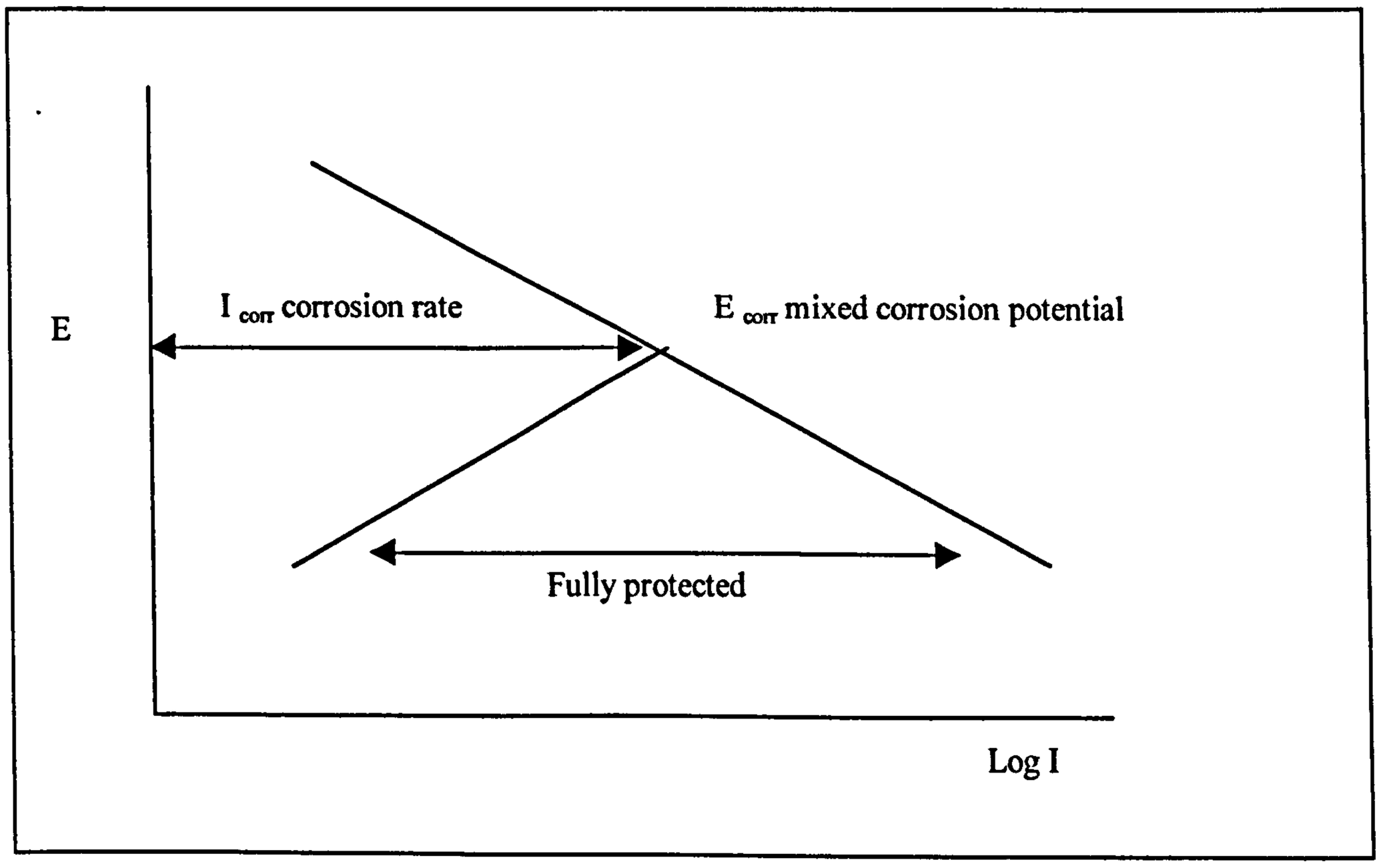
Electrochemical Control

The Galvanic series illustrates that cadmium or zinc coating systems would cathodically protect steels and aluminium components from corrosion. Cathodic protection has to be implemented with care to balance the beneficial effects of corrosion prevention against

the detrimental effects of induced hydrogen embrittlement from overprotection. Electroplating can also be a form of sacrificial cathodic protection, but it may cause hydrogen embrittlement during its application or by subsequent corrosion while in service (re-embrittlement).

Cathodic and anodic protection systems use external polarisation that can be modified (depending on the situation requirements) to electrochemically reduce the corrosion rate. FIGURE 19 is an example of an Evans diagram that is a plot of potential against log current for a system, this illustrates the way in which a parameter can vary the susceptibility of a system to corrosion[102].

FIGURE 19: Evans Diagram of Cathodic and Anodic Polarization



Cathodic protection displaces the corroding metals electrode potential below the corrosion potential, E_{corr} . This lowers the mixed potential and reduces corrosion by making it the cathode. If a small uniform corrosion rate remains it may be deemed acceptable if regularly monitored. Attachment of a sacrificial anode of lower potential or an impressed current or a combination of these two methods may be employed in certain situations, to lower the corrosion rate. Anodic protection (AP) uses a low level impressed current to maintain the passive condition of a metal. Careful planning and

design of the system on which it will be used is also often required, as it is often more complicated to implement and monitor.

CORROSION OF ZINC-ALLOY COATINGS

Zinc-alloy coatings containing iron-group metals have been used extensively as corrosion protection by the automobile industry in response to de-icing salts used on roads in Europe and America. Their performance is well established. Much of the available corrosion data is from specific accelerated tests peculiar to the automotive industry. However, analysis of the data generated has provided useful information that can be used for aerospace and other applications.

Binary zinc-alloy electrodeposits have been considered as corrosion resistant coatings due paint adherence problems after phosphate treatment of hot-dip galvanised sheet. Annealing treatment of the galvanised sheet allows interdiffusion of iron with zinc producing a brittle alloy coating that could crack when the steel was worked during forming. Electrolytic processes are advantageous because they can be easily modified to control the thickness and physical properties of the coating. An added benefit is that the coating can be applied to just one side of the substrate. Zinc alloys including elements such as; iron, nickel, cobalt, manganese, chromium, copper and tin, have all been tested. Each corrosion prevention system has certain useful characteristics that will be described briefly in the following sections.

Zinc-iron

Zinc-iron electrolytes are harder to control than other types but they are more compatible with industrial phosphating treatments required for automotive paint adhesion and are cheap to produce. Higher iron levels have better uniformity and paint bonding, so layered coatings with the upper coat containing 50% iron have been produced for both zinc-iron and zinc-nickel electrodeposits [17]. Ternary electrodeposits of zinc-nickel-iron have also been produced which have better surface appearance and hardness without the use of brighteners or multiple layers [103].

Zinc-nickel/ zinc-cobalt

Zinc-nickel and zinc-cobalt electrodeposits provide better barrier protection than zinc-iron electrodeposits. Zinc-nickel electrodeposits are less cost effective than zinc-cobalt electrodeposits because they require 10 – 14% by weight of the alloying metal rather than 1-4% [19]. There are now concerns over the toxicity of nickel salts and the difficulty in chromating the electrodeposited coatings.

Zinc-manganese

Industrial zinc-manganese alloys produced from acidic sulphate based electrolytes can contain 60-80% manganese by weight. They exhibit excellent corrosion resistance in the unpainted condition as well as having good paint adhesion[13]. Co-deposition of the two elements can only be achieved with the use of citrate complexing agents that displace the potential of zinc closer to that of manganese[13]. The operating current density of these systems is high, and the typical current efficiency of 20% is further lowered with an increase in manganese composition[14]. Additions to the bath, such as thiosulphate or selenic acid can increase the efficiency or deposit manganese content. However, despite the highly corrosion resistant deposit produced, the low efficiency values lead to hydrogen embrittlement concerns.

Zinc-chromium

Environmental concerns over the use of chromate passivation treatments to improve corrosion resistance of coatings led to the development of zinc-chromium alloy electrodeposits. These can be electrodeposited from mildly acidic baths to produce up to 10% chromium in the alloy. The coating can then be treated with permanganate solutions to produce a type of chemical conversion coating. Such coatings were found to have good levels of corrosion protection in salt spray tests while containing relatively low levels of chromium [17].

Zinc-copper

A type of zinc-copper electrodeposit known as 'white brass' was produced in the 1950's in response to a worldwide shortage of nickel. It contained 28% by weight copper and was used as a bright nickel plate substitute because of its bright white appearance. However, it now has limited usage [17].

Zinc-tin

Zinc-tin alloys have been produced from acid, alkaline cyanide, alkaline[11] and neutral pH baths[10]. They readily accept conversion coatings that bind strongly with tin particles in the alloy coating [12]. It is believed that zinc is present as small particles distributed through a tin matrix [11]. When corrosion of the coating occurs there is no bulky white corrosion product formed unlike pure zinc coatings [11, 12]. The soft deposits generally contain 70-80% by weight tin and provide excellent protection after deformation by bending or crimping of electroplated parts. They exhibit good corrosion resistance on steel and aluminium contacts which would make them useful for steel aerospace fasteners [11, 12]. Vasantha determined experimentally that less hydrogen was permeated during electrodeposition of tin-zinc coatings compared with either pure zinc or cadmium [10]. The deposits resist contact with car brake fluid and gasoline[12] and also have superior conductivity and solderability characteristics to cadmium.

Aircraft Requirements

Cadmium coatings are used on aircraft for two main reasons; they are effective in a marine environment as they adopt an anodic potential to steel and are galvanically compatible to many of the aluminium alloys that are used in aircraft construction. This is important, as the aluminium panels are normally fastened to the airframe using cadmium plated steel bolts.

However, cadmium and its corrosion products are known to be toxic and therefore are a serious health risk. Disposal of the waste from the cyanide baths is difficult and expensive, as is the eventual disposal of the electroplated part. Cadmium can also cause solid metal embrittlement of titanium alloys at ambient temperature and high strength steels above 225°C. Due to the concerns discussed and new legislation such as EPA

33/50, a replacement for cadmium is essential [8]. Any replacement must provide a coating for aircraft fasteners with a potential close to that of aluminium, to prevent galvanic corrosion, while being sacrificial to steel.

Electroplated zinc is a simple and cheap alternative. However, it is not considered to give adequate protection in marine environments and the corrosion products formed are voluminous which could cause wedging of fasteners. Chemical interactions with aircraft fuel are also a concern, making its use inappropriate. The major disadvantage, however, is its highly anodic electrochemical potential, shown in FIGURE 1. This causes a high rate of galvanic corrosion when in contact with steel or aluminium and leads to a prematurely short component service life. Corrosion resistance and galvanic behaviour can be improved by alloying additions and some suitable replacements will be discussed in the following section.

CORROSION PERFORMANCE OF ZINC-ALLOY COATINGS

Accelerated corrosion testing is often undertaken by determining the time taken for red-rust to form on a plated specimen surface subjected to salt spray testing. However, experimental data carries discrepancies in methodology, which these have to be considered when comparing data from different workers. Baldwin describes a simple method for normalising corrosion data by a 'red-rust ratio' that compares time to red-rust (t_{rr}) for a zinc-alloy and a pure zinc specimen of the same thickness by the relationship shown in EQUATION 15 [17]. Using the ratio and available literature data, Baldwin established the results summarised in TABLE 3.

EQUATION 15: Red-Rust Ratio

$$\text{Red-rust ratio} = t_{rr}\,(\text{Zn alloy}) \;/\; t_{rr}\,(\text{Pure Zn})$$

TABLE 3: Alloy Coating Performance in Salt Spray Testing

Alloy	Optimum Noble (%)	Advantage	Disadvantage
Zn-Ni	12-16	5-6 times more efficient than pure zinc. Microcracking.	Susceptible to white rust and dealloying. Difficult to chromate. Toxicity of nickel salts.
Zn-Fe	15-25	2 times more efficient than pure zinc. Cheap.	Voluminous red corrosion products formed may cause paint delamination. High Fe levels required.
Zn-Co	4-8	2-3 times more efficient than pure zinc. Low levels of Co required.	Susceptible to white rust.
Zn-Mn	50	Up to 100 times more efficient than pure zinc.	High Mn levels required. Low cathode efficiency.
Zn-Sn	70-80	2-5 times more efficient than pure zinc. Bright coating readily obtained.	High Sn levels required. Difficult to chromate. Cyanide bath often used.

Zinc-nickel

Zinc-nickel electrodeposits have shown improved corrosion resistance of up to six times that of pure zinc coatings. Chromate treatment of the alloy coating may further increase the corrosion resistance up to fifteen times more efficient than pure zinc[17]. A feature of sacrificial zinc-nickel electrodeposits, containing over 9% nickel is microcracking, during exposure in a corrosive environment. Cracks form perpendicularly to the metal surface due to stresses in the coating as a result of corrosion product formation in cracks and other existing flaws. This may increase corrosion protection by preventing localised attack by distribution of the anodic sites over the surface of the specimen. It may also provide a hydrogen pathway through the coating during de-embrittlement baking treatment.

Zinc-iron

Zinc-iron coatings are sacrificial to steel and while high levels of iron are required for effective protection, the cost of the alloying element is low. Despite a two times increase in corrosion protection compared to zinc coatings, zinc-iron coatings are not as effective as zinc-nickel coatings. The major disadvantage with this coating system is the voluminous red corrosion products formed. These products may cause wedging of parts, delamination of paint layers and may also be mistaken for the corrosion products of the steel substrate.

Zinc-cobalt

Short obtained zinc-alloy coatings with up to 20% cobalt for salt spray testing[19]. The optimum corrosion performance was obtained with a 4-8% cobalt content range and the highest red rust ratio obtained was 3.5. An increase over 8% caused a decline in corrosion protection similar to the trend observed for zinc-nickel. Commercial zinc-cobalt alloys generally contain small levels of cobalt <1%, sufficient to give rise to an improvement in corrosion protection over zinc coatings alone [9]. Sharples showed that chromate passivation treatment of 0.6% zinc-cobalt coatings increased the salt fog performance to almost nine times longer than pure zinc[17].

Zinc-manganese

Zinc-manganese coatings with 25% manganese gave similar protection to 12-16% zinc-nickel (red rust ratio of 5-6). No decrease in performance was seen with an increase in alloying addition unlike zinc-nickel and zinc-cobalt, indeed doubling the manganese content increased the corrosion performance to 100 times that of pure zinc. Manganese oxides formed on the surface of the coating during test exposure provide a non-voluminous barrier, detectable by cathodic polarisation studies. The corrosion rate was therefore lowered by suppression of the cathodic oxygen reduction reaction [13].

Zinc-tin

Zinc-alloys with 20-80% tin gave five-times the corrosion performance of zinc compared with an addition of only 14% nickel to zinc, which increases the corrosion performance by eight times. Zinc-tin alloys with 25% tin have shown better corrosion

performance than cadmium and zinc in salt spray tests. Alloys corrode faster in aerated solutions and low level tin alloys, like zinc, are consumed rapidly once red rust has formed and coatings with over 80% tin have a decreased corrosion performance. However, an 8μm zinc-alloy coating of 70-80% tin, shows a significantly reduced weight loss rate to a 14% zinc-nickel coating of comparable thickness.

CORROSION RATE MEASUREMENTS

The corrosion rate of coatings can be determined using the linear polarisation resistance technique (LPR) and potentiodynamic polarisation sweeps in sodium chloride solution. Polarisation sweeps can be used to obtain the anodic and cathodic Tafel constants required for the calculation of corrosion rates from polarisation resistance data, (see Chapter 3). The electrochemical potential of a system is particularly important when assessing galvanic interaction of the substrate and coating, as well as the sacrificial behaviour and any enoblement of the coating that may occur after an extended immersion time. The barrier protection afforded by a coating can also be assessed over time using these electrochemical techniques. LPR is particularly useful as it is quick and the data obtained can be directly compared with many of the literature values.

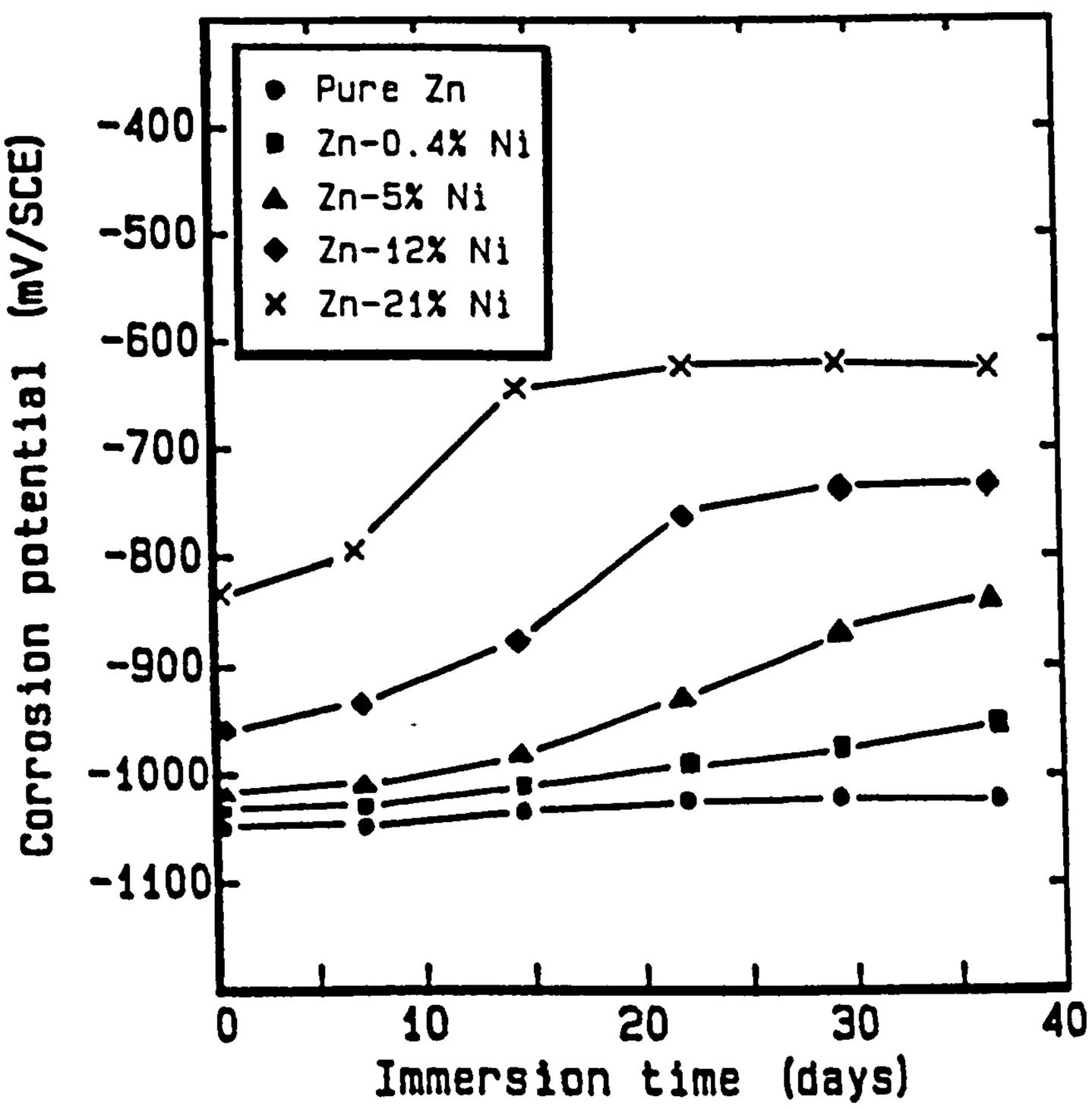
Zinc-nickel

As expected, the corrosion rate of zinc-nickel alloys decreased with increasing nickel content up to a level of 14% as the potential becomes more noble. There is a significant potential shift that occurs at 20% by weight nickel but past this level the effect is less pronounced. The nickel phase present also affects the corrosion rate. A single nickel phase improved the corrosion rate compared to multi-phase deposits. A multi-phase deposit could form galvanic corrosion sites that increase the corrosion rate. Zinc-nickel is sacrificial and up to 100mV more negative than steel in the same environment.

The corrosion rate of zinc-nickel coatings decreased with increased immersion time for most of the specimens tested as shown in FIGURE 20. FIGURE 20 indicates increased levels of corrosion resistance after 20 days immersion, probably due to the formation of an enriched nickel film on the alloy surface. This so-called enoblement phenomenon can be said to occur when the potential and so the coating becomes less active. This is

attributed to de-alloying and a preferential dissolution of the zinc from the coating that leads to a reduction in the protective sacrificial behaviour of the coating. Specimens that showed an increased corrosion rate might have formed local galvanic sites that led to increased zinc dissolution.

FIGURE 20: Variation in Open-Circuit Potential of Electrodeposited Zinc-Nickel with Immersion Time in Neutral 5% NaCl Solution [17]



De-alloying of binary electrodeposits has been compared to the dezincification of zinc-copper (brass) where a critical level of zinc (18 atomic percent) is required for the dezincification. This does not occur in the low levels of nickel seen in zinc-nickel alloys. Iron-chromium alloys also undergo dezincification. In this case a chromium rich upper surface layer is formed by selective dissolution of iron from the matrix and a passive layer of Cr-O-Cr chains is formed on the surface. These chains halt the dissolution of iron, and passive corrosion behaviour is seen. Zinc-nickel alloys under 25% do not exhibit a passive region and anodic polarisation curves show that the metal is in active dissolution. Much higher levels of nickel would be required in the coating, to possibly cause a passive region.

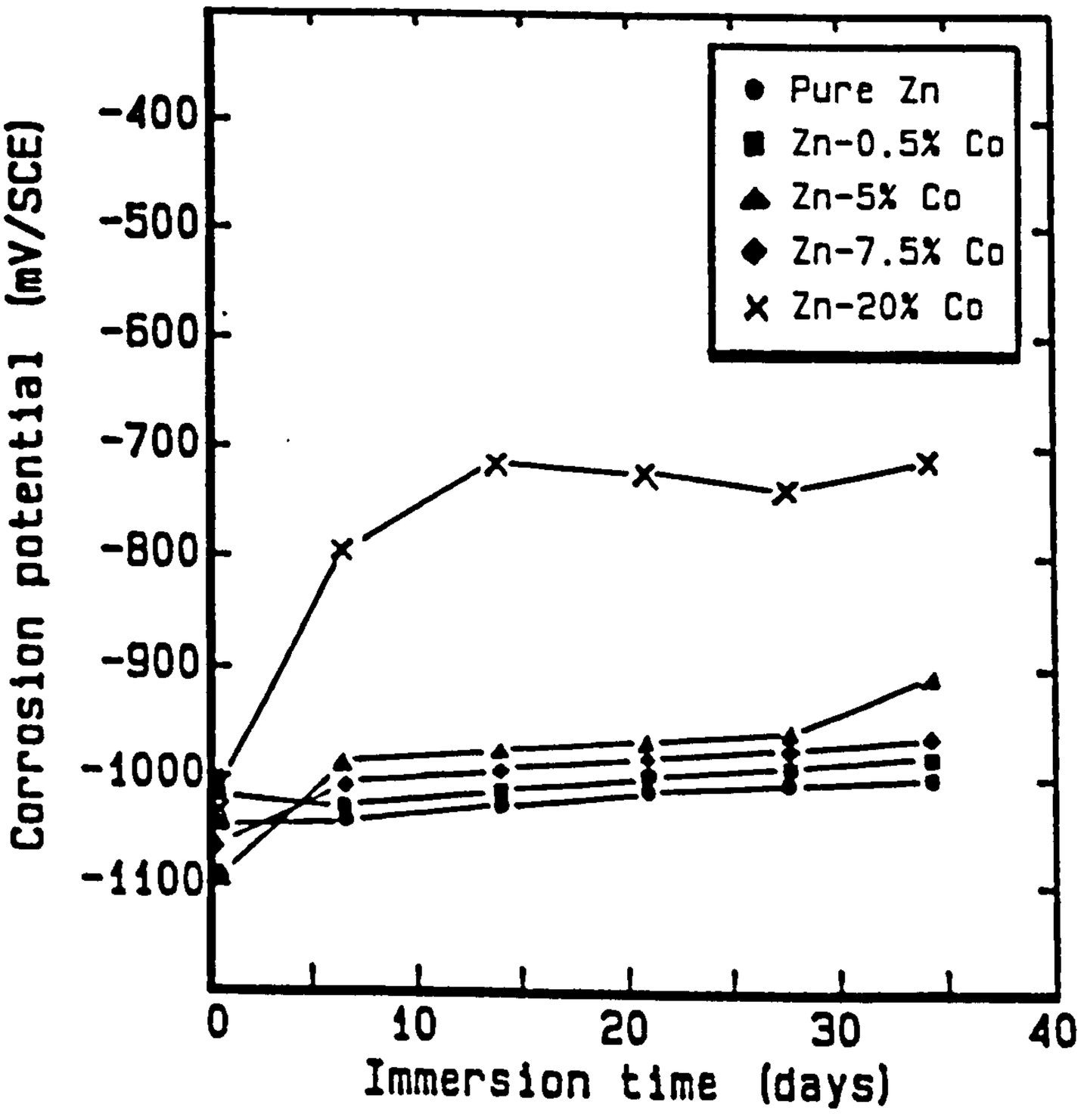
Zinc-iron

Zinc-iron alloys were found to become more noble as the proportion of noble metal was increased in the coating. The iron phase that was present was also a determining factor in the coating potential. The potential of zinc-iron alloys was however, always found to be more negative than iron, suggesting that zinc-iron coatings will provide sacrificial corrosion protection, regardless of the alloy composition.

Zinc-cobalt

Enoblement of zinc-cobalt coatings was only observed for coatings with relatively high levels of cobalt, after immersion for over 5 days, unlike zinc-nickel coatings that display enoblement with coatings containing as little as 1% nickel. The potentials of zinc-cobalt alloys with small levels of alloy addition were close to that of pure zinc, indicating that they would exhibit a similar galvanic corrosion behaviour.

FIGURE 21: Variation in Open-Circuit Potential of Electrodeposited Zinc-Cobalt with Immersion Time in Neutral 5% NaCl Solution [17]



Zinc-manganese

The corrosion rate behaviour of zinc-manganese alloys in sodium chloride solution, found by a Tafel extrapolation technique, was the reverse of that seen in neutral fog testing [17]. The corrosion rate of the coating decreased to a minimum for a coating containing 20% manganese, past this level the corrosion rate increased towards the rate of pure manganese. Zinc-manganese coatings are unique in that they require over 50% manganese by weight to influence their potential. Zinc-manganese coatings usually have a potential equivalent to that of pure zinc (-1030mV), in 3% sodium chloride solution. Increasing the alloying additions leads to a shift in potential towards that of pure manganese (-1270mV), which is much more active than pure zinc. These coating are likely to remain active, despite any galvanic corrosion between zinc and manganese, or any de-alloying process that may occur, unlike zinc-nickel alloys. The high sacrificial protection level of these coatings provides long term protection for steel substrates.

Zinc-tin

The potential of tin indicates that a zinc-tin coating would become more noble as the tin composition was increased. Zinc-tin alloys containing up to 75% tin have been found not to be sacrificial to steel in a corrosive environment. This is due to low corrosion rates, once red rust had been formed. However, zinc-tin coatings with 15% tin and improved corrosion performance have showed a passive state in certain circumstances and tin enrichment at the surface in sodium bisulphate by selective anodic dissolution of zinc. Prolonged exposure causes zinc to deplete and the remaining tin improves the protection of the surface layer[104].

Corrosion testing techniques

Other common testing techniques, such as weight loss, can be employed to determine an average corrosion rate for a coating. However, it is important to remember that galvanic, sacrificial or barrier protection mechanisms can be interrelated; and all influence the corrosion rate and behaviour of a system. The significance of each must be assessed, along with the alloy composition, cathodic current electroplating efficiency and any environmental and health concerns of the protection system's application.

The corrosion resistance of zinc is improved by additions of more noble metal. These additions can also result in more acceptable galvanic corrosion behaviour than pure zinc. From the previous section it can be seen that zinc-cobalt may provide a suitable corrosion resistant coating. However, the electrolytic bath needed to produce effective zinc-cobalt coatings is subject to strict compositional controls and addition of a surfactant, to prevent holiday formation is also usually necessary.

METALLIC COATINGS

Metal coatings are mainly used to improve the corrosion life of a component, however, consistent low electrical contact resistance (gold, silver), high and constant reflectivity (chromium) or oxidation resistance (aluminium on iron) can also be achieved by coating. Coatings themselves can be treated to a further enhance their performance by means of a passivation treatment, zinc layers are often chromated for added protection or wear resistance. Chemical deposition can also be used to co-deposit non-metallic material (e.g. Teflon, PTFE) [3, 105] along with the metal, to produce a layer with a specific pore structure, or altered frictional, corrosion or wear properties. The following section describes commonly used metallic coatings.

Zinc

A large quantity of mild steel is covered with zinc (galvanised) because the zinc is preferentially corroded in moist environments due to its anodic nature. Since its protection ceases when the area of steel exposed renders the polarization caused by zinc to be insufficient, the thickness of the zinc coating determines the protection. The protective capacity is not dependent on the deposition mechanism, and can be altered significantly by addition of alloying elements. A sacrificial zinc layer can block corrosion sites, by zinc hydroxide precipitation formed through the combination of zinc ions with hydroxyl ions. This voluminous corrosion product can be of benefit, filling minute gaps in the coating caused by cracks or slight deformations, but can also cause undesirable wedging of threaded parts.

While steel parts can be dipped into molten zinc or heated with zinc dust (Sherardizing) for protection, they can also be electroplated or sprayed [1]. Vapour deposition can be used where the metal coating is volatile and readily decomposable. At high temperatures, the coating metal can diffuse into the metal substrate and result in intermediate phases being formed [2].

Zinc coatings used for protecting steel in aqueous environments may also further reduce the corrosion rate by the zinc hydroxide formed acting as a passive protector [106]. However, this action is only beneficial in certain formation conditions. If the oxidation layer consists of zinc oxides and basic carbonates, formed in unpolluted atmospheres, it shows good adherence, compactness and corrosion inhibition of the substrate. Conversely, if oxysulphates were formed in a polluted atmosphere then the layer formed is poorly compacted and does not protect the metallic zinc. Temperature also significantly affects the corrosion rate of a material. The corrosion products that are formed at temperatures above 60°C change from a loose gelatinous form to a condensed, compact form that reduces the corrosion rate significantly.

Cadmium

Cadmium is also sacrificial to steel substrates but the galvanic potential developed is much less than for zinc. Although it appears to be better in marine environments because its chloride is less soluble and so more protective than zinc, it performs less well in sulphate containing environments. Zinc or a zinc-alloy coating may therefore be expected to perform at least as well as cadmium or better in a polluted or sulphur containing environment. Cadmium is also carcinogenic and can cause serious damage to kidneys, liver and lungs. It is considered to pose serious environmental and health hazards during production, application and use. The cyanide based effluent remaining after electroplating is also expensive to treat, hence replacements are urgently required.

Nickel

Cathodic nickel coatings are widely used to protect steels and can be electrodeposited or chemically deposited. However, they can suffer from fogging (nickel sulphate production in a sulphide environment) and so are often plated with a protective crack-

free chromium layer. Chromium forms a resistant Cr_2O_3 film on the surface in non-chloride environments and it can be electrodeposited or vapour deposited. However, it is generally only used in conjunction with a nickel under layer, due to its porous nature. The thickness of the coating is again a very important factor in determining the protection that it provides. Nickel corrodes preferentially to chromium and so if the coating is not continuous, the pores or gaps will lead to pitting. Many chromate conversion coatings are also widely available for use with zinc-alloy systems to improve the corrosion performance or other characteristics such as paintability [4, 7, 20, 22, 24]. However, concerns over the use of chromates have led to the research into safer and more environmentally acceptable alternatives [7].

Noble metals

Pure noble metal coatings are generally only used when a specific situation demands it because of their cost. They are sometimes used as a thin intermediate under layer to reduce the large galvanic potentials that might otherwise develop. Care needs to be taken when using these types of layers, because their porous nature, and poor bath throwing power can often result in a patchy coating.

Summary

Each coating type has its own characteristic problems, but the overriding concern is the difficulty in obtaining a perfect coating. It is particularly challenging to produce a perfectly continuous, non-porous, uniform metal coating by electrodeposition. Hydrogen evolution may produce cracks in the deposit, or high compressive and tensile stresses may arise in deposits that may cause cracks to form. The adhesive properties of the metal substrate surface can also vary considerably if residual grease, oxides or etching reagents remain.

ELECTROPLATING

Electrodeposition of a metal from a single element bath is relatively straightforward but when more than one electrolytic element is present, complications can occur with different deposits being possible. This is due to the variety of deposition mechanisms that can operate depending on the prevailing conditions. In a two metal ion electrolyte,

the metals maybe deposited in isolation or combination. For example, zinc can be alloyed with the iron group metals (iron, cobalt and nickel), by electrodeposition from aqueous solutions of their uncomplexed salts such as sulphates or chlorides. The compositions of binary zinc-alloy deposits from such electrolytes depend greatly on the current passed through the plating cell, and also the electrolyte temperature and pH. The more noble of the metals would be expected to always be deposited first (normal deposition) but actually the reverse is often found (anomalous deposition).

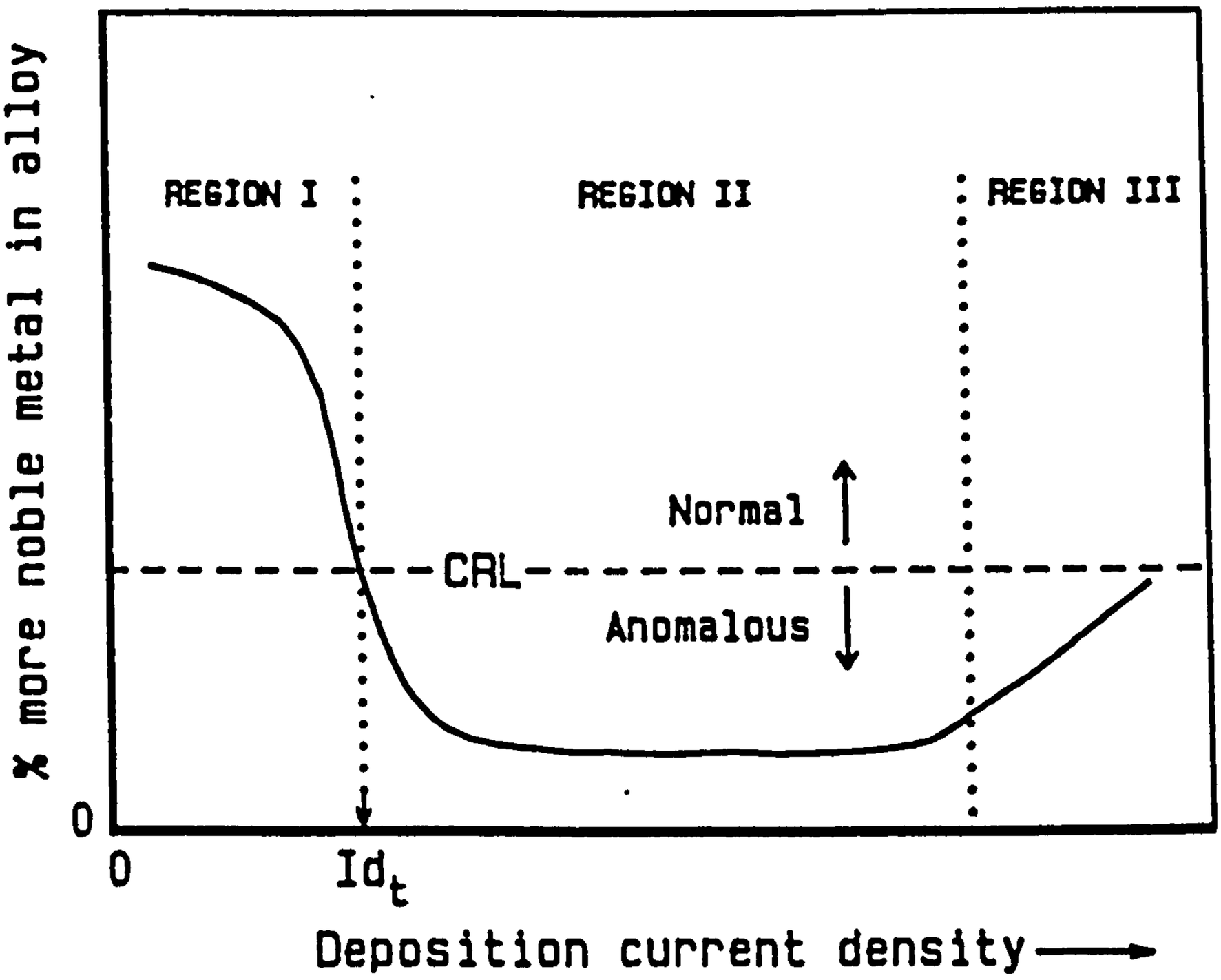
Normal Co-Deposition

Normal deposition is thermodynamically dependant and the reaction with the maximum Gibbs free energy, EQUATION 13, predicted from a comparison of elemental electrode potentials, should predominate. This results in the more electropositive element being deposited preferentially. However, if the two elements have similar electropotentials, they may co-deposit due to polarization effects reducing the gap in potential. A difference of >0.2V is usually considered to be sufficient to prevent the co-deposition of two different metal ions [107]. This is an over simplification as current and concentration can also effect a potential shift and therefore must be considered.

Anomalous Co-Deposition

Anomalous co-deposition is a relatively rare phenomenon usually associated with the co-deposition of zinc with iron-group metals, or the mutual co-deposition of iron, cobalt and nickel, where the less noble metal is deposited preferentially [108]. The current at which the electrolyte and the deposit contain an equal quantity of the more noble metal is known as the transition current density (Id_t). This represents the point at which the electrodeposition changes from a normal to an anomalous type [109]. The relationship between the normal and anomalous co-deposition mechanisms and change in current density for a zinc-cobalt electrodeposit is illustrated by FIGURE 22 [110]. The broken line is the composition reference line CRL and shows the weight percentage composition of the alloy that just equals the metal percentage of the bath [111].

FIGURE 22: General Relationship of Composition and Deposition Current Density for Zinc-Iron Group Alloys



At low current densities, REGION I, normal deposition occurs, demonstrated by the higher level of more noble metal in the deposit than the electrolyte. As the current density is increased, REGION II, the reverse situation begins to occur and the percentage of more noble metal in the bath is more than that of the deposit, indicating that anomalous co-deposition is occurring. This region usually spans a wide current density range, over which the zinc alloy composition remains stable, if no other parameters are varied. However, if the current density is increased further, REGION III, the normal co-deposition behaviour is seen to reappear, i.e. the deposit is richer in the more noble metal.

Development of the Anomalous Co-Deposition Model

Anomalous co-deposition has been observed since the turn of the century, but it was not until 1924 that Glasstone and co-workers proposed a mechanism to explain the behaviour[17]. They suggested that the deposition of nickel from a zinc-nickel electrolyte, occurred via the formation of a less noble metastable intermediate, rather than the divalent nickel ion/nickel metal couple. Conversion of the intermediate to metallic

nickel was retarded by the presence of zinc cations allowing the preferential deposition of zinc. However, the metastable intermediate was not detected and no experimental evidence was published to support the theory.

Lustman, using an acid sulphate bath, detected considerable cathodic polarisation at the transition current density for zinc-nickel alloys [112]. He proposed that a change in the deposition phase from the α-solid solution of nickel in zinc at low current densities to the γ-solid solution at high current densities was responsible for this effect. Lustman attributed the further changes in cathode potential to the transformation from γ to δ or η solid solutions of nickel in zinc. However, his phase stability model does not explain the sudden noble metal suppression or why temperature or pH also effects the electrolyte in a similar way to current density.

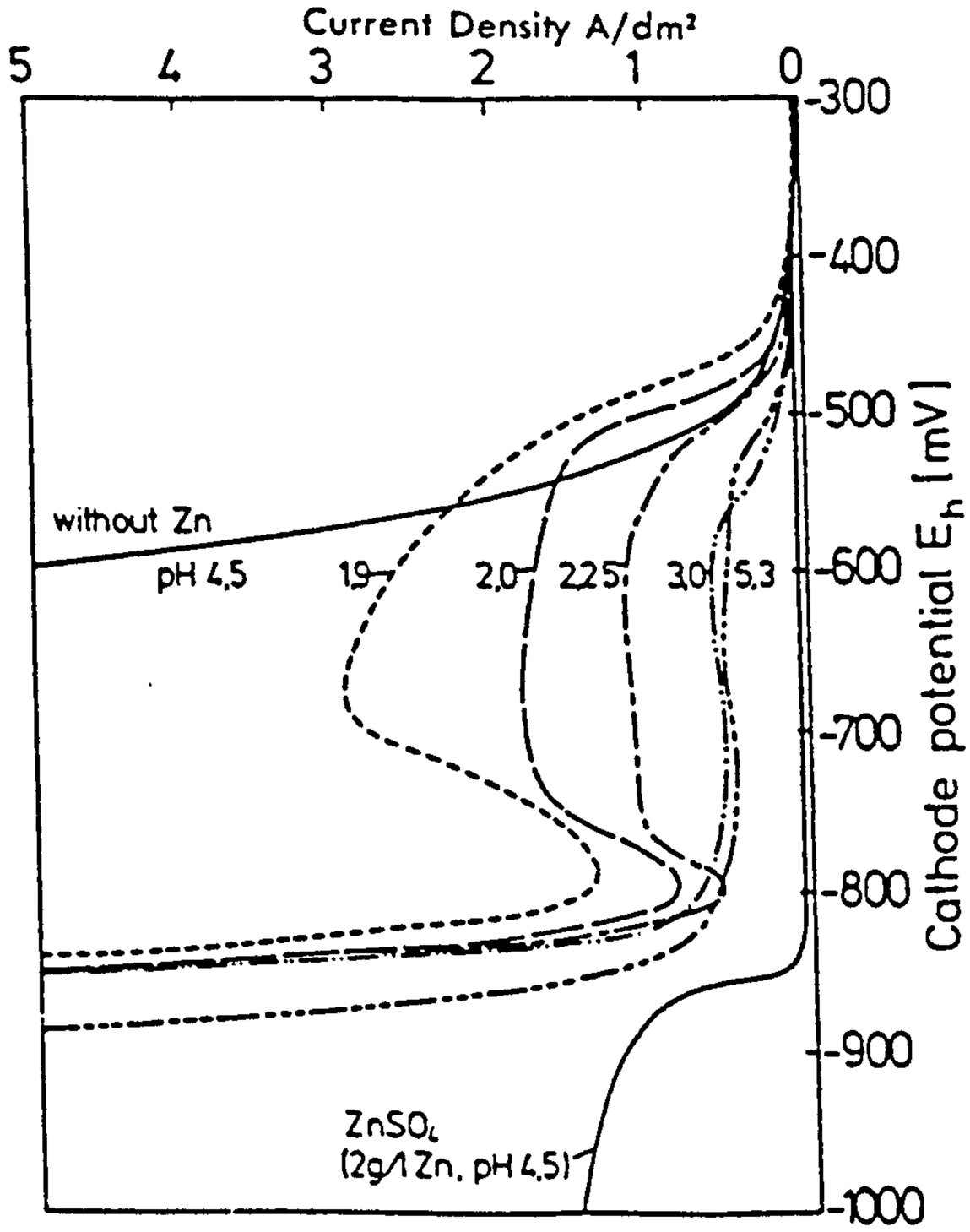
In 1963 Brenner proposed that an 'addition agent' formed by the cathode reaction was responsible for the suppression of the iron-group metal [108]. Nickel deposition is suppressed by certain organic compounds used as brightners e.g. polyoxyethylenes. Brenner believed that the suppression was due to small concentrations of a species formed on the cathode surface, rather than variation in the electrodeposited phase. The transition current density is the point at which the applied current density is high enough to produce sufficient cathodic hydrogen evolution to affect a pH rise and cause a critical level of the 'addition agent'. The noble metal deposition is limited at this point and so the anomalous co-deposition mechanism dominates. Although Brenner's explanation did account for the observed effects, he did not experimentally identify the 'addition agent'. The term he used was confusing as many compounds can be added to electroplating baths to effect the appearance and mechanical properties of the electrodeposits formed. However, most investigations from the mid 1960's onwards, supported his model of a precipitated species on the surface of the cathode causing the anomalous co-deposition behaviour.

Dahms used a dropping mercury electrode to study the mutual co-deposition of the iron-group metals while eliminating the evolution of hydrogen as a means of raising the pH at the cathode [113]. He found that in oxygenated electrolytes anomalous co-deposition occurred due to the formation of metal hydroxides on the cathode surface. In the absence of oxygen, normal co-deposition occurred. Rotating disc experiments in nickel-iron electrolytes were used to confirm the model. They proved ferrous hydroxide precipitated at the cathode by a rise in pH, and only suppressed deposition of the more noble metal, nickel [114]. This 'hydroxide suppression mechanism' attributed anomalous co-deposition to a build up of metal hydroxides that suppressed the more noble metal's deposition.

Raub reviewed the electrodeposition of zinc alloys in 1976 [115]. He reported on earlier work by Knodler who examined the effect of zinc additions to a Watts bath on the cathodic polarisation behaviour of a copper cathode. The deposition of nickel was suppressed by the presence of small quantities of zinc in the electrolyte. The potential shifted to that of the cathode in zinc sulphate alone which is 200 to 300mV more negative than that of nickel in the same conditions. Increasing the electrolyte pH also shifted the polarisation curve to that of pure zinc, presumably because the conditions for zinc hydroxide were favoured in more alkaline conditions, as shown in FIGURE 23.

Raub likened the cathode behaviour seen with zinc salts from a Watts bath to that seen for organic inhibitors like diols. He postulated that zinc hydrolysis products had a strong inhibiting effect on nickel deposition and zinc deposition occurred via the reduction of zinc hydroxides ($Zn(OH)_2$ or $(Zn(OH)^+)$ acting as an intermediate, rather than by direct zinc ion reduction.

FIGURE 23: Influence Of 30mm/L Zinc on the Cathode Potential verses Current Density Curves of a Watts Nickel Electroplating Bath at Different pH Values

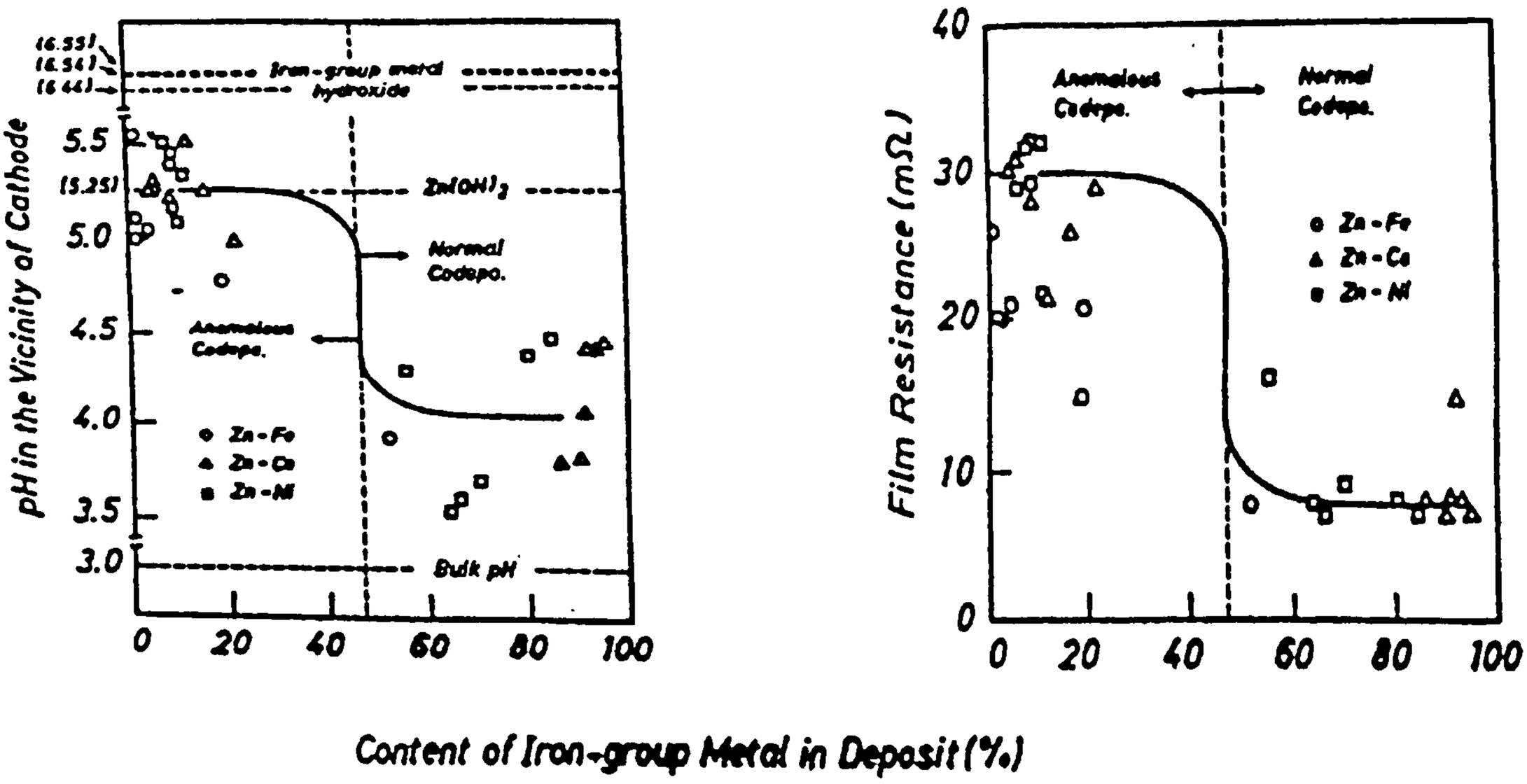


Electrodeposition of binary zinc alloys from acidic and mainly sulphate baths has been extensively studied over a wide range of current densities by Fukushima, Higashi and co-workers [110, 111, 145]. They reported that cobalt deposition was suppressed in zinc-cobalt electrodeposits by the presence of zinc cations. Deposition was proposed to occur by the formation of zinc hydroxide through which the discharge of cobalt cations then occurred. The cobalt in the electrodeposited alloy was expected to be present in the metallic state only not as the hydroxide, this was confirmed using X-ray photoelectron spectroscopy (XPS) [110]. This was considered to be evidence to support the hydroxide suppression mechanism.

The pH in the vicinity of the cathode during electrodeposition was measured using an antimony reference electrode 10μm from the cathode [111]. In each alloy, (zinc-iron, cobalt or nickel) the pH was found to rise to pH5.25 (the pH for zinc hydroxide precipitation) at the current density where the transition from normal to anomalous co-deposition occurred. This pH was below the precipitation pH for the iron group metal

and remained constant due to the buffering effect of zinc hydroxide formation. This was the first experimental evidence supporting the premise that hydroxyl ion formation at the cathode surface was a precursor for anomalous co-deposition. The surface film resistance was also measured by application of a short current pulse to the cathode, and was shown to rise abruptly in the anomalous region. This was attributed to the formation of zinc hydroxide on the cathode surface [111]. The film resistance of zinc hydroxide on the cathode surface suppressed cobalt deposition and resulted in anomalous co-deposition. The relationship between film resistance and pH is shown in FIGURE 24.

FIGURE 24: Relationship between Alloy Content and (a) Cathode pH or (b) Film Resistance at Various Current Densities



Cathode Efficiency

Onset of anomalous co-deposition, shown in REGION II of FIGURE 22, is accompanied by a sharp decrease in cathode potential due to the zinc hydroxide layer resistance, illustrated in FIGURE 24. The thickness of this layer, is maintained due to the equilibrium rate of deposition and reduction, and suppresses nickel and hydrogen ion reduction at the surface. This consequently leads to a reduction in noble metal deposition and an increase in current efficiency. At higher current densities, REGION III of FIGURE 22, the zinc hydroxide layer becomes less thick (reduction rate is higher than the deposition

rate) or its buffering capacity is exceeded, and both hydrogen and the more noble metal can be reduced at the cathode surface. This increases the quantity of noble metal in the deposit and reduces the cathode efficiency as more hydrogen gas can be produced at the cathode surface. A decrease in pH makes the formation of the zinc hydroxide harder, so raises the transition current density for the start of anomalous co-deposition. An increase in pH is also correctly predicted to increase cathode efficiency.

Underpotential Deposition Model

While the hydroxide suppression mechanism has led to a greater understanding of anomalous co-deposition behaviour of zinc iron group alloys, it does not fully explain the role of the hydroxide or the exact nature of the hydroxide species. The magnitude of the transition current density and the factors controlling the deposition of the iron group metal in the anomalous region requires further clarification. The presence of small quantities of zinc in the normal region has also not been adequately explained.

The most significant alternate mechanism for anomalous co-deposition is underpotential deposition of the less noble metal in a given binary electrolyte. The predomination of the less noble metal leads to an anomalous co-deposit. However this theory is not widely accepted as an appropriate explanation for the anomalous behaviour, and has not been proved to be applicable to iron group alloys.

Electrolyte Additives

Generally zinc iron group electrolytes consist of concentrated sulphates or chlorides in acidic baths. Anomalous co-deposition behaviour requires a low noble metal ion electrolyte percentage. The current efficiency for these systems is high over a wide deposition current density. The high value, approaching 100% in some cases, indicates that only small amounts of hydrogen are evolved, suggesting the possibility of a reduced hydrogen embrittlement risk.

Throwing power

Zinc alloy electrolyte throwing power can be increased by the addition of ammonium, sodium or potassium salts that increase conductivity. Other counter ions such as

sulphamates (organic complexing agents), pyrophosphates, fluoroborates and acetates have also been used. Chloride electrolytes are believed to have better throwing power than sulphates, although both are used in commercial applications. The throwing power of both bath types can be improved by the addition of cyanides, however, these are toxic and produce unacceptably low concentrations of iron group metal in the electrodeposit.

Ammonia containing zinc-nickel electrolytes readily produce bright deposits but are costly to dispose of and require careful electrolyte pH control to prevent zinc hydroxide precipitation (pH5.25 at 25°C). Alkaline ammonia free zinc-nickel electrolytes have high throwing power at room temperature, unlike ammonia based electrolytes. However, despite alkaline electrolytes being cheap and environmentally more sound they have slow plating times, lack deposit brightness and require additional complexing agents to maintain the nickel level.

Gabe states that organic 'addition agents' are added to commercial zinc alloys to relieve stresses in the electrodeposit by modification of their initiation and growth. Deposits that have high internal stress levels can crack and spall from the cathode surface but this can be reduced, for zinc-nickel electrolytes, by regulation of the pH from 3 to 4.5. Acetic and boric acid can both be used to buffer the pH, but acetic acid has been found to reduce electrolyte throwing power.

Wetting agents

The surface tension of an electrolyte can be lowered by organic additions called 'wetting agents' or surfactants such as sodium laural sulphate or other long chain sulphonic acids. They minimise the build up of hydrogen bubbles on the cathode surface that can lead to the formation of holes, referred to as holidays, in the electrodeposit surface.

Brighteners

Organic brighteners can be added to zinc alloy electrolytes to improve electrodeposit brightness. Bright deposits are required for many applications for decorative and quality control reasons, and passivation treatments to increase corrosion performance are

usually only applied to bright deposits. Brightener development has not produced a common mechanism to explain how they operate, despite work being carried out in specific cases on the effect certain addition agents have on electrodeposits.

There are two main types of brighteners, primary and secondary [17]. Primaries are used to reduce internal stress and brittleness of the electrodeposit and preserve brightness. They are usually aromatic sulphur compounds such as sulphonic acids or surface active polymers such as polyoxyethylenes. Secondary brighteners are usually unsaturated organics with strong surface absorption tendencies such as aromatic aldehydes, ketones and carboxylic acids. They provide a mirror bright finish.

Low concentrations of brighteners are required but most are consumed during electroplating by either decomposition or occlusion into the electrodeposit along with the metals[17]. This necessitates monitoring, of the brightener concentrations during electroplating, further increasing the cost. They are expensive to purchase and need to be of high purity as impurities affect their performance. Brighteners can also affect the composition of the electrodeposit. Studies by Tsuji and co-workers have shown the nickel content of a zinc-nickel electrodeposit can be reduced by over 10%, but the effect was partially addressed by an increase in the current density [117]. Despite their disadvantages brighteners are considered essential to eliminate post-plating buffing procedures [17].

Anodes

Various anodes can be used in zinc alloy electroplating. Soluble (active) anodes of zinc and nickel are common and can be used alone or together (dual types require separate circuits and rectifiers in a conventional tank). Soluble anodes are advantageous because they replenish the electrolyte metal ions which is generally less expensive than using metal salts. They need to be used with care however, as they may introduce impurities to the bath and their activity precludes use in certain situations (zinc anodes can be replaced with nickel anodes alkaline nickel baths, if they are too active). Insoluble (inert) anodes do not replenish the electrolyte metal ions but they can be permanently

installed and do not require much maintenance. They are usually made from stainless steel or lead.

ZINC-COBALT ELECTROLYTES

Electrolyte composition is a major determining factor for alloy deposition and there are three common types of electrolyte baths used for component electroplating; alkaline cyanide, alkaline cyanide free (zincate) and acid chloride. Zinc-cobalt electrolytes are usually ammonia free and mildly acidic, avoiding the use of complexing agents (and cyanide) that ensures simple effluent treatment. However, not all are considered suitable for zinc alloy deposition, especially when cobalt is the co-deposited metal.

Alkaline Cyanide

Cobalt forms strong macro-complexes with cyanide in alkaline cyanide baths. This invariably makes the co-deposition of cobalt experimentally difficult without the use of further additives. The use of cyanide also requires special effluent treatment, increasing the cost of using this type of electroplating bath.

Alkaline Cyanide Free (Zincate)

Incorporation of cobalt salts in a zincate electrolyte is impossible without the use of complexing agents that selectively hold cobalt ions preventing precipitation while still allowing deposition. Their presence and the excess of sodium hydroxide, along with other additives required to produce desirable deposit characteristics results in the need for extra effluent treatment. Zincate electrolytes have good throwing power, are cheap and non-corrosive, and can be used in any zincate equipment to produce zinc-cobalt alloys containing 1% w/w cobalt [9]. However, the zincate process has a low efficiency, mainly due to anode control complications, which makes electrolyte maintenance extremely difficult [116]. Alkaline processes are however, more tolerant of poor component cleaning and iron contamination [9].

Acid Chloride

Acid chloride zinc electrolytes do not exhibit the complications discussed for the other bath types and have proved to be useful for the development of zinc-cobalt alloy

processes [116]. Preferential cobalt deposition might be expected but the more complex anomalous co-deposition mechanism occurs [108].

Embrittlement Implications

The type of bath used can also affect the degree of hydrogen embrittlement seen for electroplated zinc specimens. Embrittlement indices can be calculated in a number of ways. One method is shown in EQUATION 16. The results in TABLE 4 demonstrate that zinc chloride baths produce the least embrittled specimens when tested [117]. It is believed that the same trend would also be observed for zinc-cobalt electroplated specimens.

EQUATION 16: Embrittlement Indices

$$EI = (\Delta L'/\Delta L) \times 100\%$$

Where: ΔL = extension of failed unplated specimen

$\Delta L'$ = extension of failed plated specimen

TABLE 4: Change of Embrittlement Index with Bath Type [117]

Bath Type	Operating Conditions	Embrittlement Index (%)
Zinc (cyanide)	2A/dm^2, 10 min	32
Zinc (zincate)	2A/dm^2, 10 min	50
Zinc (chloride)	2A/dm^2, 10 min	94

ZINC-COBALT ELECTROLYTE COMPOSITION

The percentage of cobalt in a binary bath has been shown to be directly proportional to the final composition in the alloy, in both rack and barrel applications [9]. Metal bath percentage can be calculated using EQUATION 17.

EQUATION 17: Metal Bath Percentage [108]

Metal bath percentage = (A x 100) / (A + B)

Where: A / B = concentrations by weight of each electrolyte metal

FIGURE 25: Effect of Metal Ion Concentration on Deposit Composition

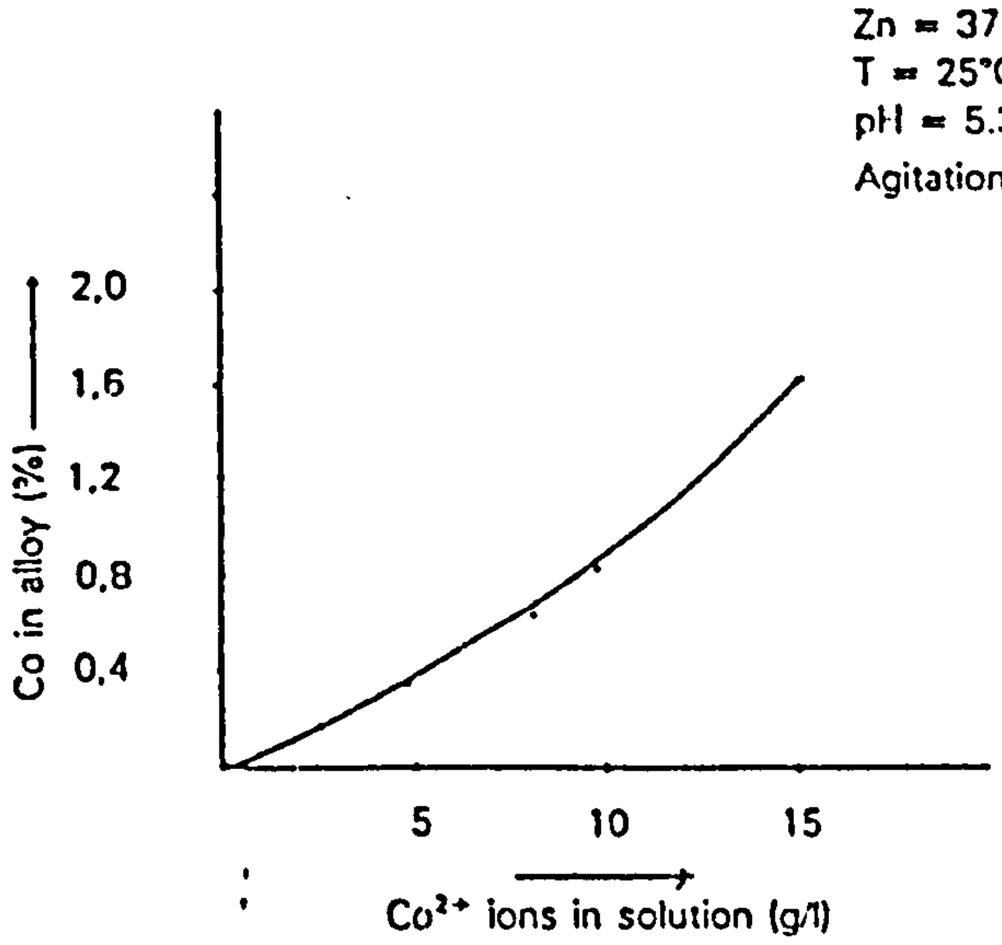


FIGURE 25 shows that increasing the percentage of cobalt ions in the bath results in an increase of cobalt in the alloy composition. Care must, however, be taken, as increasing metal ion bath concentration can result in powdery black deposits, while lowering the metal ion concentration reduces the buffer capacity of the bath [118]. Varying the total metal ion concentration in the bath while maintaining the same ratio of the two metal ions usually has a very small effect on the deposit [119]. Other electrodeposition parameters such as: deposition current density, electrolyte temperature and pH can be varied to produce compositional changes in the electrodeposit.

Choice of Electrolyte

While commercial zinc-cobalt electrodeposits have mainly been produced from sulphate/chloride electrolytes using different complexing agents, cyanide and acetate baths have also been used with some success [116]. TABLE 5 gives some common bath compositions of zinc-cobalt electrolytes.

TABLE 5: Bath Composition of Various Recent Zinc-Cobalt Plating Systems

Bath Type	Metal Ions/Additives	Reference
Cyanide (formaldehyde) 25-40° C	$ZnSO_4.7H_2O/CdSO_4/CoSO_4.7H_2O$ $CH_3COONa.3H_2O$ Additives	121
Zincate (NaOH) 20-25°C	ZnO/ Co^{2+} ions Complexant Brighteners	9
Acid chloride (H_3BO_3) pH = 5 - 5.5/20 - 35° C	ZnCl/ Co^{2+} ions NaCl Additives	116
Acid sulphate (H_3BO_3) pH = 2.4 -5.4/30-40°C	Zn/ $CoSO_4$ NH_4Cl Additives	118
Acid sulphate (H_2SO_4) pH = 3.0/40°C	$ZnSO_4.7H_2O/CoSO_4.7H_2O$ $CH_3COONa.3H_2O$	111

PRESENT STUDY

The acid zinc-cobalt sulphate electrolyte shown in TABLE 5 (final entry), was employed in the present work. Alteration of the bath composition to find the optimum electroplating parameters was achieved without the use of brighteners or other additives. Additives can disrupt even alloy distribution, lower cloud point (the point at which crystallisation begins), cause complete insolubility and lower the iron group metal percentage in the deposit [116, 120] . These are all unacceptable effects and may obscure determination of the optimum plating conditions. A surfactant (Teepol) was used to prevent holiday formation in the coating, which is a general feature of zinc-alloy electrodeposits [120]. Once formed the electrodeposits were analysed to assess their deposition mechanism and any embrittlement effect they had on the steel substrate. Their corrosion performance was compared experimentally with zinc, zinc-nickel, zinc-cobalt-iron and cadmium coatings and also bare steel, which was used as a control.

EXPERIMENTAL

METALLOGRAPHICAL EXAMINATION OF THE TEST MATERIAL

The high tensile strength steel used in this project work was AISI 4340. The material when it arrived from the manufacturers had a grain size of 7μm and was of aircraft quality. The hardness taken before specimen machining heat treatment was given as 197 BHN. It is a deep hardening steel and its composition is given in TABLE 6.

TABLE 6: Chemical Composition of AISI 4340 Steel

Element	C	Si	Mn	P	S	Cr	Mo	Ni	Al	Cu	Fe
Composition (%)	0.41	0.23	0.79	0.009	0.003	0.88	0.22	1.67	0.024	0.13	balance

As mentioned in Chapter 1, the microstructure of steel is a very important factor in determining its particular susceptibility to HE, and can be ameliorated by its heat treatment and tempering. The AISI 4340 steel was examined metallographically to determine its microstructure, and to detect any discernible change after it had been subjected to the baking treatment that was necessary for parts of this project.

Sections of material in the as received normalised condition, after quenching and tempering and quenched tempered steel which had been and baked at 200°C for 24 hours were taken and mounted in Bakelite. They were polished on grinding wheels using 220-grit and then 1200-grit carborundum paper, and finally to a mirror finish using 6μm and 1μm diamond paste. The specimens were then etched using 2% Nital to reveal the microstructure before examining under an optical microscope, photographs are presented in Chapter 3.

ELECTRODEPOSITION PARAMETER VARIATION

One of the simplest methods for controlling electrodeposit composition is by varying the standard electrolyte parameters used [121]. The effects of a number of test parameters on the deposited coating were investigated as part of this study. The parameters that were examined were time, temperature, pH and current density. Once a trend had been established for electrodeposit composition, optimum conditions could be determined and used throughout the project.

The standard electroplating parameters that were chosen for the electroplated coatings used in this work, listed in TABLE 7, gave a smooth bright deposition layer, while maintaining the requirements for an 8μm thick coating, (deposition under the anomalous co-deposition mechanism for the binary coatings was also maintained). Zinc-cobalt electroplating was performed for 15 minutes at 50°C and pH4.2 using a deposition current density of 10mA/cm^2. Zinc-nickel electroplating was performed for 15 minutes at 25°C and pH5 using a deposition current density of 20mA/cm^2. Zinc-cobalt-iron electroplating was performed for 10 minutes at 43°C and pH3 using a deposition current density of 30mA/cm^2.

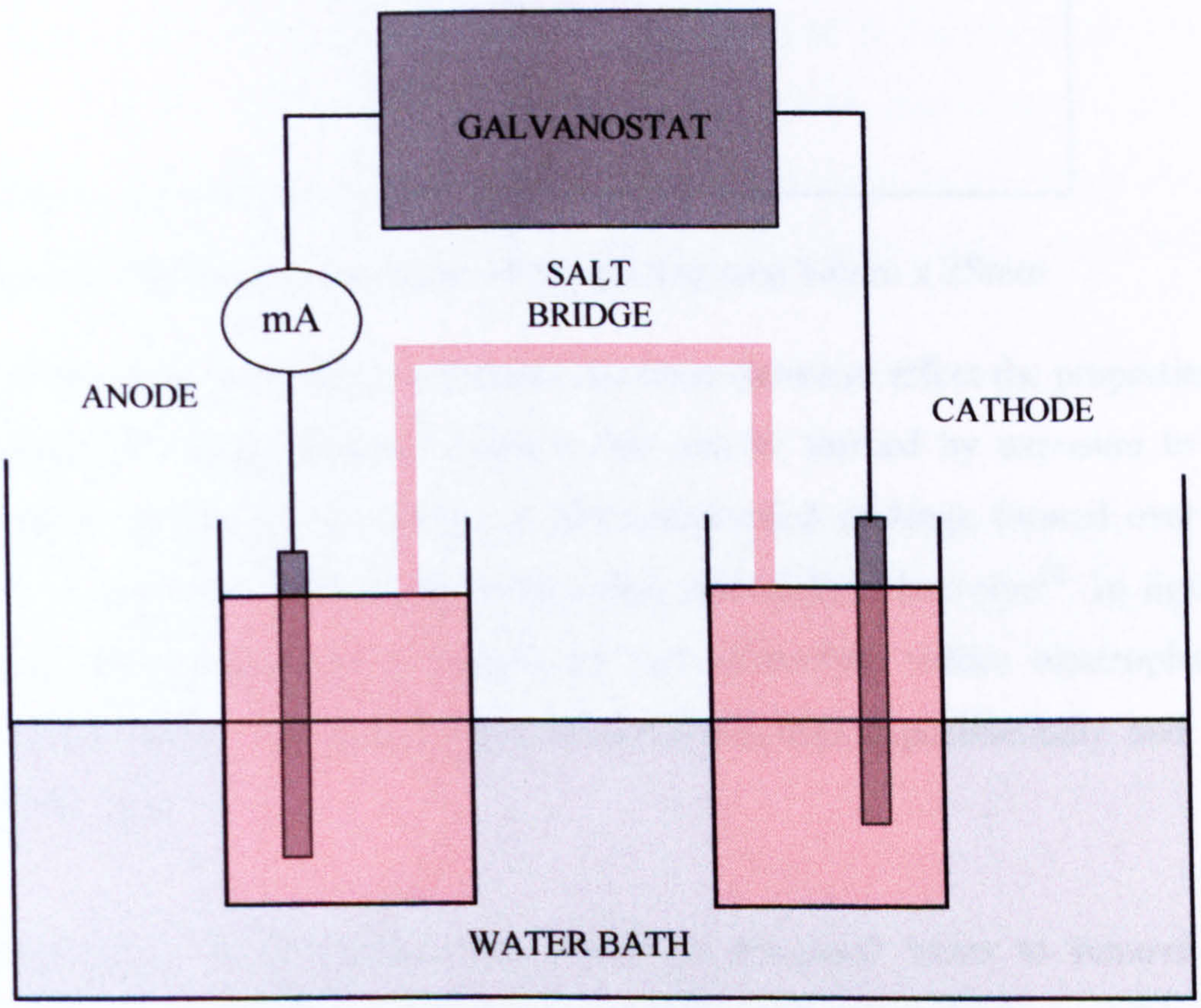
TABLE 7: Electrolytes Used with Standard Operating Parameters

System	EDAX Deposit Composition (%)	Current Density (mA/cm^2)	Time (minutes)	pH	Temperature (°C)	Electrolyte Constituents(mol/dm^3)			
Zn	Zn 100	10	15	1	50	$ZnSO_4.7H_2O$	1.2	H_2SO_4	0.6
Zn-Co[110]	Zn 99 Co <1	10	15	4	50	$ZnSO_4.7H_2O$ Na_2SO_4	1.7 0.4	$CoSO_4.7H_2O$ $MeCOONa.3H_2O$	0.2 0.1
Zn-Ni[18]	Zn 92-89 Ni 8-11	20	15	5	25	$ZnSO_4.7H_2O$	0.92	$NiSO_4.7H_2O$	0.58
Zn-Co-Fe *[103]	Zn 79 Co 12 Fe 9	30	10	3	43	$ZnSO_4.7H_2O$ $FeSO_4.7H_2O$ $MeCOONa.3H_2O$	0.4 0.06 0.3	$CoSO_4.7H_2O$ Na_2SO_4 H_2SO_4	0.4 2.5 0.5

* This coating was modified to produce 10% cobalt in the electrodeposit, (determined by EDAX), by reducing the quantity of cobalt sulphate used to 0.3 mol/dm^3

The electrolytes were prepared in accordance with the constituents listed in TABLE 7, using deionised water and analytical grade reagents. The bath conditions were then altered to determine the optimum electroplating parameters that are also shown in TABLE 7. All the specimens were electroplated galvanostatically in a beaker, using a consumable zinc counter electrode (99.99%). The set up, shown in FIGURE 26, was held in a water bath to maintain the temperature required for each experiment. A small quantity of surfactant or wetting agent, in this case Teepol, was added to all the electrolytes used to help prevent the formation of holidays (small holes formed by adherence of bubbles) on the electroplated metal surface.

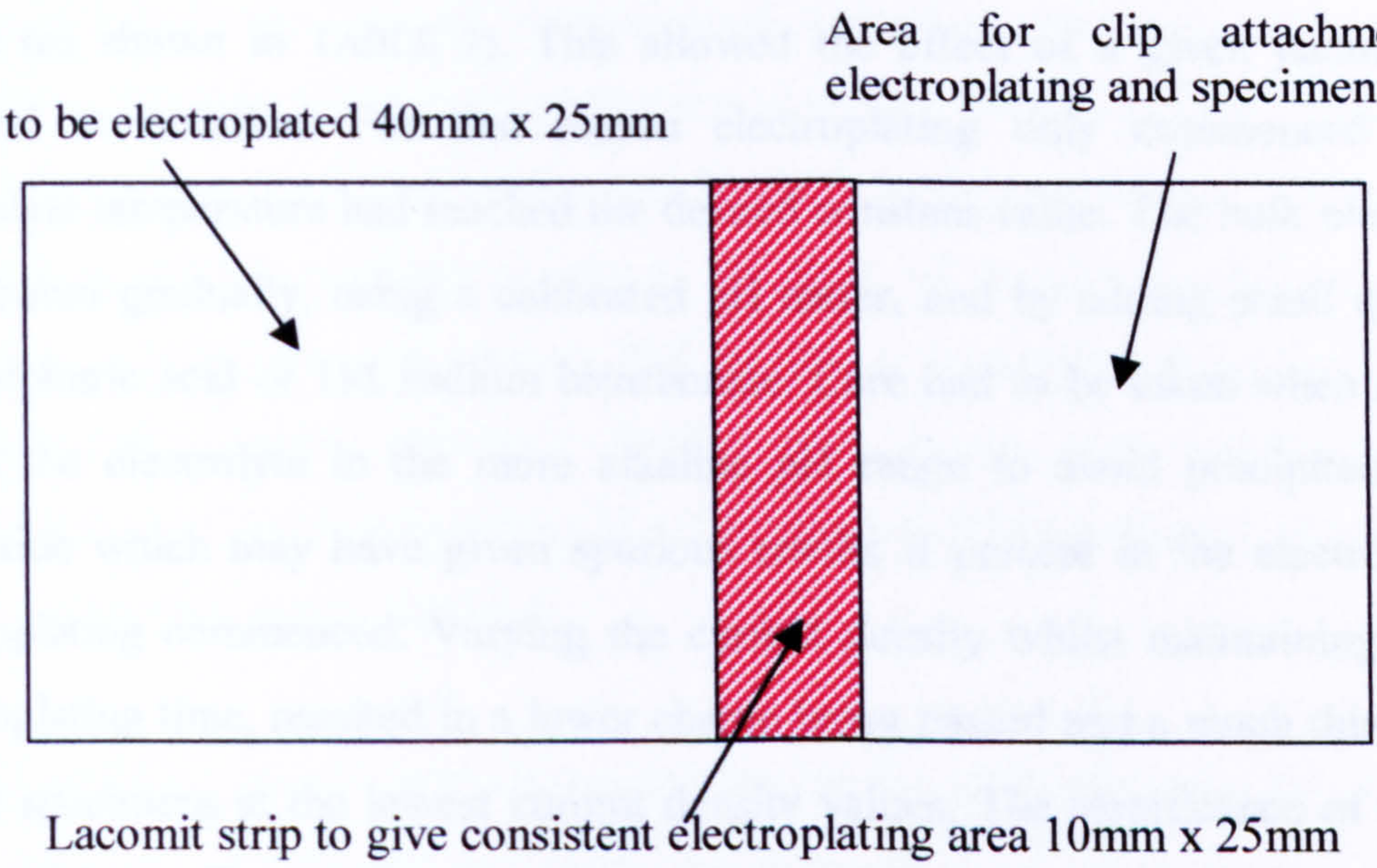
FIGURE 26: Basic Galvanostatic Electroplating Set Up



The electrodeposits were formed on a thin steel shim (approximately 57μm thick). The metal surface was gently abraded with 1200-grit carborundum paper, on both sides, to remove any oxides on the surface, and then degreased in an ultra sonic bath containing propan-2-ol for 5 minutes. Once a satisfactory surface had been obtained, the specimens were dried, cut to size (approximately 90mm x 25mm) and the area to be electroplated was measured. Part of the front and all of the back was masked using lacomit protective

varnish, as shown in FIGURE 27, to give a consistent electroplating area. After preparation the metal strip was electroplated according to the particular parameters of the experiment.

FIGURE 27: Shim Specimen to be Electroplated



The nature of the initial layer that is deposited has been shown to effect the properties of an electrodeposited coating. Contact deposits that can be formed by exposure to the electrolyte can have contrary properties to electrodeposited coatings formed over the same period, as shown by Carr in his work using zinc-nickel electrolye[18]. In light of these findings the contact time for specimen and electrolyte before electroplating, during all of this work, was kept to the minimum possible experimentally and was considered to be zero.

After electroplating, the specimens were rinsed in deionised water to remove any remaining electrolyte, and dried. The deposit thickness was estimated by weighing the prepared steel strip before and after coating. Comparison with the thickness determined by Faraday's law from the charge provided, made it possible to determine current efficiency, by the method used is given in the APPENDICES. Each specimen was visually and compositionally examined after the coating process had been completed. The composition of the coating was determined by direct measurement using energy dispersive X-ray analysis (EDAX) on the electroplated specimen. The validity of these

results were confirmed by dissolving the coating and using the inductively coupled plasma spectrometer (ICP). Both these techniques will be discussed in more detail later in this chapter.

Each parameter was varied in turn with the remaining parameters set at the standard values (as shown in TABLE 7). This allowed the effect of a given parameter to be assessed in isolation. For that reason electroplating only commenced when the electrolyte temperature had reached the desired constant value. The bulk electrolyte pH was altered gradually, using a calibrated pH meter, and by adding small quantities of 1M sulphuric acid or 1M sodium bicarbonate. Care had to be taken when altering the pH of the electrolyte in the more alkaline pH range to avoid precipitation of zinc hydroxide which may have given spurious results if present in the electrolyte before electroplating commenced. Varying the current density whilst maintaining a constant electroplating time, resulted in a lower charge being passed and a much thinner coating on the specimens at the lowest current density values. The significance of this will be discussed in the Chapter 4.

TABLE 8: Range of Electroplating Parameters Examined

Parameter	Range investigated						
Time (minutes)	0.5	1	2	Then 5 to 30 minutes @ 5 minute intervals			
Temperature (°C)	25 to 60 @ 5 degree intervals						
pH	1	2	3	Then 3 to 5.5 @ 0.5 pH unit intervals			
Current density (mA/cm^2)	0.1	1	2	5	10	* either 20/50 or 30	100

The variation in parameters investigated for each electrolyte is given in TABLE 8. The range of each variable tested was the same for each electrolyte except for current density. *The current densities of 20 and 50mA/cm^2 were assessed for zinc-cobalt and zinc-nickel but not for zinc-cobalt-iron, as the standard current density of 30mA/cm^2

was considered to be adequate in this region. The effect of agitation during electroplating was also examined for the zinc-cobalt electrodeposits.

ELECTRODEPOSIT SURFACE EXAMINATIONS

The composition and type of electrodeposit formed is very important for corrosion resistance, desirable physical properties (conductivity, wear, ductility, friction etc) and susceptibility to hydrogen embrittlement. It was therefore crucial to examine the surface of an electroplated specimen to reveal the type of deposit formed, to deduce the deposition mechanism, and ensure that parameter variations produced the required electrodeposit. Careful specimen rinsing and drying was undertaken prior to examination, to remove any electrolyte that was left behind after electroplating, so as not to confuse the results obtained.

Several surface methods were chosen to examine the electrodeposits that were formed. They were used to try and determine the microstructural phase present, the average composition of the coating, the presence of any zinc-hydroxide and nature of the initial layer that is formed during electroplating. Energy dispersive spectrometry, Inductively coupled spectrometry, Auger and X-ray photoelectron spectroscopy were all used in this work and will be discussed in the following sections.

Scanning Electro Microscopy (SEM) / Energy Dispersive Spectrometry (EDAX)

Scanning electron microscopy (SEM) can be used to produce detailed information about the surface structure and morphology of an electroplated specimen. It can also be used in conjunction with energy dispersive spectrometer (EDAX) to provide elemental data. The apparatus used in this study was a Cambridge 250 MKIII stereoscan with a Link 860 EDAX analyser.

The specimens for analysis were scanned with a high-energy electron beam (typically 5 to 30 KeV) in a raster pattern that causes the ejection of a number of particles including; secondary electrons, backscattered electrons and X-rays. Elemental identification is provided by analysis of the characteristic X-rays that are emitted. The X-ray detector

can be set to detect energies within a narrow range, the collected data can then be used to generate elemental distribution maps or line scans [122].

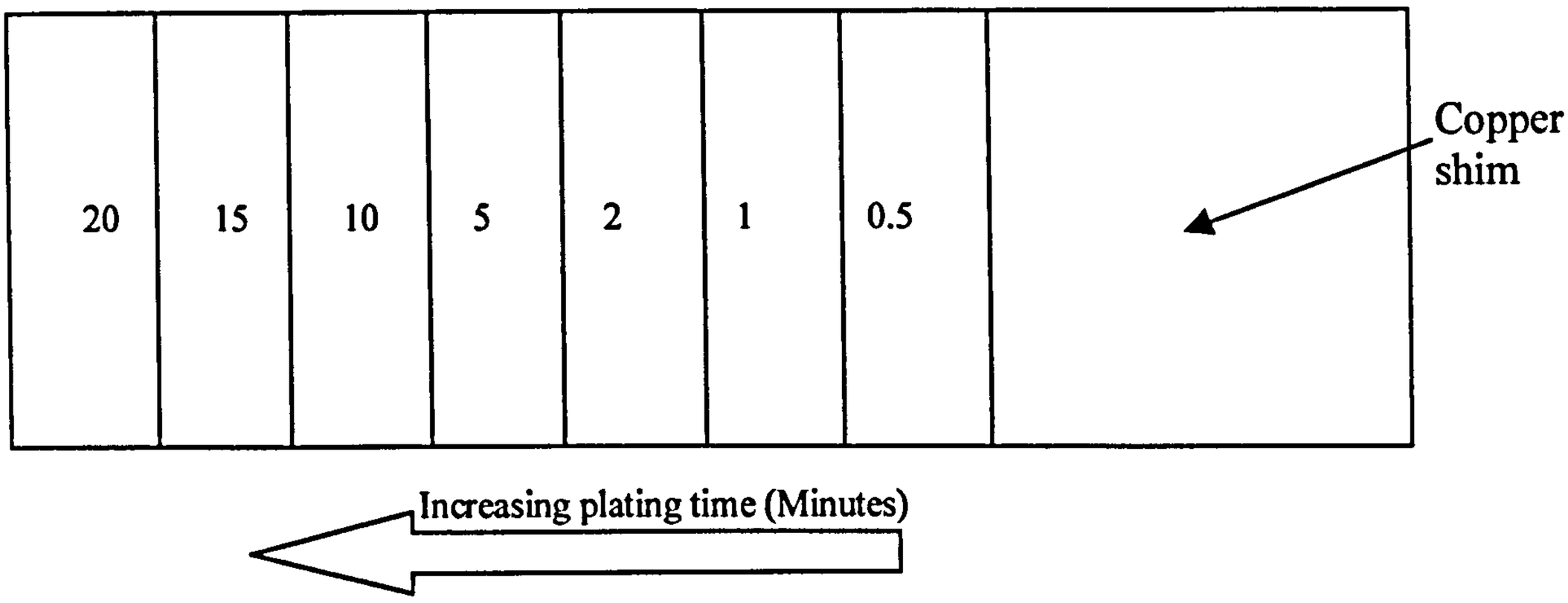
The EDAX technique is described as a near surface technique because it penetrates about 1μm into the surface of the specimen. This can be a disadvantage when examining very thin coatings and will be discussed in more detail in Chapter 4. The main benefits of this technique include; that it is non-destructive, quick, minimal sample preparation is required and an image of the area under investigation can be chosen and actually seen while the data is being gathered. Electroplated metal specimens for examination are already conductive (a requirement for SEM/EDAX studies) and so they are simply attached to the sample platform in the equipment chamber. The chamber is put under vacuum so that the analysis can be carried out. After this has been done the vacuum is released and the specimen is simply removed from the chamber.

The electroplated specimens from the parameter variation investigation were examined under the SEM to determine their morphologies. The EDAX was used to determine their compositions.

The EDAX was also employed to determine the composition of the initial layer formed on the metal substrate. It was assumed that the initial layer formed on the steel substrate was cobalt, formed by the normal deposition mechanism. This initial premise was investigated as follows. Surfaces that had been electroplated for a very short time were analysed. A clean abraded copper shim of approximately 50μm was plated using the standard zinc-cobalt electrolyte. (Copper was used to eliminate any interference problems from the over lapping of iron and cobalt EDAX signals). The strip was then mounted sideways in Bakelite and polished. It was examined on the SEM, and using EDAX over its electroplated thickness to determine any compositional variations in its profile. A clean abraded copper strip was also plated for different lengths of time over its surface area at a constant current density, as shown in FIGURE 28. This was undertaken to investigate whether there was a detectable variation in composition with coating depth.

Elemental mapping of the specimens was also undertaken using EDAX to determine the pattern of elemental distribution through out the electroplated thickness. Although mapping can be more accurately determined using a number of other more complicated techniques, EDAX can be used to give a quick estimate of regions of high concentrations of a particular element within a specimens surface.

FIGURE 28: Schematic of Copper Shim Electroplated over Varying Time



Inductively Coupled Plasma Spectrometry (ICP)

The ICP technique is an excellent tool for determining both electrolyte metal ion content and the alloy composition of electroplated samples. This is because it was designed to combine sensitive solution analysis with the capability for simultaneous multi-element analysis. However, being a wet chemistry technique, its major disadvantage it that it is destructive and the specimens that are tested cannot be reused[123].

The Thermo Jarrel Ash atomscan 25 Spectrometer system used in this study is a nebulising ICP unit. The prepared liquid sample is drawn into the apparatus and then into a flame. The resulting "spray" formed from the incorporation of the atomised sample and the plasma base, in this case argon, is detected at a set wavelength for the element under examination, and displayed as a peak on the screen. The ICP unit then uses the calibrated standard peak areas to work out the concentration of that particular element in each sample. This operation is repeated 4 times, so detection levels are very accurate with correct calibration and using the appropriate standards[124].

The specimens for parameter variation were tested using the ICP but due to the low metal levels seen in the electroplated coatings, it was considered necessary to perform a separate calibration and measurements for each element. Monitoring the electrolyte composition of the baths was also carried out using the ICP but because the metal concentrations were much higher the double element technique was used. The detection limits of the ICP used were: Zinc ions at 213.9nm, 1.7µg/l and Cobalt ions at 228.6nm, 5.1µg/l[124].

Sample preparation for ICP analysis included blank solutions for both the bath mixture and the electroplated specimens. These were an attempt to combat signal interference's caused by impurities in the solutions from either contamination or from any non-metal additions made. They contained everything in the solutions apart from the metals themselves and a small quantity of concentrated nitric acid, which is used to stabilise the solution. The metal concentration was calculated and an appropriate standard solution was made up including nitric acid and entered into the unit. The bath standards were 500ppm while the solution standards were 10ppm. Although these values were entered into the specially produced programme, they were recalibrated for each new set of data to ensure accuracy.

The bath solution was entered straight into the unit through the nebulising tube after filtering to remove any solid particles that would interfere with the measurements. The coated specimens had to be submerged in a 20ml aliquot of 25% hydrochloric acid to dissolve the surface deposit. (The other recommended method using ammonia and ammonium hydroxide was deemed unsuitable, as there was insufficient dissolution in the subsequent dilution with deionised water). The sample was then made up to 100ml with deionised water and 0.5ml of concentrated nitric acid and the solution was shaken until all the particulate material had dissolved. This could then be analysed after it had digested for 30 minutes.

Auger Electron Spectroscopy (AES)

Auger electron spectroscopy (AES) uses a high-energy electron beam (typically 2 to 20 KeV) in a vacuum to eject a core electron from an atom to form an atomic inner shell

vacancy. An outer level electron will then fill the inner level vacancy producing an excited state. The atom can then relax in a number of ways. If it is by emitting another electron to form a doubly ionised species, this electron is known as the Auger electron. Auger transitions are named after the 3-electron orbitals involved, such as KLL and provide characteristic energies for each element. Differentiation of the data allows emphasis of the characteristic electron peaks and sometimes the oxidation state of the element to be calculated. The depth level to which the analysis can be carried out on a sample surface is very shallow, typically 0.5nm to 1nm. However, a map of the surface at that depth can be built up to give an over view of the element distribution over the surface. Auger spectrometers can also be used with an ion-beam that can etch the surface and hence provide depth profiling analysis of a specimen.

Auger is a useful technique but it suffers from several deleterious effects when ion-beam etching is used for depth profiling. The initial surface of a specimen can be artificially enriched in an element by the tunneling effect sometimes encountered with Auger analysis. As the etching beam excites the electrons of an atom, it can push the atom towards the lower layer of the surface under investigation, resulting in a higher level of that element being detected than was actually representative.

The samples to be tested were produced under the standard parameters and conditions for each of the electrolytes that were examined. Depth profiles were obtained for zinc-cobalt, zinc-nickel and zinc-cobalt-iron electroplated specimens that had been electroplated to a thickness of 0.2μm.

X-Ray Photoelectron Spectroscopy (XPS)

X-Ray photoelectron spectroscopy (XPS) is similar to AES but uses an X-ray beam with a wider spot size to obtain surface information. It is more effective at producing oxidation state information on a specimen and can be used for depth profiling by varying the tilt angle at which the specimen is viewed. However, the difficulty in focussing X-ray beams often results in poorer detectability than the Auger technique. Surface etching can cause the removal of a non-planar layer and so depth profiling may not be an accurate representation of the surface. Ionised atoms may re-attach to the

sample surface and the argon beam used can cause tunneling of the detected atoms into the substrate rather than removing them so they are detected at a lower level from that which they originally came.

Each of the electrolytes under investigation, were used produce several specimens under standard conditions for different lengths of time. This gave layers of differing thickness, which were examined by XPS to determine if any difference in composition could be detected. TABLE 9 illustrates the thickness of the layers that were examined.

TABLE 9: Thickess of Electroplated Layers Investigated

Electrolyte	Thickness (μm)			
Zinc-cobalt	0.2	1	5	15
Zinc-nickel	0.2	1	5	15
Zinc-cobalt-iron	0.2	1	5	15

MECHANICAL TESTING

There are many mechanical test methods that can be used for assessing the effect of hydrogen embrittlement including; constant load testing, notched c-ring testing, double cantilever beam testing and slow strain rate tensile testing. Slow strain rate testing has been used extensively to quantify the degree of hydrogen embrittlement produced in low alloy high strength steels, (such as AISI 4340, used in military and commercial aircraft), after it has undergone electroplating or chemical maintenance[99]. A slow strain rate test, unlike conventional testing, allows time for the hydrogen to diffuse and so will detect the effect of embrittling hydrogen present in the sample structure, as discussed in Chapter 1. The strain rate for these tests was set to 1.1×10^{-6} ms^{-1} and periodically checked to ensure a constant strain rate was maintained for all the specimens.

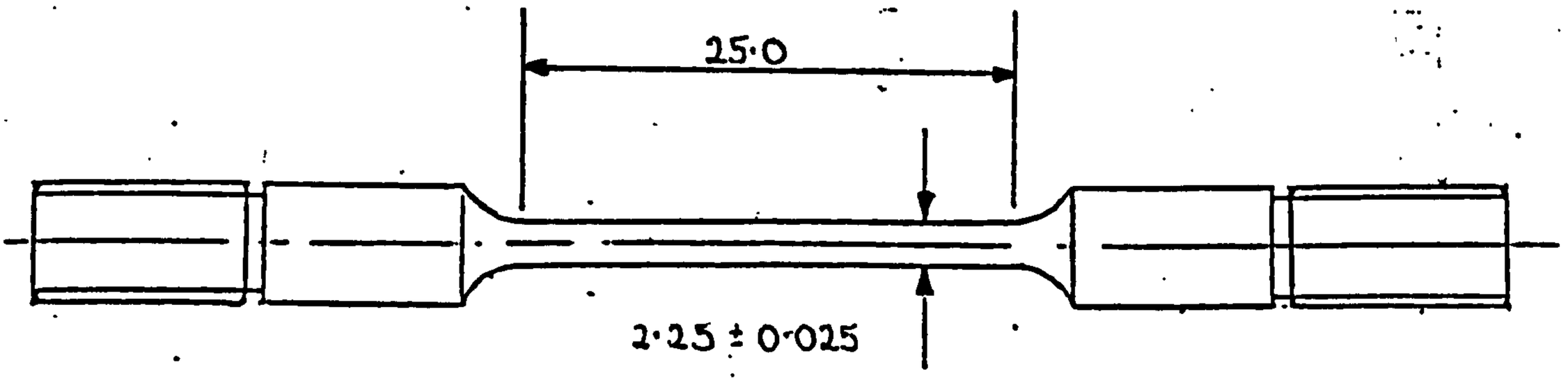
Specimen Design

The tensile specimens were prepared from high strength AISI 4340 steel bar by CNC machining. Due to de-embrittlement baking treatment being required after electroplating, the BAe baking recommendations and defence standards were

consulted [6]. Careful consideration of the effects of the temperatures involved was necessary and the specimen baking in this project was carried out at 200°C for 24 hours unless otherwise stated. This temperature allowed hydrogen to be removed by diffusion but did not reduce material strength, obtained by previous tempering, by altering the microstructure. Once diffusion of hydrogen begins, hydrogen can be lost to the atmosphere or absorbed by traps.

The specimens were prepared to the specification shown in FIGURE 29, to give a tensile load bearing circular cross sectional area of 3.98mm^2. Previous work carried out at Cranfield used the same specimen cross sectional area but with a rectangular specimen cross sectional profile [18].

FIGURE 29: Tensile Specimen Specifications



Heat Treatment

Once the specimens had been produced, they were sent to Holt Brothers Ltd., Halifax for heat treatment. To ensure uniform heating, each specimen was individually suspended on wires, immersed in a neutral salt bath, at 835-840°C and soaked for 15 minutes, before being quenched in oil at room temperature. Tempering was carried out at 250°C for 2 hours, so that during subsequent baking at 200°C there would be no further microstructural or tensile property alterations. The heating to high temperatures followed by an oil quench hardens the specimens to the required values for this work. Tempering allows a reduction in internal stresses and further precipitation hardening but it can reduce strength if the time is not monitored carefully, as discussed in Chapter 1.

Quality control of the tensile specimens was carried out in a number of ways. Firstly, visual inspection before cleaning determined any obvious imperfections in the machining of the tensile test specimen. Further inspection of the surface was undertaken once cleaning had occurred and measurement of the gauge length was performed under the profile projector and a micrometer. If significant 'faults', such as under cutting, machining marks or an uneven diameter, were found, the specimen was discarded. Finally, a Vickers Pyramid Hardness measurement was also taken on a clean, flat section of all the tensile test specimens and the strength values were compared. Holt Brothers achieved excellent reproducibility of the hardness for each of the heat treatment batches of test specimens. The mean UTS of the specimens was 1843MPa (+/- 39MPa).

Tensile Specimen Preparation

All the tensile specimens were prepared for testing by polishing the gauge length with 1200-grit carborundum paper to remove the oil on the surface, due to heat treatment, and then degreasing in an ultra sonic bath for 15 minutes containing propan-2-ol. Care was taken not to alter the diameter of the specimens by removing any of the metal. After cleaning, each specimen was dried and the diameter carefully measured with a micrometer and on a Mitutoyo Profile Projector Type PJ-300. A series of measurements were taken over the length of the specimen gauge, the average calculated and used later for determination of the embrittlement index. The gauge dimensions of the specimen affect the embrittlement results observed as a larger diameter would need to absorb more hydrogen, over a longer period, before a critical hydrogen concentration would accumulate in a specimen to cause failure.

The specimens were then electroplated, and if required baked to the specification of each experiment. Control tests were also performed on unplated specimens to determine the response of specimens in the untreated baked and unbaked conditions and investigate if any microstructural change had occurred. Each set of conditions was repeated to produce a set of results that could be examined statistically.

Alloy Plating

Specimens that were electroplated at Cranfield were prepared as before but were masked at the threaded ends with lacomit protective varnish to provide a constant area to be plated. The specimens were weighed before and after plating in each electrolyte to allow calculation of the coating thickness and cathode efficiency. Before the second weighing, any remaining electrolyte was removed by rinsing in deionised water and then propan-2-ol to assist with drying. Once the specimen was dry, if no further treatment was required, it could be tested.

Specimens were electroplated with zinc, zinc-nickel, and zinc-cobalt using the same experimental set-up used for electroplating the shim used for parameter variation investigations, as shown in FIGURE 26. The zinc-cobalt specimens were also tested using electrolyte at different pH values, to see if there would be an effect on the time to failure for the specimens. The ternary deposit based on the Younan electrolyte, with cobalt substituted for nickel, was also investigated for its embrittlement performance[103]. (The ternary electrolyte was later altered to give a deposit with a slightly lower cobalt percentage in the coating and the effect investigated).

Layered Electroplated Coatings

A compositionally modulated multi-layered (CMM) approach was also investigated to see what effect a very thin layer of cobalt or nickel on the specimen surface followed by zinc or zinc-alloy coating would have on failure time. The dual bath technique (DBT) was chosen for experimental accuracy and simplicity [15, 125]. The specimen was prepared as usual, then plated in the first electrolyte for 30 seconds under standard conditions, then washed in water to remove any excess, rinsed in propan-2-ol, dried and weighed. It was then plated using the second electrolyte again under standard conditions, washed, dried and re-weighed. The thickness of each layer and the cathode efficiency at each stage were determined by weight gain calculations. These experiments effectively replicated the anomalous co-deposition mechanism, by providing an interlayer of known thickness at the surface of the specimen. Once the specimens had been electroplated, they could be immediately attached to the slow strain rate apparatus for testing, if no baking treatment was to be undertaken.

Cadmium Plating

Cadmium plating was carried out by Stotfold Plating Limited, Stotfold, Hertfordshire. The specimens were prepared, as described in the tensile preparation section, labelled and taken to the plating shop. The specimens were plated to a thickness of 8μm. The specimens had no further passivation or surface treatment once they were coated with cadmium,[126] and were immediately placed in liquid nitrogen until testing commenced. This low temperature effectively immobilised the untrapped hydrogen in the specimens until they were heated to room temperature before testing[127].

Baking Treatment

All the basic single layer electroplated coatings that were tested also had the effect of a post-electroplating baking treatment investigated. The specimens were prepared (as before), electroplated, washed, dried and then immediately baked in a vacuum oven for 24 hours at 200°C[6]. Cadmium electroplated specimens were immediately placed in liquid nitrogen at Stotfold, and baking was carried out at Cranfield after they had been allowed to reach room temperature.

The effect of a longer 48 hours baking time was investigated for the standard zinc-cobalt electrolyte. As was a delay of 12 or 24 hours, after electroplating the specimens and before baking was undertaken. This was in response to concerns over the effect delays before baking treatment has on the hydrogen embrittlement seen for electroplated specimens.

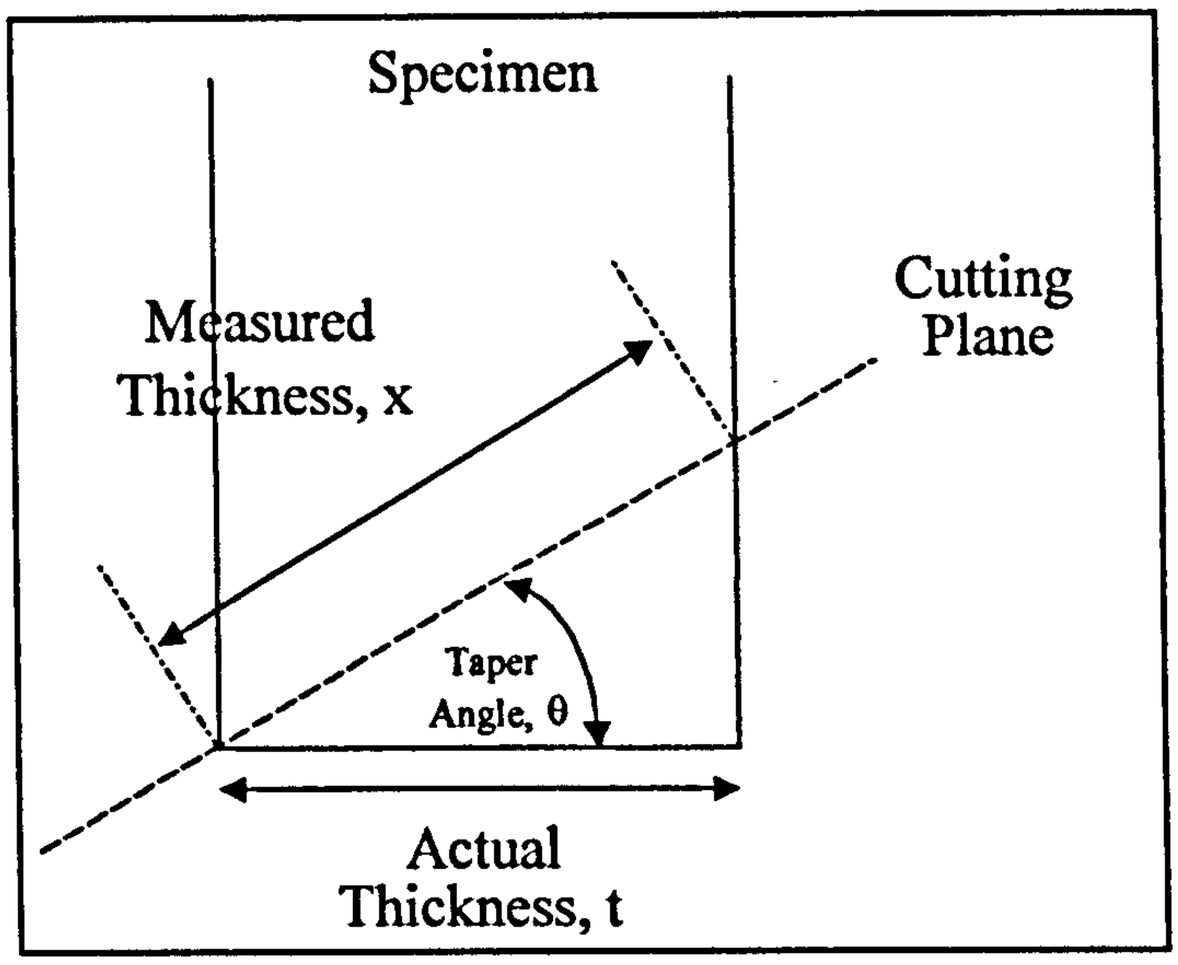
The DBT specimens that had been electroplated with an interlayer of cobalt or nickel and then electroplated with zinc-cobalt electrolyte were also baked under standard conditions to investigate the effect.

Coating Measurement and Polishing Technique

In addition to weight gain calculations, the thickness of the coatings were measured on the SEM after careful mounting, sectioning and polishing of the electroplated tensile specimens. Problems were encountered with Bakelite mounted electroplated specimens, because the electrodeposited coatings were removed by subsequent polishing. Resin

mounted specimens, which were placed in a vacuum oven for 24 hours allowed some of the resin to penetrate into the uneven surface of the electrodeposited coating. The mounted specimens were polished at an angle, which improved the electroplated layer's resistance to polishing removal, allowing accurate measurements to be made. The polishing arrangement is shown in FIGURE 30.

FIGURE 30: Cross Section of Polishing Arrangement



The mounted specimens were polished to a mirror finish that allowed the interface to be examined both by optical microscopy and SEM. The specimens were initially polished on 220-grit and 1200-grit carborundum papers. This was followed by 6μm diamond paste (revealing the microstructure) and finally 1μm diamond paste (revealing the interface and electroplated layers that were present).

The coating thickness was measured under the optical microscope, using the eyepiece graticule, and on the SEM from the on screen image and from photographs that were taken. The specimens were mounted, polished and prepared prior to measurement as previously detailed and the resin mounted specimens were made conductive to prevent charge build up during SEM examination. This was achieved by application of a thin coating (approximately 50nm) of conducting gold-palladium to the examination surface. A thin line of silver-dag was also painted on the specimen from the surface to be examined to the base of the sample in order to complete the conductive path. SEM techniques are very sensitive and can be used to measure coatings as thin as 50nm.

Slow Strain Rate Test Procedure

After the test specimen had been prepared it was mounted into the Cortest Incorporated, C.E.R.T. system sensotec D/3971-03 slow strain rate test rig and a constant pre-load of 300N (+/- 20N) was set. This was used to align the specimens, remove any slack in the equipment and standardise the testing regime by providing a consistent starting point for all the specimens. Load versus time measurements were recorded on a chart throughout the testing and these values were converted into stress-strain diagrams for each type of coating tested. The initial extension, needed for the strain calculations, was calculated by extrapolation of the stress-strain diagram.

When the slow strain rate specimens had broken, the ends of the specimens were re-measured to determine if a reduction in area had occurred. The fractured ends were cut to a convenient length and mounted on stubs and either polished to determine the coating thickness as described in the last section, or their fracture surfaces were examined on the SEM. These observations along with the time to failure for the specimen were used to determine the fracture mode of the specimens, i.e. ductile (non-embrittled) or brittle (embrittled).

Weibull statistical analysis allows for random factors within a given distribution, such as variations in size, shape and position of inclusions and defects between different tensile specimens[i]. The simplified Weibull model is explained in EQUATIONS 18a –18c.

EQUATION 18a: Probability of Survival

$$P_s = (i/n+1)$$

Where: P_s = probability of survival*

i = ordered specimen number

n = specimen population

EQUATION 18a demonstrates how the probability of survival for an ordered specimen from a total set of n specimens can be calculated. Once this has been established, the Weibull probability can be applied using EQUATION 18b.

EQUATION 18b: Weibull Probability

$$F_w = \exp - (t/\zeta)^{\beta}$$

Where: F_w = Weibull probability of failure

t = time

β = shape parameter

ζ = location parameter

A simplified version of EQUATION 18b can be used when the shape parameter (β) is equal to 1 and is shown by EQUATION 18c.

EQUATION 18c: Simplified Weibull Probability

$$P_s = 1 - P_f = 1 - \{\exp - (t/\zeta)^{\beta}\}$$

Where: P_s = probability of survival

P_f = probability of failure

t, ζ, β = as defined in EQUATION 18b

The shape parameter β is assumed to be equal to 1 unless otherwise stated for all the experimental data. The simplified equation, (EQUATION 18c), was used to produce a Ln (P_s) versus t plot, which is related to the time taken for initiation of a crack large enough to cause failure. In this work the Weibull plots that were calculated are given as time to failure (TTF) versus Ln(P_s) and are shown in Chapter 3.

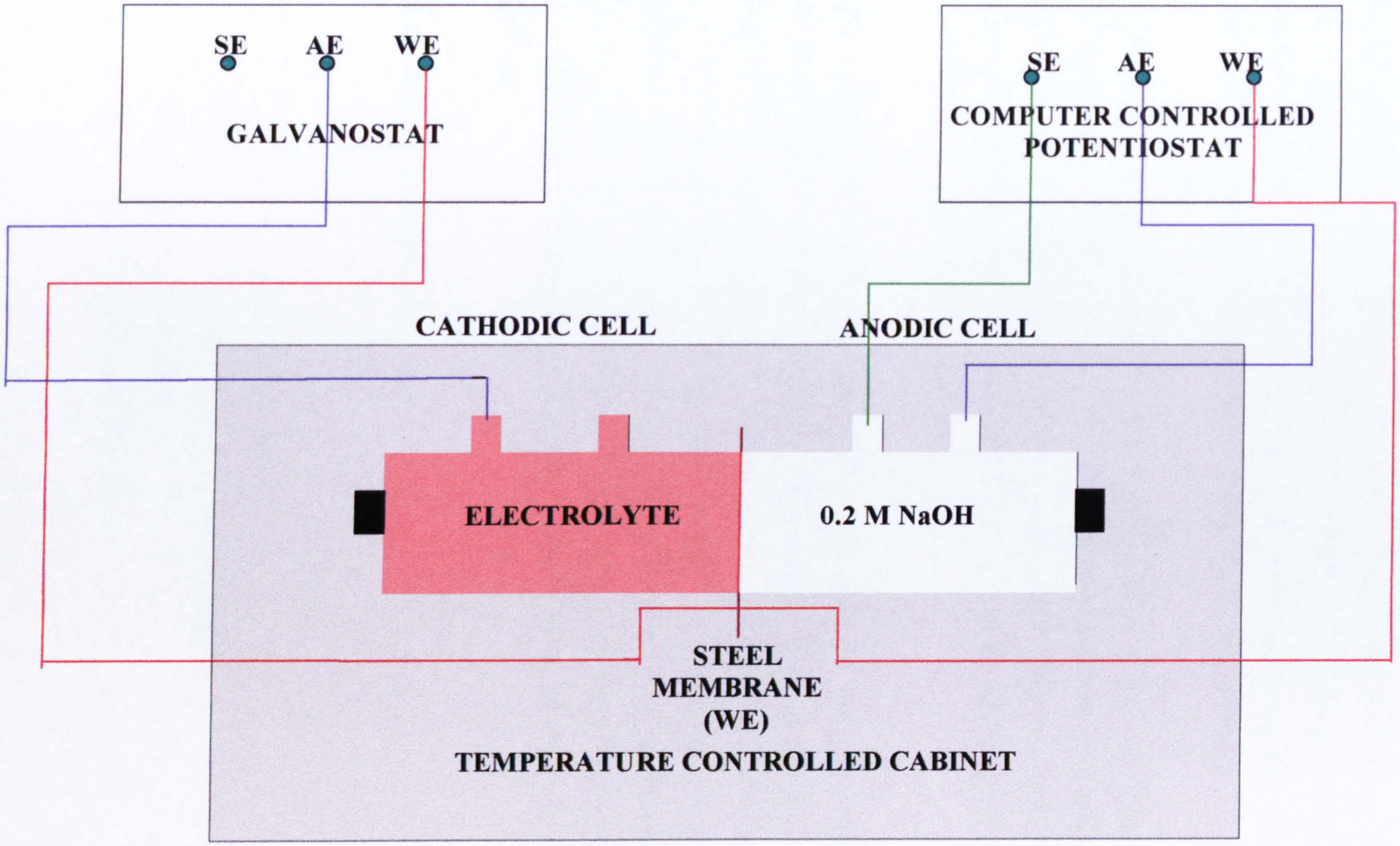
PERMEATION STUDIES

The permeation studies were concerned with determining the extent of hydrogen uptake resulting from the zinc-cobalt electroplating process. Permeation experiments were conducted to rank the amount of hydrogen permeating a steel shim electrode as a result of the deposition of 8μm of a range of different zinc-alloys onto that shim, so that comparisons could be made with zinc-cobalt. A Sycopel Scientific AEW-2 potentiostat, laptop and Sycopel electrochemical software were used for all the measurements.

All the experiments were carried out in a rectangular Perspex temperature-controlled cabinet set at the required plating temperature of the electrolyte under investigation. The cabinet measured 325mm x 450mm x 750mm and was covered in insulating foil to reduce electrical noise and signal interference. The cabinet was fitted with a thermostatically controlled heater blower fan that was capable of maintaining a constant environmental temperature of up to 60°C (+/-1°C).

The Devanathan and Stachursky double–cell technique discussed in Chapter 1 was used for the investigations, and the set-up is shown in FIGURE 31 [39]. A thin shim electrode (50μm thick steel) was the sole material isolating 2 different electrochemical cells. One surface of the membrane acted as the cathode in one of the cells, and the other surface acted as the anode in the opposite cell. The anodic (exit) cell was used to deplete hydrogen from the surface of a clean abraded shim, which was maintained at + 150mV (NHE) in order to allow oxidation of the hydrogen as it reached its surface. The electrolyte in this cell was 0.2M sodium hydroxide solution, which removed the hydrogen ions as they were formed. This maintained the anodic surface at a zero hydrogen ion concentration, giving a fixed point for diffusion rate calculations.

FIGURE 31: Experimental Set Up for the Permeation Apparatus



Once a satisfactory background level had been reached, the cathodic side of the clean shim was galvanostatically electroplated using a standard 2-electrode system and a mini-potentiostat. This produced a current that was measured on the exit section of the apparatus after a time delay referred to as the break through time. After electroplating the shim surface to a thickness of 8μm, (the requirements to achieve this had been established from earlier parameter investigations and weight gain data), the electrolyte was removed from the cell to prevent spurious results from being obtained.

The experimental procedure described was repeated using zinc, zinc-nickel, zinc-cobalt and zinc-cobalt-iron electrolytes. Each of the different electroplated coatings were deposited under their standard bath parameters as quoted in TABLE 7 with both the electrolytes and cabinet at the required temperature. The zinc-cobalt coatings were also produced at different electrolyte pH values.

The effect temperature had on hydrogen uptake and permeation through a steel shim was also investigated, due to the different standard temperatures needed for various electrodeposited coatings examined. Temperature alters the diffusion coefficient for a given system, as shown by Bockris in extensive studies [87]. As a consequence, the rate and magnitude of this change is seen in the resulting transients. The Arrhenius equation, EQUATION 19, shows that a change in experimental temperature should have a log scale effect on the amount of hydrogen that is permeated through a specimen, in a given period of time.

EQUATION 19: Arrhenius Equation

$$K = A e^{-Ea/RT}$$

Where A = Avagadro's number

E_a = hydrogen diffusion activation energy

R = gas constant

T = temperature (Kelvin)

Parameter variation investigation work had shown that changes in the experimental temperature of the electrolyte had a direct effect on the composition of the deposited coating. This may have been to convection of the bath ions and other temperature effects, and these would cause interactions that may affect the permeation results observed. A simple charging experiment was therefore chosen to investigate temperature effects. This was so that the electrolytes being investigated were not heated to a temperature other than their standard value.

Charging experiments were carried out on an unplated steel shim, in a 0.2 M sodium hydroxide solution using the same double-cell arrangement [39, 87]. The cabinet and sodium hydroxide solution were allowed to equilibrate to the temperature chosen for the experiment (25°C, 43°C and 50°C). The steel shim was depleted, as for the electroplating experiments, but the electrolyte in the entry side was also sodium hydroxide. This solution was galvanostatically charged at a current density of 10mA/cm^2, for 15 minutes to replicate the conditions for standard zinc-cobalt electroplating. The resulting permeation transient was recorded and compared to experiments performed at the other temperatures investigated.

The difference in the permeation transient observed for each temperature was used to establish a set of calibration data, which could be used to directly relate the amount of hydrogen permeated under different temperatures. These calibration results could then be used to relate the experimental hydrogen uptake to an equivalent rate at a standardised temperature. Therefore the electrolytes which were used at temperatures other than 50°C, could be compared without having to change the experimental temperatures. This allowed direct comparison of the electrolytes used at their optimum electroplating parameters, without having to alter the experimental conditions.

A similar charging technique was also employed to study the effect of a thin layer of pure electrodeposited cobalt on the surface of a clean steel shim. The shim was prepared and the area to be electroplated was left bare, while the rest of the shim was masked front and back with lacomit protective varnish, then dried and weighed. The electrode area was plated with 8μm of cobalt, rinsed in deionised water and propan-2-ol, dried

and reweighed. The protective varnish was then removed and the shim was placed in the double-cell set up and charged at different current densities, (5, 30 and 70mA/cm^2). A fresh specimen was used for each new current density to be investigated.

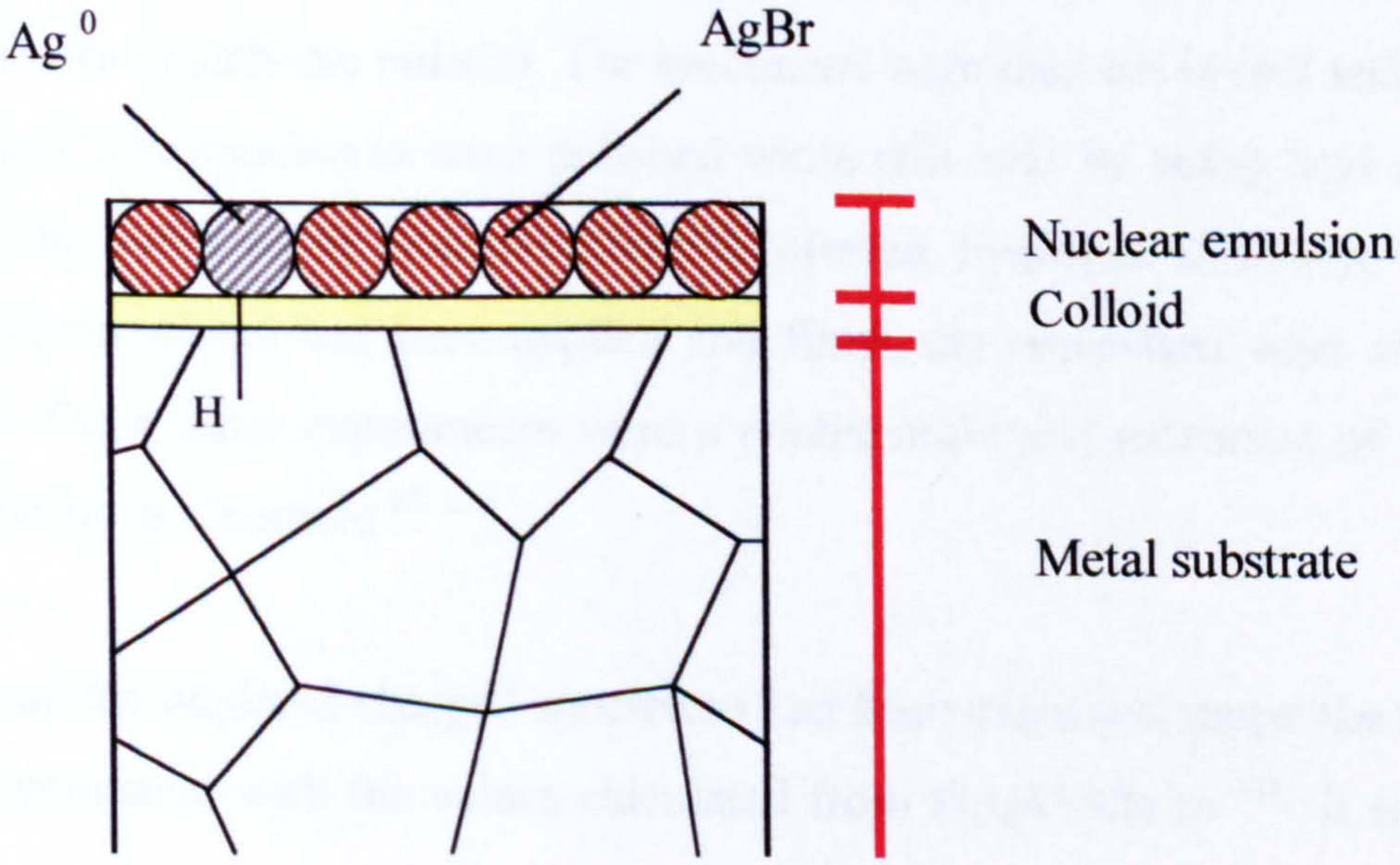
This set of experiments demonstrated the effect of current density and provided calibration data in the same way as the temperature experiments had done. The calibration results allowed direct comparison of the considered coating systems to be made using data gathered whilst coating under optimum conditions. They also enabled determination of the effective diffusion coefficient for cobalt, which was critical in establishing the effect that cobalt contained within an electroplated coating had on the observed hydrogen embrittlement. It also gave an indication of the thickness of the cobalt layer that was needed to prevent ingress of hydrogen into the metal substrate.

HYDROGEN DETECTION

HYDROGEN MICROPRINT TECHIQUE (HMT)

Once a specimen had been mounted in Bakelite, and polished to 1μm, a mono-atomic layer of Ilford Scientific L4 silver bromide emulsion was placed over the metal surface, using a metallic loop. Silver ions in the emulsion could then be reduced to form silver particles by diffusing hydrogen close to the specimen surface, as discussed in Chapter1 and EQUATION 7. FIGURE 32 shows the surface of a specimen after the silver reduction reaction has occurred during developing [48, 86].

FIGURE 32: The Hydrogen Mapping Technique



After the developing stage, any of the silver bromide ions that were reduced to silver by the diffusing hydrogen were fixed and any of the remaining unreacted emulsion was removed with a fixer solution. This solution contained 5% sodium nitrite to prevent corrosion of the metal surface during testing. After subsequent rinsing and drying cycles, the specimens were viewed under the SEM, the metallic silver particles if present, were clearly visible. The silver that remained correlated to the position of the detectable hydrogen that had diffused from within the metal substrate.

The hydrogen microprint technique (HMT), was used initially to determine if etching a polished specimen with 2% Nital alone could introduce a detectable quantity of hydrogen into the steel.

Experiments were subsequently carried out on zinc-cobalt, zinc-nickel and zinc-cobalt-iron electroplated specimens, mounted and polished to 1μm, to determine if any remaining trapped hydrogen was detectable in the coating. The silver reduction reaction was established as a real effect, by repeating the experiments using baked specimens mounted in resin, to see if there was a chemical reaction with the coating. DBT specimens were also examined in this way.

The effect of variation in charging time for unplated specimens was also examined to see if there was a discernible difference in the extent of hydrogen penetration detected. Unplated specimens were charged at a constant current density of 120mA/cm^2 for various lengths of time, in a solution of 10% sulphuric acid doped with a small quantity of thiourea (a cathodic poison). The specimens were then cut in half and placed in liquid nitrogen. The specimens were polished while still cold by being held in a metal jig to keep the temperature to a minimum to prevent hydrogen diffusion. Once the silver bromide emulsion had been applied and fixed, the specimens were viewed under the SEM. These latter experiments were a continuation and extension of work previously carried out at Cranfield [85, 129].

Once all the unplated charged specimens had been examined under the SEM, the results were compared with the values calculated from EQUATION 20 [130]. It was assumed that

initially the specimen had a uniform concentration of hydrogen on its outer surface and effectively no hydrogen within the steel. An average value was taken for the edge of the diffusion band, as viewed under the SEM and the outside of the specimen. The limiting factors in this method are detection limits set by the experimental preparation time, grain size of the emulsion (150nm) and also the diffusion coefficient used in the theoretical calculations.

EQUATION 20: Diffusion of Hydrogen in a Metal Specimen

$$\frac{C - C_0}{C_1 - C_0} = 1 - \left(\frac{4}{\pi}\right)\sum_{n=0}^{\infty}\frac{(-1)^n}{(2n+1)^2}\exp\left[\frac{-(2n+1)^2\,\pi^2\,Dt}{4L_T^2}\right]\cos\left[\frac{(2n+1)\pi X}{2L_T}\right]$$

Where:	C	=	Surface hydrogen concentration at time (t)
	C_1	=	Constant surface hydrogen concentration
	C_0	=	Steady state surface hydrogen concentration
	X	=	Distance penetrated into specimen (cm)
	L_T	=	Total length of specimen (cm)
	n	=	Positive integer (between 1 and ∞)
	D	=	Diffusion Coefficient (cm^2/seconds)
	t	=	Time (seconds)

CORROSION MEASUREMENTS

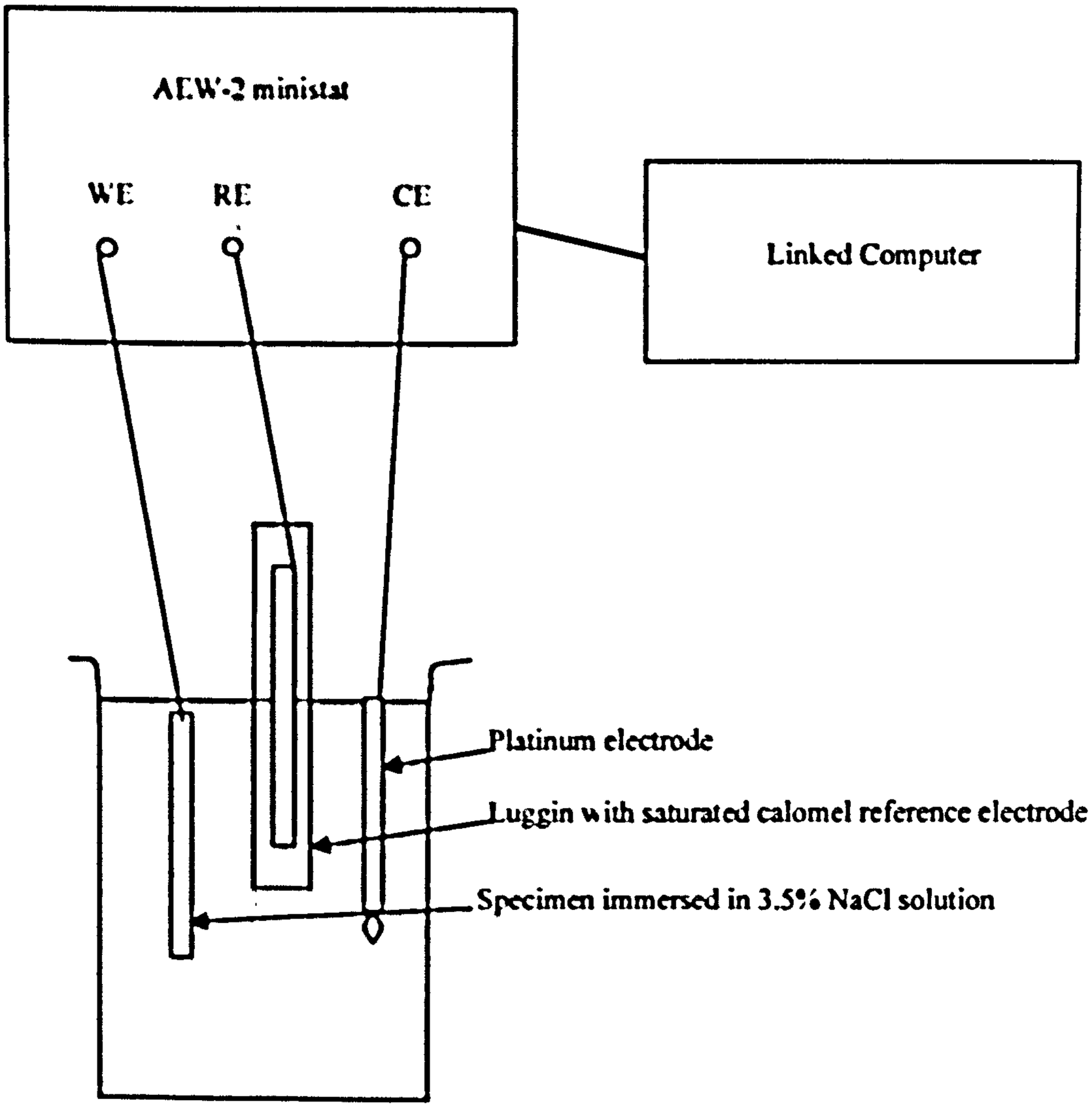
The corrosion protection provided by metal coatings on steel can be assessed by a variety of accelerated corrosion tests. Salt spray, weight loss specimens and electrochemical techniques can provide useful information, which can be used to estimate corrosion rates. This work calculated corrosion rates from linear polarisation resistance scans (LPR) and weight loss measurements. Potentiodynamic polarisation scans were also performed to enable the determination of the anodic and cathodic Tafel constants. These were used in the determination of the corrosion rates from the polarisation resistance data obtained. Electrochemical measurements were performed using an AEW-2 ministat and a laptop computer with Sycopel Scientific Electrochemistry software.

Potentiodynamic Polarisation Scans

Potentiodynamic polarisation scans were performed on the electroplated alloy specimens and these results were compared to several standards including bare steel specimens, cadmium electroplated specimens (industry standard, produced by Stotfold Plating Ltd.) and zinc electroplated specimens. The thickness of the coating chosen allowed measurement of the corrosion resistance in the absence of any substrate material interaction. The specimens were prepared from abraded, clean, dry steel measuring 90mm x 25mm. The specimens were masked with lacomit protective varnish, to reveal an area of 40mm x 25mm only on one side, which was subsequently electroplated to a thickness of 40μm, as illustrated in FIGURE 27. The upper part of the specimen that was unplated, was attached via a clip lead to the electrochemical measurement equipment, the clip lead also used to suspend the coupon into the 3.5% sodium chloride test solution. The initial composition and weight of all the specimens were recorded before testing was undertaken.

Potentiondynamic sweeps were carried out for the test specimens in 3.5% sodium chloride solution at 25°C using a 3-electrode configuration; the test specimen which was the working electrode (WE), a platinum counter electrode (CE) and an external calomel reference electrode (RE). The test electrodes were immersed in the sodium chloride solution. Whilst a Luggin capillary was positioned adjacent to the surface of the test specimen to provide solution contact with an external saturated calomel RE. At the start of each polarisation scan, the WE was allowed to stabilise for 30 minutes in the test solution. At the end of this stabilisation period the working electrode was polarised at a rate of 25mV/min. The same experimental set up was used for the full polarisation scans and the LPR measurements and is shown in FIGURE 33.

FIGURE 33: Polarisation and LPR Measurement Experimental Set Up



Linear Polarisation Resistance (LPR)

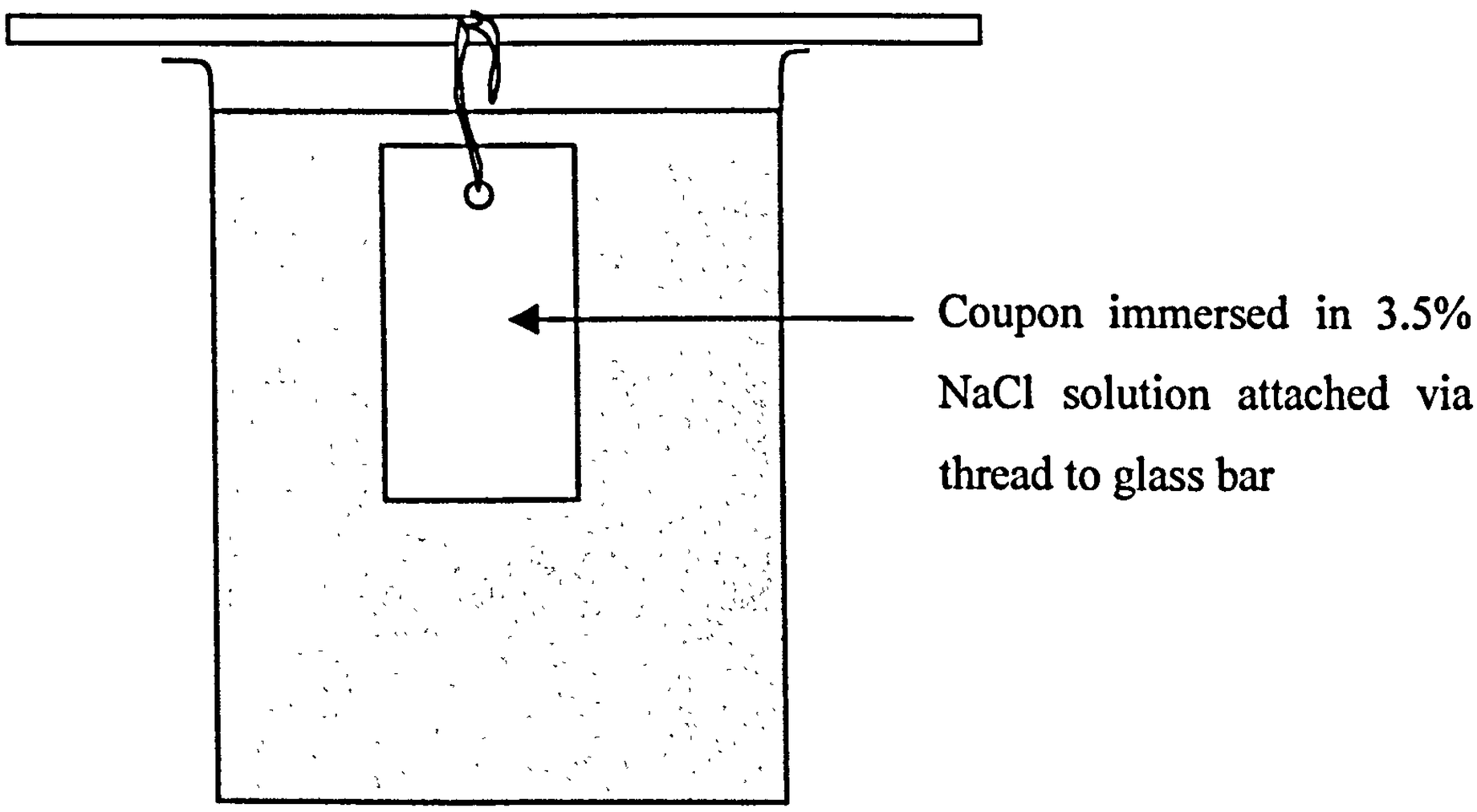
Specimens for LPR measurements were prepared in the same way as the specimens for the potentiodynamic polarisation scans, from rectangular steel coupons measuring 90mm x 25mm. They were then weighed and electroplated with the required coating to a thickness of 40μm. The specimens were reweighed and compositionally analysed by EDAX before the start of the experiment. A clip lead was attached to the top of the unplated portion of the specimen and adjusted so that only the electroplated section of the coupon was immersed in the solution. The specimens were left in 3.5% sodium chloride solution for 30 minutes to stabilise and their open-circuit potential was monitored before the polarization measurements were begun. The specimens were then polarized 10mV below E_{corr} and then polarized 20mV in the other direction (i.e.

returned to their rest potential and a further 10mV above it), and finally back to the rest potential again, using the same experimental set up as in FIGURE 33. The scan rate used was 10mV/minute and the current produced on polarization was measured and recorded every second. The experiments were repeated after 3 and 6 months immersion.

Weight Loss

The specimens to be used for weight loss were prepared in sets of 4, so that an average could be taken for each set of conditions. The specimens were prepared from 15mm x 20mm steel coupons that had been electroplated on both sides to a thickness of 40μm. A hole was drilled 4mm from the edge of one of the short sides, for easy suspension from a nylon thread in 3.5% sodium chloride solution at 25°C, as shown in FIGURE 34.

FIGURE 34: Weight Loss Experimental Set Up



The types of deposit that were investigated were as follows; unplated steel (control), cadmium electroplated steel (industry standard, produced by Stotfold Plating, as mentioned previously), zinc electroplated steel, zinc-cobalt electroplated steel, zinc-nickel electroplated steel and zinc-cobalt-iron electroplated steel. These coatings were tested in the baked and unbaked conditions and their initial composition (by EDAX) and weight was recorded, before the specimens were immersed in 3.5% sodium chloride solution for periods of 3 and 6 months.

Inspection, cleaning, and weighing took place in accordance with Defence Standard 03/2 for pure zinc and cadmium coated specimens[131] by immersion in hot chromic acid (100g/l) or by immersion in 30% w/v glycine solution for all the other alloy specimens[106]. After the corrosion products had been removed, the specimens were rinsed in deionised water, followed by propan-2-ol to assist with drying. The specimens were left in a desiccator overnight before reweighing, to ensure they were at room temperature and were completely dry. The weight loss was calculated by subtracting the weight of the coupon after cleaning from the weight determined prior to testing.

RESULTS

MATERIAL TESTING

FIGURES 35-37 show the microstructure of the AISI 4340 steel in the as received state and after undergoing the various treatments used in this work. The as received material showed a normalised steel microstructure with pearlite in a ferrite matrix. Quenching and tempering the material produced a tempered martensitic structure. Further baking did not significantly alter the microstructure of the steel. Therefore, any changes in material behaviour seen for baked specimens is due to a real effect from the electroplating process and not the baking treatment undergone. Vickers hardness measurements taken before and after baking which are given in TABLE 10 confirm that the steel strength was not significantly affected by the baking treatments undergone.

FIGURE 35: As Received

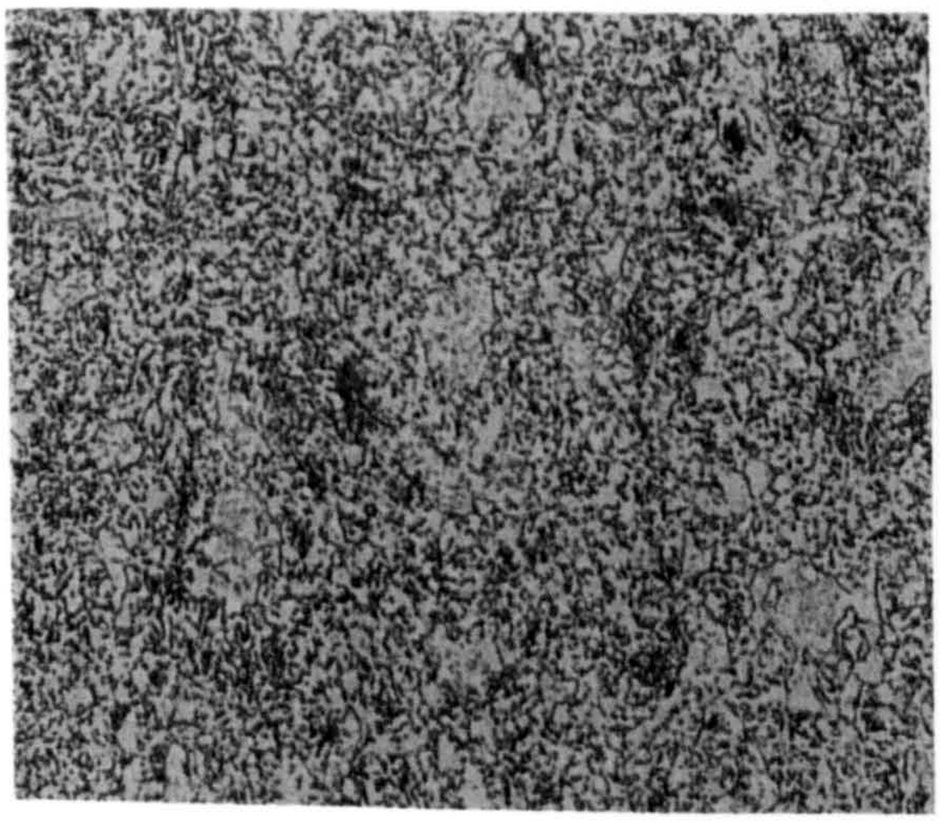


FIGURE 36: Quenched and Tempered (QT)

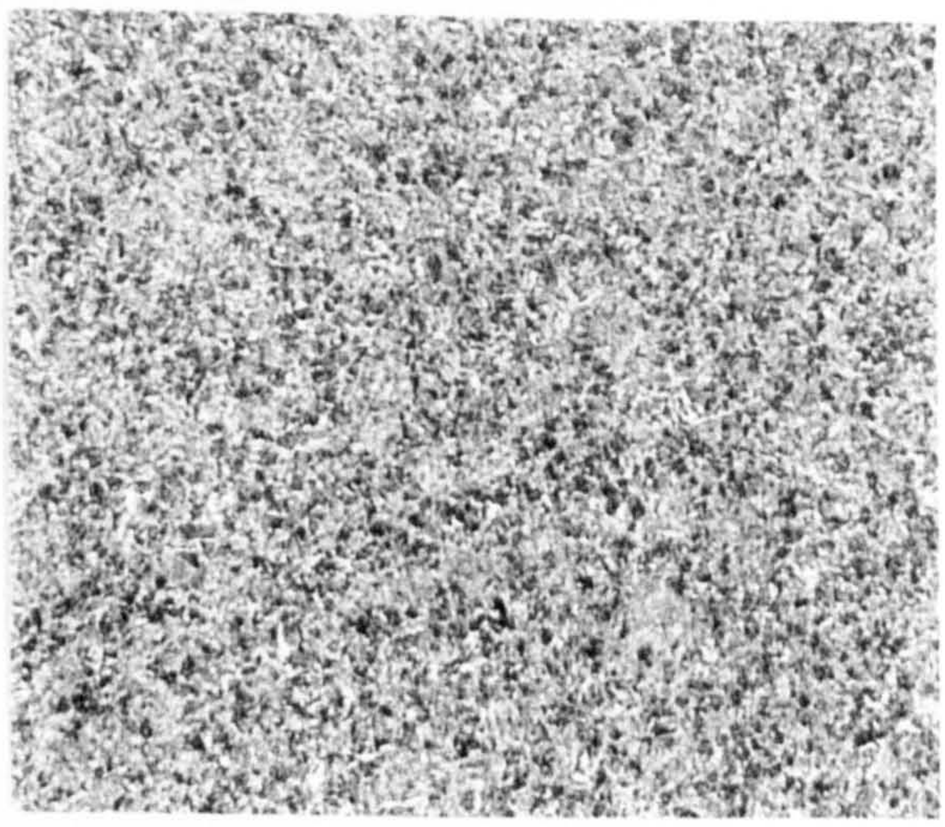


FIGURE 37: Baked and (QT)

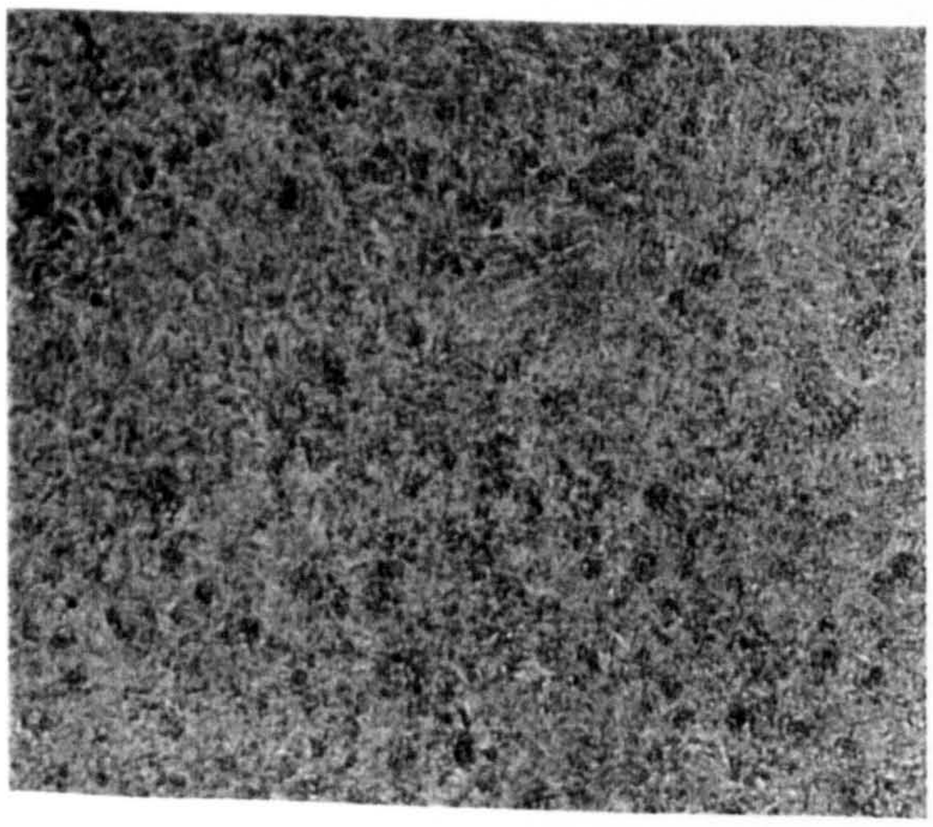


TABLE 10: Vickers Hardness Values for Baked and Unbaked AISI 4340 Steel

Material	Mean HV_{10} Value	Strength (MPa)	Standard Deviation
UNBAKED	537	1848	39
BAKED	534	1838	39

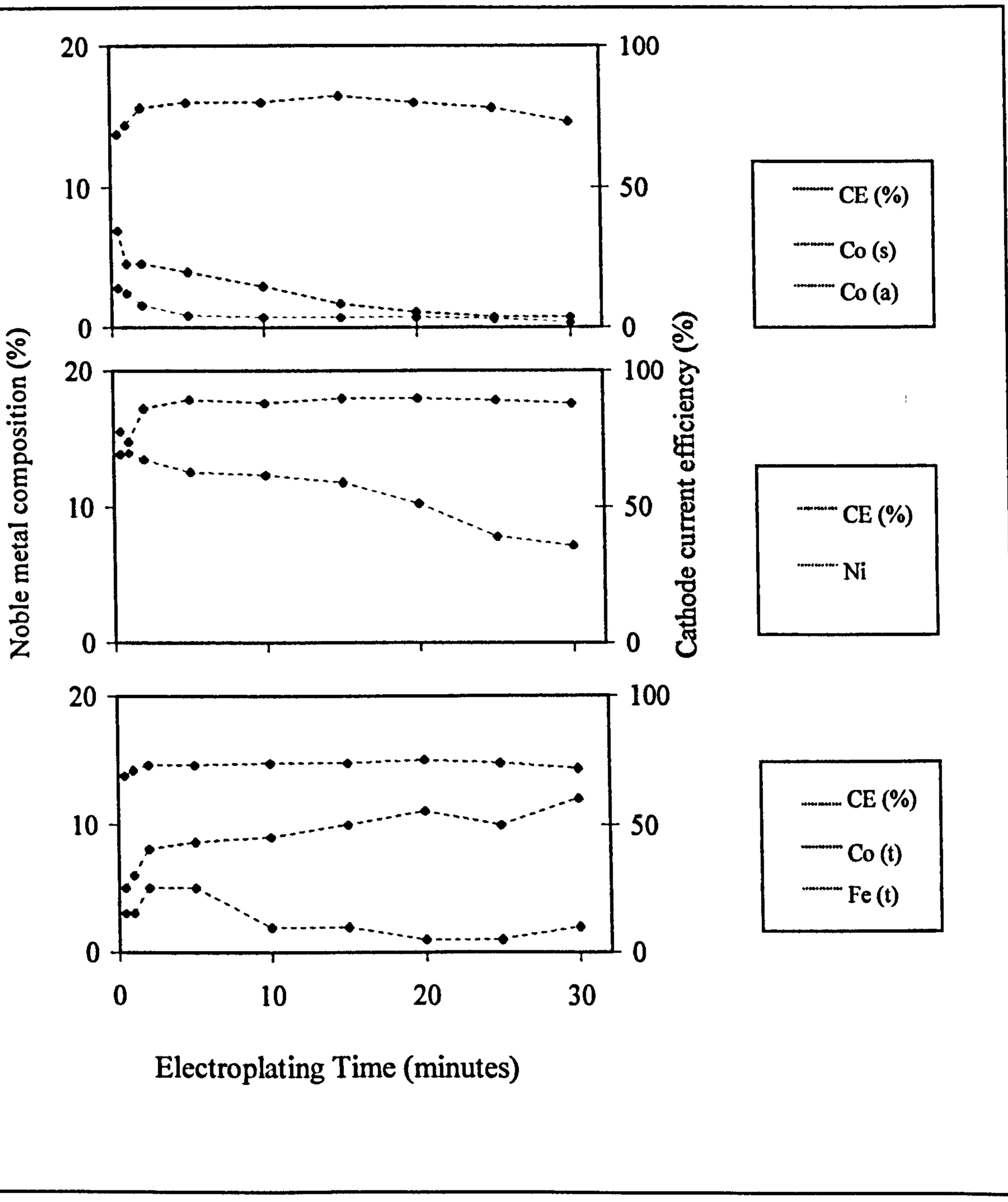
PARAMETER VARIATION

The parameter variation investigations were used to determine the effect of changing the electroplating time, temperature, pH and current density on the deposit composition and cathode current efficiency. All the results shown in FIGURES 38-41 were calculated from the EDAX measurements and were used to establish the optimum electroplating parameters for each of the electrolytes used. The ICP data showed the same trend, however this technique was used primarily for monitoring the bath composition.

Time

The results for the time variation investigations are given in FIGURE 38 and discussed in the following section.

FIGURE 38: Effect of Time on Deposit Composition and Cathode Efficiency



Zinc-Cobalt

Zinc-cobalt electrodeposit composition was tested in agitated and stagnant conditions for the time investigation and results are shown in FIGURE 38. The stagnant series consistently had a higher percentage of cobalt present in the deposit than the agitated series. However, both zinc-cobalt data series mirrored each other's trends. As the time increased from 0.5 to 30 minutes, the cobalt percentage in the electrodeposit decreased, from 7% to 0.7% for the stagnant series and 3% to 0.4% for the agitated series. The thickness of the electrodeposit increased with plating time but the quality and appearance of deposit was largely unaffected. The cathode efficiency remained constant after an initial increase, during the first 2 minutes, from 69% up to 80%.

Zinc-Nickel

The percentage of nickel in the coating decreased from 16% to 7%, as the plating time increased, as shown in FIGURE 38. The thickness of the zinc-nickel electrodeposit increased with time, while the quality did not seem to vary greatly. The cathode efficiency of 69% at 0.5 minutes plating time increased up to 88% over the first 2 minutes and then remained relatively constant after this time.

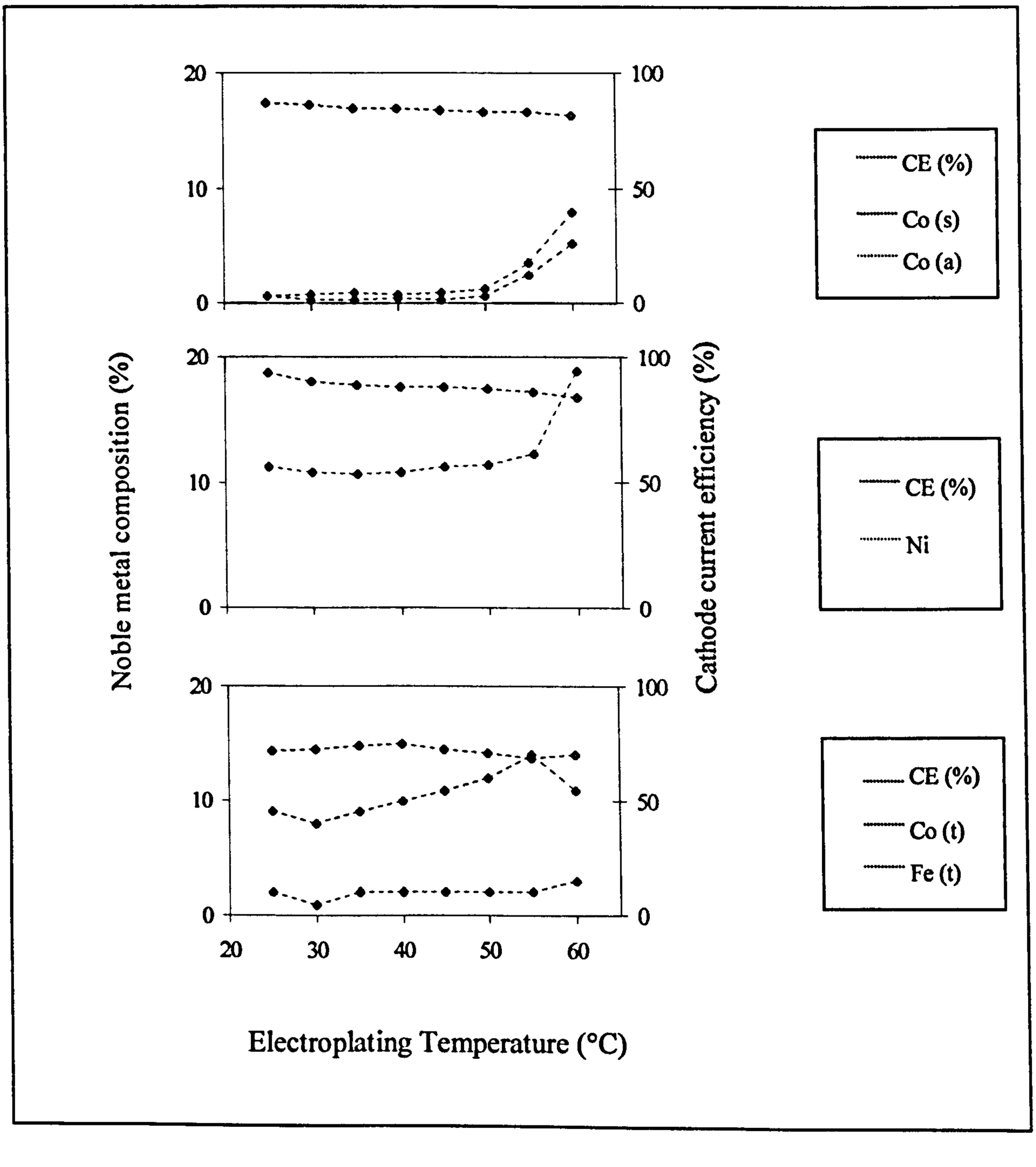
Zinc-Cobalt-Iron

The compositional trend for cobalt in the ternary coatings is the reverse of that observed for either of the binary alloy electrolytes. The thickness of the deposit increased with time, but there was a slight overall increase in the iron group metal percentage in the coating as shown in FIGURE 38. There was no effect on coating appearance observed. The percentage of cobalt in the coating increased with electroplating time, until a maximum level of 12% was reached at about 20 minutes. The quantity of iron in the coating decreased proportionally and also became fairly constant at about 1.5% after about 10 minutes plating time. Once again the initial cathode efficiency increased with time until a relatively constant value of 73% was reached after 2 minutes plating time.

Temperature

The results for the temperature variation investigations are given in FIGURE 39 and discussed in the following section.

FIGURE 39: Effect of Temperature on Deposit Composition and Cathode Efficiency



Zinc-Cobalt

The specimens plated at higher temperatures appeared to be brighter and smoother when examined. The percentage of cobalt in the deposit increased with an increase in the temperature range investigated as shown in FIGURE 39. There was a constant level of cobalt found between 25 - 45°C of 0.6% with a sharp rise at temperatures above this to 5%. As with the electroplating time investigations, stagnant plating conditions produced a higher level of cobalt in the deposit than agitated conditions. The weight of the deposit formed varied little, but the cathode efficiency decreased gradually over the temperature range investigated from 87% to 82%.

Zinc-Nickel

Variation in temperature altered the appearance and the composition of the coatings slightly, but the weight of the deposit varied little. Increasing the temperature increased the percentage of nickel in the deposited alloy as shown in FIGURE 39. The percentage of nickel increased gradually between 25 – 45° C, above this temperature range the level of noble metal content increased sharply from 11% to 19% (at about 60° C). Cathode efficiency decreased gradually from 94% to 84% over the increasing temperature range investigated.

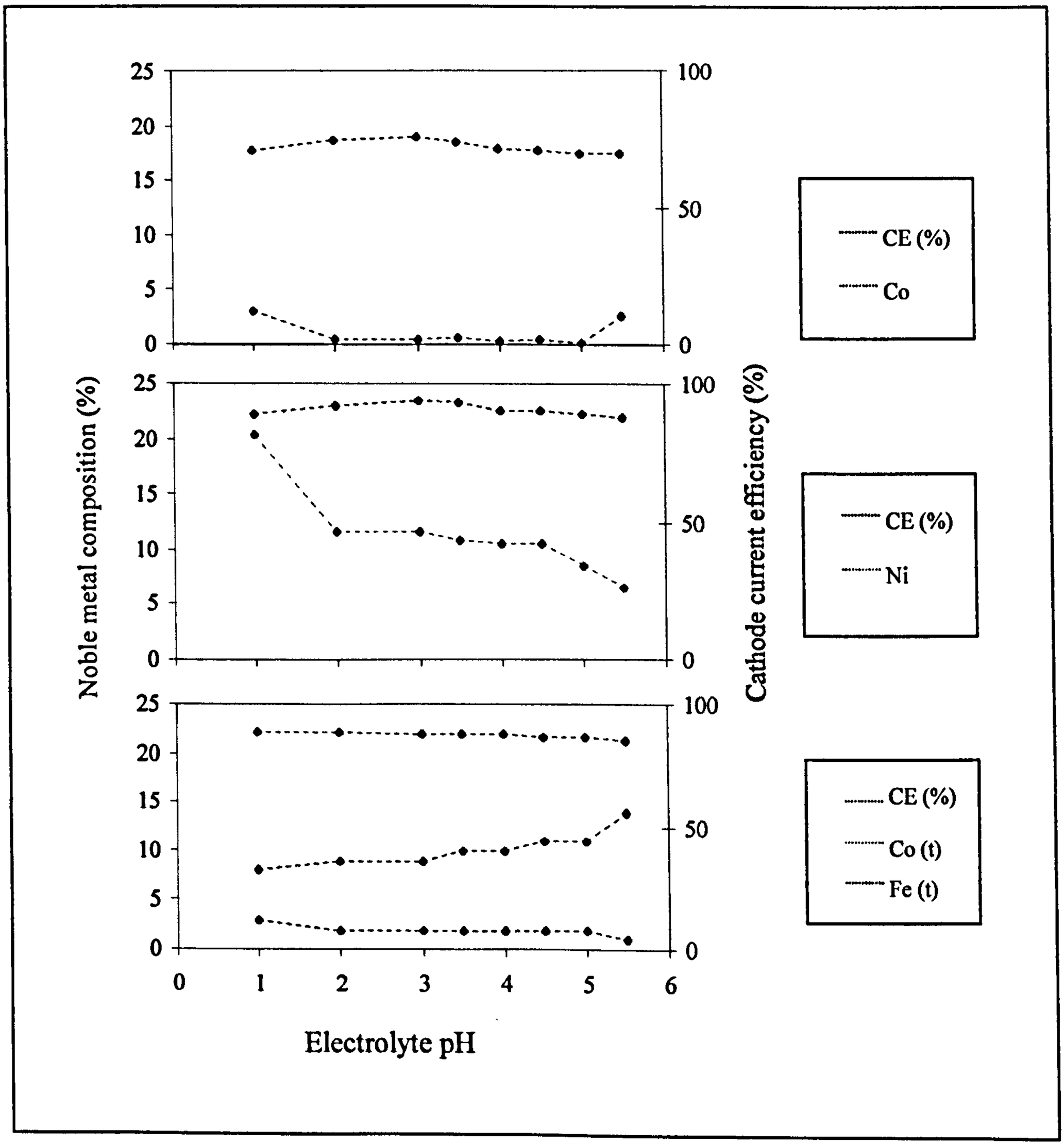
Zinc-Cobalt-Iron

Plating at higher temperatures increased the brightness and smoothness of the ternary coatings. The percentage of cobalt in the electrodeposits increased with temperature, an effect that was also observed for the binary zinc-cobalt coatings as shown in FIGURE 39. The level of cobalt increased from 9% to 11% in the deposited coating, while the level of iron decreased slightly over the series from 3% to 2%. The level of noble metal content increased beyond 35°C, until 55°C where it reached a maximum and then began to decrease again. The cathode current efficiency remained relatively constant at about 73%. However, it decreased slightly after 40°C with a further rise in temperature and higher cobalt deposit content.

pH

The results for the pH investigations are summarised in FIGURE 40 and discussed in the following section.

FIGURE 40: Effect of pH Value on Deposit Composition and Cathode Efficiency



Zinc-Cobalt

The maximum cobalt level of 3% was seen at pH1, after this the cobalt level dropped to about 0.5%, as shown in FIGURE 40. The pH range 2-4.5 saw little change in the cobalt content of the alloy. At more alkaline pH values there was an increase in the amount of cobalt in the final deposit to almost 3%. The cathode current efficiency for the zinc-cobalt varied little. The initial value was 71% at pH1, increasing slightly to 76% at pH3 before gradually falling at more alkaline pH values back to 70%. Change in pH did not alter the coating appearance greatly.

Zinc-Nickel

The highest level of nickel in the coatings, (20%), was seen at pH1, as shown in FIGURE 40. Between pH2 – 4.5, there was little change in the relative nickel composition, with it remaining at approximately 11%. The amount of nickel in the electroplated layer decreased at more alkaline pH values dropping to 7% at pH5.5. The cathode current efficiency of the zinc-nickel electrolyte rose from 89% to a small peak of 94% at pH3, then it gradually fell to 88% at pH5.5. Variation in electrolyte pH did not cause any great change in the coating appearance.

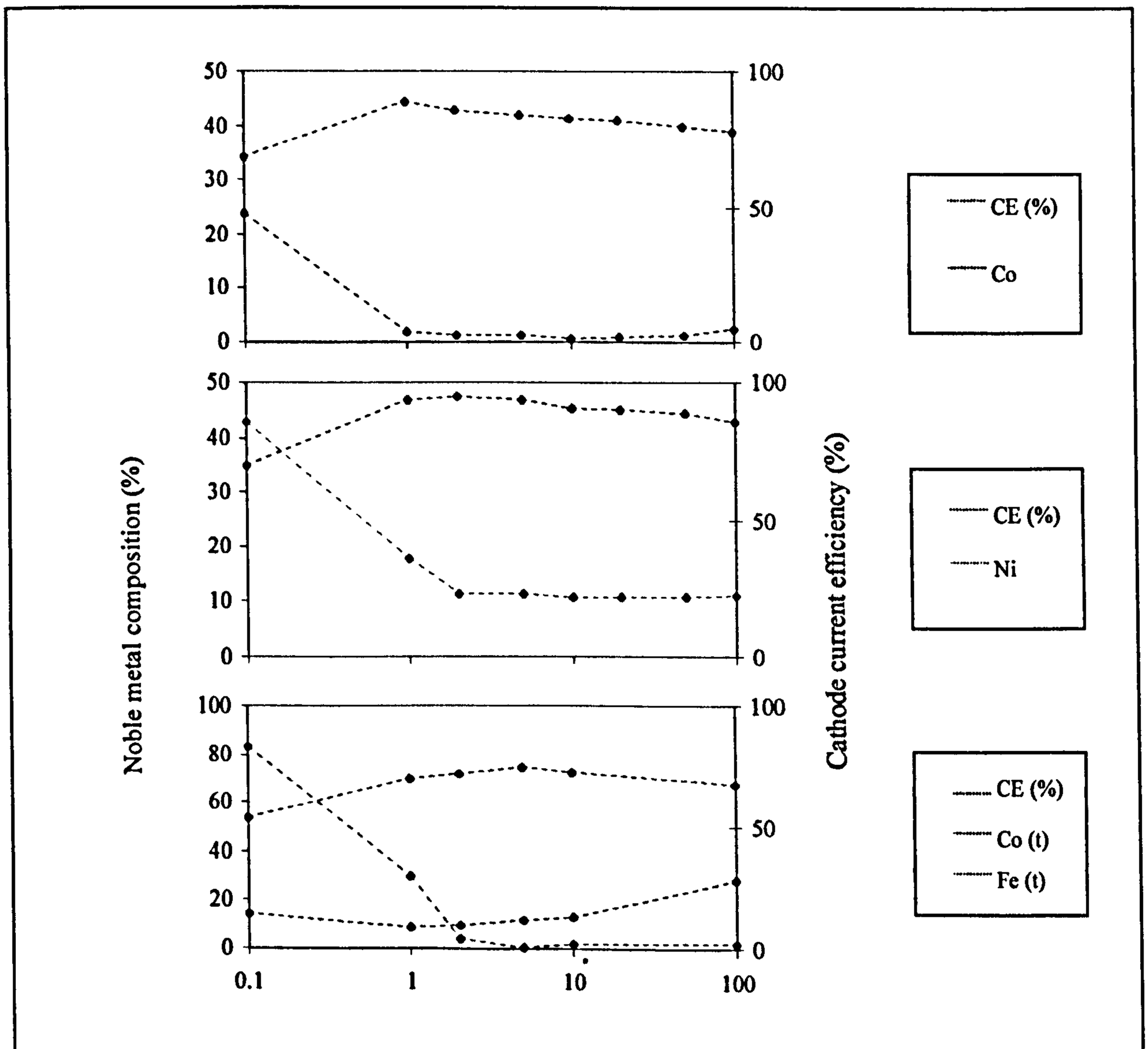
Zinc-Cobalt-Iron

Like the binary zinc-cobalt coatings the cobalt content of the zinc-cobalt-iron coatings increased at more alkaline pH values from 8% at pH1 to 14% at pH5.5, as shown in FIGURE 40. The iron composition of the deposit fell over the series from 3% at pH1 to 1% at pH5.5. There was little change in appearance of the specimens with a change in pH value but the cathode current efficiency decreased from 77% to 68% with a corresponding increase in alkalinity and cobalt content in the coating.

Current Density

The results for the current density investigations are summarised in FIGURE 41 and discussed in the following section. Current density variation produced the most pronounced differences in the appearance and composition of coatings of any of the variables that were examined.

FIGURE 41: Effect of Current Density on Deposit Composition and Cathode Efficiency



Zinc-Cobalt

The composition of the zinc-cobalt electrodeposits varied as expected within the current density range investigated and is shown in FIGURE 41. At very low current densities the cobalt percentage in the deposit was 24% which was greater than the 8% cobalt composition of the bath. At current densities of 1mA/cm^2 and above, the level of cobalt deposited decreased to ≤1%, but at 100mA/cm^2 it rose to 2.5% Increased current density led to a direct increase in the thickness of the deposited coating. As the current density increased to 1mA/cm^2 the cathode efficiency rose from 69% to its maximum value of 89%. As the current density was increased past 1mA/cm^2 the cathode efficiency gradually decreased to 78%. The coatings produced were all smooth and even, but those deposited at a current density >50mA/cm^2 appeared to be more nodular when examined on the SEM.

Zinc-Nickel

The initial percentage of nickel in the coating at very low current densities was 43%, as shown in FIGURE 41. This level quickly decreased to a value of 10-12% at 2mA/cm^2 and remained constant for the rest of the current density range investigated. An increase in current density increased the amount of coating deposited. At higher current densities the quality of the deposit deteriorated, becoming brighter but more nodular in appearance. The minimum current efficiency of 70% was seen at the lowest current density investigated and the highest 95% at a value of 2mA/cm^2, above which it began to steadily decrease to 86%.

Zinc-Cobalt-Iron

A current density of 0.1mA/cm^2 gave the highest iron content of 83%, which decreased with an increase in current density to a minimum level of 2%, as shown in FIGURE 41. The cobalt content of the coating at the lowest current density was 15%, which fell to 9% at 1mA/cm^2 and then gradually rose to 28% with a deposition current density of 100mA/cm^2. At current densities of 2mA/cm^2 and above the cobalt content of the coatings remained above the 10% cobalt composition of the bath. An increase in current density resulted in a direct increase in deposited material. At a current density of 0.1mA/cm^2, the cathode current efficiency was at a minimum value of 54%. This

increased to a maximum of 75% at 5mA/cm^2. Above 5mA/cm^2 the current efficiency gradually to 68% at 100mA/cm^2. Despite the low cathode efficiency at small current densities, the appearance of the coatings was still smooth and even. At densities >50mA/cm^2 the coatings appeared more nodular when examined under the SEM, this point also corresponded to a slight drop in cathode efficiency.

ELECTRODEPOSIT EXAMINATIONS

FIGURE 42 shows a typical zinc-cobalt electroplated surface with holidays clearly visible produced without the use of a surfactant. FIGURES 43-44 are zinc-cobalt electrodeposits formed for different lengths of electroplating time displaying zinc hydroxide whiskers.

FIGURE 42: Zinc-Cobalt Deposit with Large Holidays

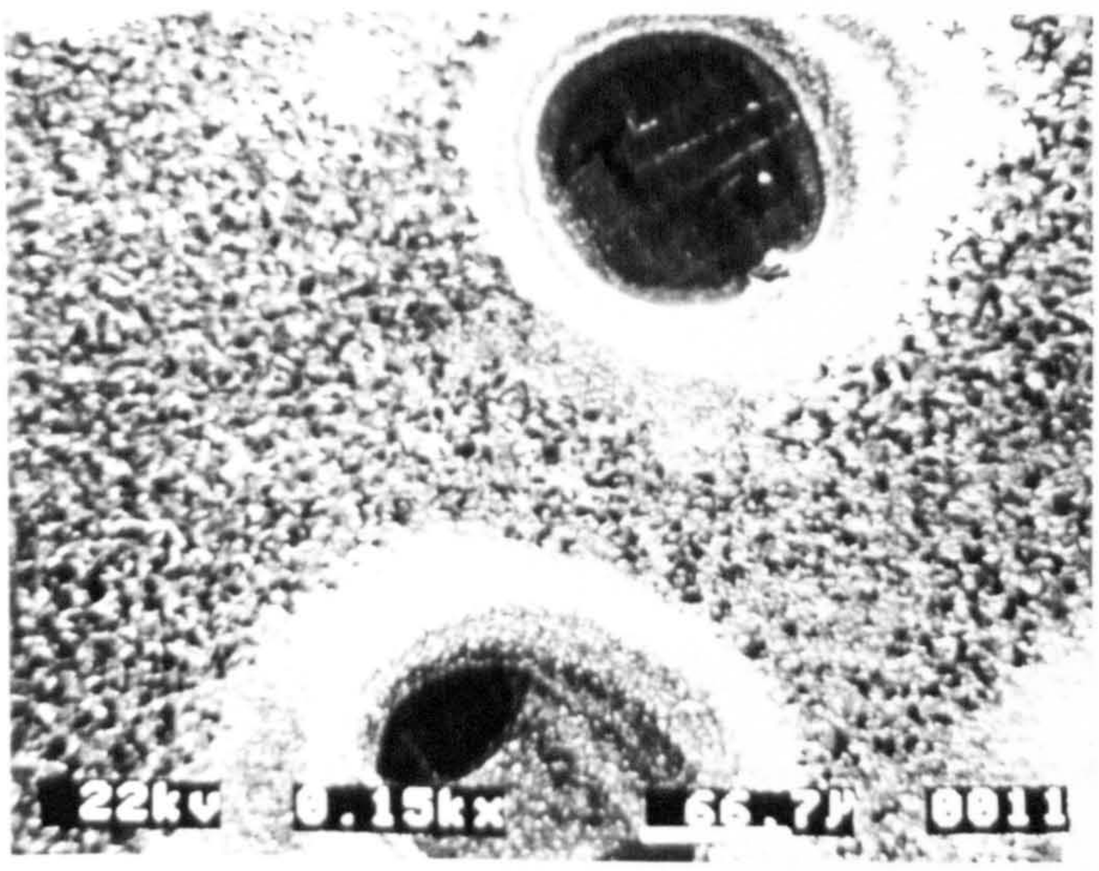
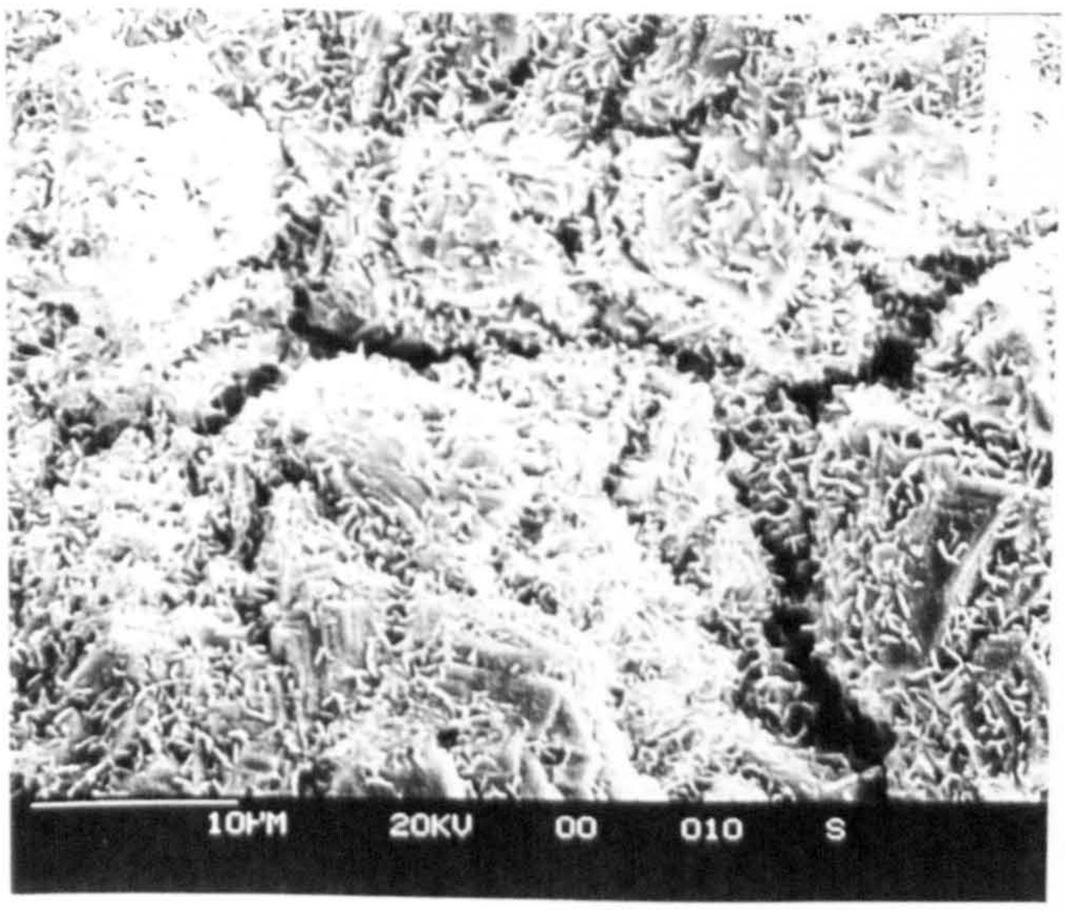


FIGURE 43: Zinc-Cobalt Deposit Formed for 1 Minute with Zinc Hydroxide Whiskers Visible



FIGURE 44: Zinc-Cobalt Deposit Formed in Stagnant Conditions for 30 Minutes Showing Zinc Hydroxide Whiskers



The initial layer formed during zinc-cobalt electroplating was of particular interest for this work and so several surface techniques were employed to determine the composition of this layer.

Parameter variation

The parameter variation testing clearly shows that for a shorter plating time or a lower current density there is a higher percentage of noble metal at the surface of the binary electroplated specimens. Both these situations produce a thin coating illustrating the near to metal surface composition of the plated layer, which has been referred to in other work as the "interlayer". The effect of this interlayer on the hydrogen transport during electroplating of the specimens is crucial to the observed embrittlement. The noble metal composition for steel specimens electroplated under certain conditions are given in TABLE 11.

TABLE 11: Initial Noble Metal Composition from Parameter Variation

Electrodeposit	Fe Group (%) at 0.5 mins	Fe Group (%) at 0.1 mA/cm^2
ZINC-COBALT	3	24
ZINC-NICKEL	16	43
ZINC-COBALT-***IRON***	5, *3*	15, *83*

The specimens electroplated at 0.1mA/cm ^{2} were electroplated for an increased time to produce an electrodeposit that was at least 0.2μm thick (e.g. Zinc-cobalt specimens were electroplated for 45 minutes, which produced a coating of approximately 0.2μm).

Copper strip plating

Due to possible interference problems with the thin plated layer and the overlap of iron and cobalt in the EDAX spectrum, a copper shim was electroplated using the standard zinc-cobalt electrolyte. The strip was continually electroplated under standard bath parameters but the copper substrate was incrementally removed from the electrolyte to produce a strip that had a time graduated electroplated area. Each section of the specimen was exposed for a set length of time, (see FIGURE 28 Chapter 2), but the area that had the shortest electroplating time was the thinnest and of most interest. Examination of this area showed the composition of the initial electroplated layer. This method was used in preference to changing the electroplating current because the resulting change in total charge passed and the difficulties experienced with the lower range thickness that would have been produced.

EDAX examination of the initial electroplated area, showed a significant difference from the percentage of cobalt seen in the same zone with the variation in parameter investigations performed on a steel shim. It can be seen from TABLE 12, that the copper substrate showed a higher cobalt percentage than the steel substrate for the same thickness of electrodeposit (0.2μm). This value suggested that the expected EDAX interference effects from using the steel shim had been over compensated for. Further surface techniques including XPS and Auger depth profiling were employed to determine the cobalt percentage and to confirm which technique gave the more accurate result.

TABLE 12: Cobalt Percentage Seen in Initial Layer

Zinc-Cobalt Electrodeposit	Copper Strip 0.5 mins	Steel Strip 0.5 mins
COBALT (% ELEMENT)	5	3

XPS

The XPS technique employed showed variation in the elemental composition of each of the electroplating types for coatings of different thickness. However, it suffered from significant background scatter, making an accurate compositional information hard to determine. It was thought that XPS data might also provide evidence of the type of deposition mechanism occurring, by indicating the chemical state of the noble metal that was present. The results obtained are given in TABLE 13.

TABLE 13: Specimens Examined Using XPS and Elements Detected

Electrodeposit	0.5 Minute	2 Minutes	2 Minutes Baked	15 Minutes
Zinc-cobalt	**O, Zn**, Co, **Fe**	**O, Zn**, Co, Fe	**O, Zn**, Co, Fe	**O, Zn**, Co, Fe
Zinc-nickel	**O, Zn**, Ni, **Fe**	**O, Zn**, Ni, Fe	**O, Zn**, Ni, Fe	**O, Zn**, Ni, Fe
Zinc-cobalt-iron	**O, Zn**, Co, **Fe**	**O, Zn**, Co, Fe	**O, Zn**, Co, Fe	**O, Zn**, Co, Fe

The bold text in the table illustrates a high level of an element present in the XPS data. As expected the 0.5 minute electroplated specimens showed high levels of iron due to the thinness of the electrodeposit. The elemental peaks after 2 minutes electroplating time became much more defined and appeared to alter little in proportion beyond this point. However, it was not possible to determine categorically the chemical state of the elements that were present using this technique.

The specimens that had been baked after electroplating and prior to examination showed a higher level of oxygen on the upper surface of the specimen than unbaked specimens electroplated for the same length of time. This was probably due to oxides being formed during the baking treatment. All the specimens, including those of only 0.2μm, clearly showed a high level of oxygen along with the coating constituent elements. This aided the determination of the deposition mechanism and will be discussed in more detail in Chapter 4. The XPS results for each electroplated coating are given in FIGURES 45-47, and contain the traces for each set of electroplating times.

FIGURE 45: Full XPS Traces for Zinc-Cobalt Electroplating

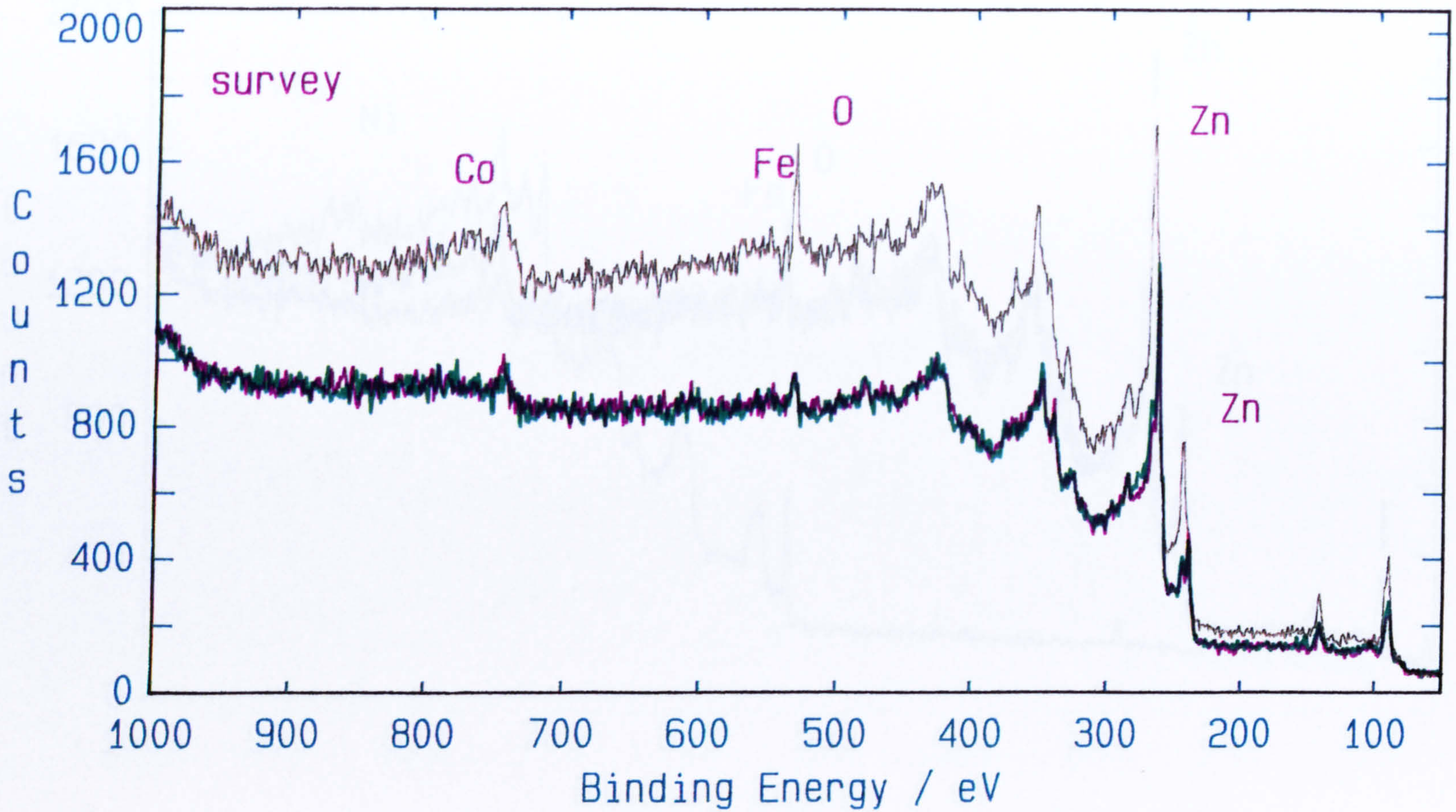


FIGURE 46: Full XPS Traces for Zinc-Nickel Electroplating

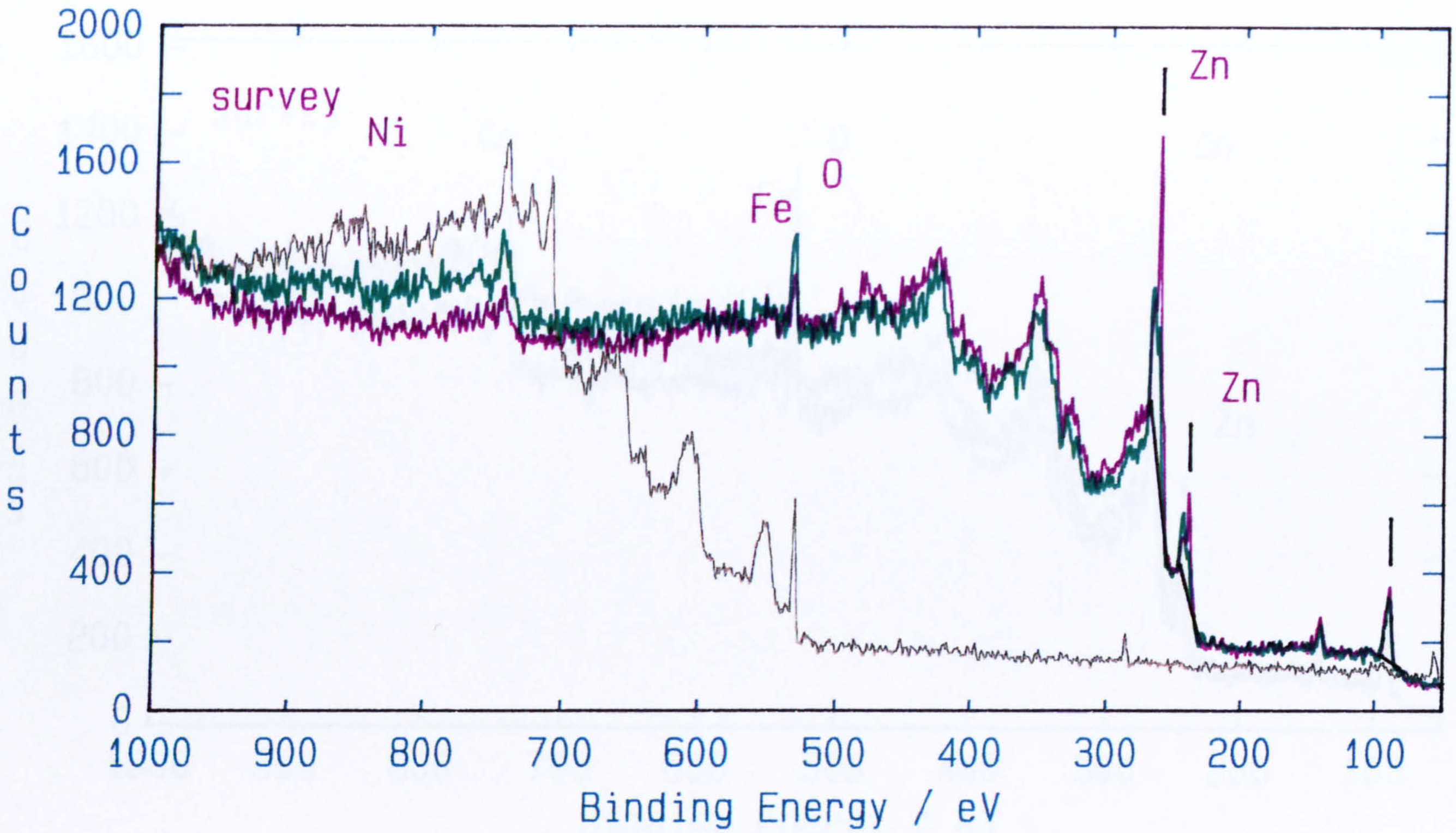
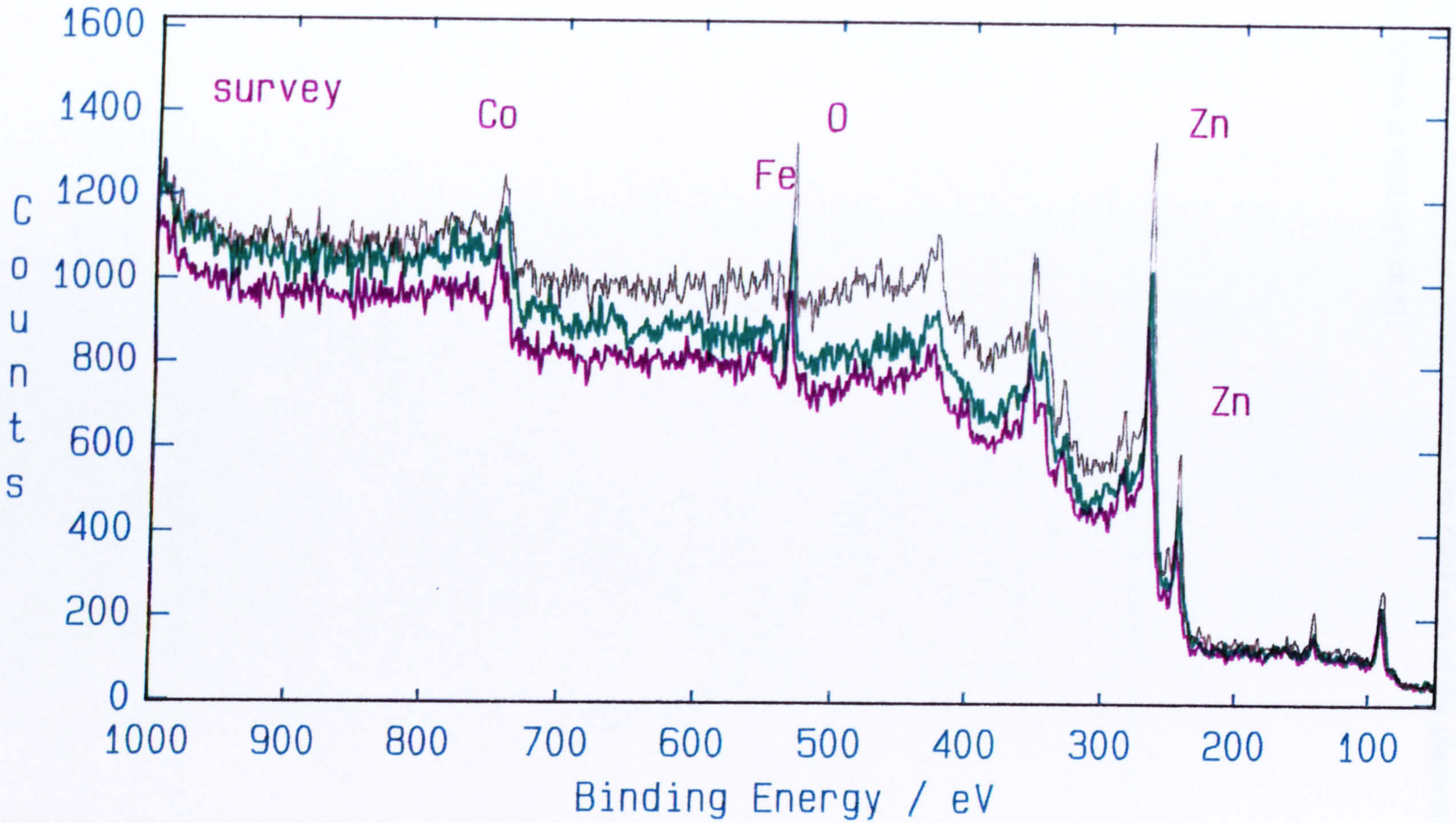


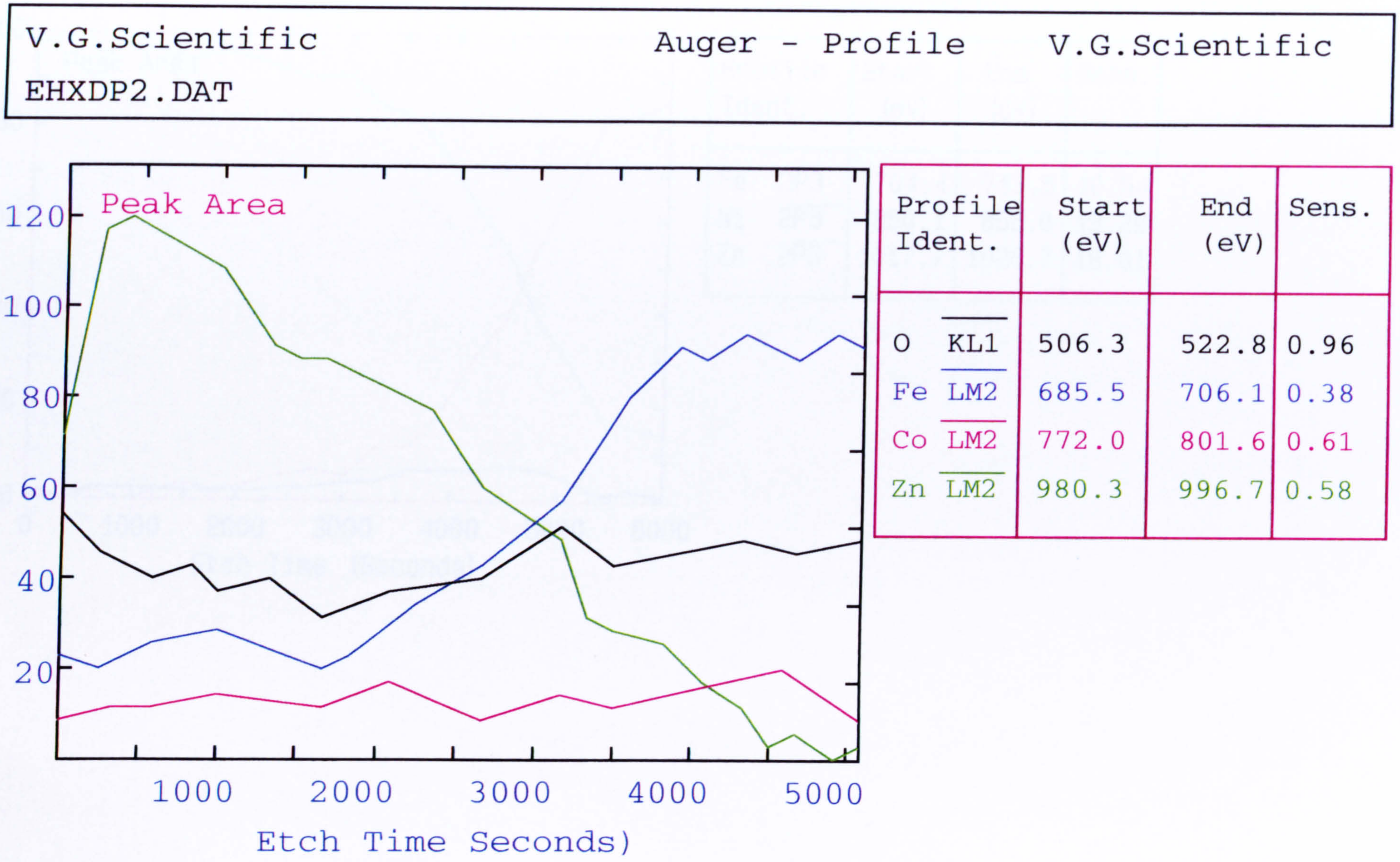
FIGURE 47: Full XPS Traces for Zinc-Cobalt-Iron Electroplating



Auger Depth Profiling

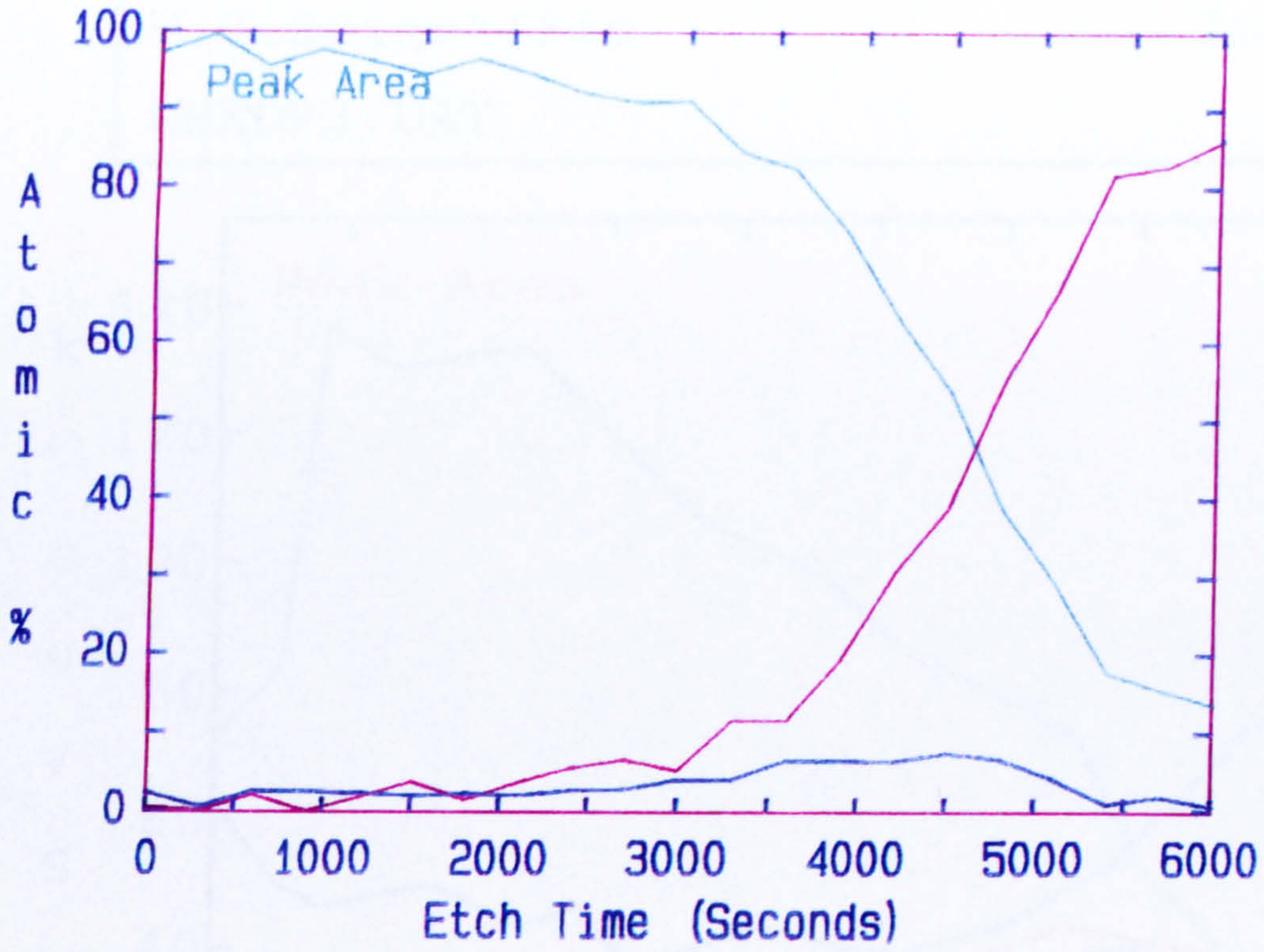
The XPS data gave the elemental constituents present in the electrodeposits tested but did not conclusively confirm their proportion or chemical state. Specimens for depth profiling were electroplated to a thickness of 0.2μm and then examined without any prior baking treatment. The specimens were progressively etched using an Argon beam, analysed and etched again. Gradually, concentration profiles were built up for iron, oxygen, zinc and cobalt or nickel through the thickness of the electrodeposit. The results are shown in FIGURES 48-51.

FIGURE 48: Auger Depth Profile of Zinc-Cobalt Electroplating at pH4.2



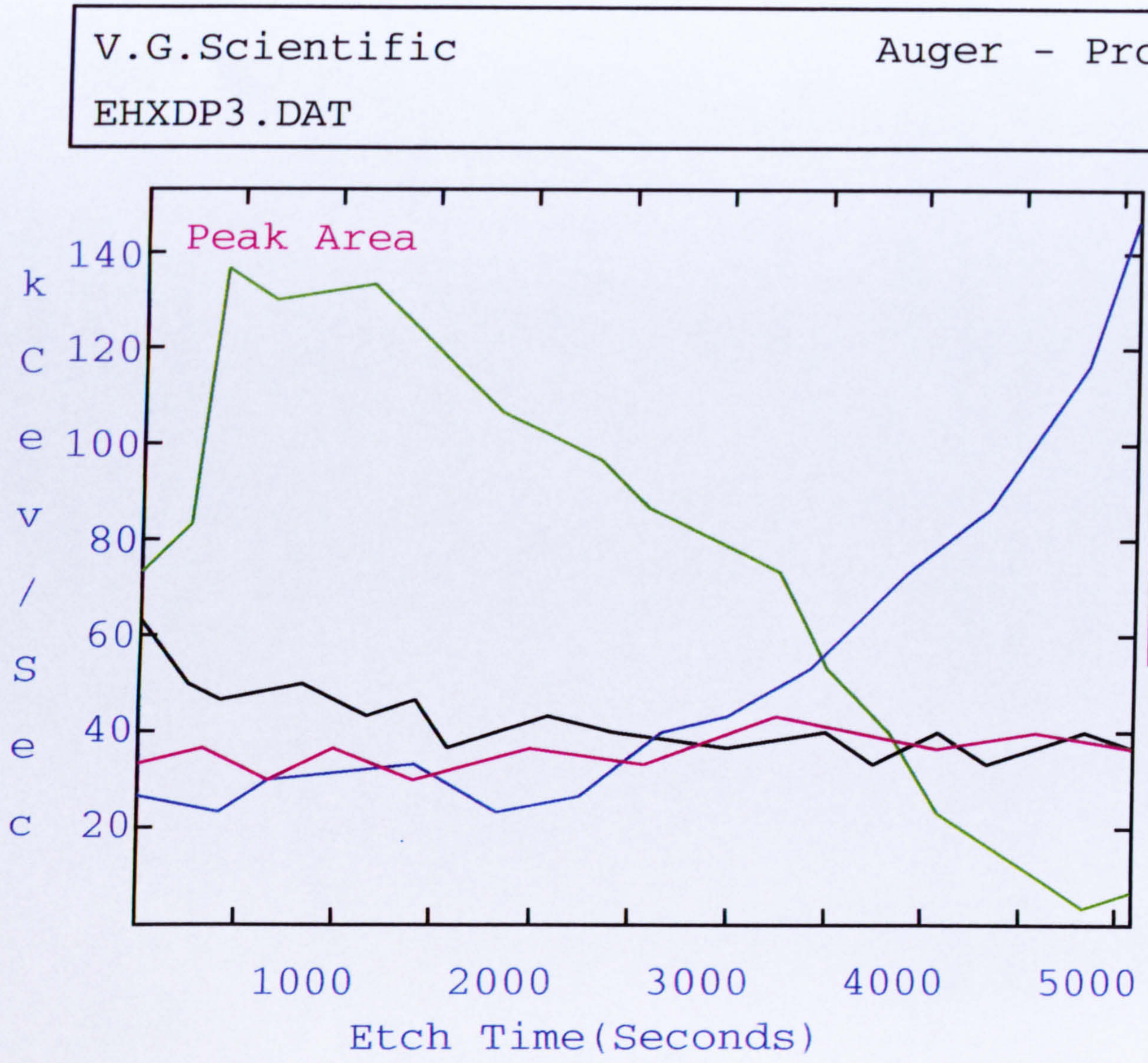
Profile Ident.		Start (eV)	End (eV)	Sens.
O	KL1	506.3	522.8	0.96
Fe	LM2	685.5	706.1	0.38
Co	LM2	772.0	801.6	0.61
Zn	LM2	980.3	996.7	0.58

FIGURE 49: Auger Depth Profile of Zinc-Nickel Electroplating



Profile Ident.	Start (eV)	End (eV)	Sens.
Fe 2P3	704.4	713.5	10.54
Ni 2P3	850.1	855.0	13.29
Zn 2P3	1017.7	1026.7	18.01

FIGURE 50: Auger Depth Profile of Zinc-Cobalt-Iron Electroplating



Profile Ident.		Start (eV)	End (eV)	Sens.
O	KL1	504.3	520.7	0.96
Fe	LM2	680.5	708.0	0.39
Co	LM2	770.0	801.6	0.60
Zn	LM2	983.2	996.7	0.59

FIGURE 48 for the zinc-cobalt electrodeposit produced at pH4.2 showed no sign of noble metal enrichment at the electrodeposit / steel interface. This may be due to the standard pH providing a cobalt level close to the detection limits of the experimental technique employed. The level of cobalt in the electroplated deposit at normal 8μm thickness is under 1%.

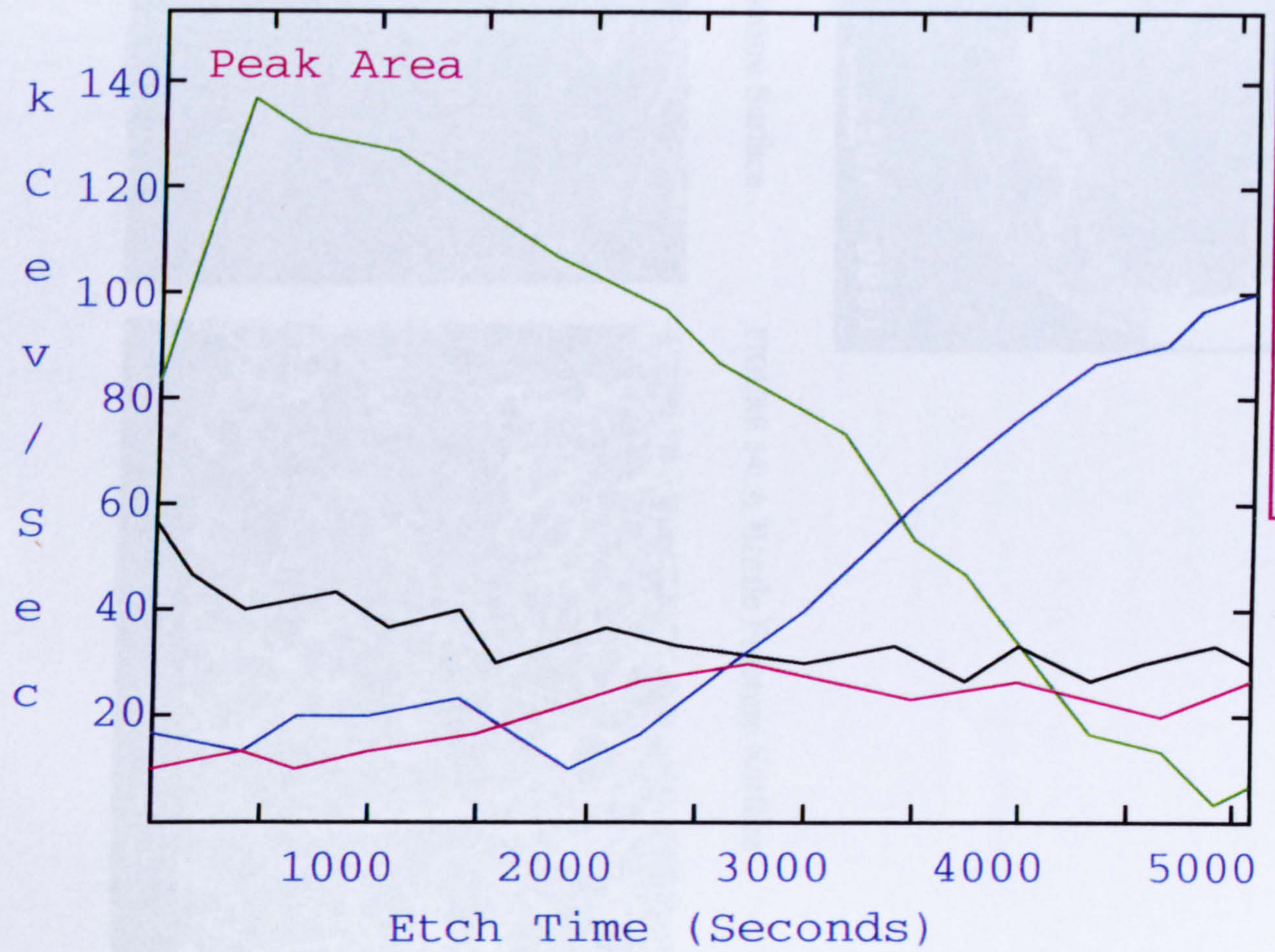
FIGURE 49 demonstrates that there was a significant increase in the nickel composition as the standard zinc-nickel electrodeposit was etched away to reveal the interface with the steel specimen. The nickel rich layer at the interface was formed via the anomalous co-deposition mechanism that has been previously described [17, 18].

FIGURE 50 shows that no noble metal ion enrichment was observed for the zinc-cobalt-iron electrodeposit at the deposit/substrate interface.

Taking an Auger depth profile of a zinc-cobalt coating that was electroplated from an electrolyte at pH1 provided evidence of the expected cobalt enrichment at the interface. This is shown in FIGURE 51.

FIGURE 51: Auger Depth Profile of a Zinc-Cobalt Specimen Electroplated at pH1

V.G.Scientific Auger - Profile V.G.Scientific
EHXDP4.DAT



Profile Ident.	Start (eV)	End (eV)	Sens.
O $\overline{\text{KL1}}$	505.3	521.2	0.97
Fe $\overline{\text{LM2}}$	681.9	709.1	0.39
Co $\overline{\text{LM2}}$	769.4	803.1	0.59
Zn $\overline{\text{LM2}}$	984.2	995.3	0.58

MECHANICAL TESTING

Photomicrographs of a typical control tensile specimens fractured end and different types of fracture surfaces are given in FIGURES 52-54. The control specimen failed in a ductile manner shown by the reduction in cross sectional area and the microvoid coalescence structure seen in FIGURE 53. Specimens that did not show a reduction in cross sectional area generally failed in a brittle manner. An example of this fracture surface is given in FIGURE 54.

FIGURE 52: Fractured End of a Plated Tensile Specimen

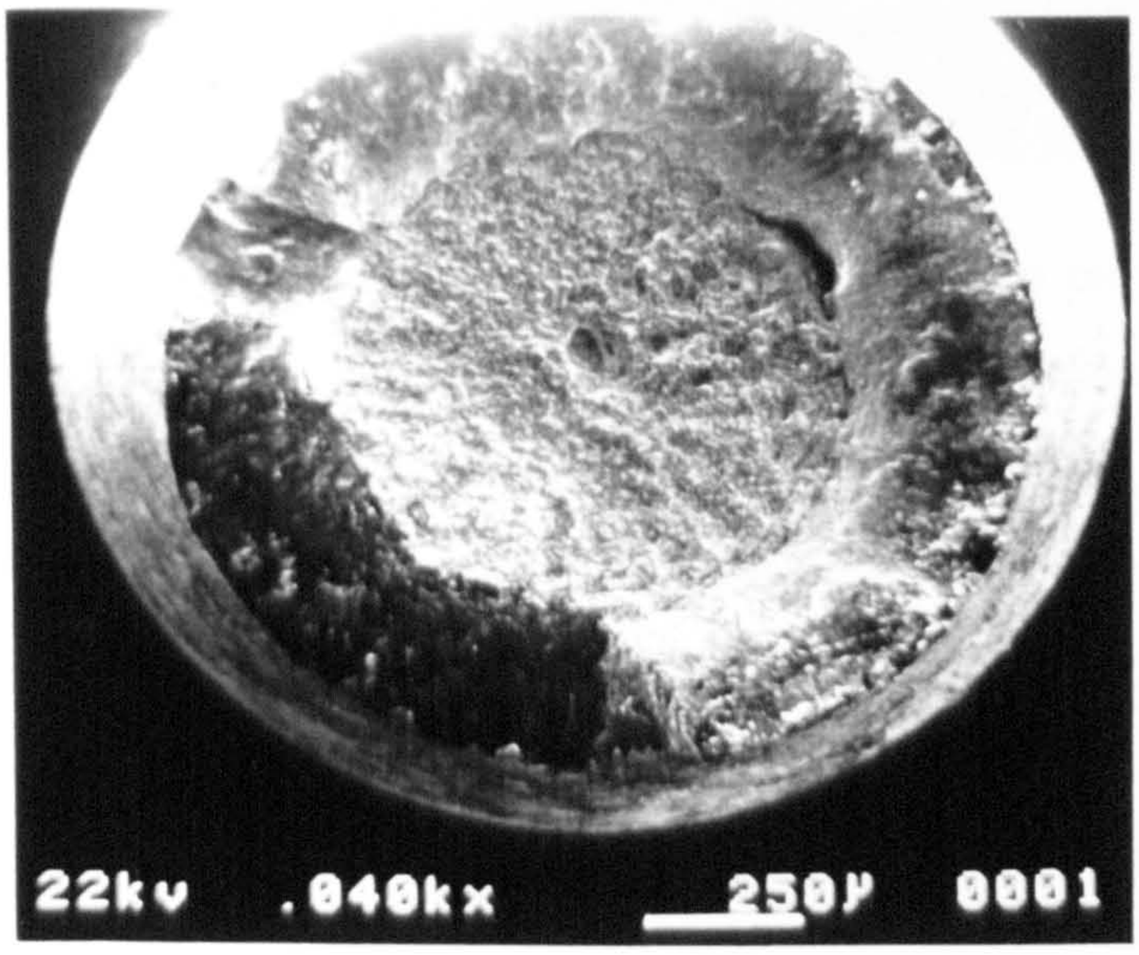


FIGURE 53: A Ductile Fracture Surface

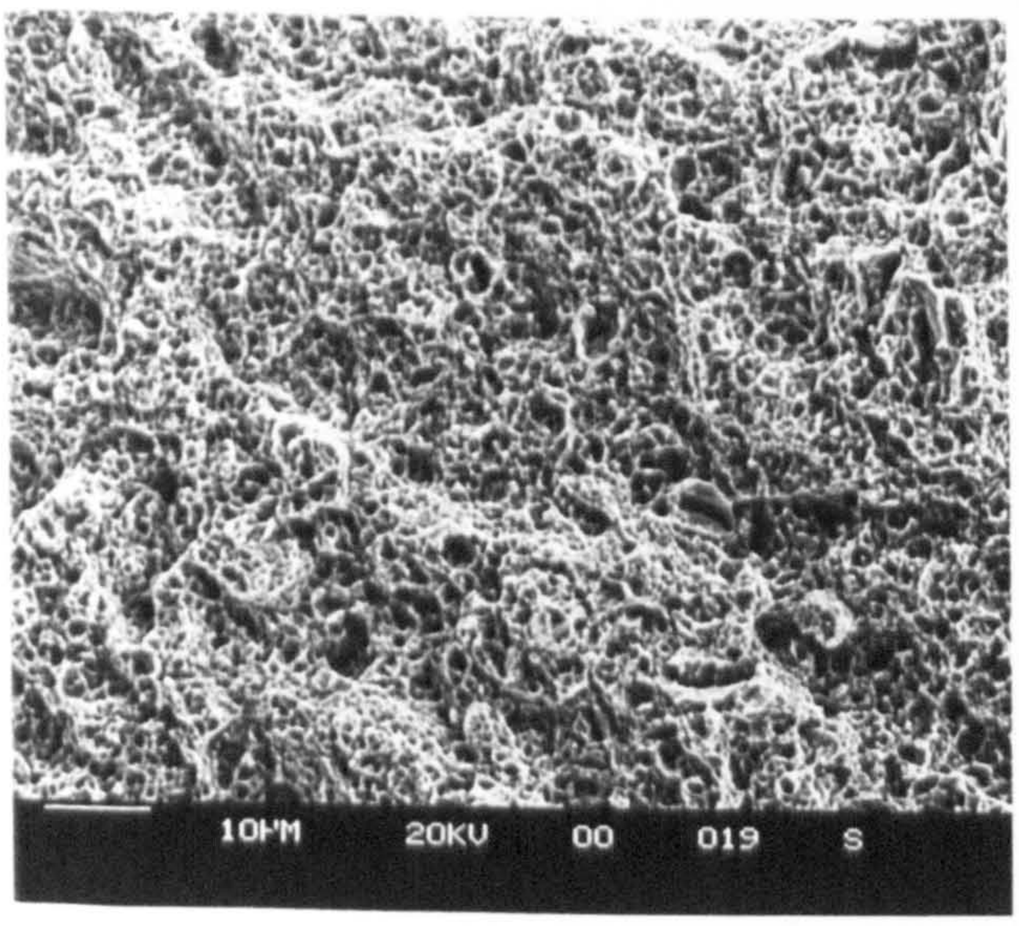


FIGURE 54: A Brittle Fracture Surface

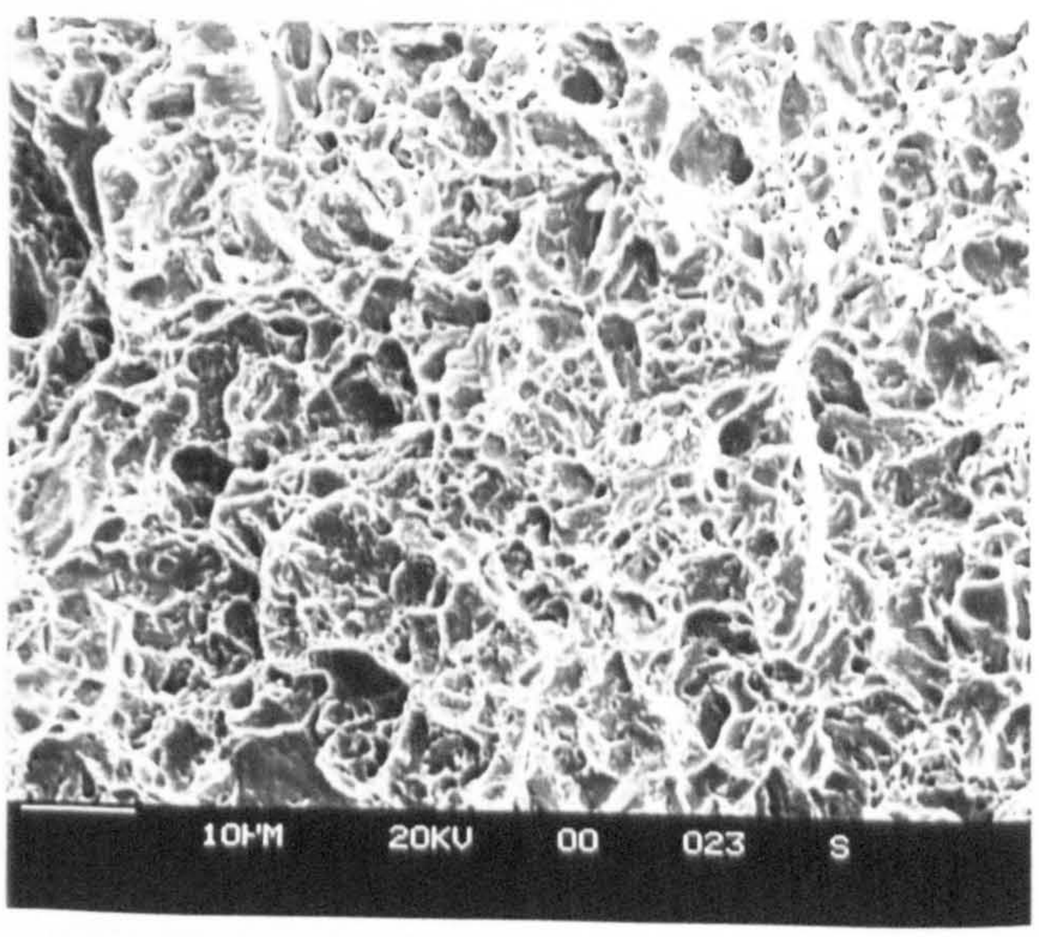
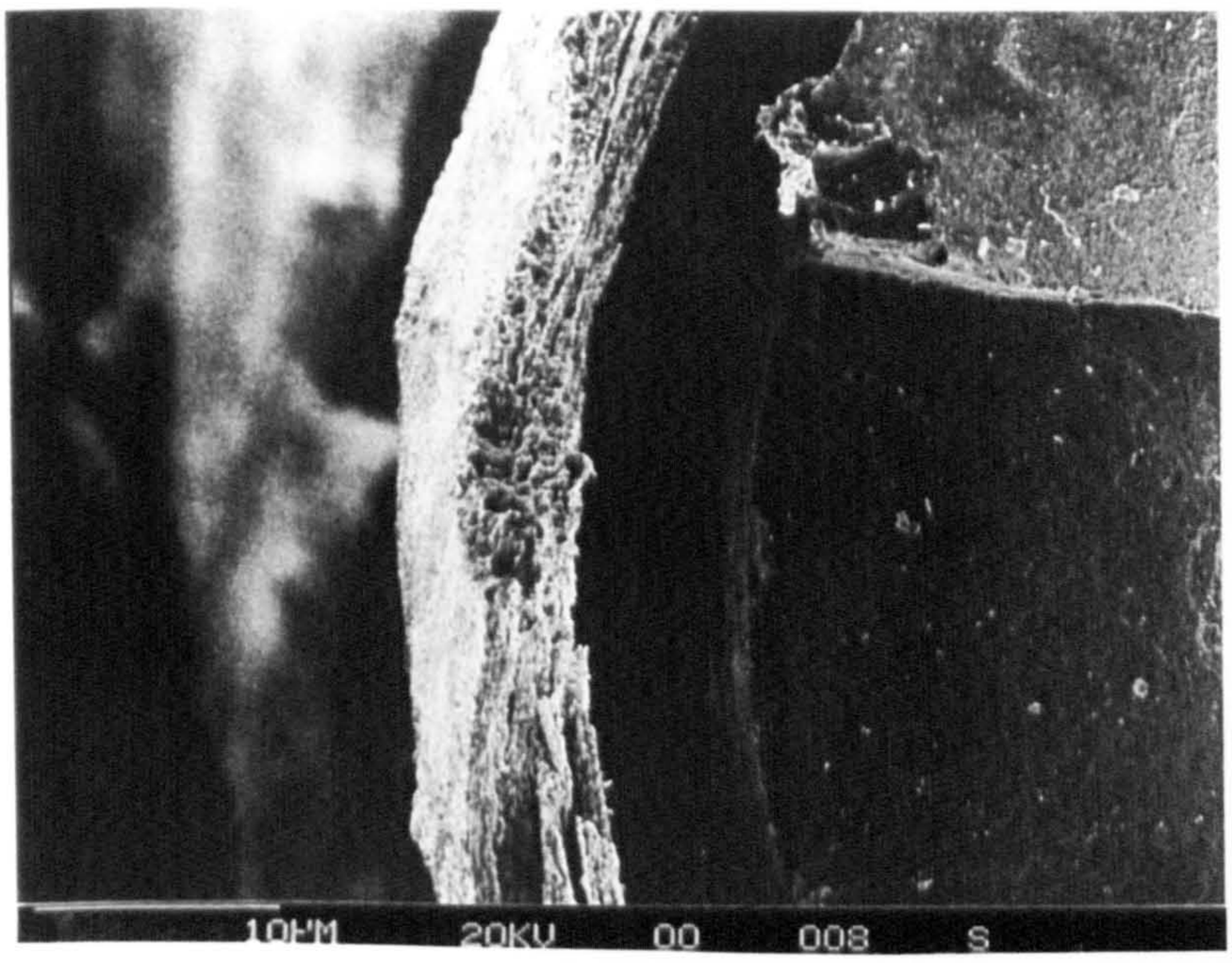


FIGURE 55: Fractured Tensile Specimen with a Partially Detached Porous Coating



The coating shown in FIGURE 55 has become partially detached during the tensile tests and on inspection its surface was seen to contain many small cracks. The side view also demonstrates the porous nature of electrodeposits, which was particularly pronounced in this specimen. Baking treatment, especially in zinc-nickel coatings, exacerbated the detachment of coatings seen after mechanical testing. Load verses time measurements were recorded for each of the specimens and some of these values were converted to true stress true strain values that are shown in FIGURES 56 –57.

FIGURE 56: Stress Strain Diagram for Baked Zinc-Cobalt Specimens

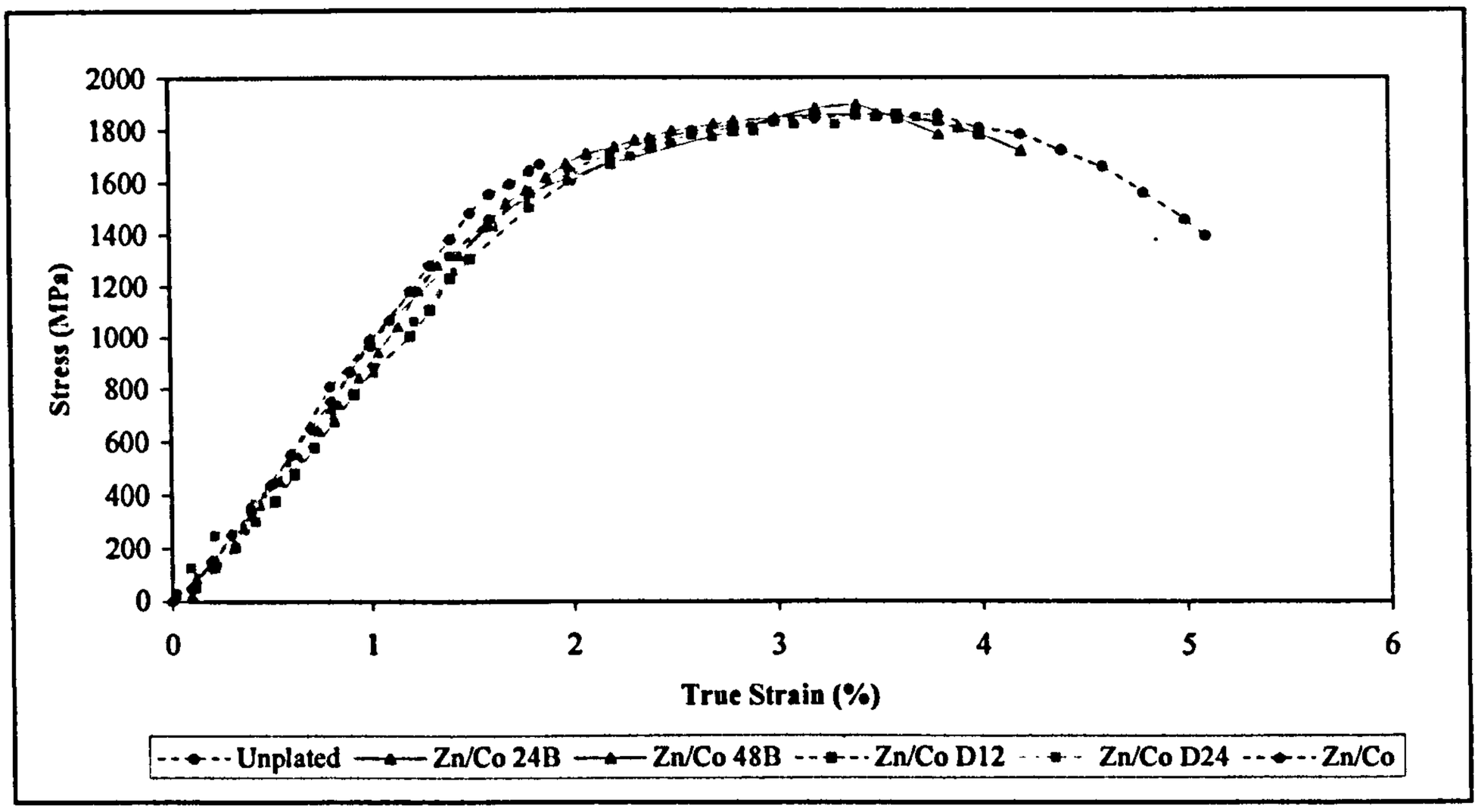


FIGURE 56 shows the tensile strength of zinc-cobalt electroplated specimens once they have been baked was largely unaffected.

FIGURE 57: Stress Strain Diagram for Zinc-Cobalt Specimens Plated at Altered pH

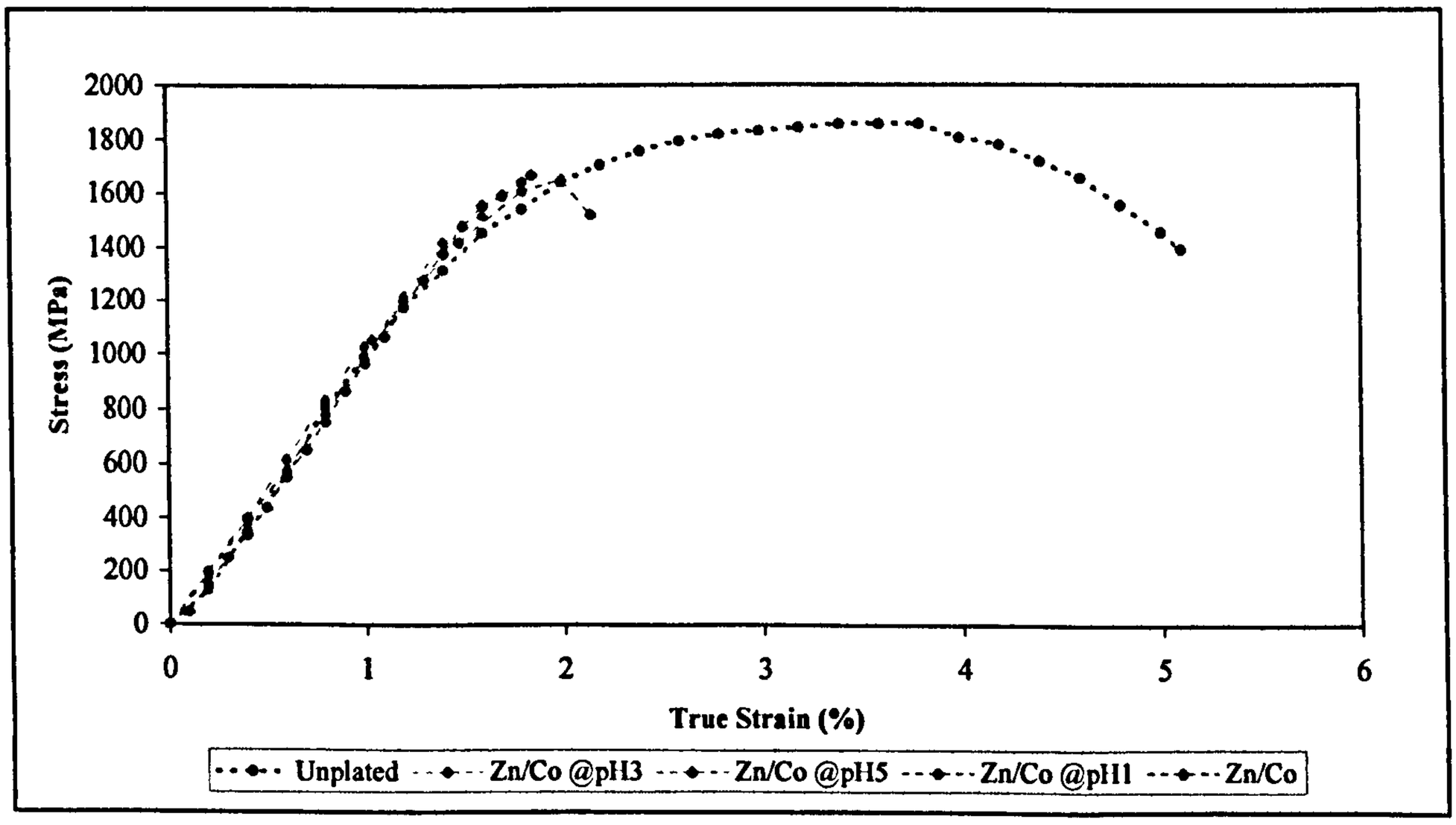
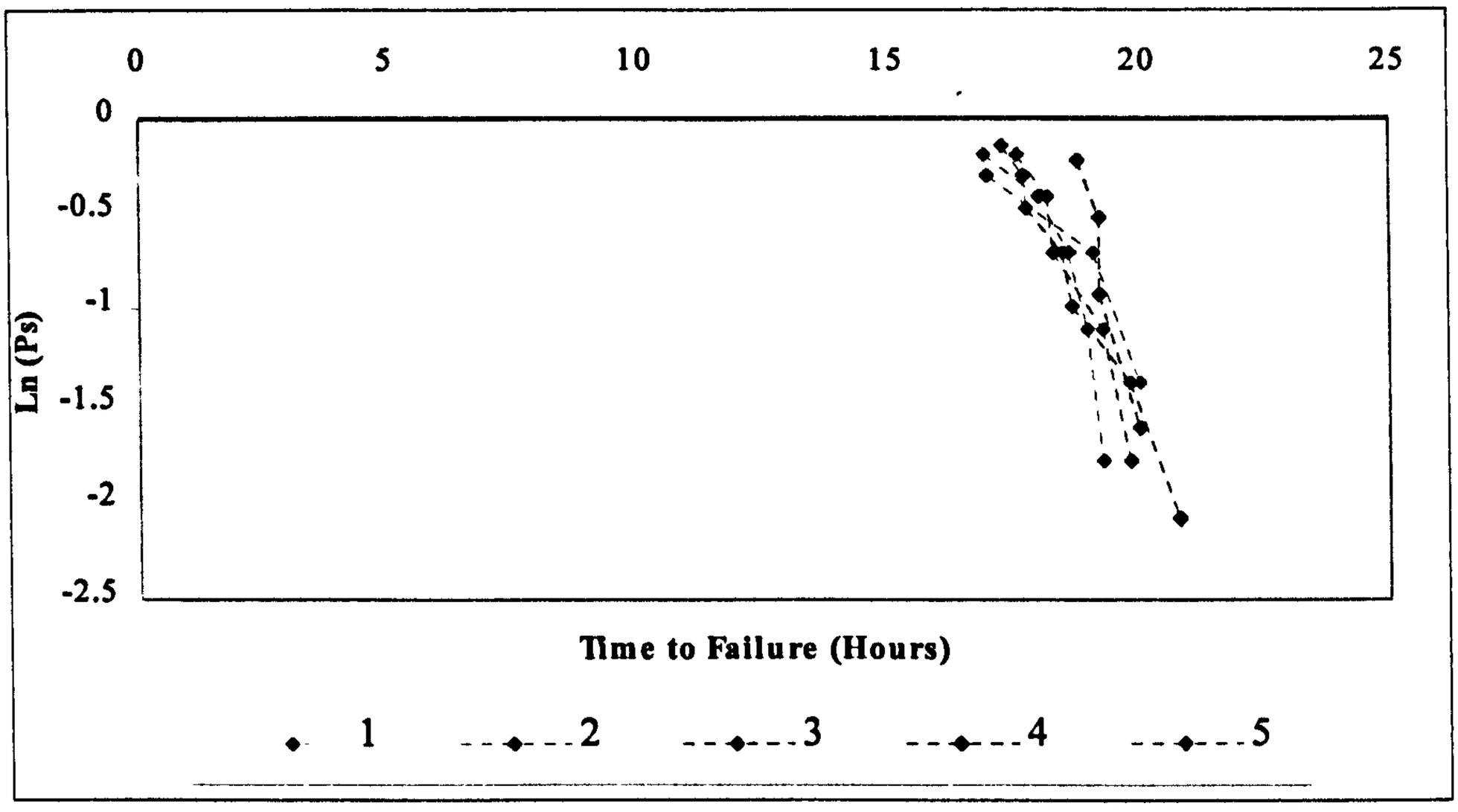


FIGURE 57 demonstrates that the tensile strength of zinc-cobalt electroplated specimens produced at different pH values was affected. These findings are discussed in Chapter 4.

FIGURE 58: Weibull Graph of SSRT Data for Each Batch of Air Test Specimens



Assuming a value of $\beta=1$ (see Chapter 2 and appendices), a Weibull graph of Ln (Ps) against t can be plotted. FIGURE 58 shows the results obtained for the heat-treated AISI 4340 steel slow strain rate specimens tested in air. Each batch was tested for reproducibility using several specimens, which appeared to belong to the same population. The set of data obtained for each batch was then tested using the Student T-test to confirm that they were from the same population and the results are given in TABLE 14.

TABLE 14: Comparision of Batches Using the Student T-Test

Batch/ Total	DOF	Limit	Result	Accept?
1	19	1.729	0.18	Yes
2	20	1.729	0.26	Yes
3	20	1.729	0.55	Yes
4	19	1.729	0.05	Yes
5	20	1.729	0.23	Yes

FIGURE 59: Weibull Graph of all the Unplated Control Specimens Together

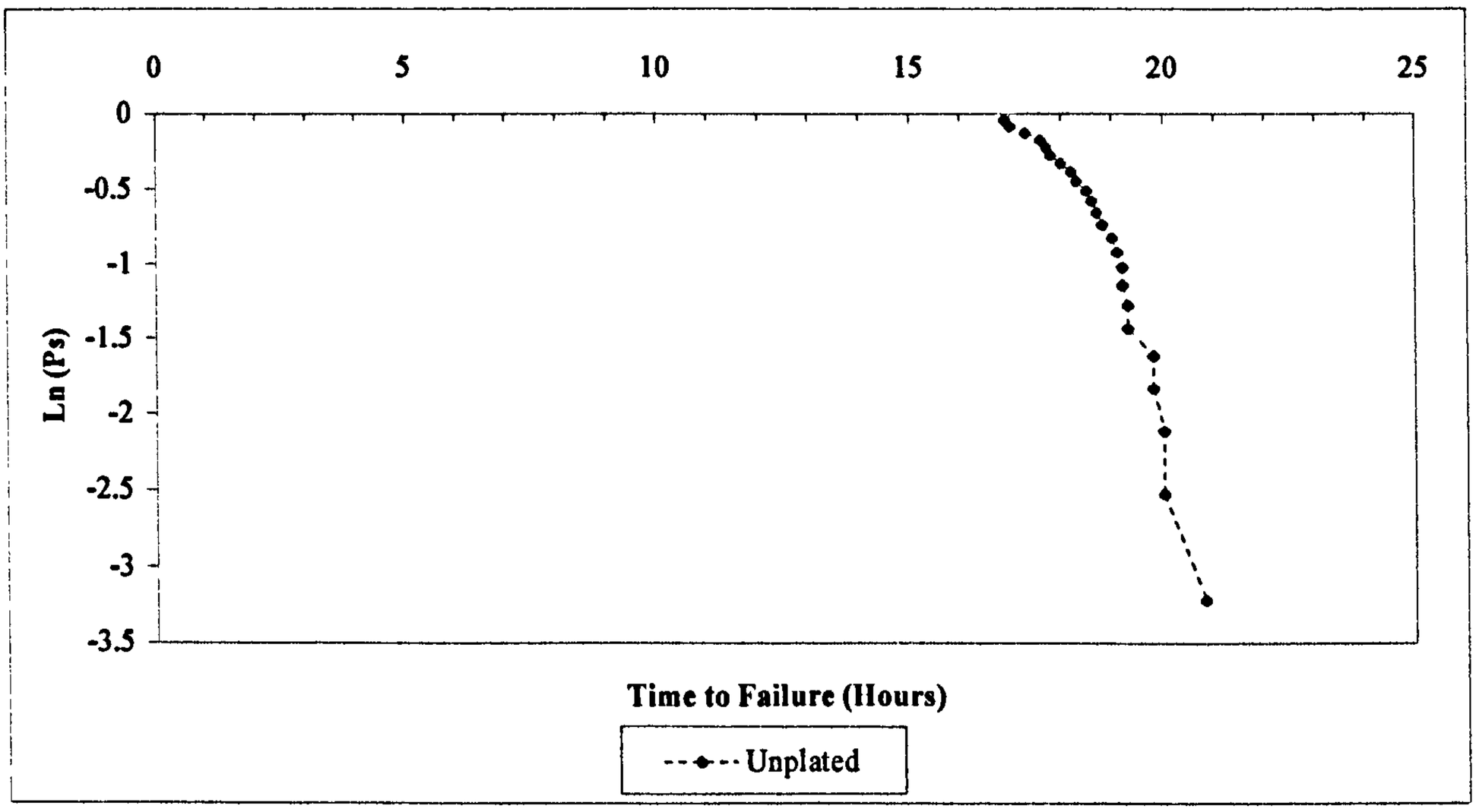


FIGURE 59 shows the steep gradient of the line produced from all the batches plotted as a single line and it indicates that there is excellent reproducibility between the times to failure of individual specimens. The control specimens provide a standard with which other treated specimens could be compared, as they would account for variation in number, size and distribution of defects in the specimens. The other specimen types provide a comparison of the experimental variables under investigation.

The time to failure for specimens in this study was shorter than for those specimens that were previously tested at Cranfield by M. Carr [18]. This was attributed to an increased susceptibility to hydrogen embrittlement as a result of the higher strength of the specimens achieved by the heat treatment process, as discussed in Chapter 1.

FIGURE 60: Weibull Graph of the Effect of Baking Control Specimens

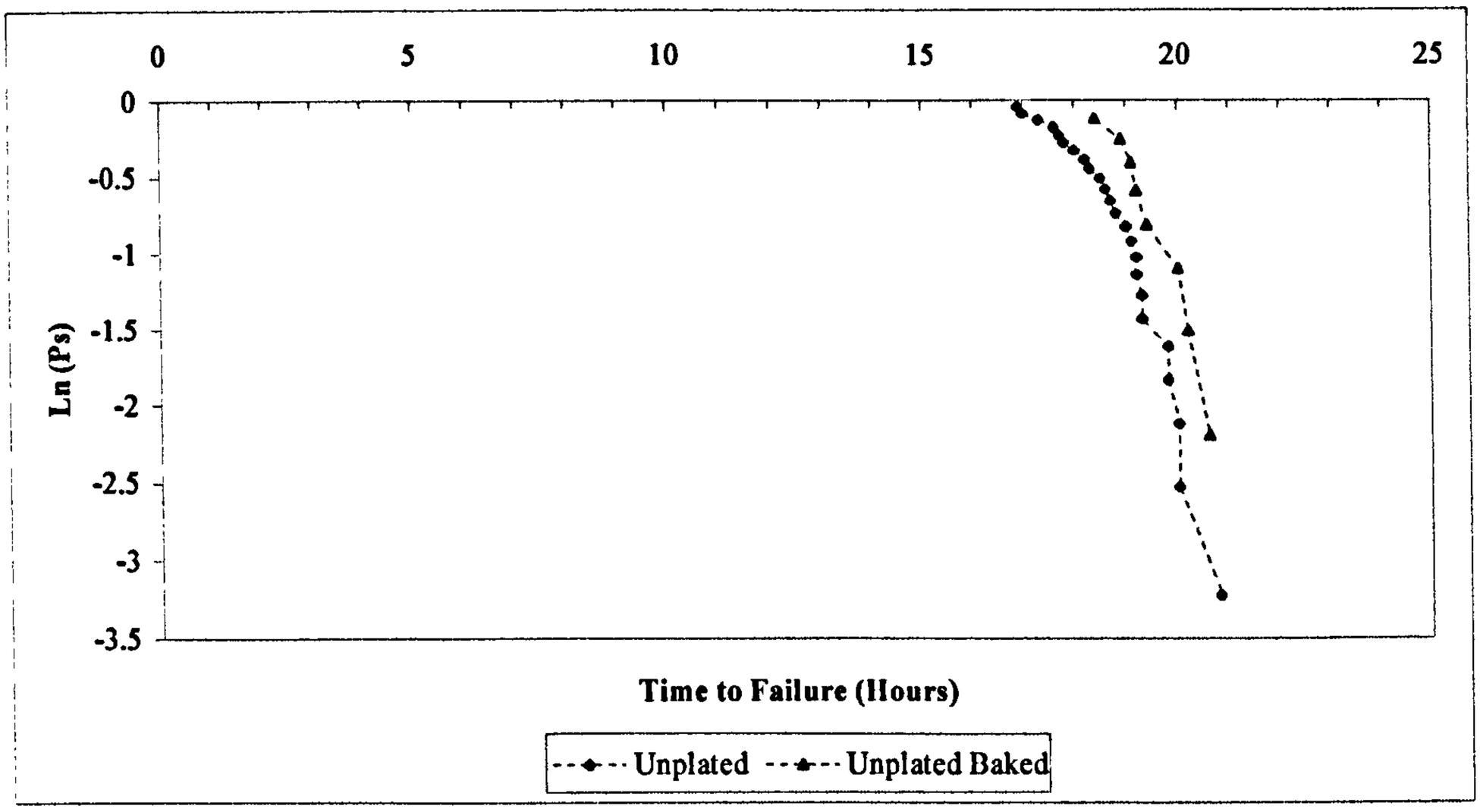


FIGURE 60 shows that the effect of baking unplated specimens before they were tested in air was negligible. The displacement seen in the sets of data was consistent with the displacement that was seen between batches of unplated specimens that had not been baked. Using the student T-test to compare the results obtained, it cannot be said that the specimens belonged to two separate populations with a confidence of 95%. There was no significant effect due to baking the material on the time to failure for the specimens, as shown by the results in TABLE 15. Therefore, all the control specimens were combined and shown as a single line for comparative purposes in all the following Weibull graphs.

TABLE 15: Student T-Test Analysis of Control Data

Baked / Unbaked	DOF	Limit	Result	Accept?
Unplated baked	16	1.746	0.23	Yes

FIGURE 61: Weibull Graph of the Effect of Cadmium Electroplating

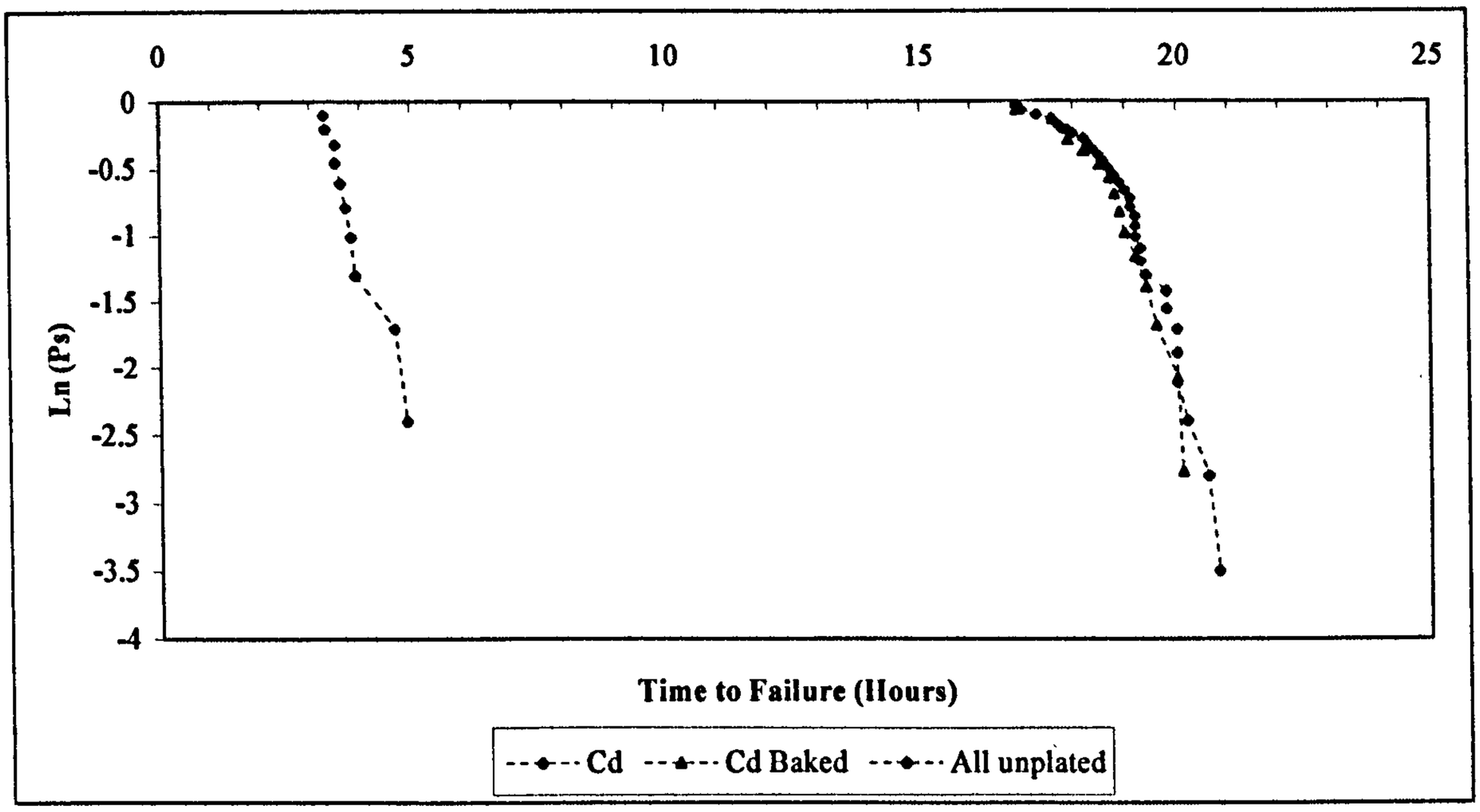


FIGURE 61 illustrates the effect of electroplating the specimens with 8μm of cadmium. The time to failure for these specimens was greatly reduced compared to the controls, illustrating that electroplating the specimens had promoted hydrogen embrittlement of the steel. Specimens that had been plated with 8μm of cadmium and immediately baked at 200°C for a period of 24 hours showed no visible displacement of their line compared with the control specimens. This demonstrated that baking the cadmium specimens had promoted loss of hydrogen from the surface and achieved complete recovery in their time to failure.

FIGURE 62: Weibull Graph of the Effect of Zinc electroplating

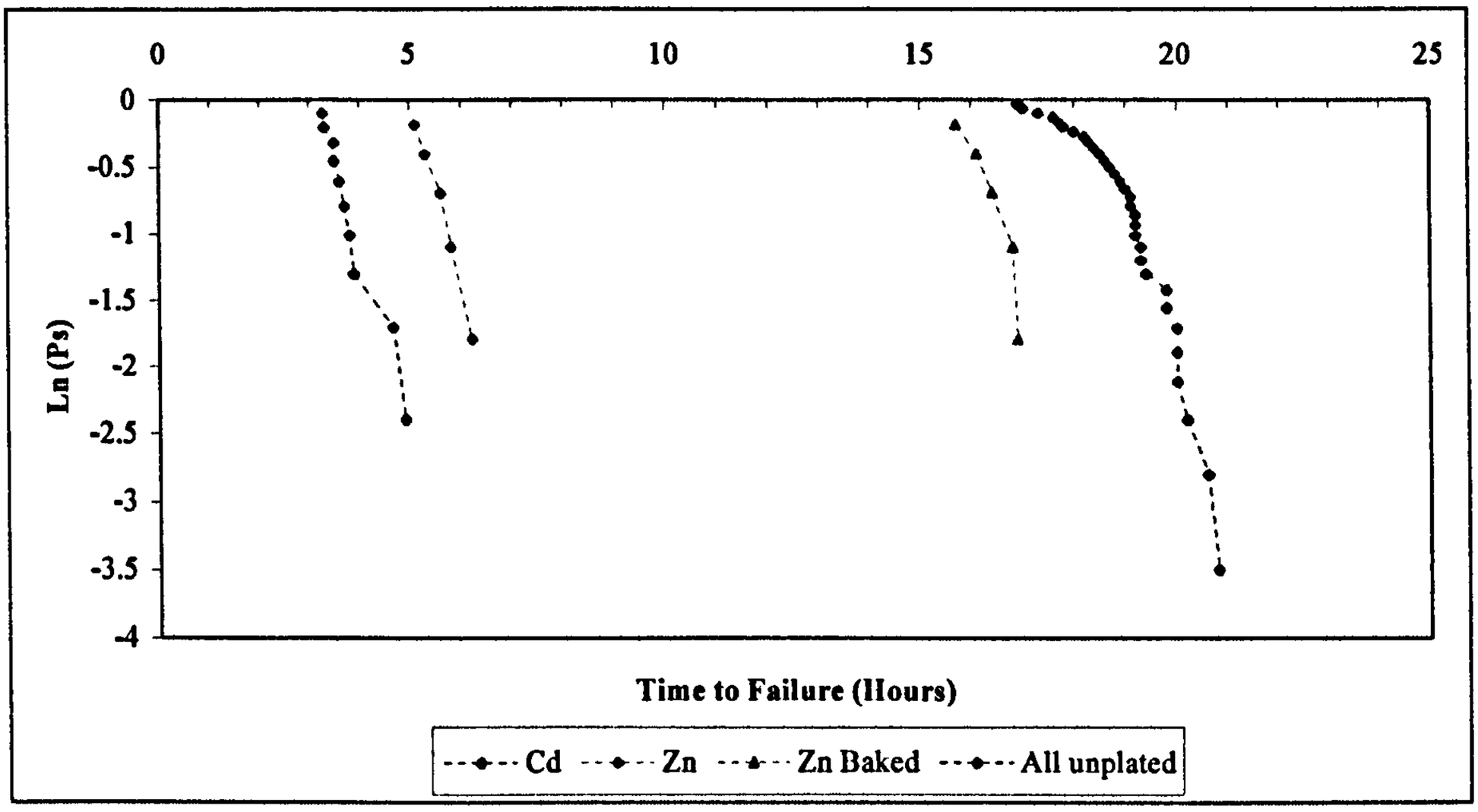


FIGURE 62 shows that the effect of an 8µm zinc electroplated layer on the embrittlement of the specimens was to reduce the time to failure for the specimens when compared to the control specimens. However, compared to the specimens that were electroplated with the same thickness of cadmium, they were clearly less embrittled as they had a longer time to failure. Baking of zinc electroplated specimens at 200°C for 24 hours did not fully recover their time to failure, unlike the cadmium electroplated and baked specimens. There was, however, a significant improvement in the time to failure for the zinc electroplated specimens which had been baked compared to those which were unbaked.

FIGURE 63: Weibull Graph of the Effect of Zinc-Nickel Electroplating

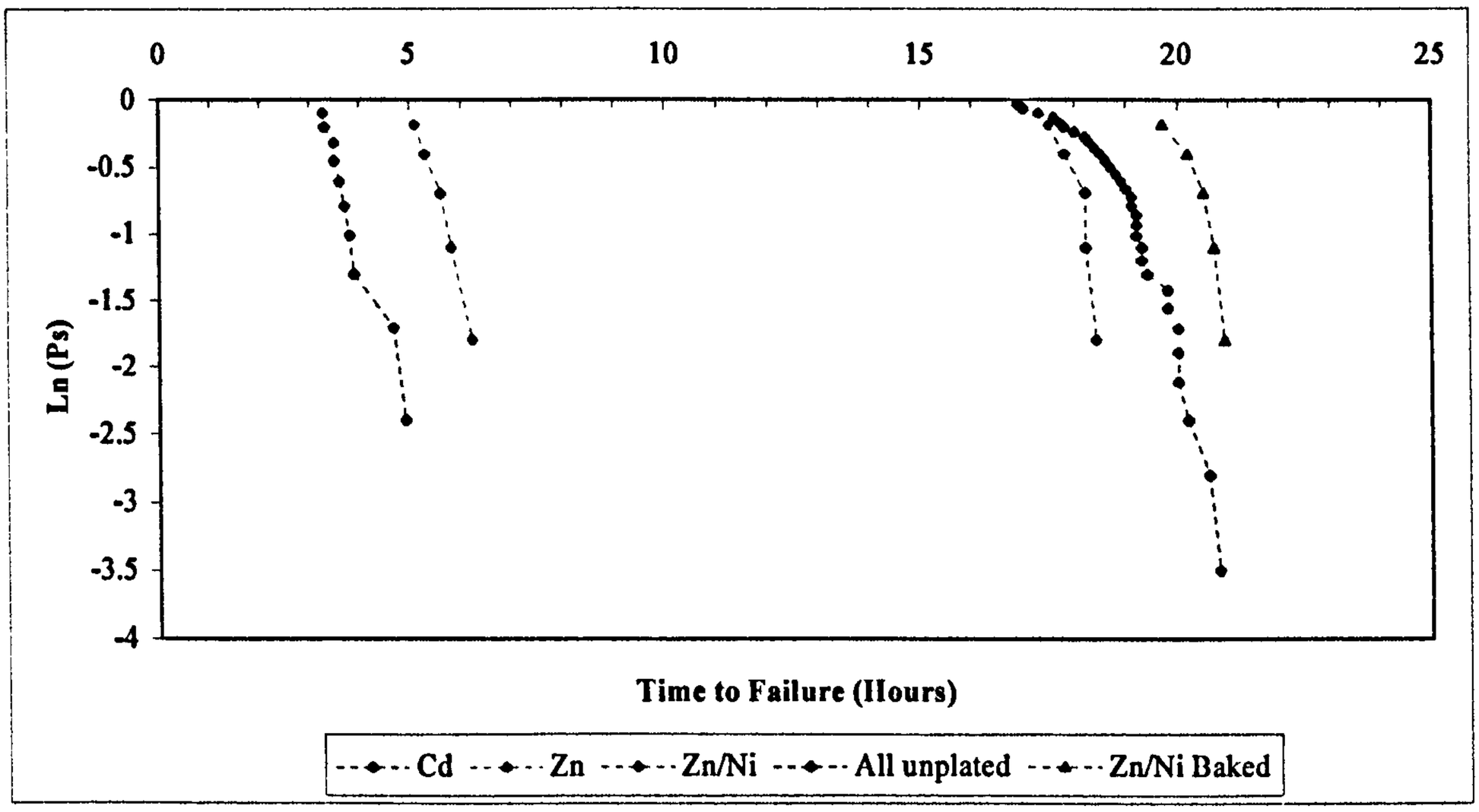


FIGURE 63 shows the effect of zinc-nickel electroplating on the time to failure of the specimens. It can be seen that zinc-nickel electroplating is much less embrittling than either cadmium or zinc electroplating. Like cadmium baked specimens, baking the zinc-nickel specimens at 200°C for 24 hours produces full recovery in their time to failure. Analysis by the Student T-test confirms that the zinc-nickel baked specimens are part of the same normal distribution as the control specimens, as shown in TABLE 16.

TABLE 16: Student T-Test of Zinc-Nickel Data

Specimen/ Control	DOF	Limit	Result	Accept?
Zn/Ni	14	1.761	0.09	Yes
Zn/Ni Baked	14	1.761	0.11	Yes

FIGURE 64: Weibull Graph of the Effect of Zinc-Cobalt Electroplating

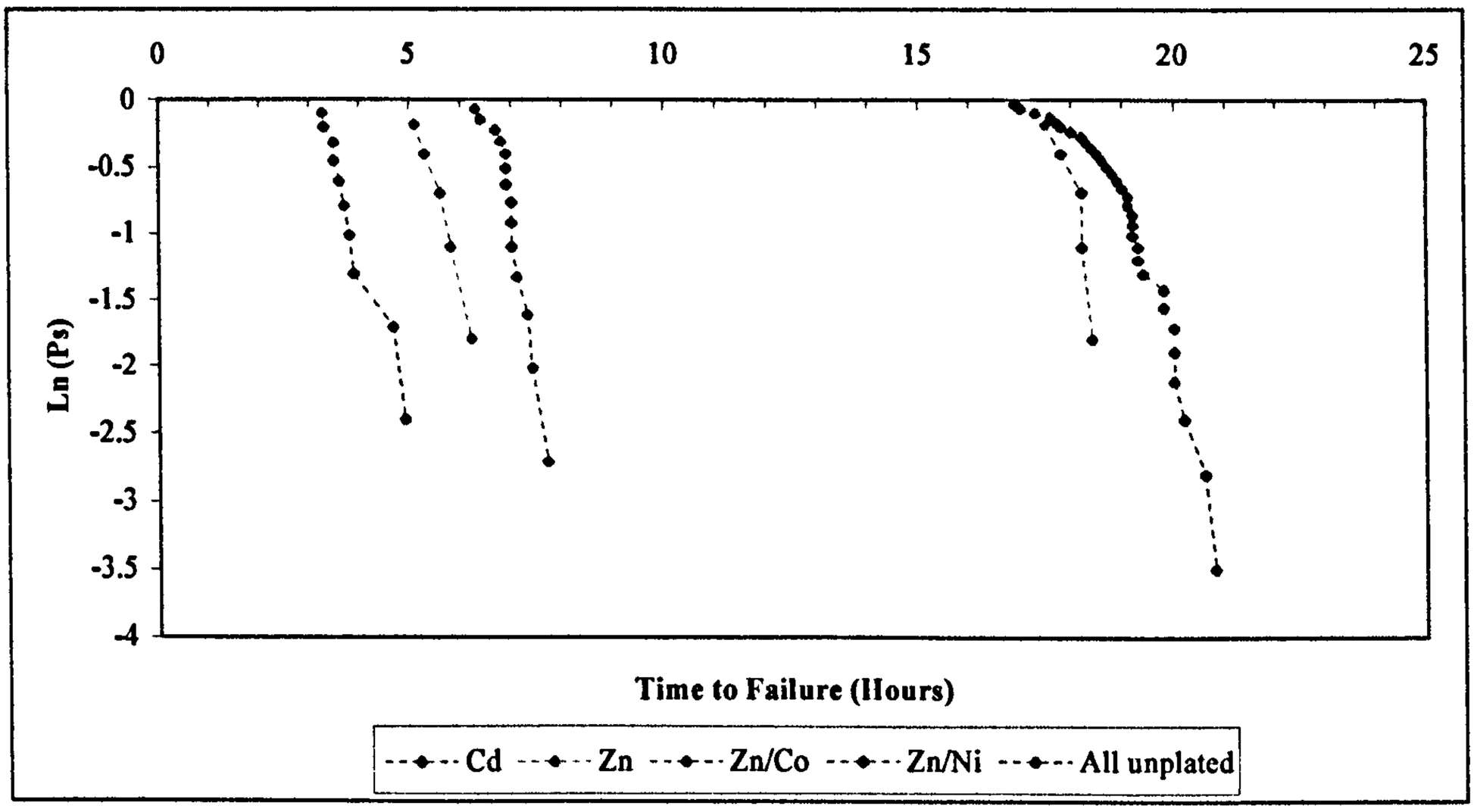


FIGURE 64 shows the effect of 8μm of zinc-cobalt electroplating on the embrittlement of the specimens. Zinc-cobalt electroplating is less embrittling than cadmium and zinc electroplating but more embrittling than zinc-nickel electroplating which had a much longer time to failure.

FIGURE 65: Weibull Graph of the Effect Baking Zinc-Cobalt Plated Specimens

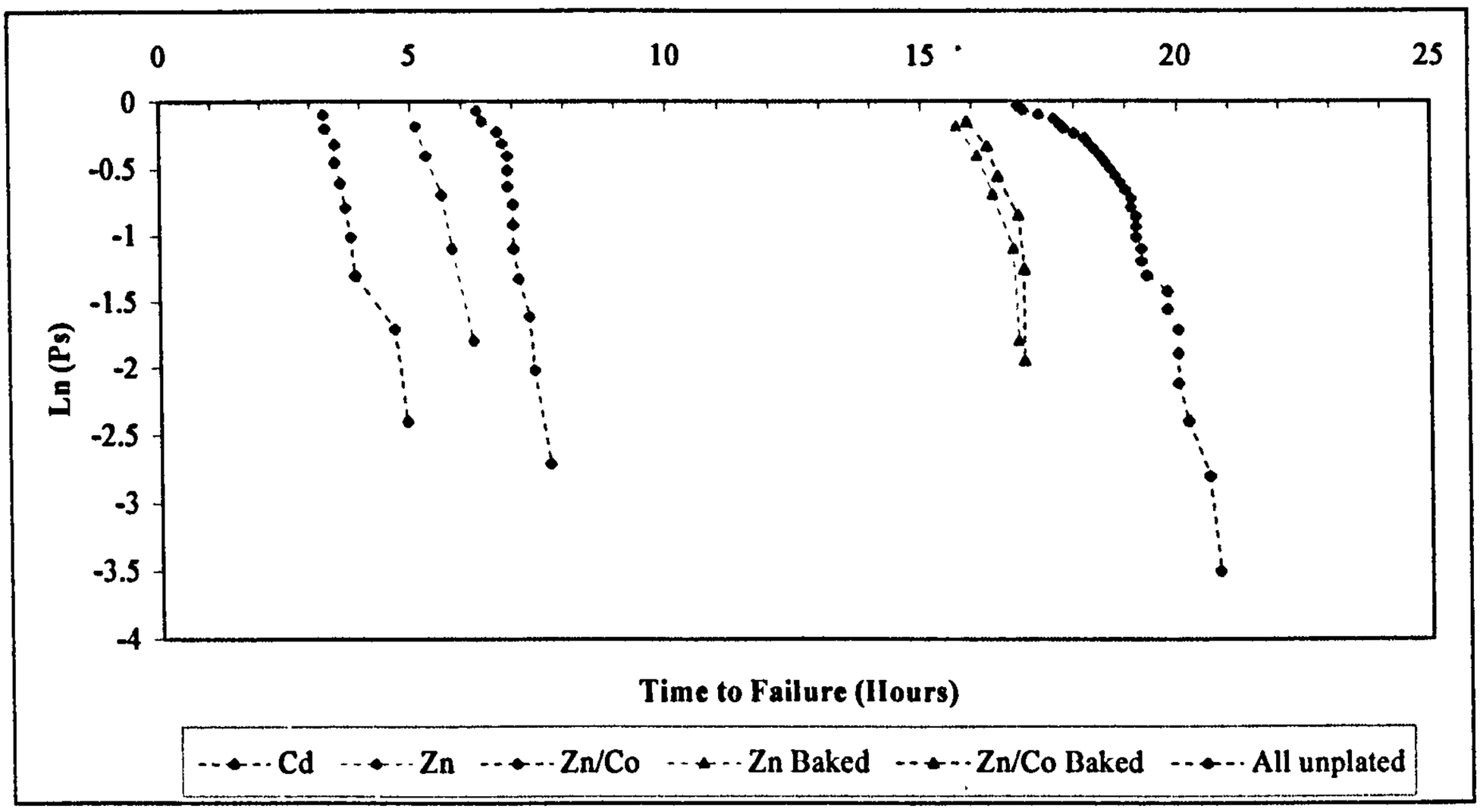


FIGURE 65 shows that baking the zinc-cobalt electroplated specimens at 200°C for 24 hours does not produce complete recovery in time to failure, but it does significantly improve it. However, the zinc-cobalt electroplated and baked specimens and the zinc electroplated and baked specimens have a very similar time to failure. The recovery seen for the zinc specimens after baking was greater than that of the zinc-cobalt specimens, as it started from a lower initial level.

FIGURE 66: Weibull Graph of the Effect of Baking Time on Zinc-Cobalt Specimens

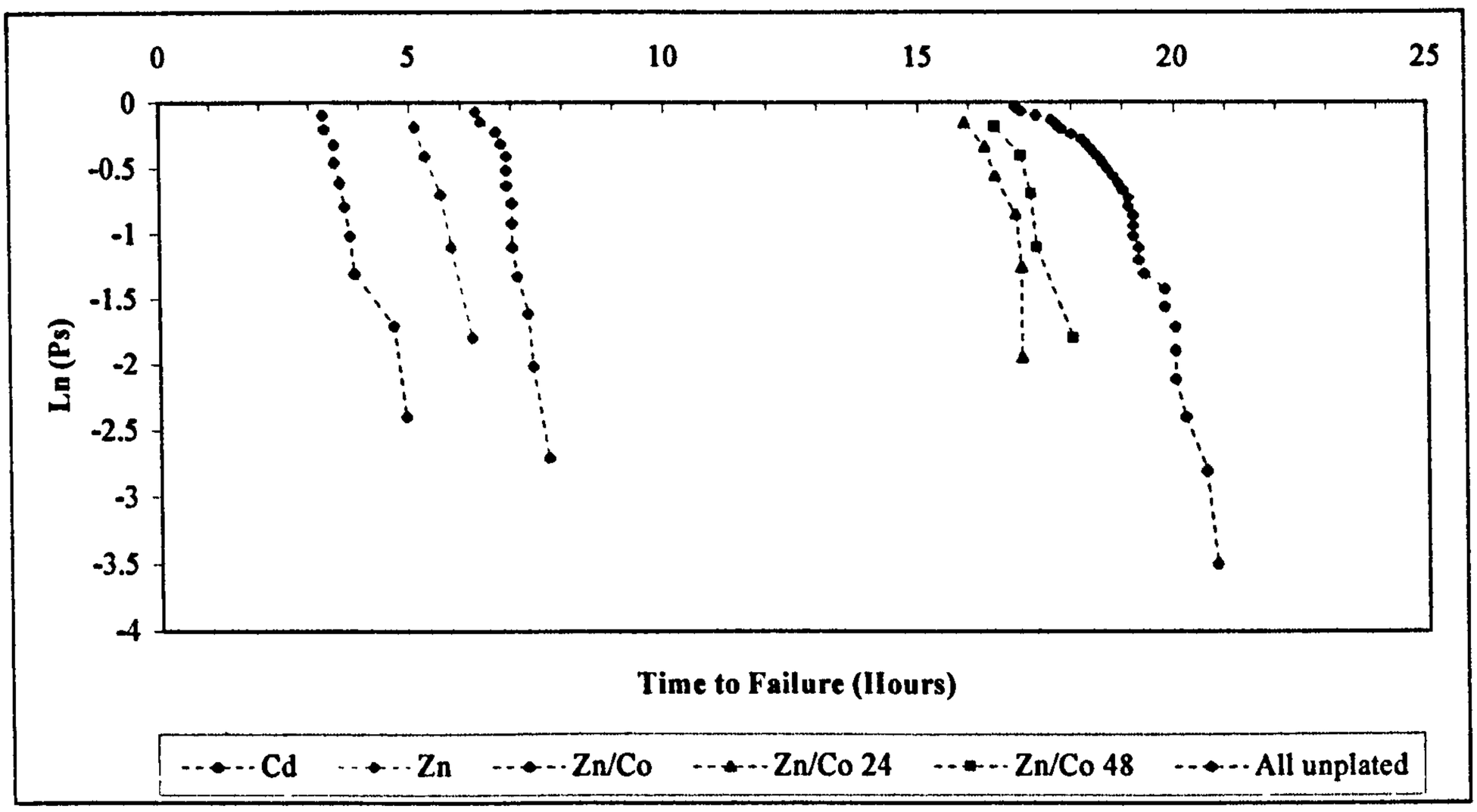


FIGURE 66 shows that an improvement in time to failure can be seen if the specimens that are plated with zinc-cobalt are baked at 200°C for 48 hours. However, they do not regain the full time to failure. Industrially the extra time taken in baking would add significant cost to the process and probably could not be justified for the slight improvement seen.

FIGURE 67: Weibull Graph of the Effect of Delayed Baking on Zinc-Cobalt Plated Specimens

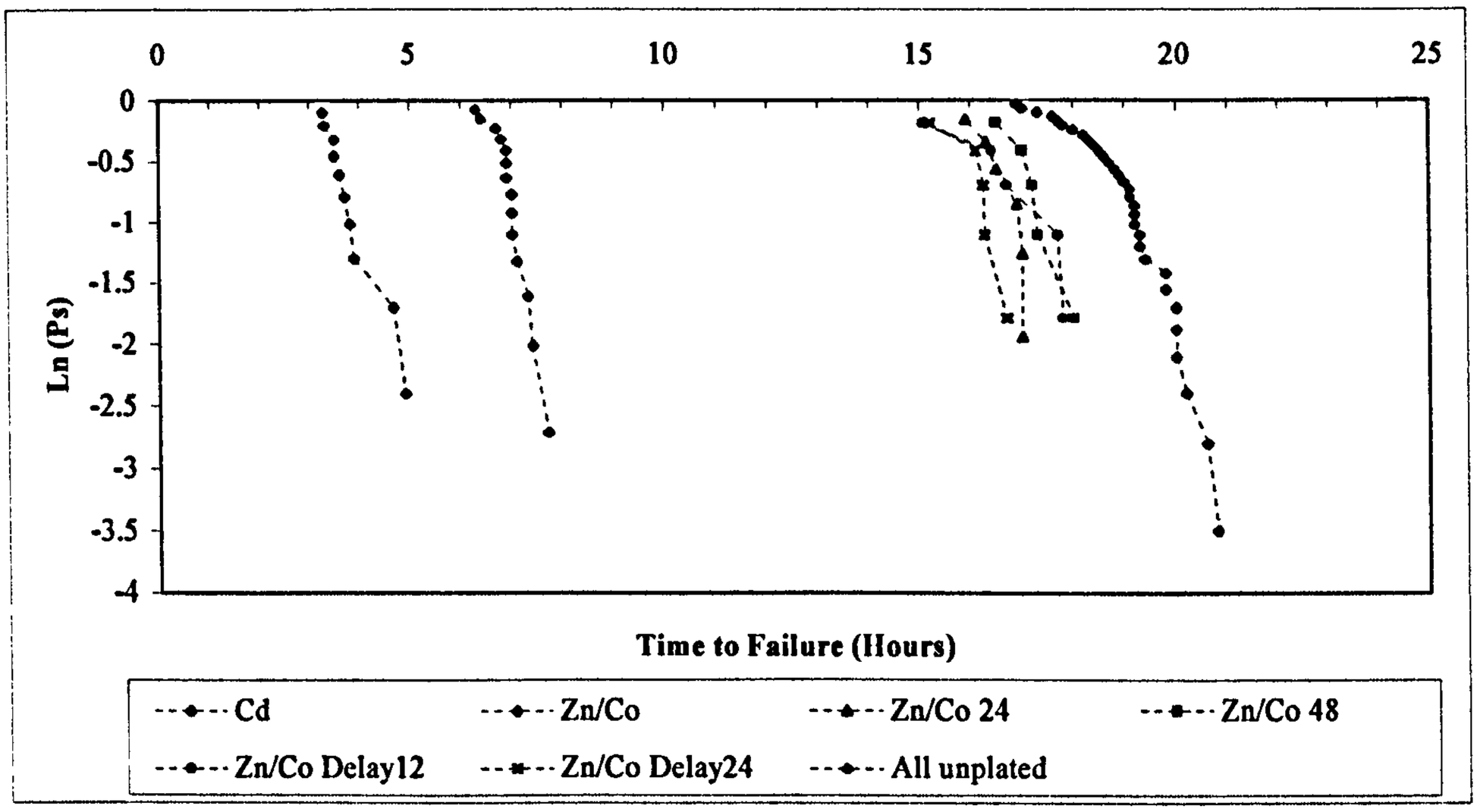


FIGURE 67 shows a delay of 24 hours before baking zinc-cobalt specimens once they have been electroplated is deleterious. A delay of 12 hours seems to slightly improve the time to failure for the specimens, compared to those that are baked with no delay. This improvement was not as good as the recovery in time to failure noted for those specimens that were baked for 48 hours. A larger spread in experimental results was observed than for other groups examined, this was expected as the specimens had undergone an increased number of processes. Each process undertaken introduced the probability of a further specimen variation.

FIGURE 68: Weibull Graph of the Effect of Electrolyte pH on Zinc-Cobalt Plating

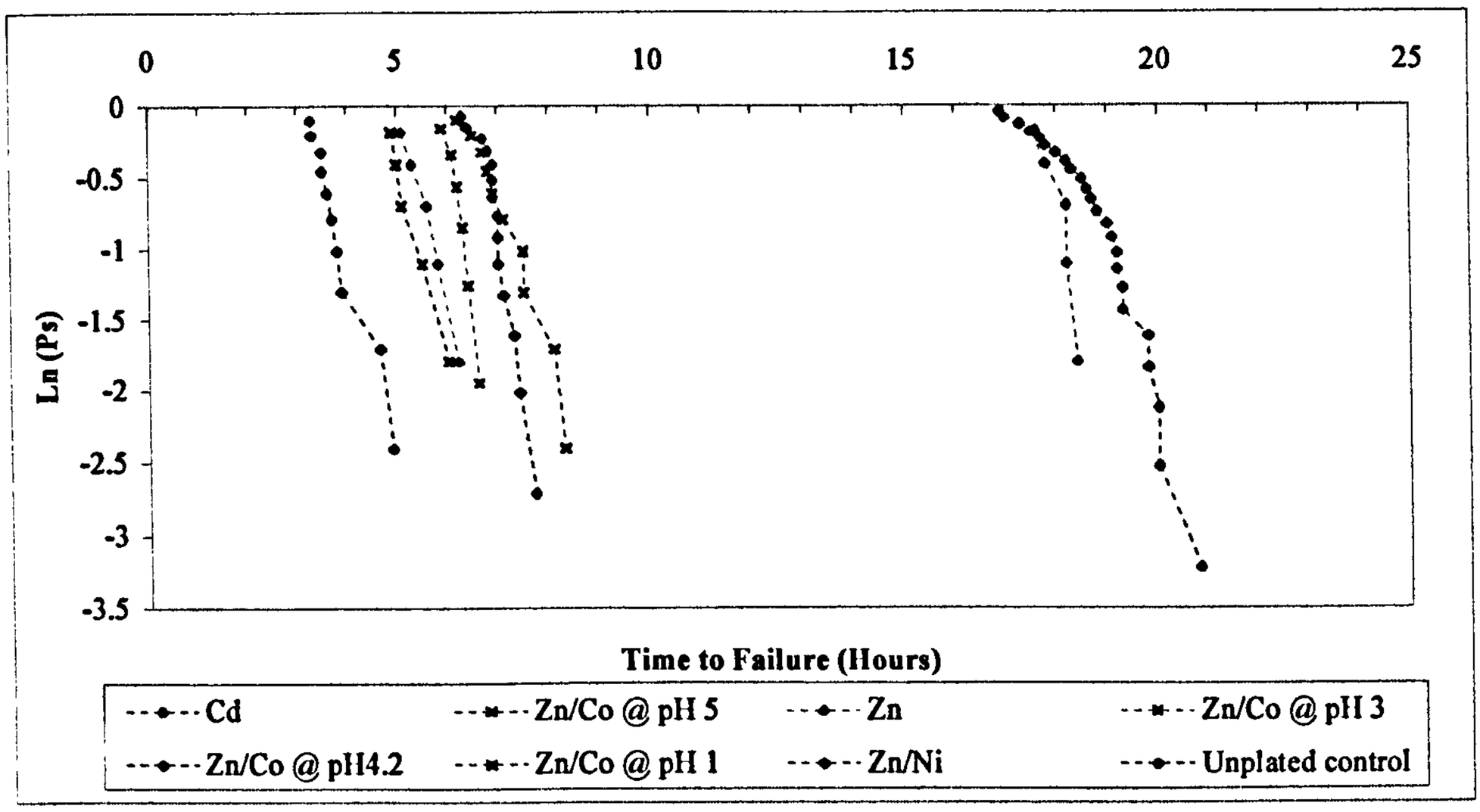


FIGURE 68 shows the effect of changing the pH of the zinc-cobalt electrolyte. The electrolyte at pH1 produced the least embrittled specimens contrary to initial expectations, while pH5 produced specimens that were more embrittled than zinc electroplated specimens. An intermediate pH of 3 was more embrittling than pH4.2 (the standard bath pH) but less embrittling than either zinc plating or zinc-cobalt plating at pH5. All the specimens that were plated with zinc-cobalt were less embrittled than those specimens that were plated with cadmium.

FIGURE 69: Weibull Graph of Unbaked and Baked Zinc-Cobalt-Iron Specimens

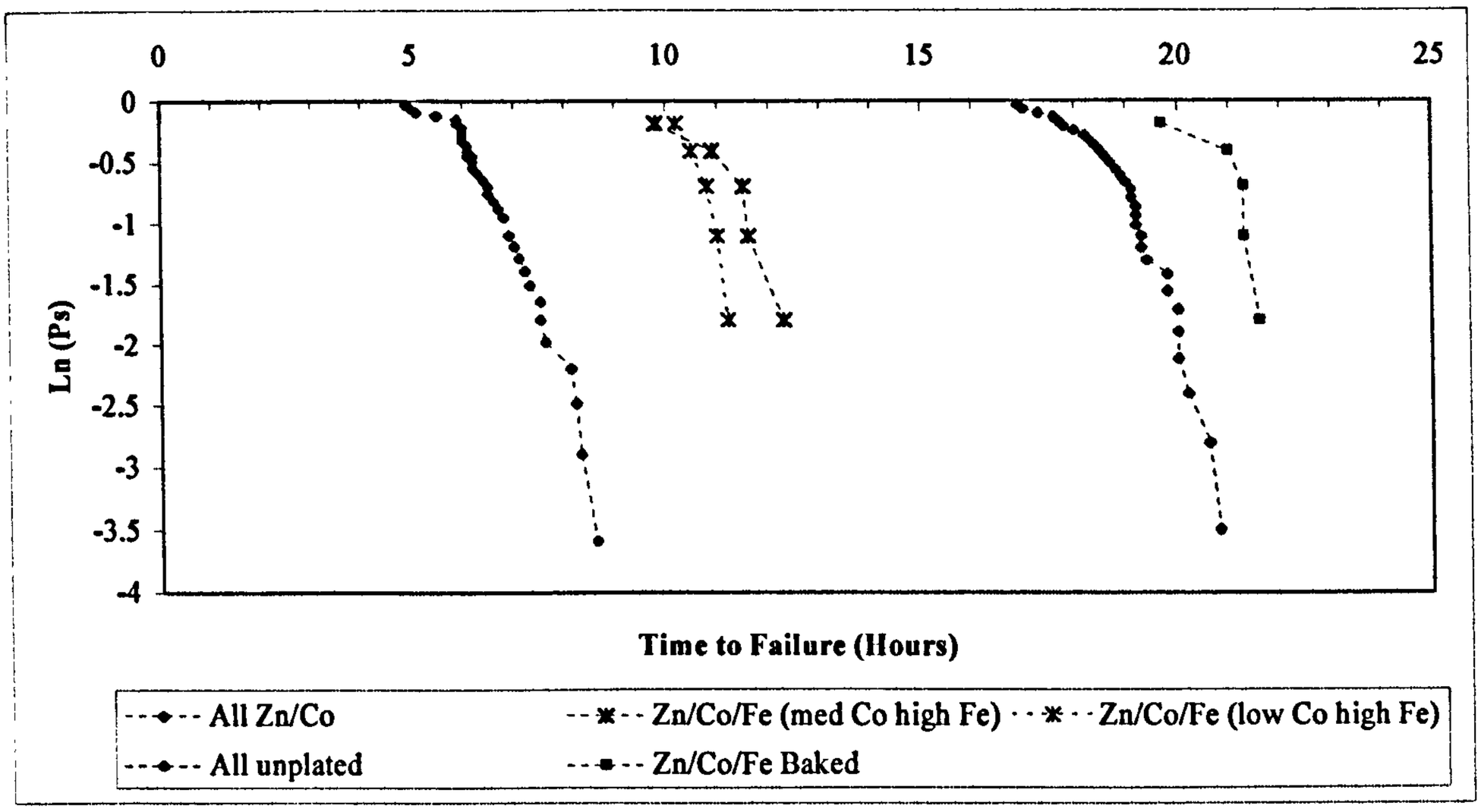


FIGURE 69 shows an improvement in time to failure for zinc-cobalt-iron electroplating compared to binary zinc-cobalt indicating a reduction in specimen embrittlement. The 2 ternary electroplating baths used were based on an acid sulphate bath, like the zinc-cobalt bath, but the ternary baths and deposits contained a much higher percentage of cobalt compared to binary baths, as well as iron of course. The ternary specimens when baked for 24 hours at 200°C fully regained their time to failure compared to control specimens. The Student T-test was successfully used to prove that the ternary baked specimens were part of the same distribution as the control specimens, as shown in TABLE 17.

TABLE 17: Student T-Test of Zinc-Cobalt-Iron Baked Data

Specimen/ Control	DOF	Limit	Result	Accept?
Zn-Co-Fe Baked	30	1.697	0.12	Yes

FIGURE 70: Weibull Graph of the Effect of an Interlayer on DBT Zinc Plated Specimens

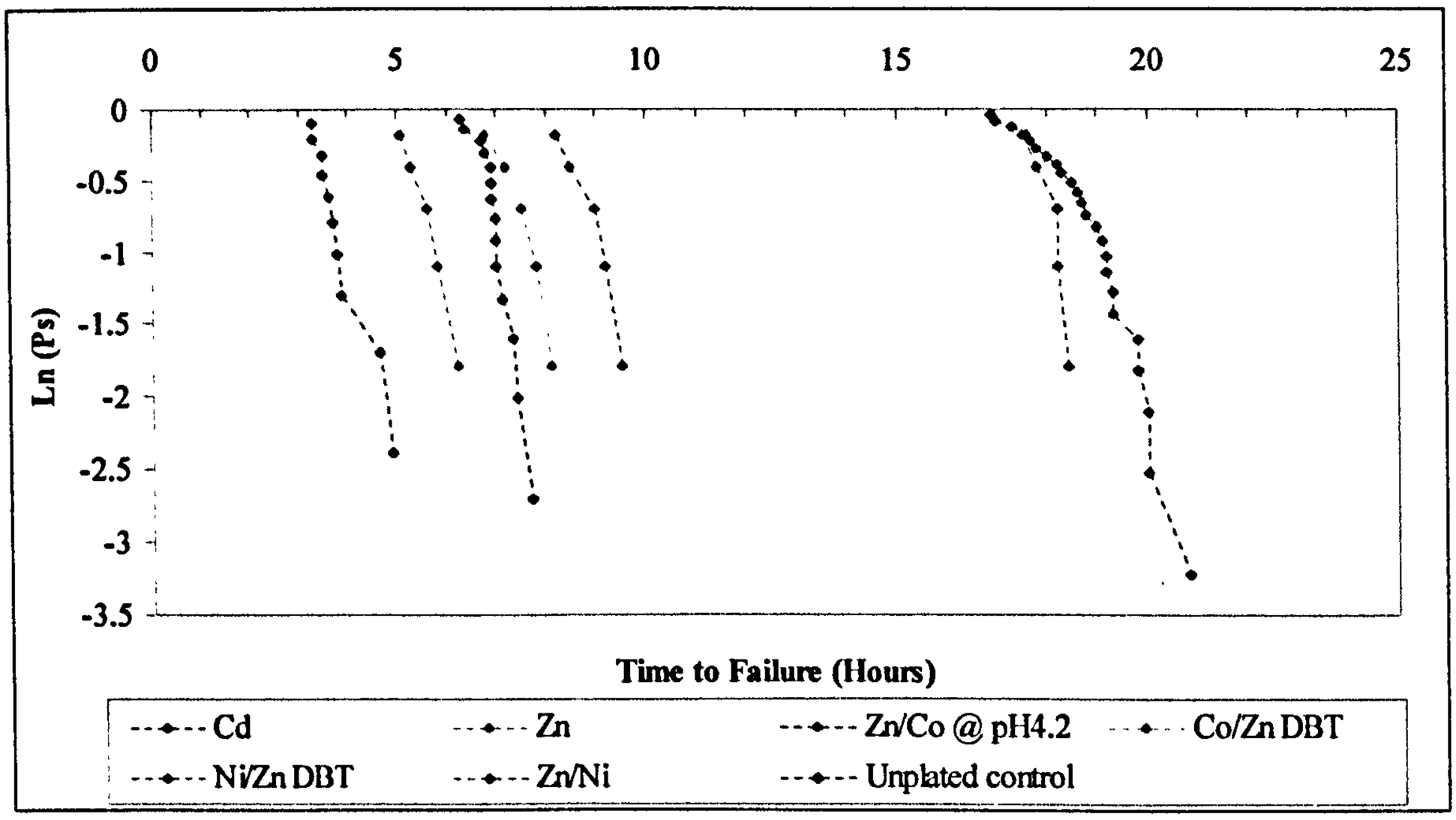


FIGURE 70 shows the effect of plating zinc over an interlayer of either cobalt or nickel. For both cases there was an improvement in time to failure for the specimens that were prepared in this way. There was a greater improvement observed in those specimens that had an interlayer of nickel electroplated before the zinc coating was plated over the top. However, the nickel / zinc DBT coating is much more embrittled than the zinc-nickel single layer plating system. The specimens that were plated with cobalt / zinc also seem to be less embrittled than those specimens that are plated with zinc-cobalt at the standard pH4.2.

FIGURE 71: Weibull Graph of the Effect of an Interlayer on DBT Zinc-Cobalt Plated Specimens

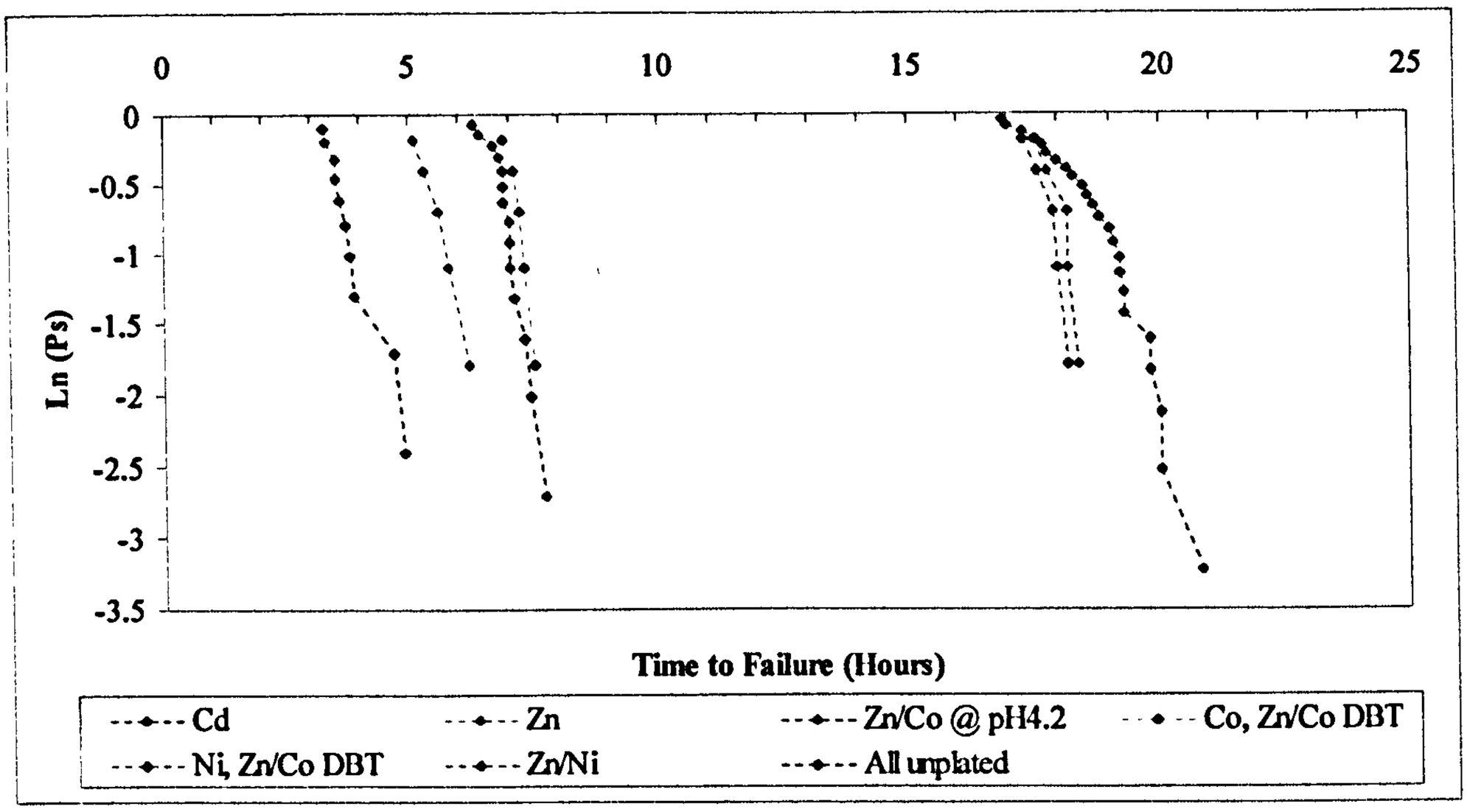


FIGURE 71 shows the effect of an interlayer of cobalt or nickel on zinc-cobalt plated specimens. There was an improvement observed for those specimens that have an interlayer of nickel plate before zinc-cobalt plating over the top. The time to failure is comparable to those specimens that were plated with zinc-nickel alone, which is in turn, comparable to unplated control specimens. However, there was not much difference observed in the time to failure for a cobalt/ zinc-cobalt DBT specimen compared to those specimens electroplated with zinc-cobalt alone. The Student T-test was used to determine whether or not each type of interlayered deposit was part of the same distribution as either zinc-cobalt or zinc-nickel electroplating alone, the results are shown in TABLE 18.

TABLE 18: Student T-Test DBT and Own Alloy Data

Specimen	DOF	Limit	Result	Accept?
Co,Zn-Co DBT/ Zn/Co	31	1.697	0.05	Yes
Ni,Zn-Ni DBT/ Zn/Ni	8	1.860	0.10	Yes

FIGURE 72: Weibull Graph of the Effect of an Interlayer on DBT Zinc-Nickel Plated Specimens

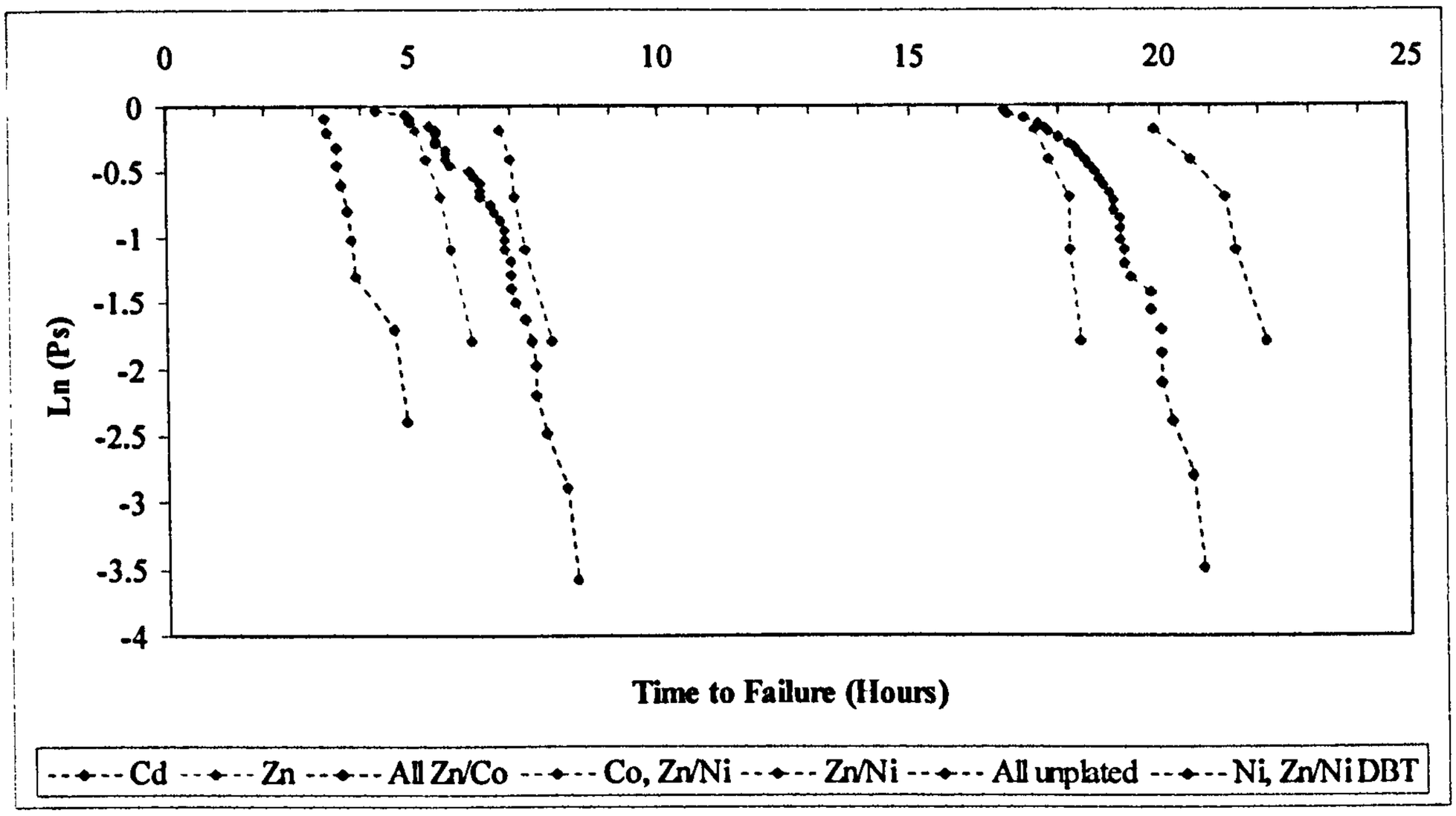


FIGURE 72 shows the effect of an interlayer of cobalt or nickel with zinc-nickel plating on the time to failure of the specimens. There is no significant difference observed for a cobalt / zinc-nickel DBT specimen compared to a normal zinc-cobalt plated specimen. An interlayer of nickel does however, improve the time to failure for zinc-nickel plating further, producing full recovery compared to control specimens. The Student T-test was used to show that the interlayered coatings were part of the same distribution as either the zinc-cobalt or zinc-nickel, as shown in TABLE 19.

TABLE 19: Student T-Test of DBT Zinc-Nickel Data

Specimen	DOF	Limit	Result	Accept?
Zn-Co/ Co, Zn/Ni	31	1.697	0.17	Yes
Zn-Ni/ Ni, Zn/Ni	7	1.895	0.24	Yes

FIGURE 73: Weibull Graph of the Effect of Baking DBT Cobalt/ Nickel then Zinc-Cobalt Plated Specimens

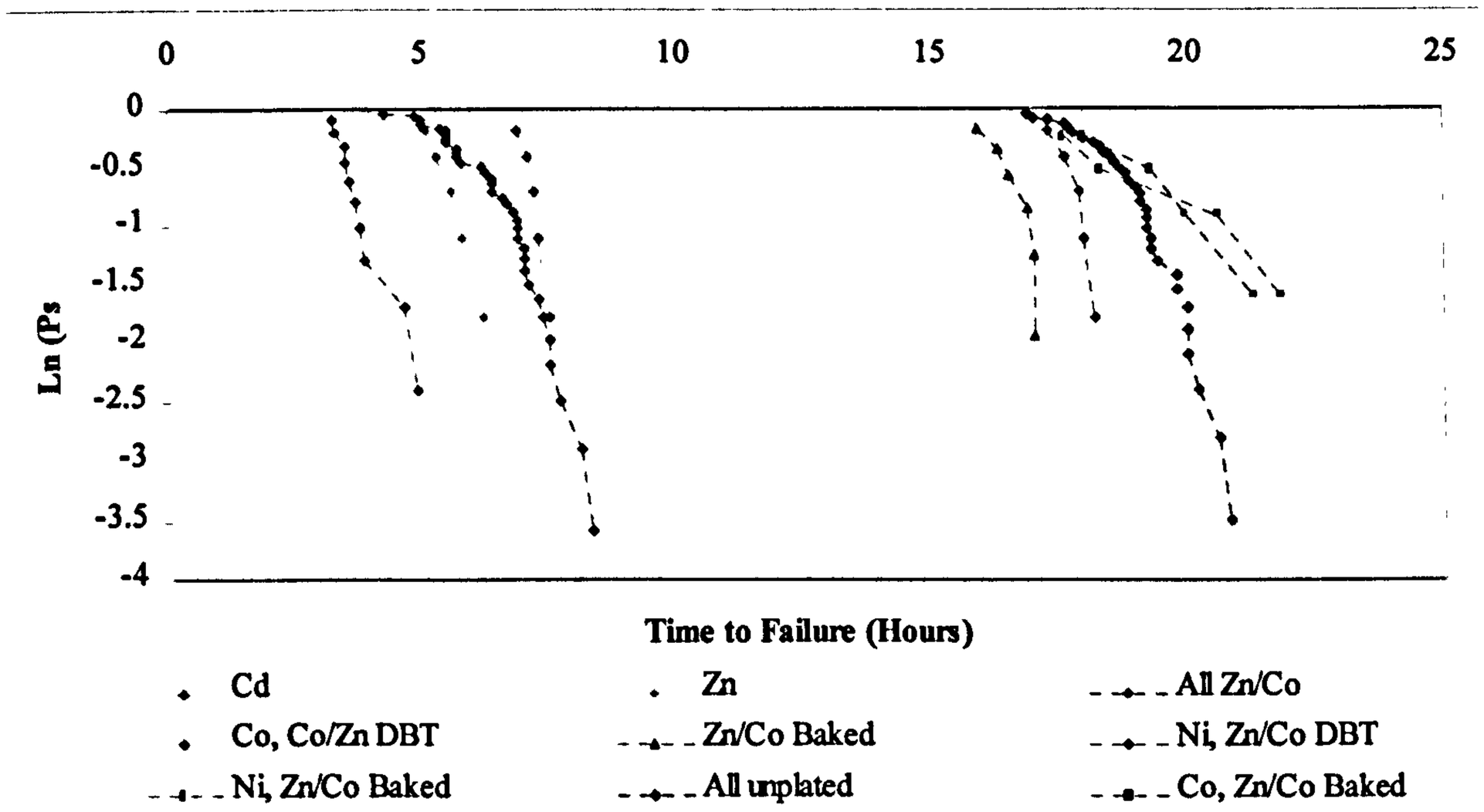


FIGURE 73 shows the effect of standard baking of the specimens which were plated with either cobalt, or nickel followed by zinc-cobalt electroplating was to produce full recovery of the specimens compared to the control specimens. (The more non-linear behaviour probably results from the assumption that $\beta=1$ is no longer valid for this distrubution, see appendices and reference 25 for further details). The Student T-test results, given in TABLE 20, illustrated that they were part of the same population with a confidence level of 95%.

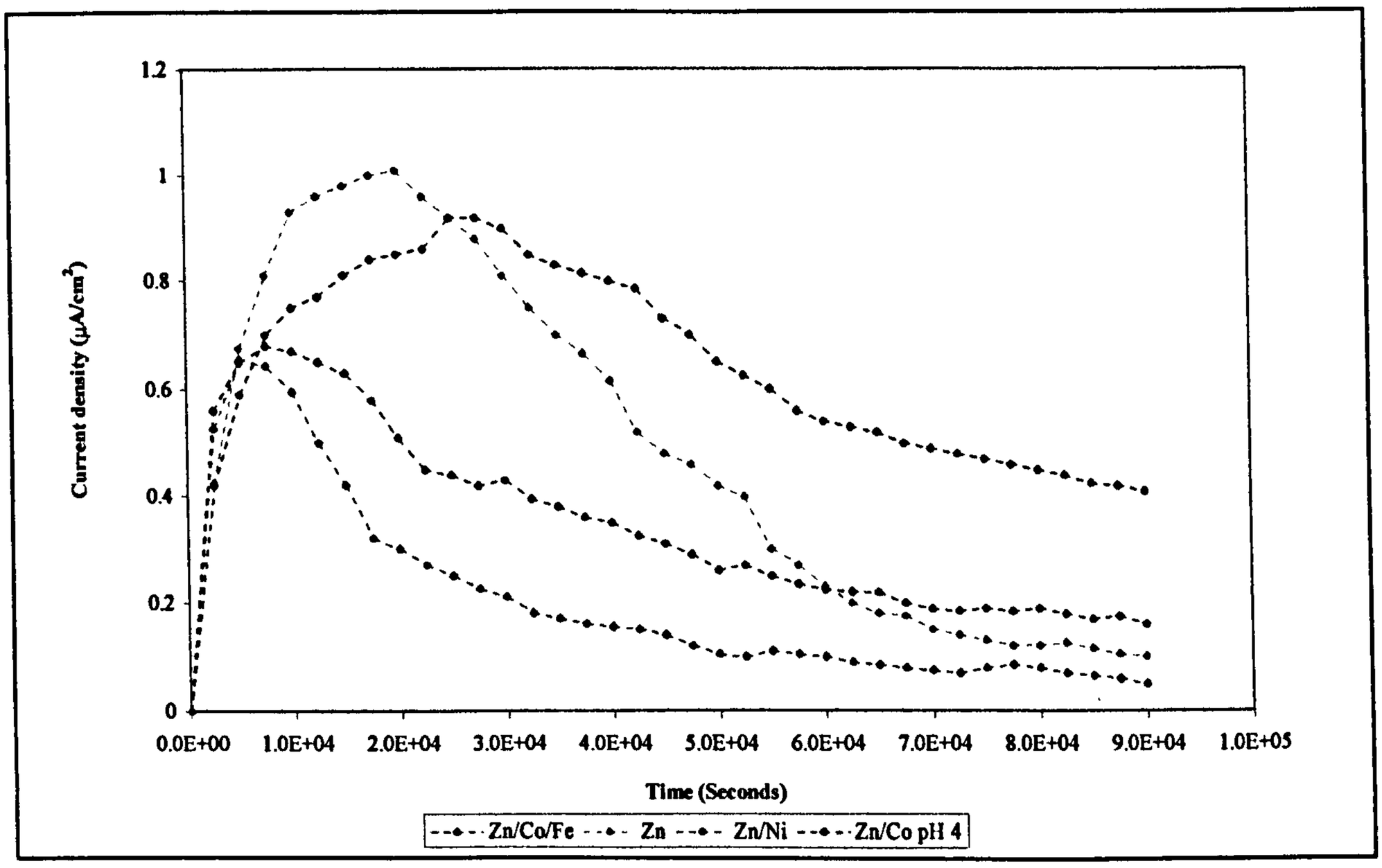
TABLE 20: Student T-Test of DBT Zinc-Cobalt Data

Specimen/Control	DOF	Limit	Result	Accept?
Co, Zn/Co	14	1.761	0.33	Yes
Ni, Zn/Co	14	1.761	0.33	Yes

PERMEATION TESTING

FIGURE 74 shows the permeation transients that were produced for the different electrolytes tested in this work. The transients that were produced for each of the electrodeposit types differ but all have a peak current density, rather than a plateau region, which was seen by Devanathan and Stahurski [39]. The zinc-nickel transients obtained in this work are in good agreement with those obtained by Carr, in terms of both the shape and the peak current density values [18].

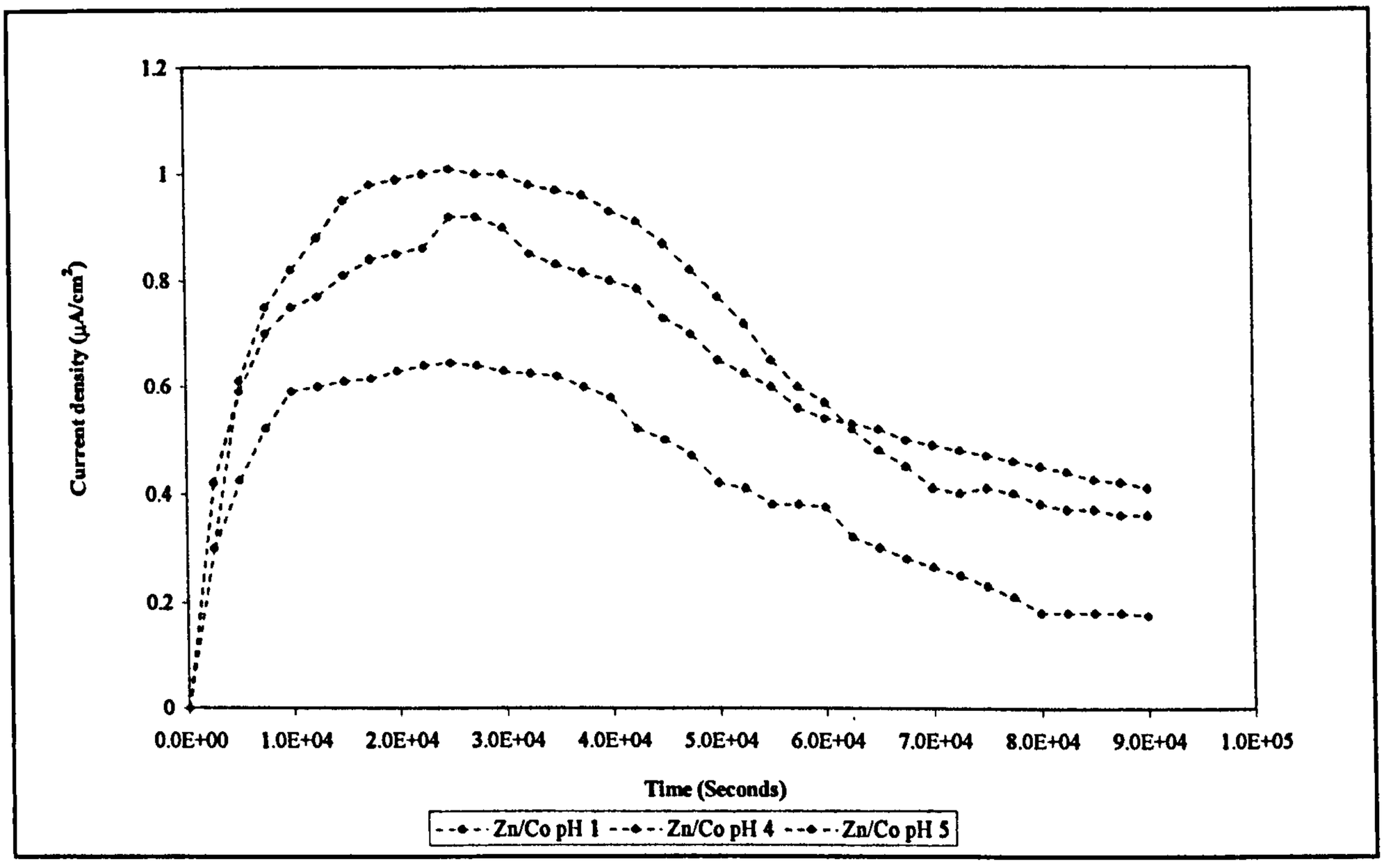
FIGURE 74: Permeation Transients for All the Types of Electrolyte Used



If the height of the transient alone were used to illustrate the embrittlement factor, the order of the most embrittling electrolyte tested was: pure zinc, zinc-cobalt, zinc-cobalt-iron and finally zinc-nickel. Despite these results agreeing with the mechanical testing results that have already been shown, zinc had the shortest time to failure and highest peak current, this method is an over simplification. It does not account for the shape of the curves that are seen, or the effect of other variables such as temperature or pH. A correct ranking method that compares the total quantity of hydrogen passed into the substrate will be used and discussed fully in Chapter 4.

The parameter variation investigations illustrated that change in electrolyte pH can have a dramatic effect on the electrodeposit that is formed. This effect can also lead to changes in the observed embrittlement behavior for the mechanical testing specimens. It is therefore not surprising that a change in the zinc-cobalt electrolyte pH has a marked effect on the height of the transient produced for the specimens, as seen in FIGURE 75.

FIGURE 75: Permeation Transients for Variation in pH of the Zinc-Cobalt Electrolyte



The pH1 electrolyte has a lower height transient than a standard pH4.2 transient and an electrolyte of pH5 gives a higher transient than both which confirm the mechanical testing findings. A specimen electroplated with a pH1 zinc-cobalt electrolyte had a longer time to failure than a standard pH4.2 specimen, which was in turn longer than a pH5 electroplated specimen.

FIGURE 76: Permeation Transients for All the Types of Electrolyte Used

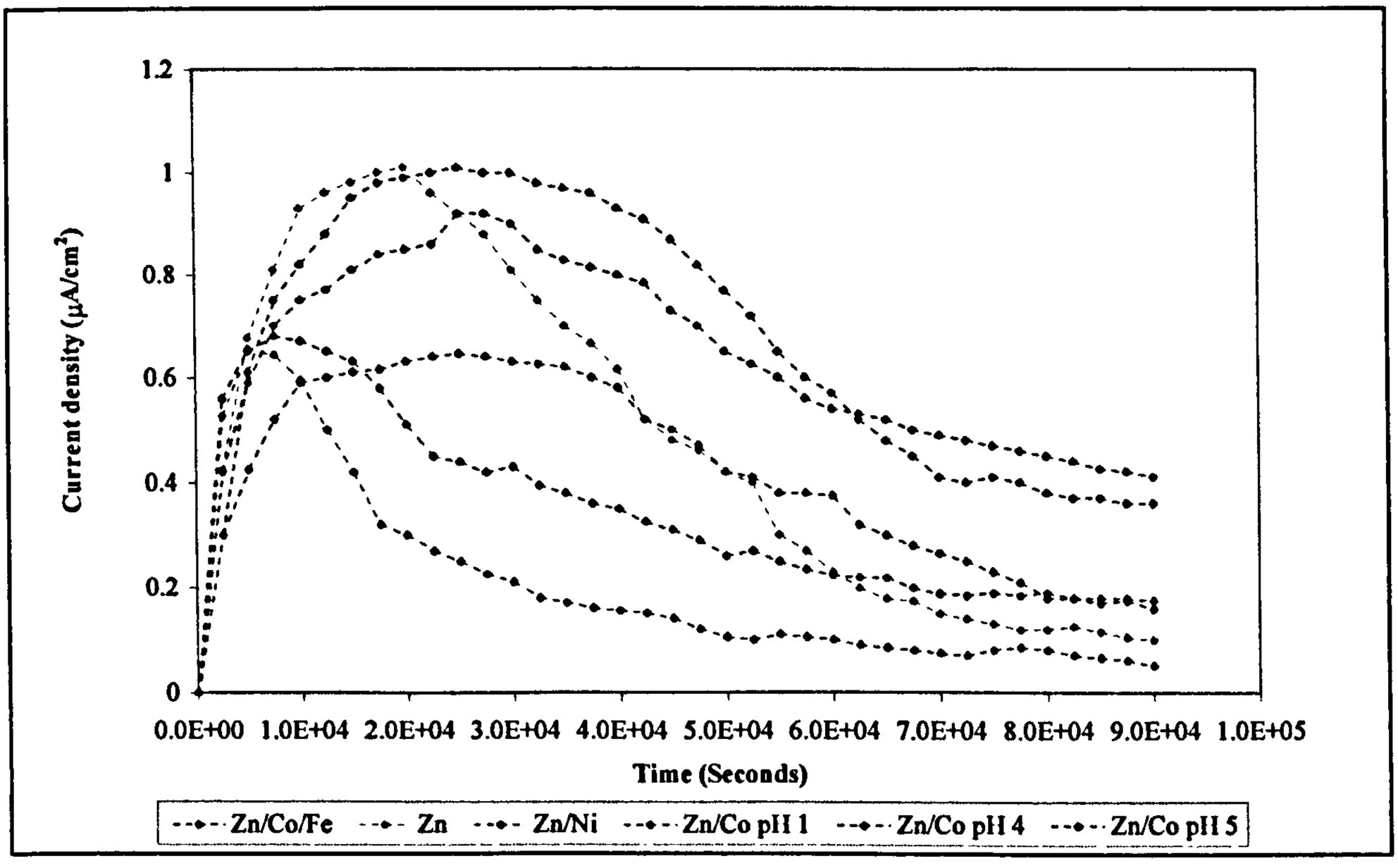
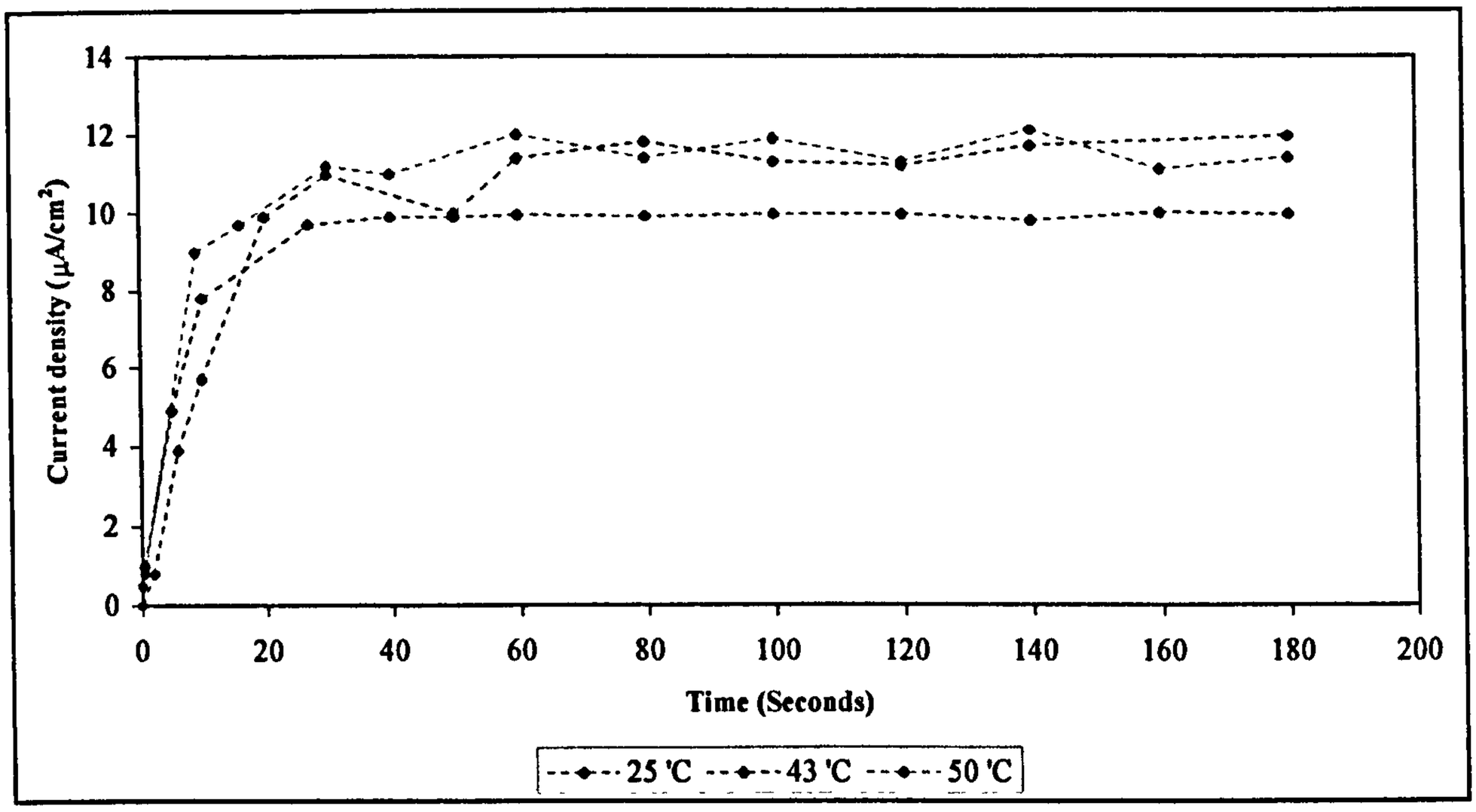


FIGURE 76 compares the transients of all the electrolytes that were tested with the transients produced for zinc-cobalt electroplating performed at different pH values. The height of the zinc transient is almost equal to that of zinc-cobalt electroplating performed at pH5. It can also be seen that the height of the transient for zinc-cobalt electroplating at pH1 is slightly lower than both zinc-cobalt-iron and zinc-nickel electroplating, which both demonstrate improved embrittlement effects compared to any zinc-cobalt electroplating.

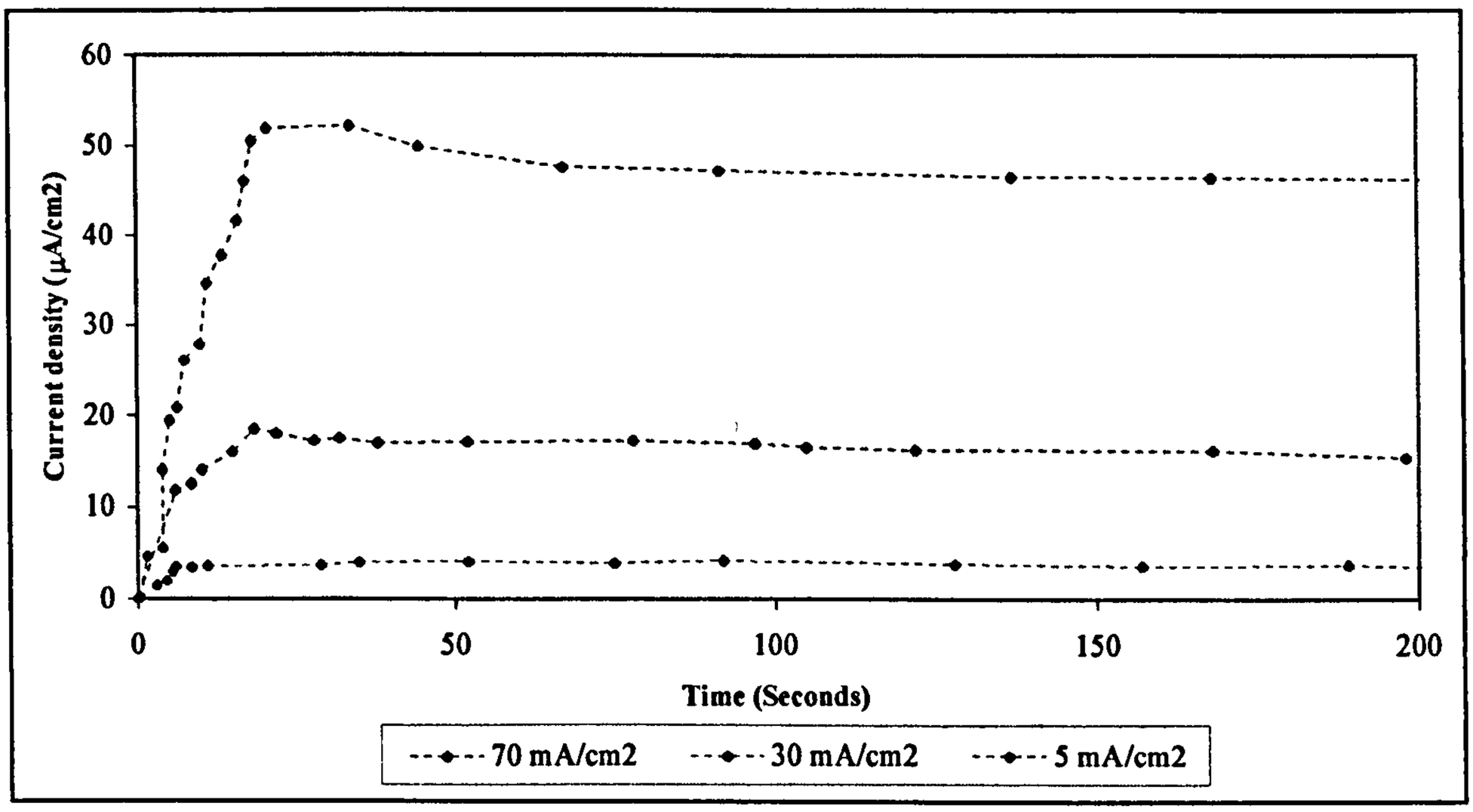
The effects of temperature and current density on hydrogen permeation were also examined. These experiments were performed using a sodium hydroxide charging cell as described in Chapter 2.

FIGURE 77: Permeation Transients Formed at Different Charging Temperatures



An unplated shim was charged at different temperatures and the general effect was to increase the height of the transient with increasing temperature as shown in FIGURE 77. However, the degree to which this happened was unexpectedly small and will be discussed in Chapter 4. These results were used to calculate a temperature factor that could be used to compare transients that were produced at different temperatures. This is a distinct advantage as heating the electrolytes may cause different electrodeposits to be formed due to conductivity, or solubility effects. These calculations will be discussed further in Chapter 4.

FIGURE 78: Permeation Transients from Charging a Cobalt Plated Steel Shim



A steel shim electroplated with a layer of cobalt was charged at different current densities in sodium hydroxide solution, to allow the diffusion coefficient for cobalt to be estimated. The expected increase in height of the transient is produced with a higher charging current density was observed and the pronounced effect is shown in FIGURE 78. Calculation of the diffusion coefficient for cobalt is discussed in Chapter 4.

HYDROGEN DETECTION BY DECORATION TECHNIQUE

The first experiments carried out were to establish if the hydrogen microprint technique produced a real effect or if there was a reaction between the coatings and the emulsion without the presence of hydrogen. Electroplated zinc-cobalt, zinc-nickel and zinc-cobalt-iron specimens were polished and then treated with the emulsion. Specimens, which had been previously electroplated and then baked to remove the hydrogen from the coating, were also prepared and treated.

FIGURE 79 demonstrates that a specimen that had been baked to remove hydrogen showed no reaction with the silver emulsion. Therefore, the effect seen with unbaked specimens, was a reaction between the emulsion and hydrogen that was present and not a chemical reaction with any of the metal coatings. FIGURE 80, shows the presence of discrete silver particles on the surface of a treated specimen.

FIGURE 79: Baked Zinc-Cobalt Coating Treated with HMT Emulsion

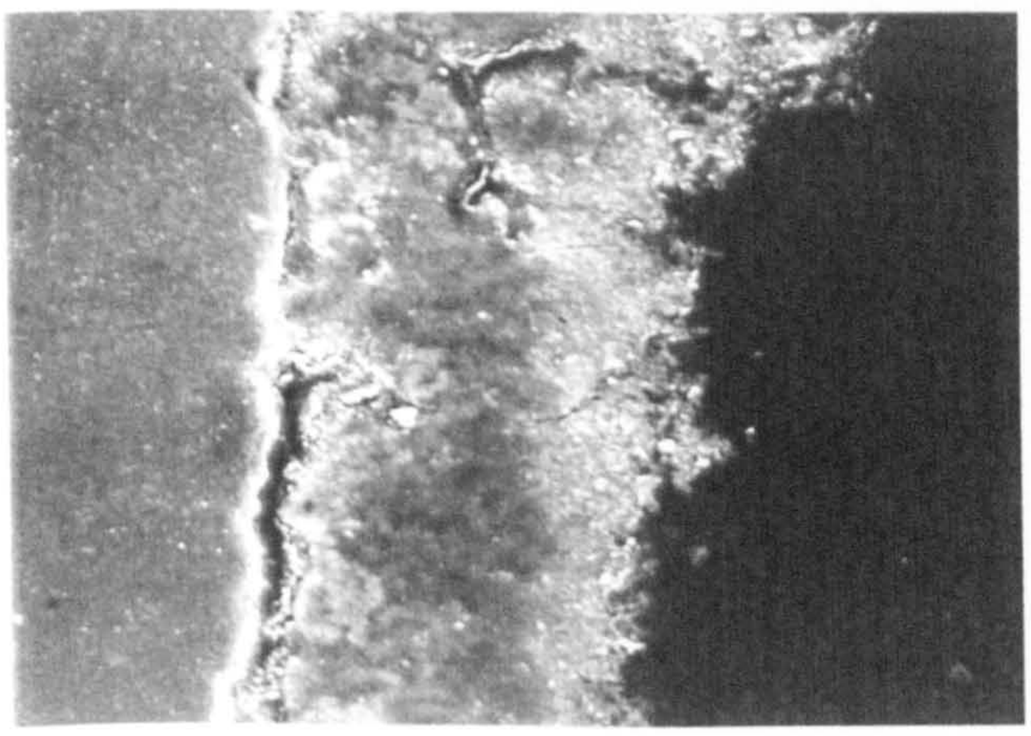
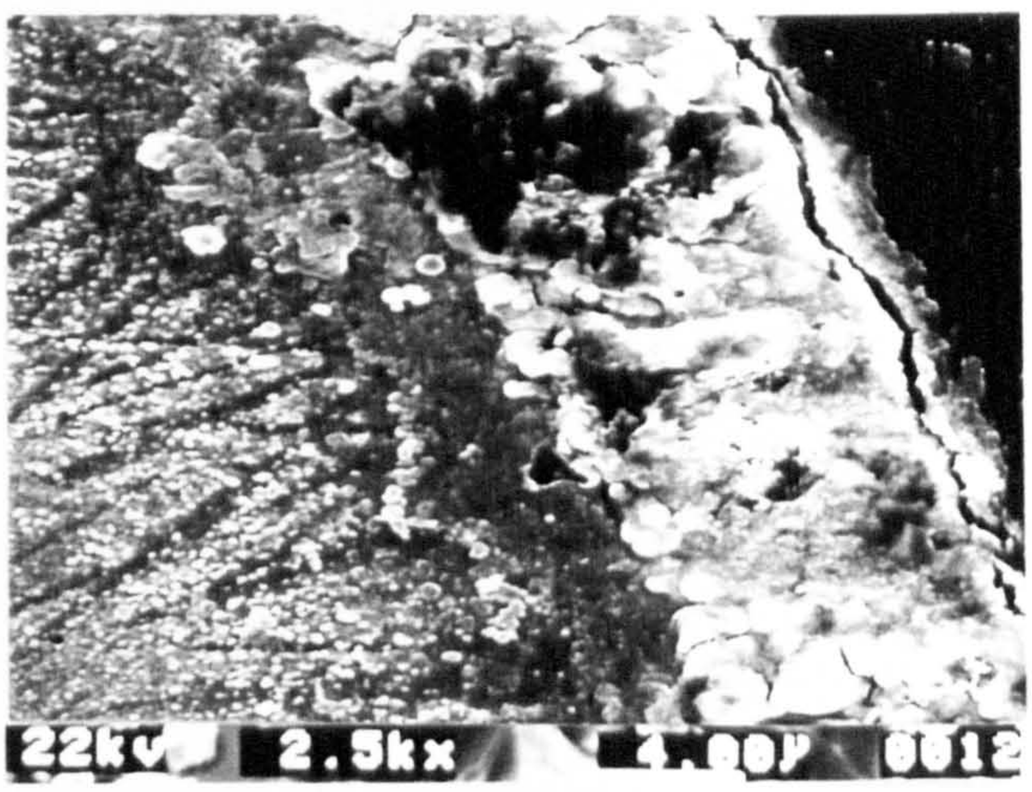


FIGURE 80: Electroplated Zinc-Cobalt Coating Treated with HMT Emulsion



Examination of the DBT cobalt/nickel specimens that had a top layer of zinc-cobalt alloy was performed. Baked DBT specimens gave no reaction when exposed to the HMT emulsion, as expected. However, generally there was no discernible difference between the intensity of response for a dual layer or single layer electrodeposit after HMT treatment on an unbaked specimen. FIGURE 81 illustrates the much greater response of the DBT coating compared to the metal substrate.

A few DBT specimens were treated with emulsion after a short delay and a more graduated response was observed as shown in FIGURE 82. The delay in treatment of these specimens allowed hydrogen to diffuse within the specimens and distribute between the layers. The initial coated layer shows a greater response than the second layer, indicating a higher level of hydrogen present. Hydrogen is detected in 'pockets' in the second layer but due to the less concentrated coating response it is easier to observe that hydrogen is present in the metal substrate.

FIGURE 81: Typical DBT Specimen after HMT Treatment

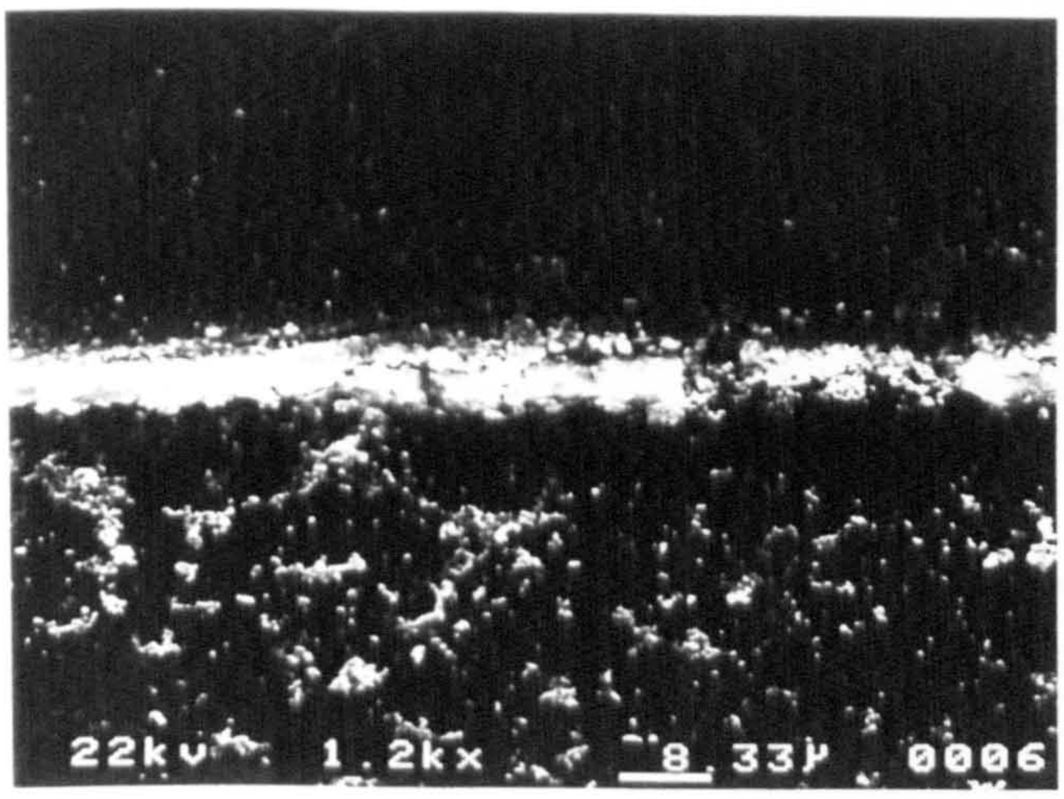
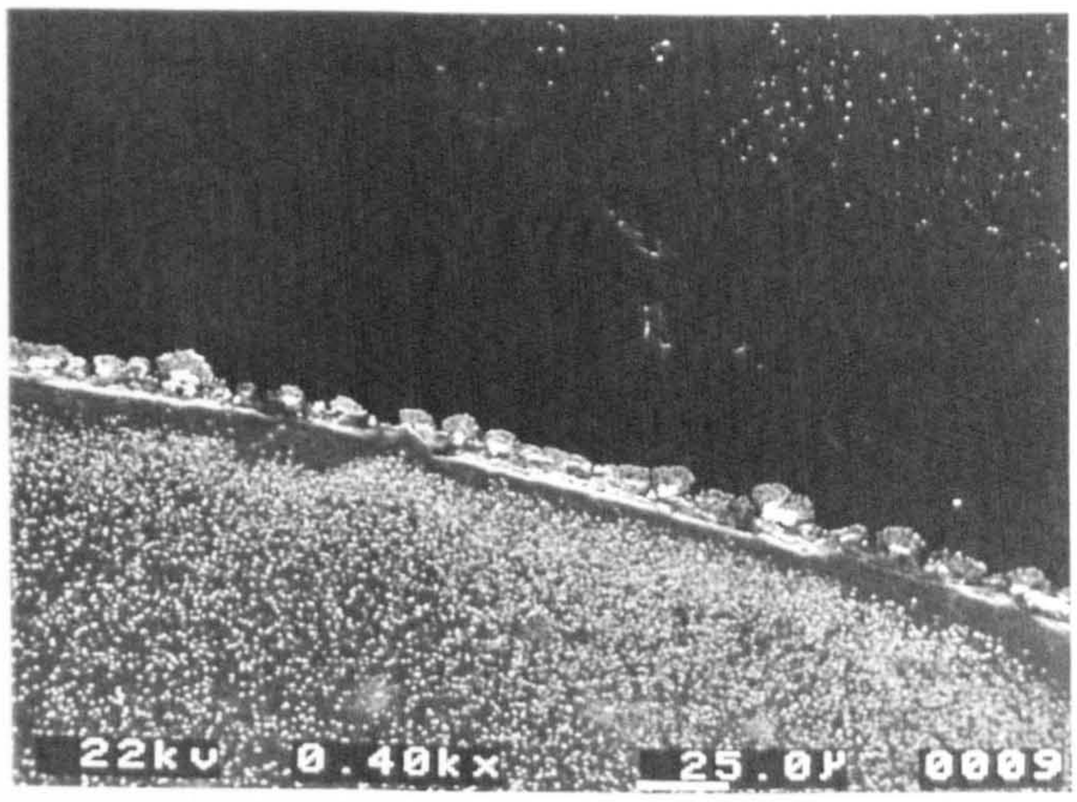
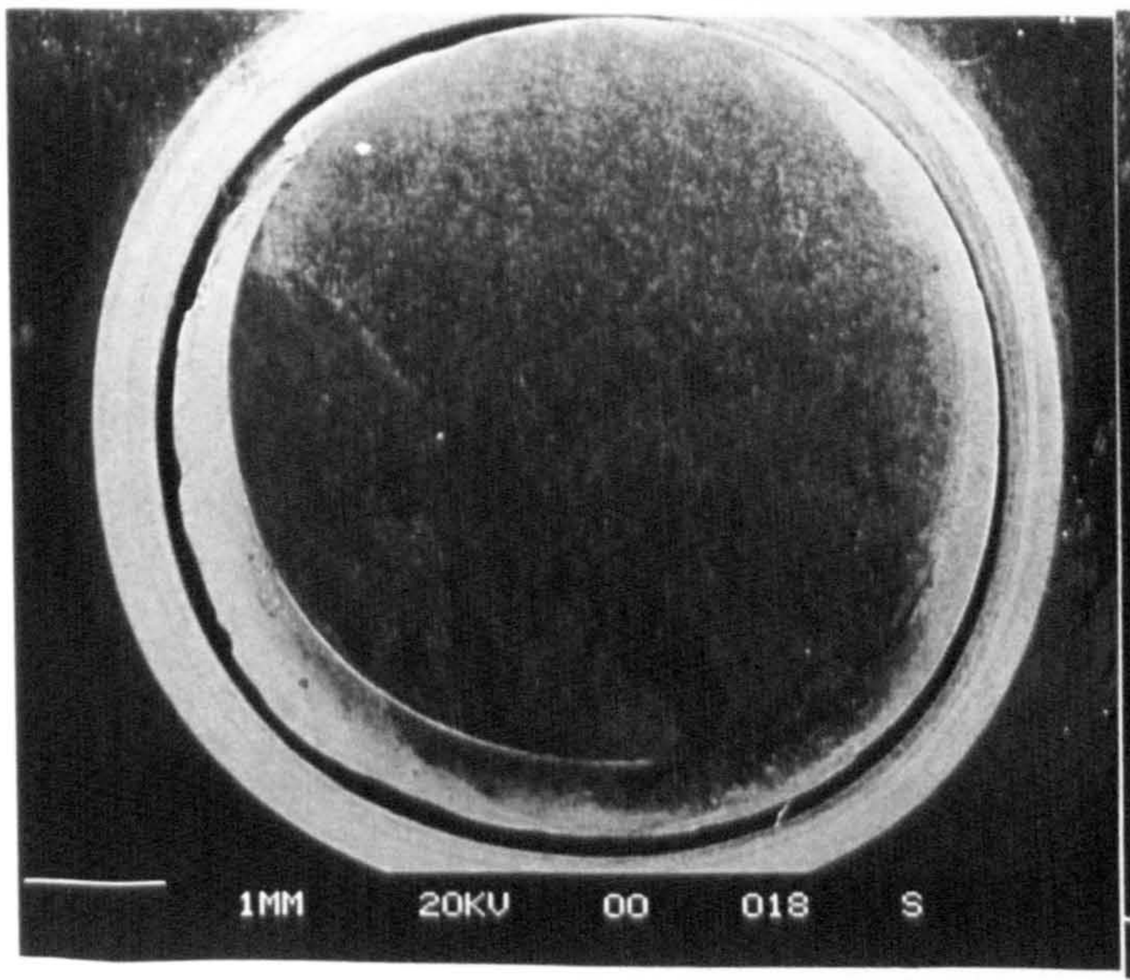


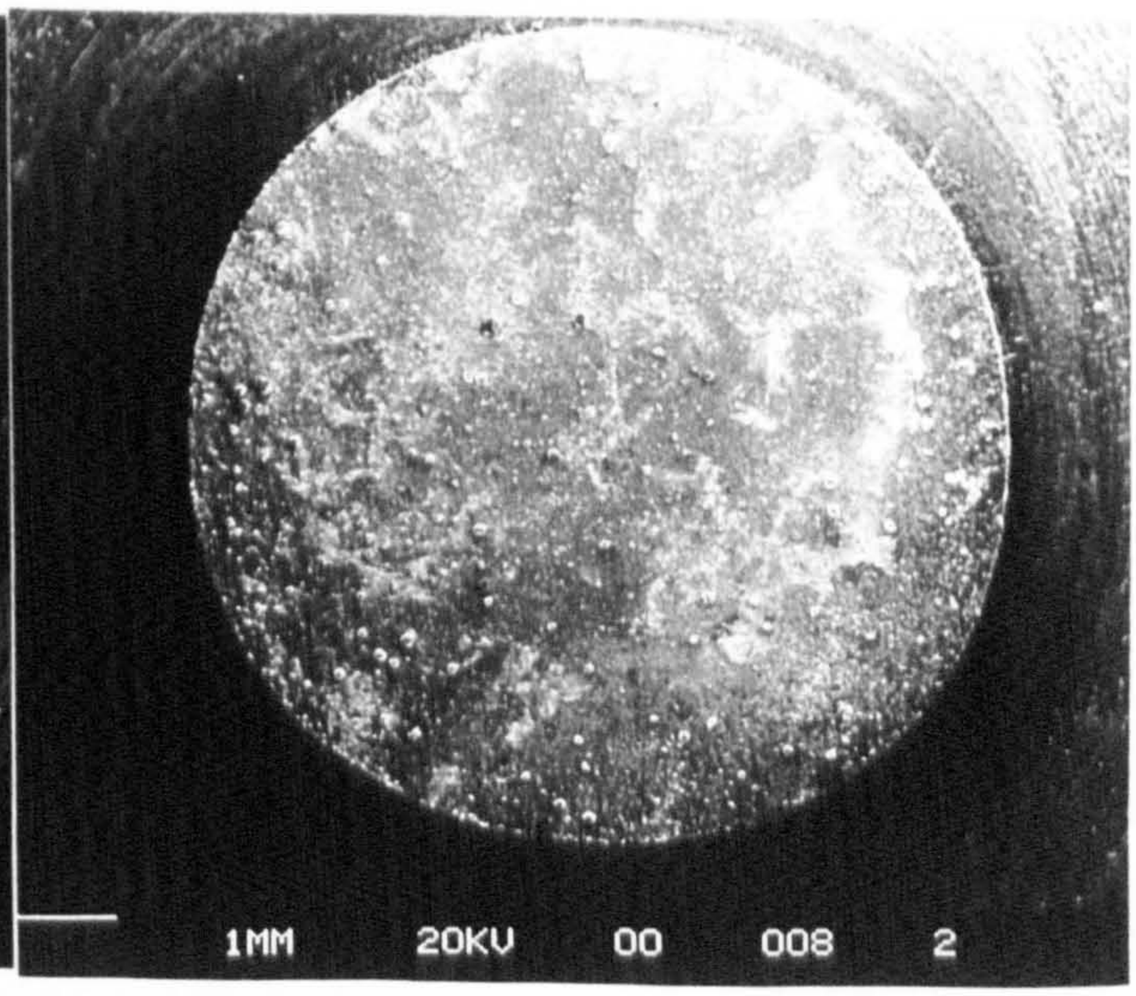
FIGURE 82: Response of Delayed HMT Treatment on DBT Specimen



The difficulty experienced with the detection limits of the technique led to charging experiments with unplated specimens. They did not suffer from the overriding reaction from the emulsion with the hydrogen that was contained in the electroplated coating, and provided information on how far the hydrogen penetrated into the metal substrate. Unplated specimens that had been charged in thiourea inhibited 10% sulphuric acid solution at room temperature were measured after HMT treatment to assess the extent of hydrogen penetration into the specimen. An average value was taken for the edge of the diffusion band viewed under the SEM. Typical charged specimens after HMT treatment are shown in FIGURE 83.

FIGURE 83: Typical Charged Steel Specimen Showing the HMT Detection Band and a Charged Specimen Showing a Complete Response





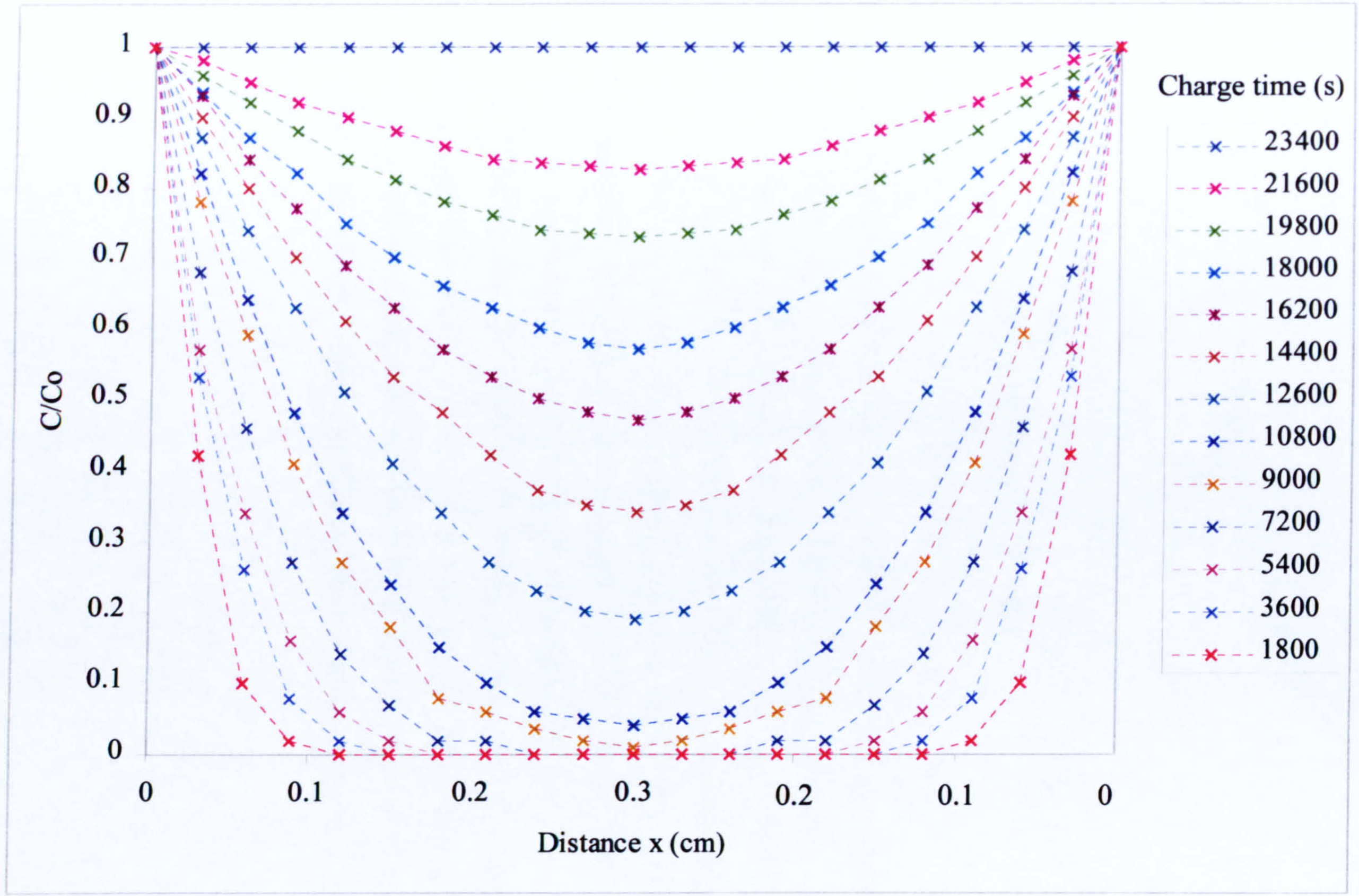
The experimental results were subsequently compared with theoretical hydrogen profiles that were calculated using EQUATION 20 and are shown in FIGURE 84.

TABLE 21: Comparison of Experimental and Theoretical Diffusion Bands

Charge Time (mins)	Experimental Distance (%)	Theoretical Distance (%)	Agreement (%)
30	1	6	17
120	60	55	109
240	73	80	91
390	100	100	100

TABLE 21 shows that the experimentally determined values for the distance that hydrogen had diffused in the charged unplated specimens was approximately 79% of that which had been calculated theoretically.

FIGURE 84: Theoretical Depth Profile for Hydrogen Penetration



POLARISATION SCAN RESULTS

FIGURE 85: Polarisation Scans for Steel Coupons

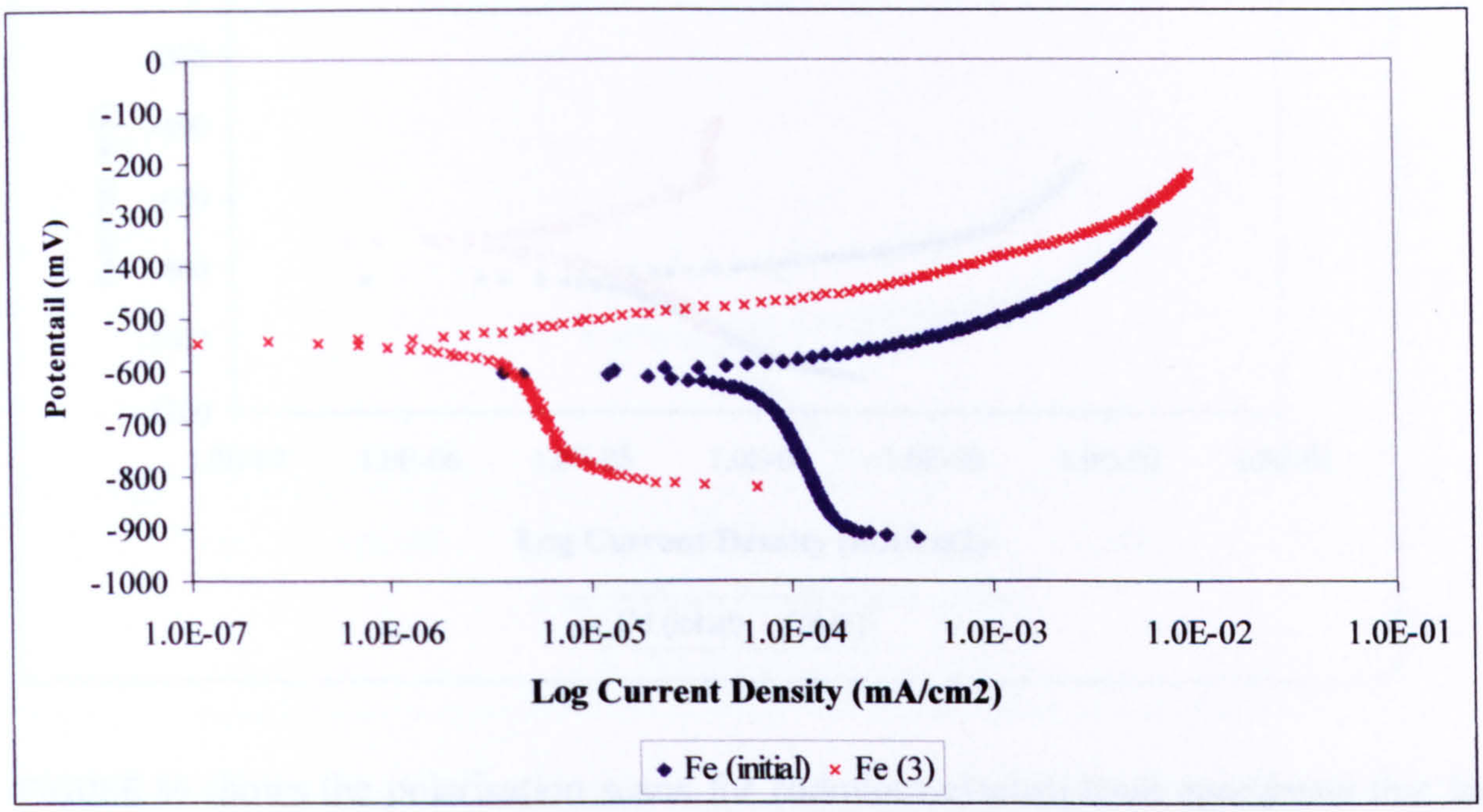


FIGURE 85 shows the polarisation scan for steel specimens that had been immersed in 3.5% NaCl solution for 3 months compared to initial tests on specimens. The unplated steel specimens that had been immersed for 3 months showed a change in corrosion potential from –600mV to -580mV. This could have been due to a difference in aeration of the tests. The lower portion of the 3 month test scan is higher than expected it indicates that the scan was obtained in a more de-aerated solution. This part of the curve is governed by the water reduction reaction and so is particularly susceptible to a change in oxygenation of the surrounding solution. However, it could also be due to less oxygen reduction after 3 months immersion. The 3 month test specimens showed a slowing in corrosion rate when compared with the initial tests, which could be attributed to a build up of corrosion product on the surface of the specimen acting as a barrier to further corrosion.

FIGURE 86: Polarisation Scans for Cadmium Electroplated Coupons

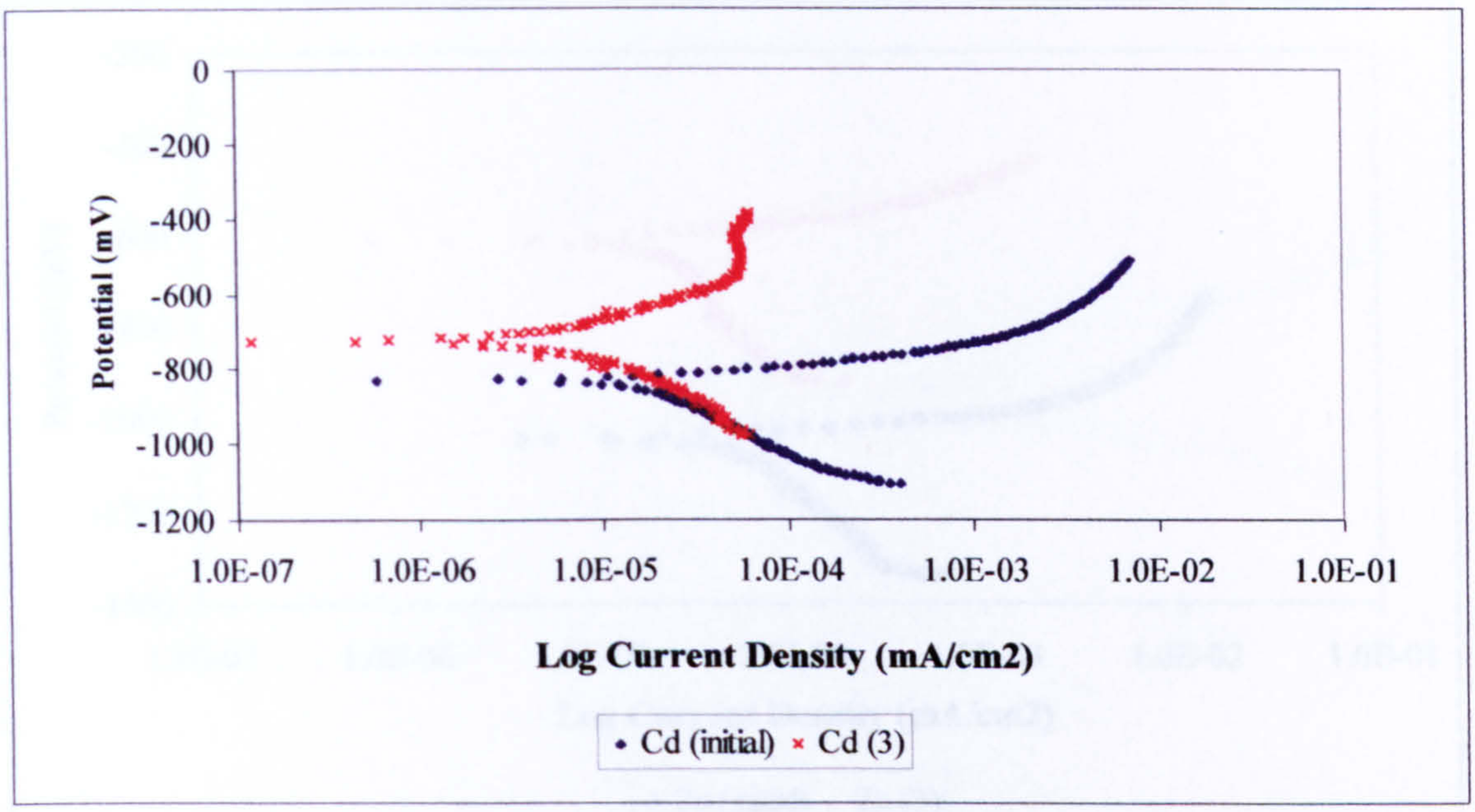
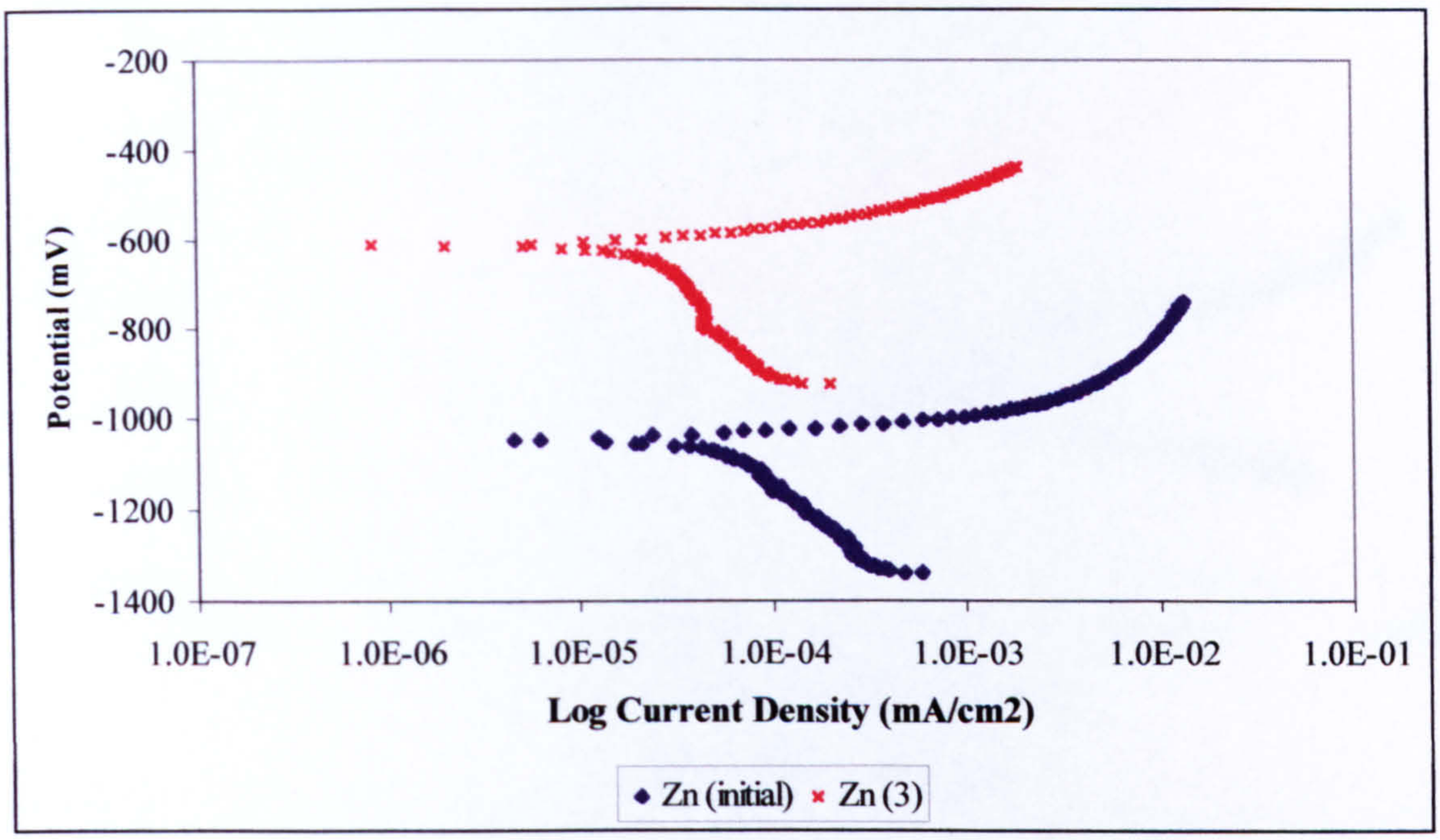


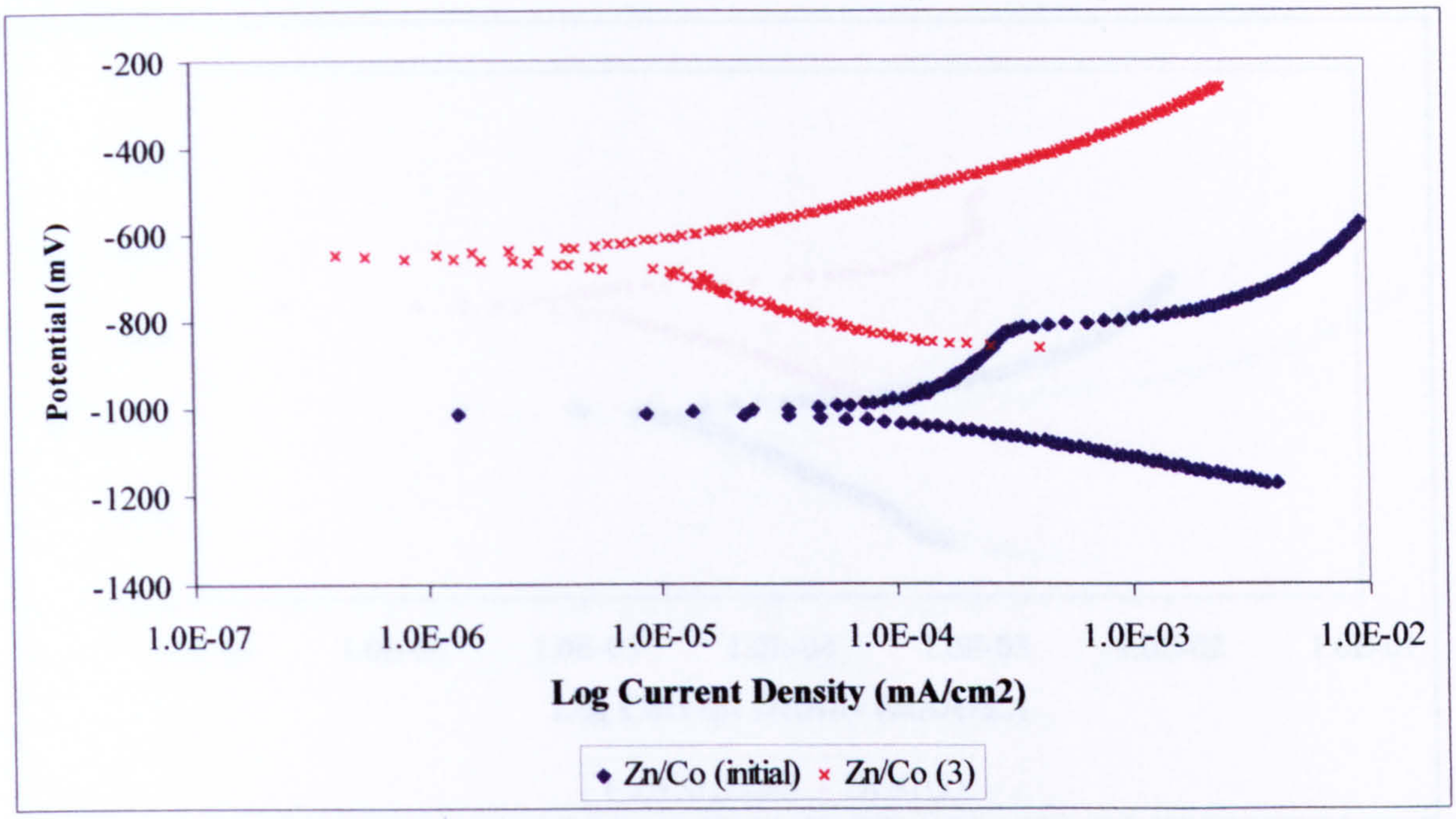
FIGURE 86 shows the polarisation scans for cadmium electroplated specimens that had been immersed in 3.5% sodium chloride solution for 3 months compared to initial test specimens. After 3 months immersion the specimens showed an increase in potential from –820mV to –720mV. The initial potential seen for cadmium is more negative than the–700mV one would expect and was probably due to the unpassivated surface of the specimens being more active than usual. Once this layer had been immersed for 3 months, the observed potential of the cadmium coating is closer to the expected value of –700mV. The 3 month immersion tests yielded a reduced corrosion rate, probably due to a layer of corrosion product restricting the corrosion of the substrate.

FIGURE 87: Polarisation Scans for Zinc Electroplated Coupons



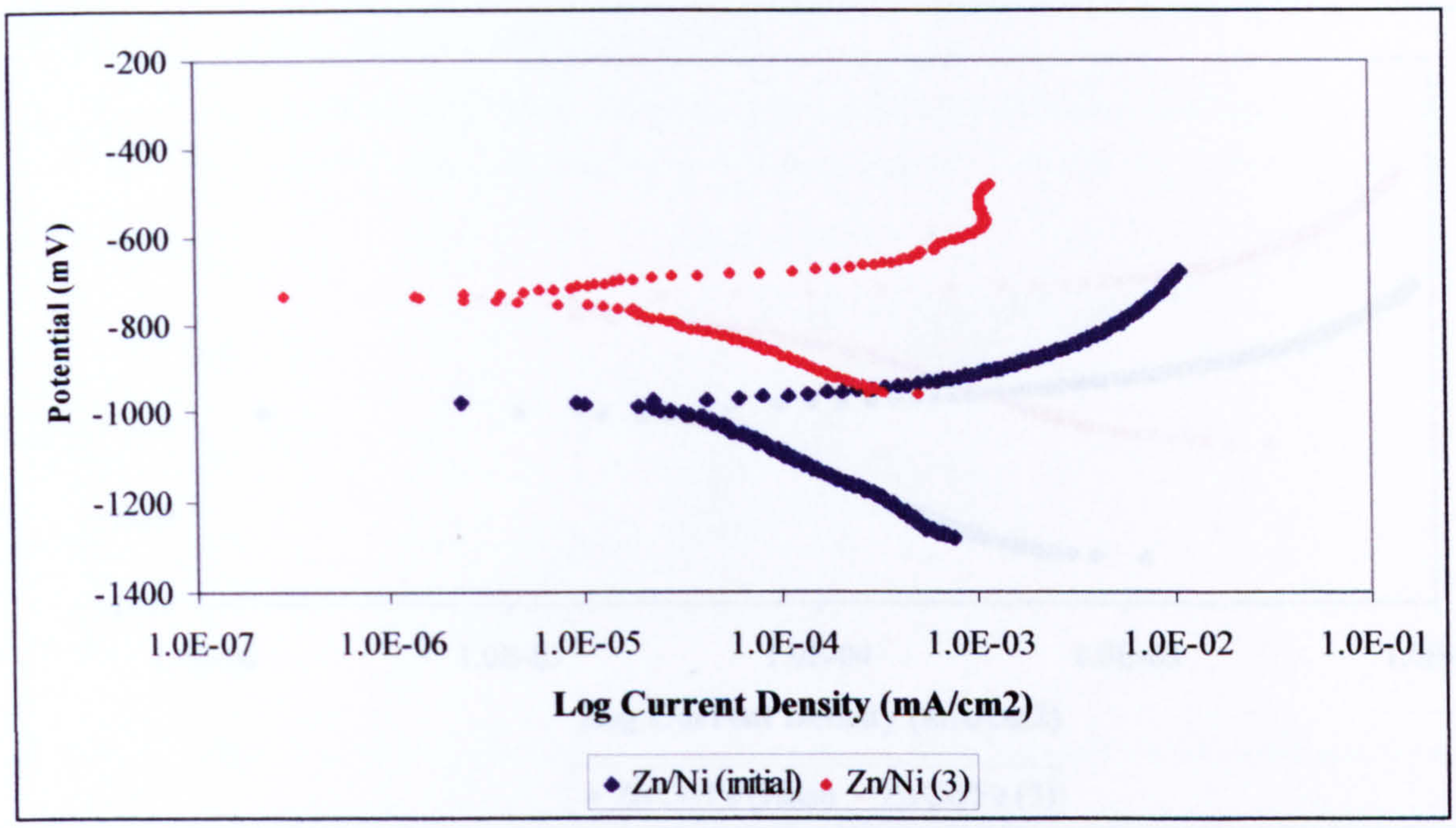
The zinc electroplated specimens that had been immersed for 3 months showed a shift in corrosion potential from -1020mV to –600mV. The large potential shift led to the conclusion that all the zinc coating had been removed after 3 months immersion and the potential measured was that of bare steel. The 3 month test had a comparable corrosion rate to that of bare steel which reinforced the argument that the zinc coating had been removed from the steel specimen.

FIGURE 88: Polarisation Scans for Zinc-Cobalt Electroplated Coupons



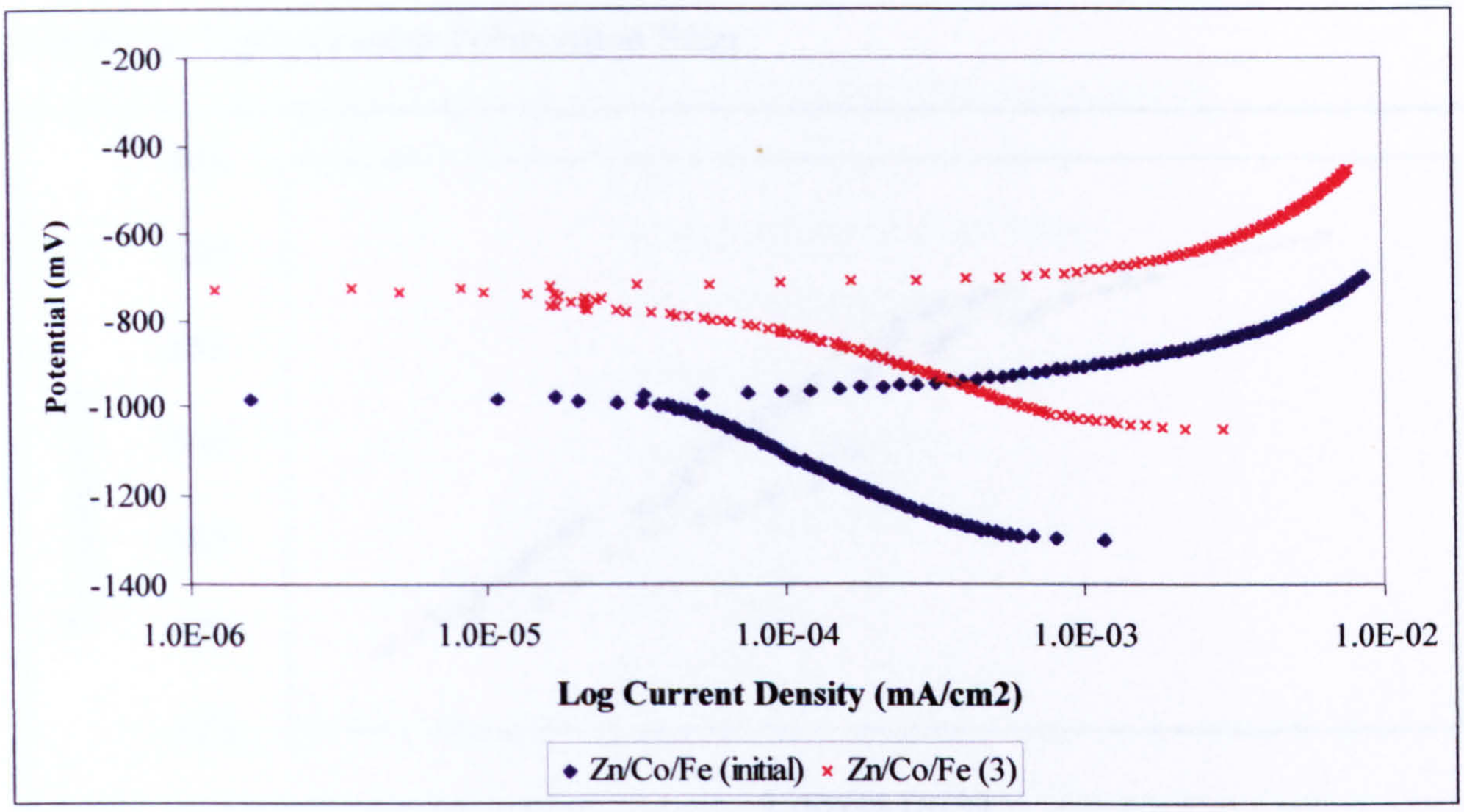
The zinc-cobalt electroplated specimens that had been immersed for 3 months showed a shift in corrosion potential from –1014mV to –648mV. This indicated that most of the electroplated coating had been removed, which was confirmed by visual inspection. The measured potential was therefore a combination of bare steel and zinc-cobalt electroplating. This was confirmed by the corrosion rate, which was also comparable to that of bare steel.

FIGURE 89: Polarisation Scans for Zinc-Nickel Electroplated Coupons



The zinc-nickel electroplated specimens that had been immersed for 3 months showed a change in corrosion potential from –979mV to –720mV and a slightly reduced corrosion rate. Visual inspection of the specimen led to the conclusion that despite some of the coating being removed, there was enough remaining for the specimen to be partially protected. The enoblement phenomenon was not thought to be solely responsible due to the length of the immersion time of the test specimens, although it had appeared to have occurred.

FIGURE 90: Polarisation Scans for Ternary Electroplated Coupons



Zinc-cobalt-iron specimens that had been immersed for 3 months showed a shift in their corrosion potential from –983mV to –732mV. This was attributed to an enoblement effect, as there was no sign of major coating loss on the surface of the specimens. There also appeared to be little change in log current density for each of the specimen types.

LINEAR POLARISATION RESISTANCE RESULTS

FIGURE 91: Typical Linear Polarisation Scan

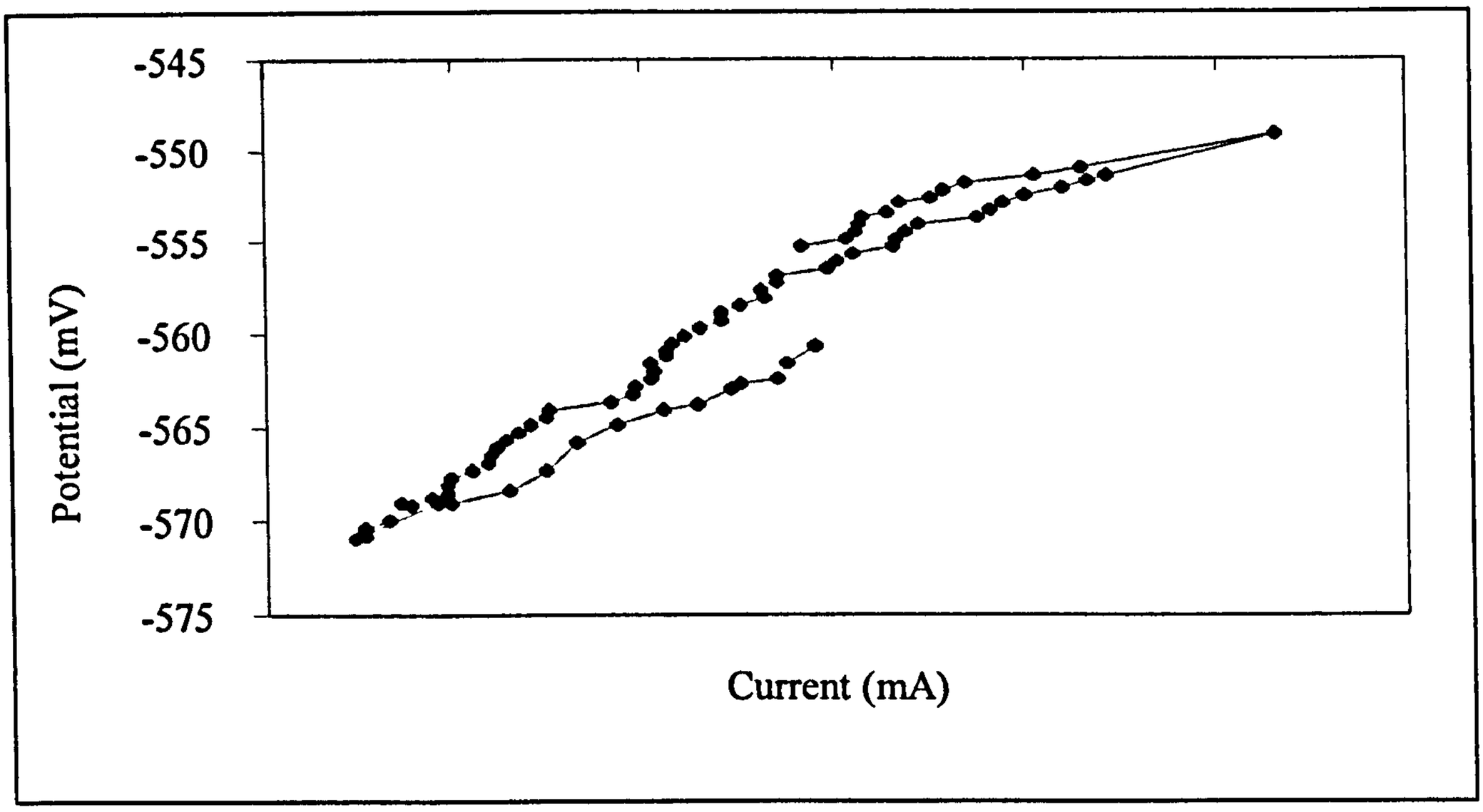


FIGURE 91 shows an example of a typical LPR scan for an unplated steel coupon. The slight shift in corrosion potential at the end of the scan from the initial value is a common phenomenon and is due to a change in surface state of the specimen. Stern and Geary developed a relationship for calculating corrosion current from linear polarisation resistance measurements [17]. At potentials close to E_{corr} (+/- 10mV) the corrosion current is inversely proportional to the polarisation resistance, which is directly proportional to the reciprocal slope of the potential-current curves obtained from the LPR experiment. If the anodic and cathodic Tafel constants are known (calculated from polarisation measurements) then a value for I_{corr} can be calculated using EQUATION 21.

EQUATION 21 : Stern Geary Equation

$$1/R_p = (\Delta I/\Delta E)_{Ecorr} = 2.3\ \{(b_a+b_c)/(b_a.b_c)\}\ I_{corr}'$$

Where:

R_p	=	polarisation resistance (Ω/cm^2)
E_{corr}	=	corrosion potential (mV)
I_{corr}	=	corrosion current density (mA/ cm^2)
b_a/b_c	=	anodic/ cathodic Tafel constant (mV/decade)

The corrosion rate can be calculated from the corrosion current by use of EQUATION 22.

EQUATION 22: Calculation of Corrosion Rate from the Corrosion Current

$$C.R.\ (mdd) = i_{corr}.t.W_a \ / \ F.A$$

Where:

C.R. = corrosion rate ($mg/dm^2/day$)

i_{corr} = corrosion rate ($\mu A/cm^2$)

t = time (86400 seconds/day)

W_a = chemical equivalent

F = 96500 Coulombs

A = area (cm^2)

The LPR technique is of benefit because it is a sensitive and rapid method. It is also non-damaging to the surface and can be therefore repeated. However, it is more likely to be affected by features such as individual pits or oxygenation and aeration differences.

FIGURE 92: LPR Scans for Immersed Steel Coupons

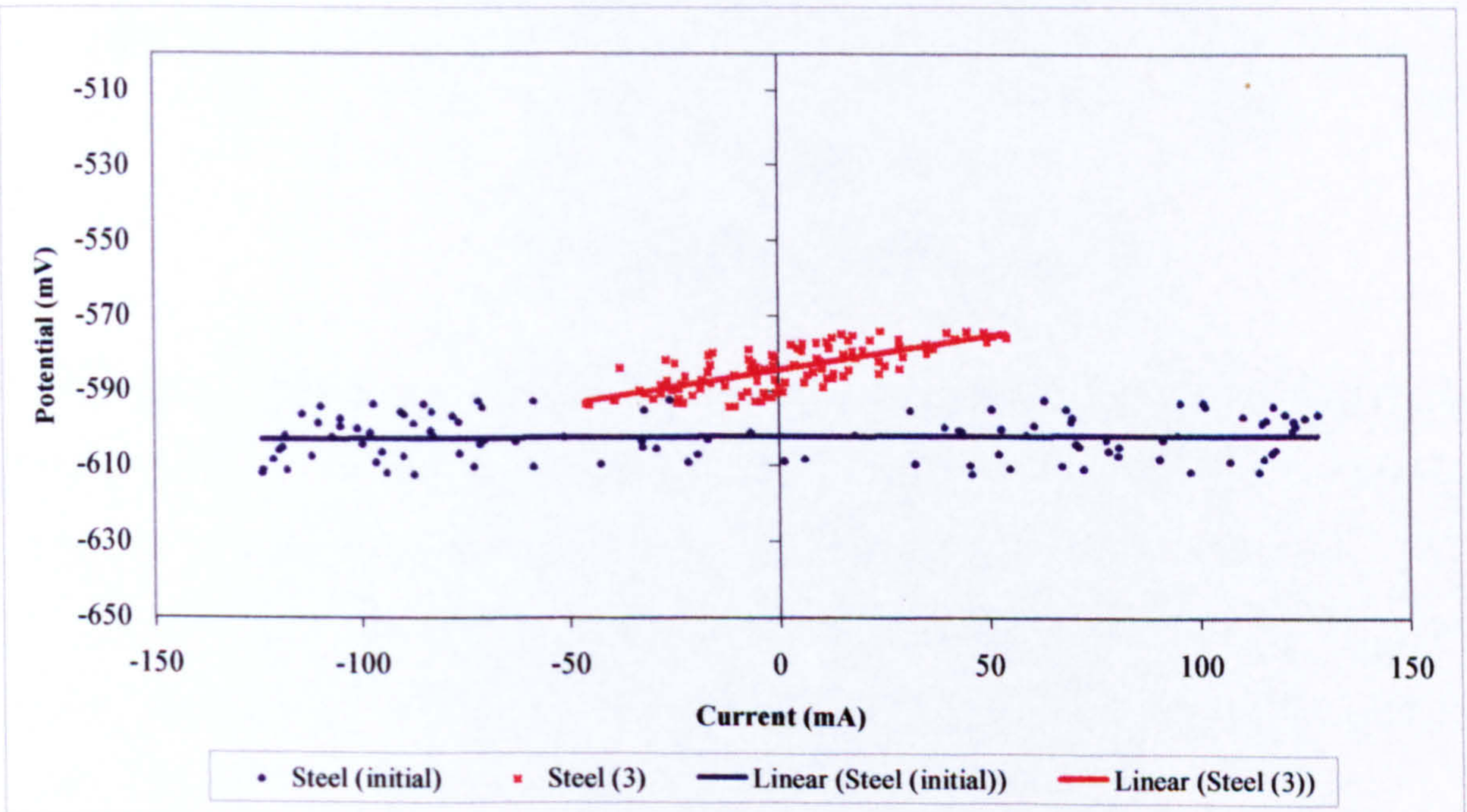


FIGURE 92 shows there was considerable scatter for the results obtained. Trend lines used to obtain the gradient have been left on the scan to highlight the comparative shift in potential and current. The steel specimens that were immersed for 3 months showed a shift in E_{corr} from –601mV recorded for the initial tests to –584mV.

The R_p value increased from 5.6 x $10^3\Omega/mm^2$ to 1.8 x $10^5\Omega/mm^2$, clearly demonstrated by the increased gradient of the graph. There was also a corresponding reduction in corrosion current (I_{corr}) for the specimens that had been immersed for 3 months compared to the initial tests. This effect was probably due to a corrosion product layer forming a barrier on the surface of the specimen over the 3 month period, slowing the corrosion of the underlying material affected by the oxygen depletion.

FIGURE 93: LPR Scans for Immersed Cadmium Electroplated Coupons

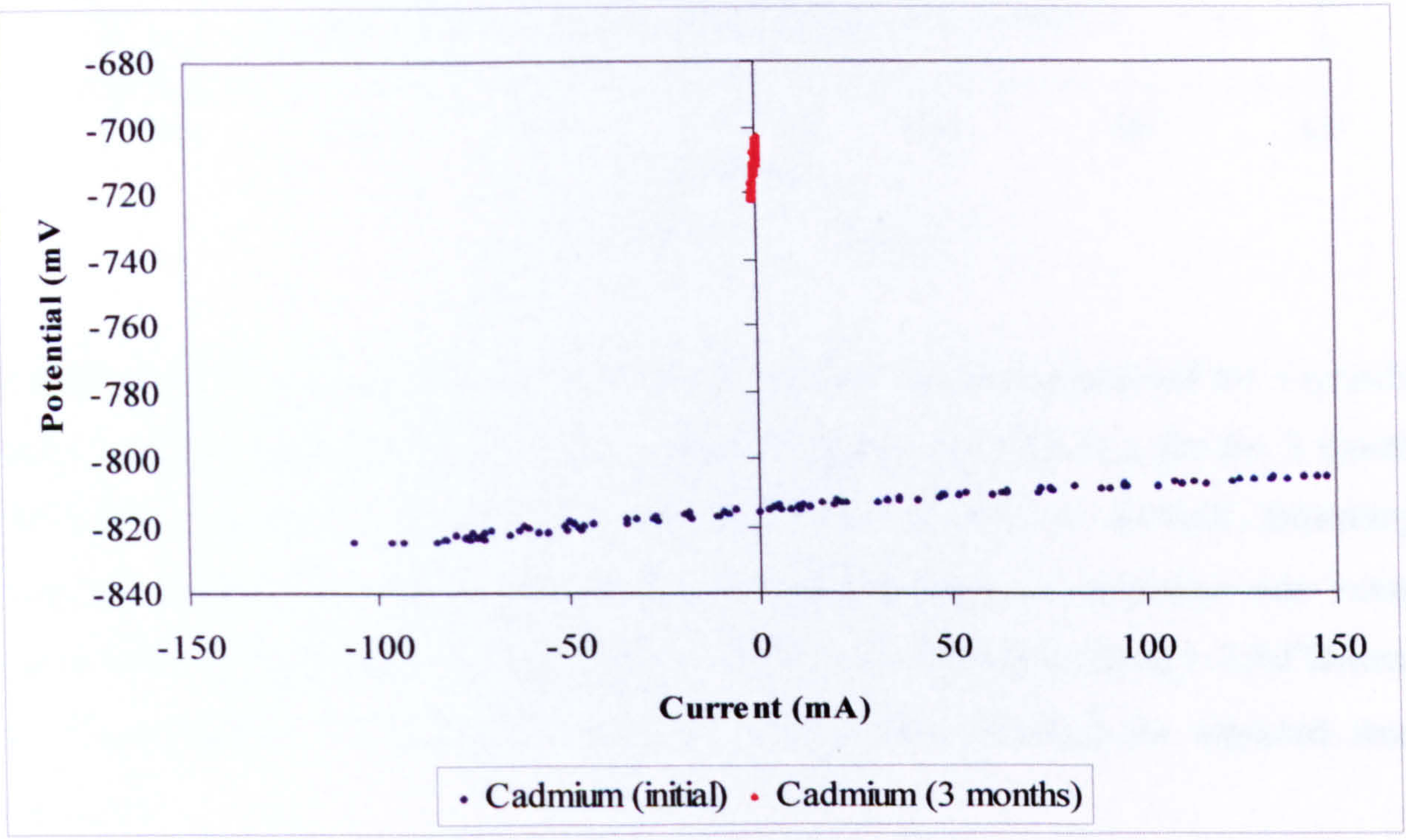


FIGURE 93 shows that the cadmium specimens that had been immersed for 3 months demonstrated a noble shift in potential from –815mV to –710mV. The increased gradient of the graph showed that the R_p value increased from 8.2 x $10^4\Omega/mm^2$ to 9.5 x $10^6\Omega/mm^2$. There was also a reduction in corrosion current for the specimens that had been immersed for 3 months compared to initial specimens. This is common feature for many corroding systems as a layer of corrosion product masks the surface of the specimen.

FIGURE 94: LPR Scans for Immersed Zinc Electroplated Coupons

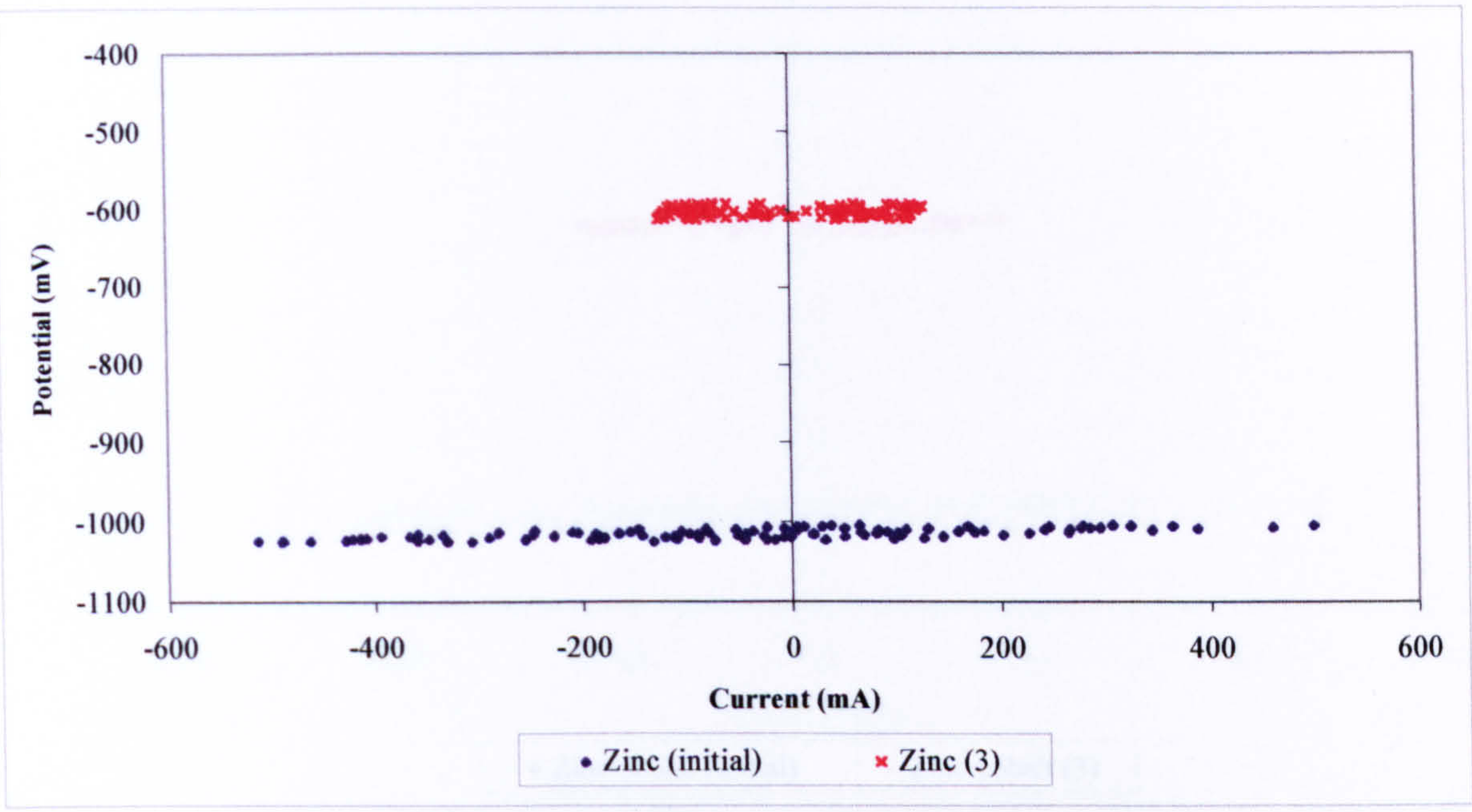


FIGURE 94 shows the zinc electroplated specimens that had been immersed for 3 months had a much smaller current range and hence corrosion rate. The E_{corr} for the 3 month specimen compared to the initial specimen rose from –1014mV to –607mV, indicating that the coating had been removed and the measurement of corrosion was being undertaken on the underlying steel coupon. The R_p value decreased from $1.7x10^4\Omega/mm^2$ to $5.6x10^3\Omega/mm^2$, which was comparable to the value obtained for unplated steel specimens.

FIGURE 95: LPR Scans for Immersed Zinc-Cobalt Coupons

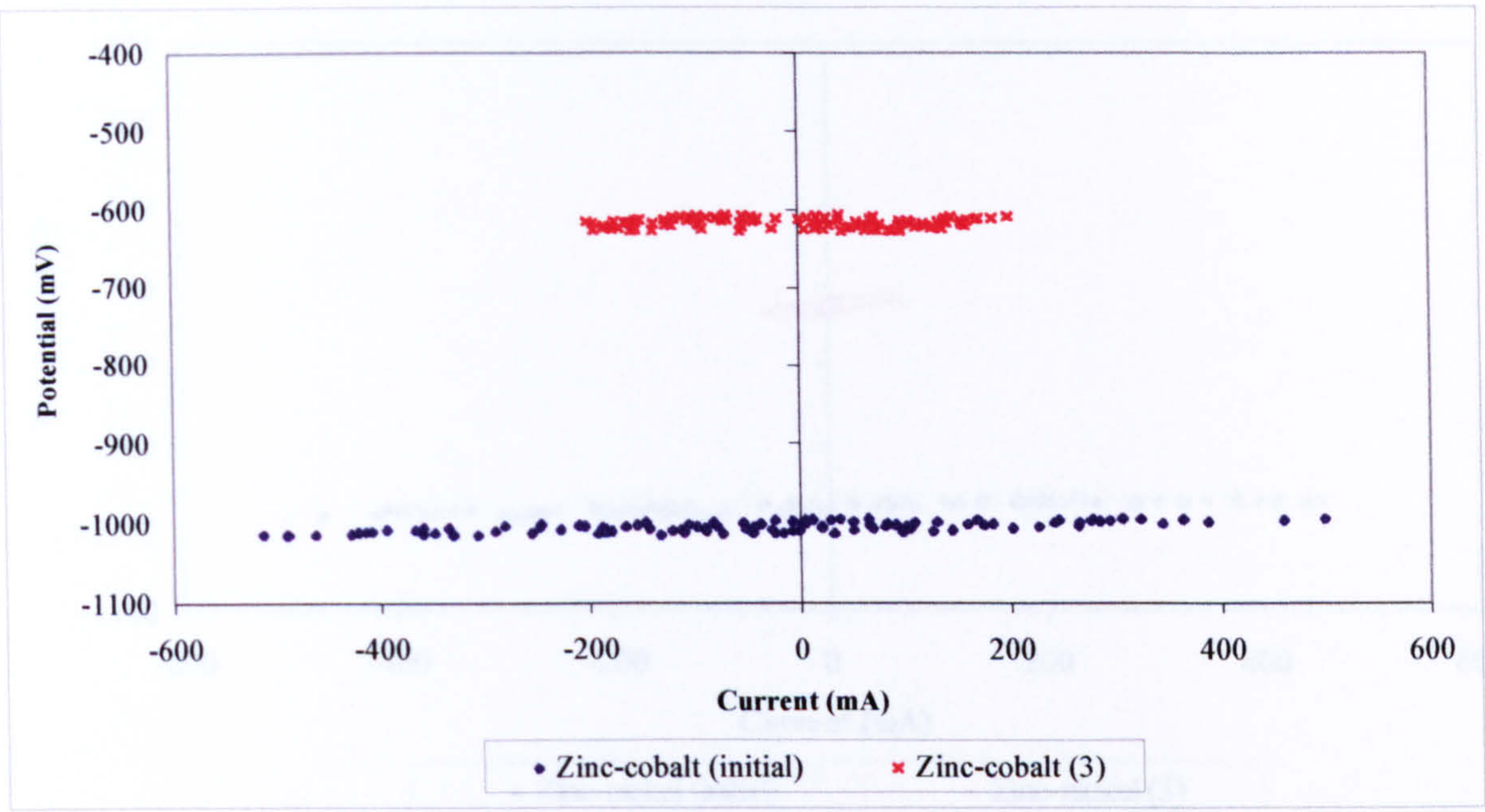


FIGURE 95 shows the linear polarisation resistance scans obtained for zinc-cobalt electroplated specimens that had been immersed for 3 months compared to initial specimens. There was no coating left after 3 month immersion indicated by the potential shift from -1004mV to -618mV. This was confirmed by visual inspection of the specimens. The corrosion current was also reduced for the 3 month specimens. The R_p value decreased from $1.7x10^4\Omega/mm^2$ to $1.0x10^3\Omega/mm^2$, which was again comparable to unplated steel specimens.

FIGURE 96: LPR Scans for Immersed Zinc-Nickel Electroplated Coupons

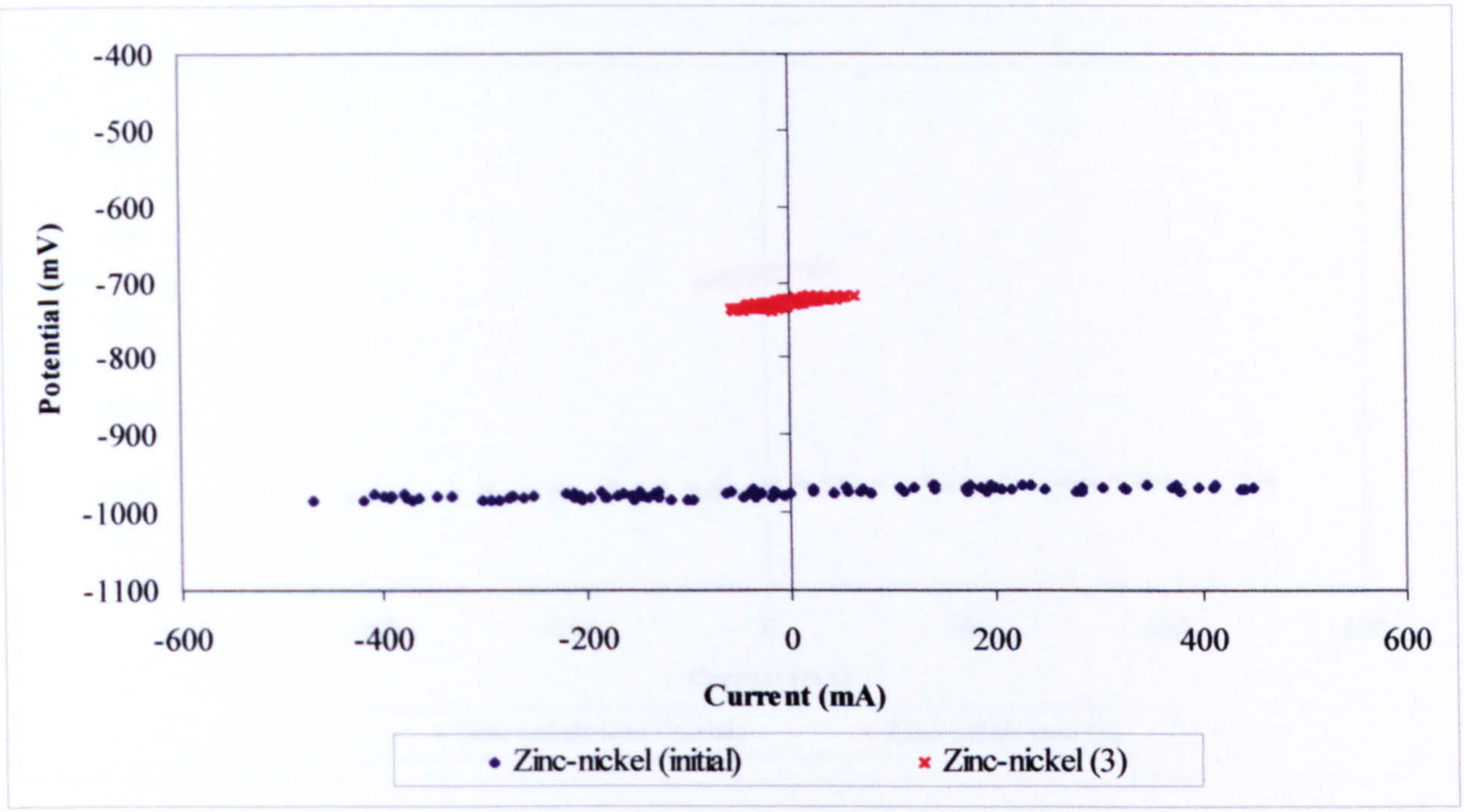


FIGURE 96 shows the linear polarisation resistance scans obtained for zinc-nickel electroplated specimens that had been immersed for 3 months compared to initial specimens. Enoblement was seen for the 3 month specimens reflected in the potential shift from -976mV to –726mV. The corrosion current also reduced for the 3 month specimens. The R_p value increased from $1.9x10^4\Omega/mm^2$ to $1.7x10^5\Omega/mm^2$ reflected by the increased gradient seen in for the 3 month specimens compared to the initial test specimens in FIGURE 96.

FIGURE 97: LPR Scans for Immersed Zinc-Cobalt-Iron Electroplated Coupons

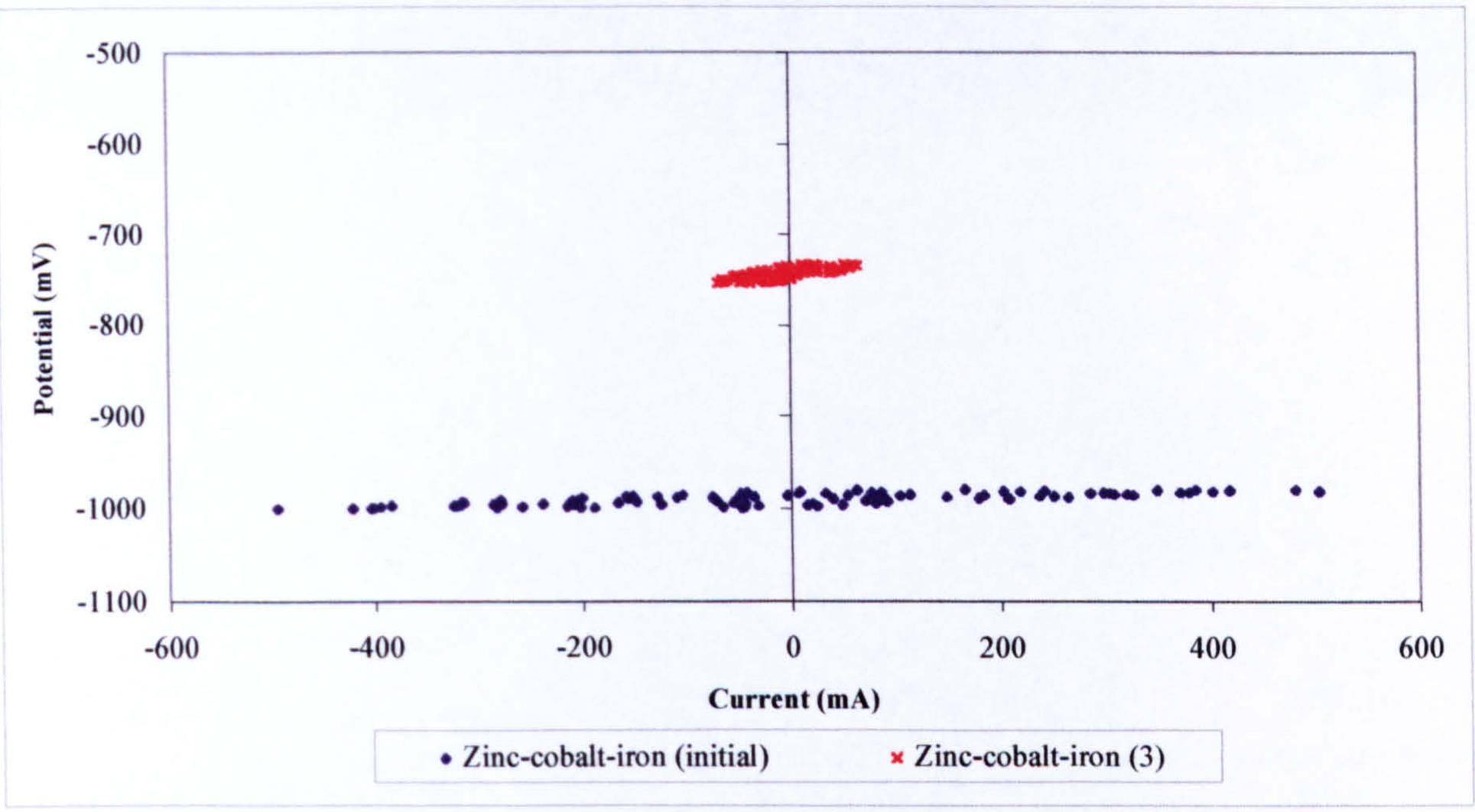


FIGURE 97 shows the linear polarisation resistance scans obtained for zinc-cobalt-iron electroplated specimens that had been immersed for 3 months compared to initial specimens. Enoblement was seen for the 3 month specimens because their potential moved from -986 mV to –743 mV. The corrosion current was also reduced for the 3 month specimens. The gradient of the 3 month specimen set was increased compared to the initial tests and the R_p value increased from $1.9x10^4\Omega/mm^2$ to $1.4x10^5\Omega/mm^2$.

A summary of the polarisation data generated is given in TABLE 22. It includes a comparison of the corrosion potential, corrosion current and calculated corrosion rate, for each of the specimen types. There was a general slowing in corrosion rate with an increase in time, unless the coating had been removed in the immersion time. In this case the corrosion rate increased, and the corrosion potential tended towards the initial steel coupon value. Zinc, because of its active nature, produced the highest average corrosion current. The zinc-alloys all had a lower corrosion current value than zinc due to the noble alloying constituents present.

TABLE 22: Comparison of Corrosion Rate, E_{corr} and I_{corr} for the Electrochemical Data

Specimen	E_{corr} (mV)	I_{corr}($\mu A/cm^2$)	Corrosion Rate (mdd)
Unplated initial	602	77.64	194.11
Unplated 3 month	584	34.25	85.63
Cd initial	816	4.29	21.62
Cd 3 month	710	0.27	1.35
Zn initial	1014	23.67	69.27
Zn 3 month	602	84.08	226.05
Zn-Co initial	1004	8.98	26.26
Zn-Co 3 month	617	61.87	180.96
Zn-Ni initial	975	19.01	54.99
Zn-Ni 3 month	727	17.71	51.24
Zn-Co-Fe initial	990	25.65	67.62
Zn-Co-Fe 3 month	742	4.33	11.42

WEIGHT LOSS RESULTS

FIGURE 98: Weight Loss for 3 and 6 Month Immersion Coupons

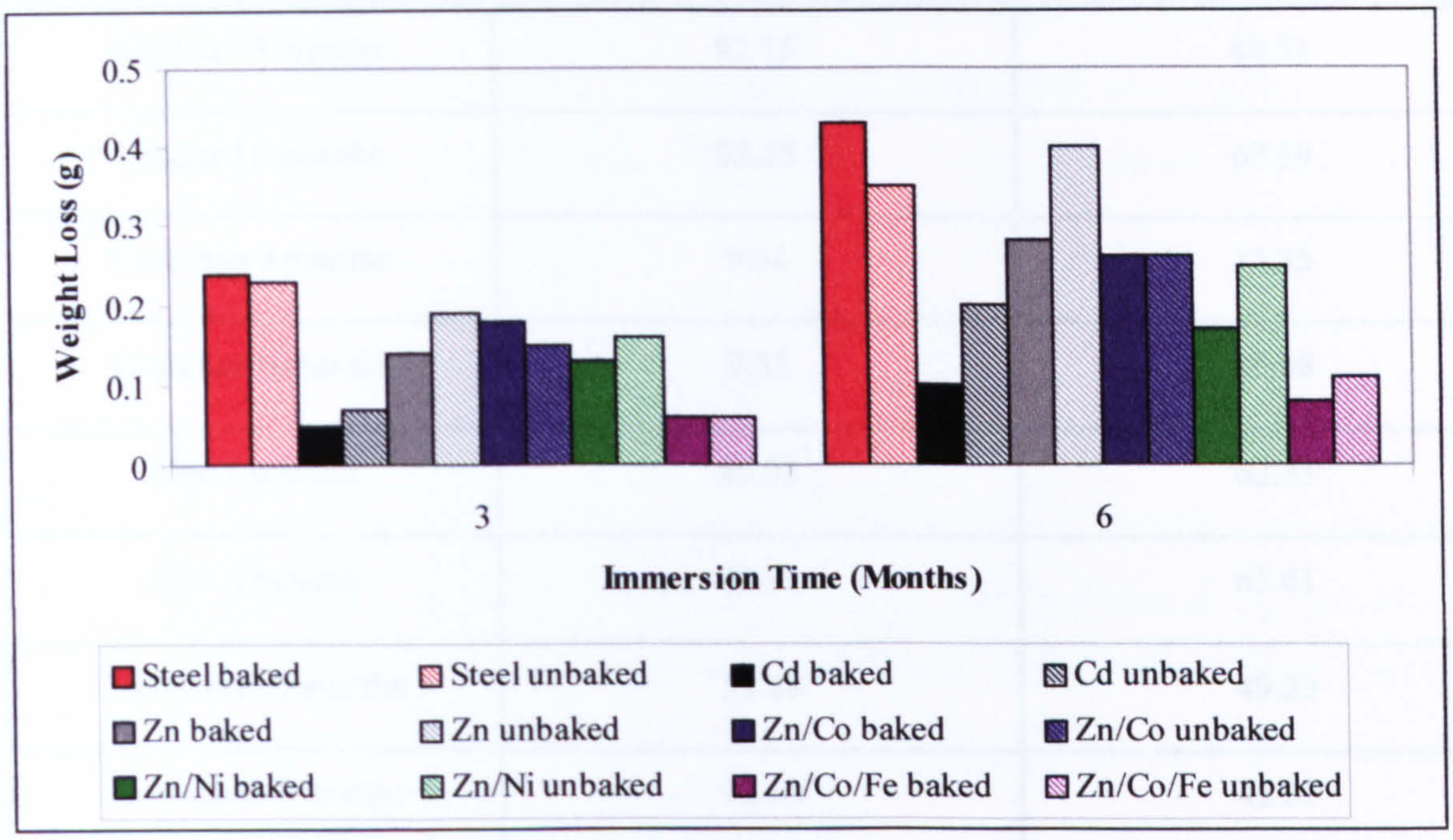


FIGURE 98 shows the weight loss found for baked and unbaked specimens immersed in 3.5% NaCl solution for either 3 or 6 months. It can be seen clearly that for each coupon type the weight loss found for specimens after 6 months immersion was greater than 3 month immersion. The unplated steel coupons lost most weight overall compared to all the coated specimen types and the ternary specimens lost least weight. The corrosion rate in mdd for each of the specimen types in the baked and unbaked conditions were calculated and are given in TABLE 23. They are discussed fully in Chapter 4.

The way in which corrosion rate is expressed can vary, as there are several common units that are used. In this work the units used are mdd. However, for completeness the relationship between the regular units can be expressed in the following way:

	5mdd	≡	1mpy
	40mpy	≡	1mm/yr
i.e.	200mdd	≡	1mm/yr

TABLE 23: Average Corrosion Rates (mdd) Calculated from Weight Loss Data

Specimen	Baked	Unbaked
Unplated 3 months	92.15	88.31
Unplated 6 months	82.55	67.19
Cadmium 3 months	9.54	13.35
Cadmium 6 months	9.53	19.08
Zinc 3 months	45.93	62.33
Zinc 6 months	45.93	65.61
Zinc-cobalt 3 months	59.08	49.23
Zinc-cobalt 6 months	42.69	42.67
Zinc-nickel 3 months	43.13	53.08
Zinc-nickel 6 months	28.20	41.47
Zinc-cobalt-iron 3 months	21.84	21.84
Zinc-cobalt-iron 6 months	14.56	20.03

DISCUSSION ZINC-COBALT

PARAMETER VARIATION

Parameter variation investigations were an important method to identify the deposition mechanism of the acid zinc-cobalt electrolyte. The parameters investigated were time, temperature, pH and current density. The results will be discussed in the following sections.

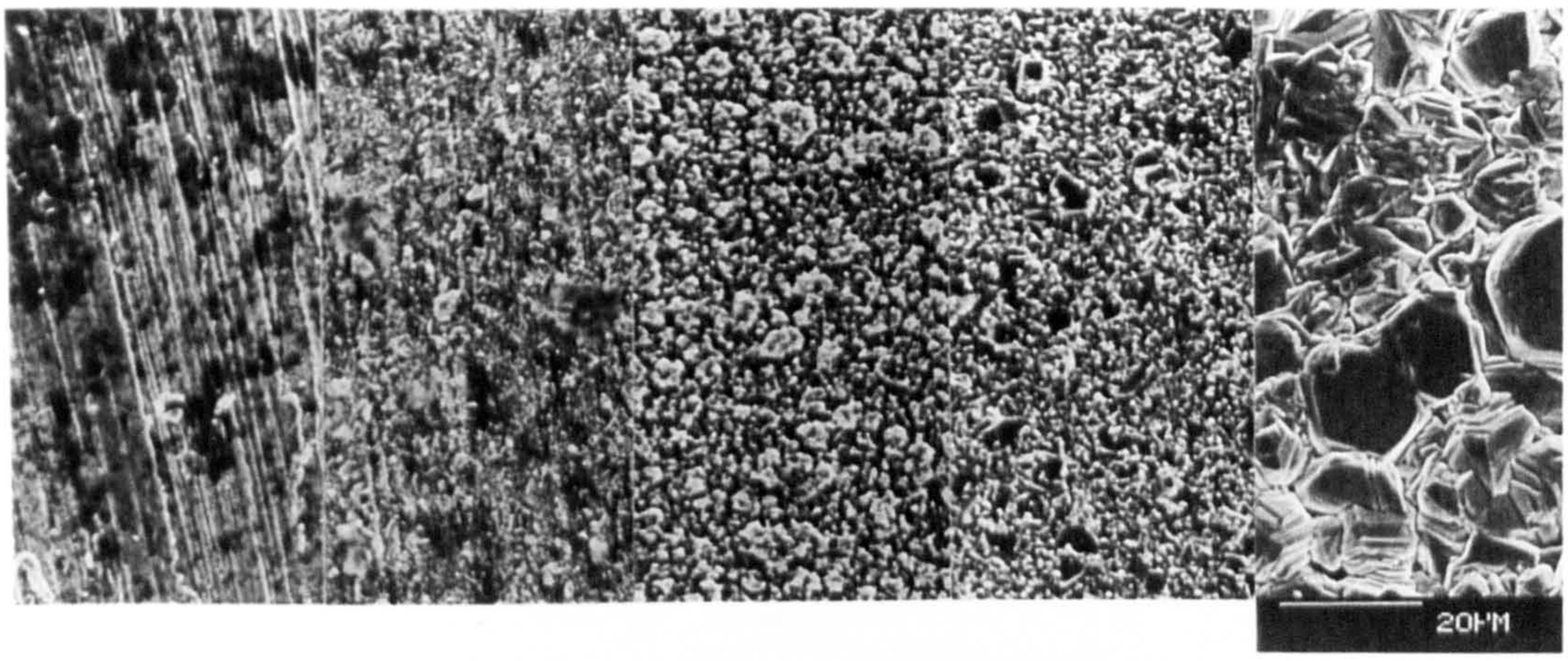
Time

FIGURE 38 demonstrates that electrodeposit thickness increased with coating time. The composition and current efficiency varied as expected for the investigated zinc-cobalt electroplating time range. Zinc-cobalt electroplating was performed in agitated and stagnant conditions to determine the effect on deposit composition. Both conditions followed identical trends with an approximate ten-fold decrease in cobalt percentage from 30 seconds to 30 minutes electroplating time.

The findings of this work were in agreement with data produced by Verberne, which showed that stagnant electroplated specimens had a higher cobalt content in the deposit compared to agitated specimens [116]. However, Zhang and co-workers observed the opposite trend [132]. In this work agitation of the bath reduced the initial cobalt composition from 7% to 3%. This may have been due to pH or oxygenation effects. If the specimen was plated for long enough, a significant local electrolyte pH change may occur, raising the surface pH to a level suitable for cobalt hydroxide (pH 6.54) to be precipitated in addition to zinc hydroxide (pH 5.25) [111]. This would lead to a higher level of cobalt being detected in the deposit by the EDAX method, as this technique cannot differentiate between cobalt present as hydroxide or reduced metal. Agitation of the bath would re-establish the character of the bulk pH and hence counteracted some of this effect. Another explanation is that the agitation of a specimen allows its surface to be more effectively oxygenated than under stagnant conditions. This may cause less zinc hydroxide to form, resulting in the normal deposition mechanism in the stagnant condition. However, as can be seen from FIGURE 38 the cobalt level in the stagnant specimens came close to, but did not reach, the electrolyte bath cobalt content of 8%.

Therefore the deposition mechanism undergone is by definition anomalous co-deposition and not normal deposition.

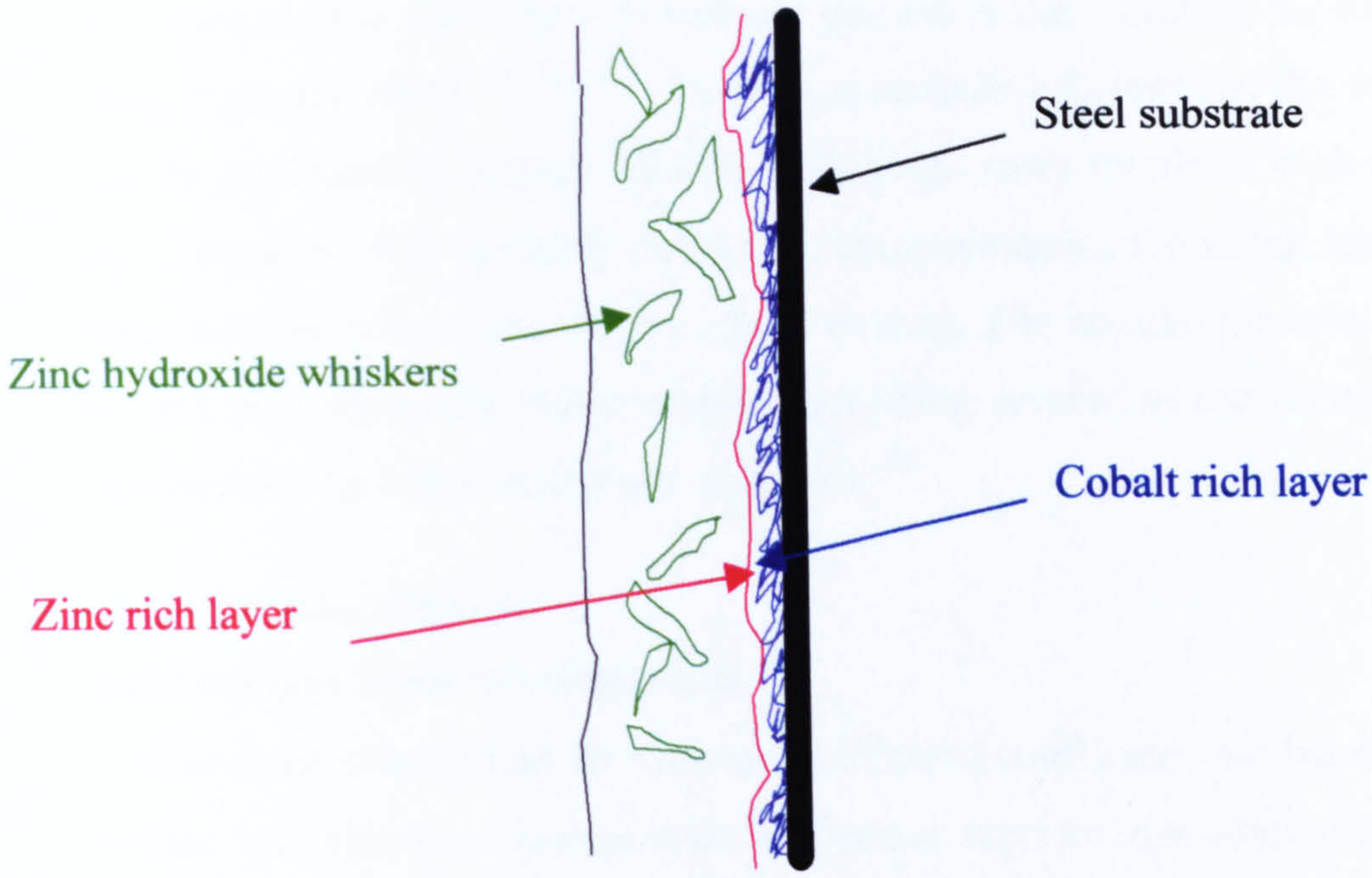
FIGURE 99: Variation of Zinc-Cobalt Specimen Morphology with Coating Time



The quality and morphology of the electrodeposits was largely unaffected by further change in electroplating time after 2 minutes, as shown in FIGURE 99. This finding is consistent with previous work undertaken in the field. The uniformity of the electrodeposit was improved by specimen agitation during electrodeposition, as Verberne and Wang had both reported previously [116, 133]. The zinc-cobalt electrodeposit that was initially produced, shown in FIGURE 99, has obvious needle-like whiskers on its surface, that have been identified as zinc hydroxide confirming the proposal that the deposition mechanism was anomalous co-deposition [7, 18]. Increase in electroplating time established a more typical nodular or grainy appearance and the zinc hydroxide whiskers were less easy to distinguish from the rest of the surface [120].

Keen and Farr have carried out work on the orientation and morphology of electrodeposits formed at different electroplating parameters for zinc sulphate electrolytes [134]. They showed zinc-cobalt electrodeposits that contain over 60% zinc are more crystalline in nature, but can form surface cracks due to the zinc level present. Surface cracks were not a significant feature in the electrodeposits formed in this work.

FIGURE 100: Schematic of Anomalous Co-Deposition



The schematic in FIGURE 100 illustrates the sequence of deposition steps that are undergone during anomalous co-deposition and the expected resulting surface morphology. Initially cobalt deposits onto the substrate surface by normal deposition. As the deposition occurs the pH changes in the vicinity of the cathode to a level significant enough to allow the precipitation of zinc-hydroxide, (pH5.25), that is seen as whiskers on the surface. These whiskers can then be reduced to metallic zinc providing a zinc rich layer that prevents the deposition of the more noble cobalt. The resulting average electrodeposit composition is therefore zinc rather than cobalt rich.

Orientation and morphology of the electrodeposit grains are important because they have a direct effect on the deposit ductility as susceptibility to hydrogen embrittlement. Zinc itself is of concern when considering hydrogen embrittlement, because although it does have a reasonably high cathode efficiency compared to other types of plating systems, (typically >90% [135]), it can cause significant hydrogen embrittlement effects. Raub and Knodler attributed this in part to occluded zinc hydroxide in the electrodeposits [136]. If the mechanism of zinc-hydroxide reduction to zinc metal results in hydrogen being passed into the metal substrate, this would be of concern for zinc-cobalt electrodeposits. This is because they are assumed to form by the anomalous co-deposition mechanism that relies on the formation of zinc-hydroxide (detected as whiskers by SEM) on the deposition surface [17].

During the time parameter investigation the cathode efficiency, only reached 80% which is low compared to the values commonly quoted in the literature for zinc-cobalt electroplating, typically >95% [20, 137, 138]. The lower cathode efficiency at the start of the series could be attributed to greater relative weighing errors involved with a smaller mass change. However, it is probably due to the composition of the initial layer that is formed being richer in cobalt than the rest of the coating. The nodular appearance of the typical electrodeposit also may indicate hydrogen being present at the cathode, which may also account for the lower efficiency observed [139].

ELECTRODEPOSIT EXAMINATION

Electroplated Copper Shim Investigations

The initial electroplated layer and its hydrogen diffusion coefficient has been shown to be an important factor in the subsequent embrittlement seen for zinc-alloy electroplated specimens, so it was vital to determine its composition [7, 18]. The initial electroplated layer in standard zinc-cobalt electrodeposits appeared to be rich in cobalt, compared to the typical average composition of <1%. However, the EDAX technique used to determine the cobalt content for both series suffered from interference problems from the secondary iron peak being very close to the primary cobalt peak in the spectrum. This overlap became more significant when the coating thickness was under 2.0μm, because of the strong signal was produced by the steel substrate[137]. The noble metal composition measured by EDAX for the thinnest electroplated coating, the initial layer, has the greatest error margins, both for weighing inaccuracy and interference difficulties.

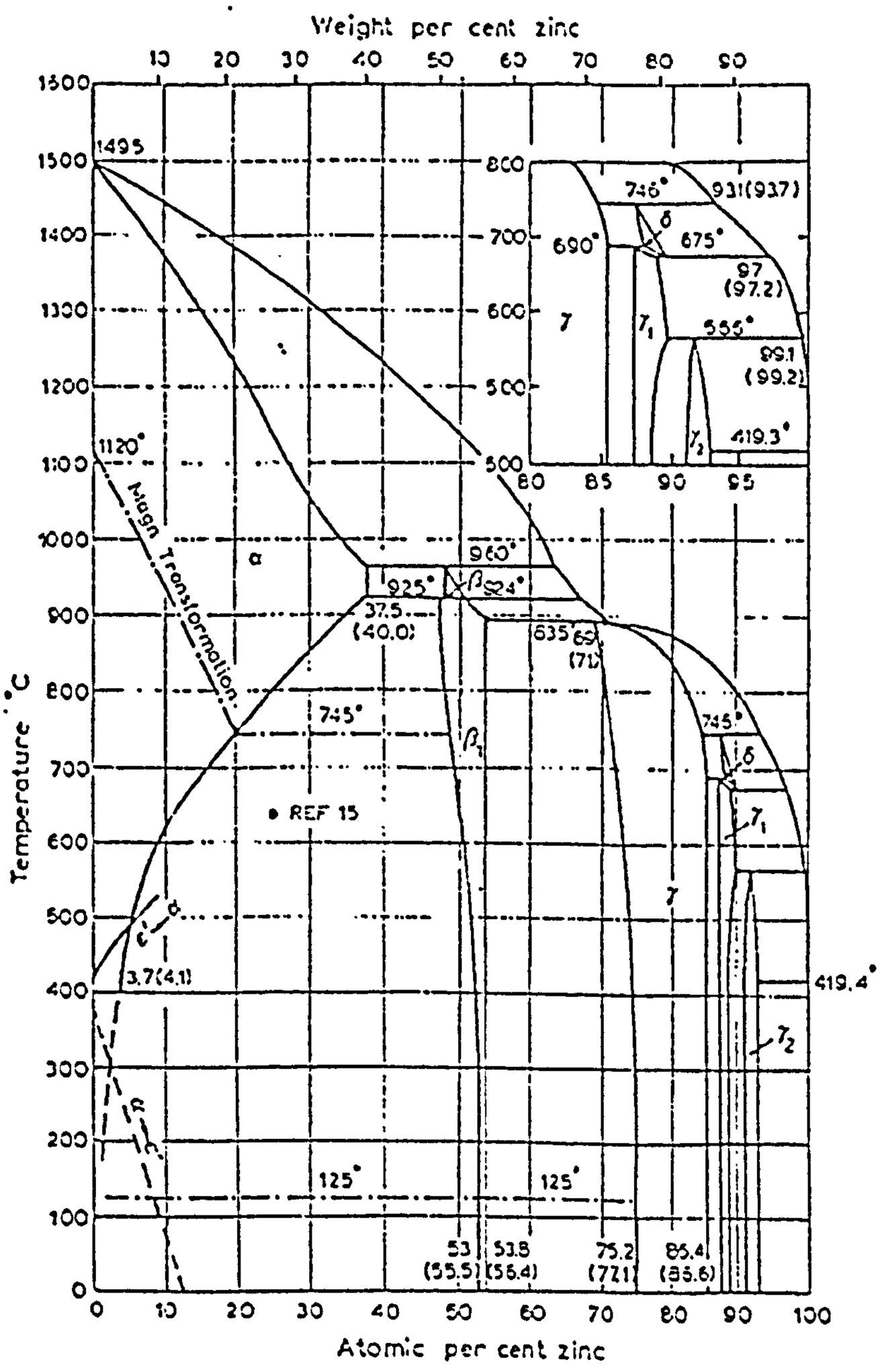
Despite the same trend being observed for both the zinc-cobalt series another method was needed to confirm the actual level of cobalt present and so a copper shim was electroplated using the standard zinc-cobalt electrolyte to counteract the EDAX interference problems [103]. The results obtained from the mounted and polished strip only differed in the initial electroplated area where the specimen had been electroplated for the shortest length of time. This area was shown to have a cobalt composition of 5% compared to the 3% cobalt seen in the same zone with the time parameter investigations performed on a steel shim. This 5% figure maybe a more accurate value, as over compensation for the EDAX interference effect with electroplated steel specimens may

have occurred. Published work on a similar zinc-cobalt alloy quoted a 10% cobalt composition in the early stages of electroplating [140]. Further surface techniques (XPS and Auger depth profiling) were employed to determine an exact cobalt content in this region and confirm which was the more accurate result.

XPS Analysis

The phase of cobalt that is deposited from a zinc-cobalt electrolyte has been shown to have a significant effect on the amount hydrogen that is absorbed by the electrodeposited layer on the substrate surface [140]. An equilibrium diagram for zinc-cobalt is shown in FIGURE 101, which demonstrates the phases of zinc-cobalt that can be formed under the conditions employed in this study [141].

FIGURE 101: Zinc-Cobalt Equilibrium Diagram



Dille and co-workers investigated 200μm thick pure cobalt electrodeposits and showed that there was a relationship between the solid phase present and its ability to trap hydrogen next to the substrate surface [142]. The β (FCC) cobalt phase determined by x-ray diffraction (XRD) has been shown to give a higher surface hydrogen content than the α form, which corresponds to a larger amount of absorbed hydrogen. The β (FCC) phase was shown to increase with lower deposition temperature and a more acidic electrolyte. This could have a significant effect on the hydrogen embrittlement of a specimen. However, Fratesi and co-workers used an XRD technique to determine that the crystal structure of cobalt in well formed, compact zinc-cobalt electrodeposits was the α form, so further investigations of this type were not under taken in the present study [143].

Higashi used the XPS technique to determine that the cobalt present in zinc-cobalt electrodeposits was in the metallic state. This was established from examination of the binding energy value obtained (778.4 eV) once the scan had been integrated using a multi-channel analyzer [110].

XPS analysis of zinc-cobalt electroplated specimens under taken in this work, shown in FIGURE 45, confirmed the compositional elements that were present in the different coatings. Significant background scatter made an exact level or chemical state hard to determine. This was probably due to the low level of cobalt that was present (<1%). It was expected that metallic cobalt would be present if anomalous co-deposition had occurred. A high level of oxygen was detected throughout the thickness of the electrodeposit, probably due to the presence of zinc hydroxide. This combined with the low level of cobalt observed provided evidence that anomalous co-deposition of the zinc-cobalt electrodeposits was occurring. However, further investigations were still necessary to determine an accurate elemental level in the interlayer area [108].

Auger Depth Profile

Depth profiles of unbaked 0.2μm thick zinc-cobalt electrodeposits were examined by progressive ion beam etching. The technique was not sufficiently sensitive to detect cobalt enrichment in coatings deposited at the standard pH4.2 zinc-cobalt electrolyte,

shown in FIGURE 48. The effect of plating at lower pH will be discussed in a later section.

PARAMETER VARIATION

Temperature

FIGURE 39 illustrates that an increase in temperature of the zinc-cobalt electrolyte resulted in an increase in cobalt content in the electrodeposit [116, 132]. There was an optimum range below 50°C, in which the electrodeposited cobalt content remained relatively constant. Above 50°C there was a rapid rise towards 60°C at the end of the examined temperature range, this effect has also been observed for zinc-cobalt alkaline systems [144]. The slow initial increase in cobalt content may be linked to an increasing buffer capacity of the bath sulphate ions with a rise in temperature up to 50°C. After this the buffer capacity can no longer be maintained and the cobalt content rises sharply probably due to increased thermal convection of the ions. Fukushima has also observed this effect in zinc-nickel electrodeposits, which generally use temperature as the principle method for controlling their nickel content[145]. The stagnant series consistently showed a higher level of cobalt in the electrodeposit compared to an agitated specimen electroplated under the same conditions. This confirmed previous findings by Verberne and Narasimhamurthy [116, 144].

FIGURE 102: Variation of Visual Brightness of Zinc-Cobalt Specimens with Temperature

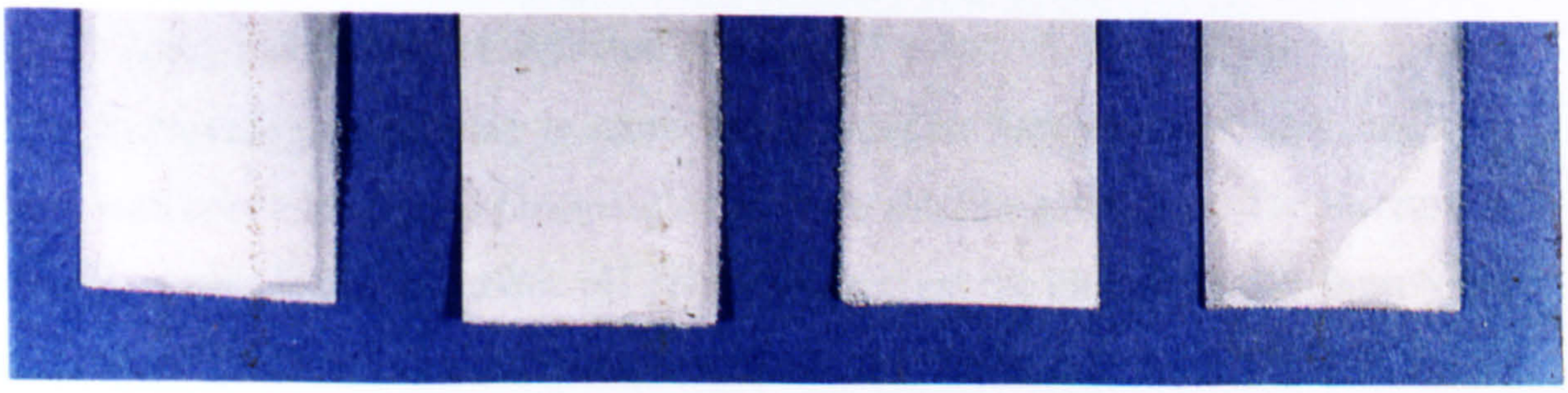


FIGURE 102 shows visually that the electrodeposit was largely unaffected by the change in electrolyte temperature. The deposits all had a reasonably fine grain structure but surface roughness decreased slightly with temperature, demonstrated by improved brightness on visual inspection. This may be linked to more hydrogen being present at the cathode at high temperatures, due to higher diffusion rates disrupting the formation of the electrodeposit and providing numerous nucleation sites[132].

There was a slight but steady reduction in cathode efficiency with the increase in temperature and cobalt concentration of electrodeposit. This commonly observed consequence has been attributed to an increase in cobalt ions in the diffusion layer at the cathode through increased rates of diffusion, conductivity[132] and convection in the bath, which also decreases the polarisation activation [138]. The increased temperature may also increase the rate of diffusion of hydrogen ions to the cathode, reducing the efficiency.

PARAMETER VARIATION

pH

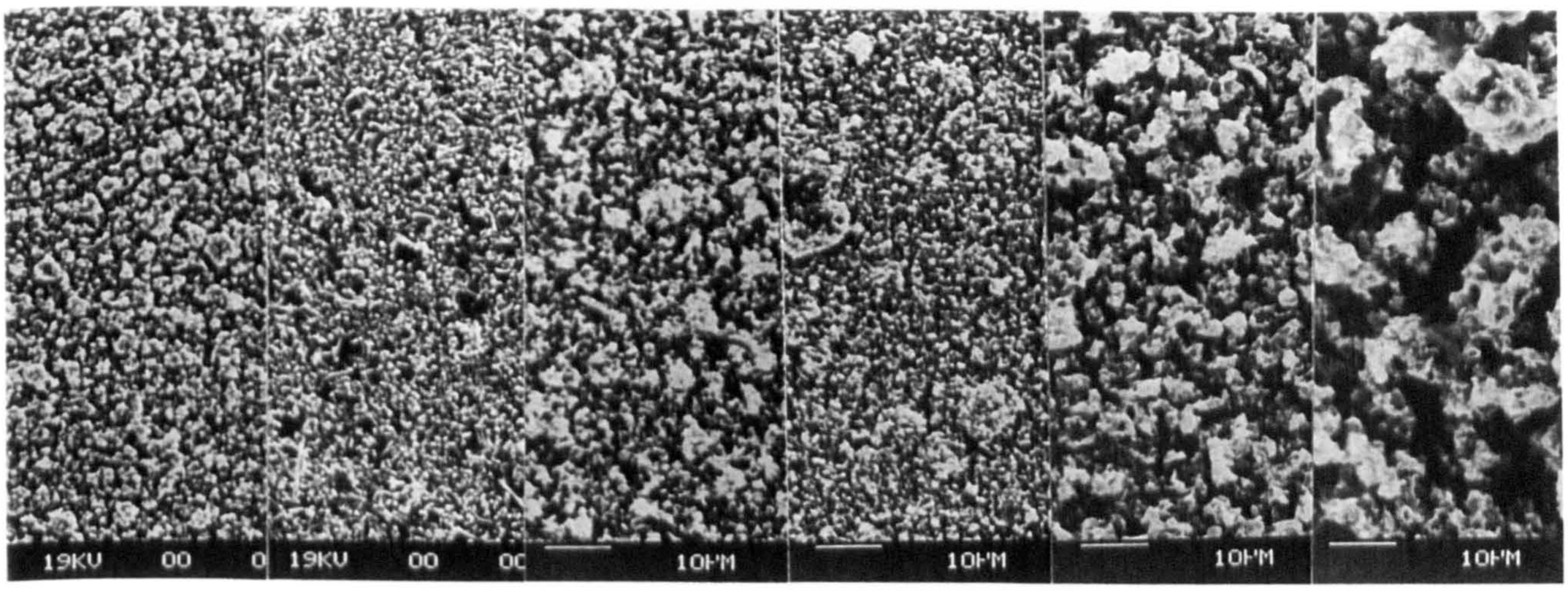
FIGURE 40 shows that there was an optimum pH range observed for the zinc-cobalt electrolyte between pH2 and 5 when the desired <1% cobalt content was attained. There was a rise in the cobalt content seen in the electrodeposit at pH1 and this level dropped in the optimum range and then rose back beyond pH5 to 4%.

The higher level of cobalt present at pH values >pH5 is probably due to cobalt hydroxide being more easily precipitated at these pH values (6.54). The pH5.25 needed for zinc hydroxide precipitation is more easily attained first and will only begin to compete with cobalt hydroxide precipitation at more alkaline pH values. The increase in cobalt seen at pH1 is due to surface pH effects preventing the zinc rich layer from being formed, which precludes zinc deposition. Without zinc hydroxide suppressing it, cobalt is more easily deposited and so the surface is rich in cobalt. An increase in pH then allows anomalous co-deposition to occur in the usual manner.

Many workers have examined the effect of change in pH on the electrodeposition of zinc-cobalt alloys and have found composition fluctuations outside a constant

'optimum' band that provides a consistent deposit [116, 132]. However, the pH band over which a constant cobalt composition was achieved has only been shown for pH4.5-5.5, not the more extensive band demonstrated in this work.

FIGURE 103: Variation of Specimen Morphology with pH



The change in morphology that was observed with changing pH, was minimal over the series examined, as shown in FIGURE 103. At more acidic pH values the grain size of the electrodeposit appeared to be smoother and finer. Abd El-Halim has attributed this to an increase in nucleation sites corresponding to an increase in the cathodic polarisation of the specimen under these conditions as a result of hydrogen production [138]. Certainly the pH change affects the composition of the electrodeposit and this alone may account for the slight change in morphology that is observed.

The current efficiency of the system increases with more acidic electrolyte until pH2 from where it gradually decreases again. These findings are contrary to literature observations that state the current efficiency increases with an increase in pH[138]. However, they may be explained by the change in composition of electrodeposit that is formed under these conditions.

ELECTRODEPOSIT EXAMINATION

Auger Depth Profile

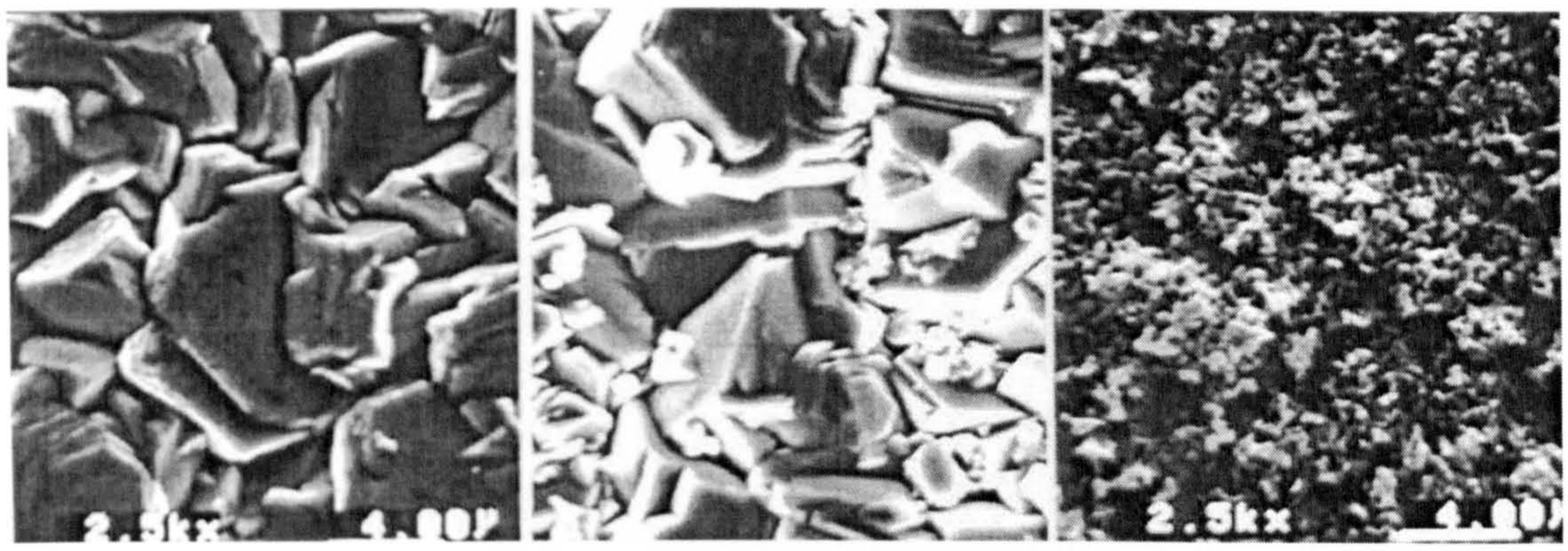
The Auger depth profile obtained for a 0.2μm zinc-cobalt electrodeposit formed at pH4.2 did not detected cobalt enrichment, as shown in FIGURE 48. However, cobalt enrichment was detected for a 0.2μm zinc-cobalt electrodeposit formed at pH1, by Auger depth profiling as shown in FIGURE 51. The layer of cobalt was presumed to be thicker at a lower pH of 1, and so easier to detect, due to the longer time needed to establish the surface pH of 5.25 required for the onset of anomalous co-deposition. This noble metal enrichment also occurs with zinc-nickel electrodeposits and identification of the nickel enrichment was only seen under acidic conditions (pH2), rather than standard pH values (pH5), probably due to detection limits[18]. The cobalt content of the layer may be responsible for the decrease in cathode efficiency of the system, when the pH of the electrolyte is of a level to allow enrichment to occur more readily. Fukushima similarly showed a link between noble metal content and current efficiency from his observations with binary zinc-iron group alloys. This work was discussed fully in Chapter 1, FIGURE 22 [110, 111].

PARAMETER VARIATION

Current Density

FIGURE 104 demonstrates that variation in the deposition current density produced the most pronounced visual differences in the zinc-cobalt electrodeposits. As the current density increased there was a direct increase in the quantity of electrodeposited material. Variation of current density while maintaining a constant electroplating time, results in a change in the total charge passed to the specimen and at very low current densities this causes a very thin coating to be electrodeposited. This condition is similar to the shortest time investigation carried out previously and exhibits the same compositional trend.

FIGURE 104: Variation in Specimen Morphology with Current Density



1 5 10

Increasing current density (mA/cm^2) ⟶

The composition varied as expected in the current density range investigated as shown in FIGURE 41. The quantity of cobalt in the electrodeposit remained relatively constant except for current densities below $1mA/cm^2$, which had high cobalt content. At these low current densities a normal deposition mechanism occurred leading to higher levels of cobalt being detected in the electrodeposit than were present in the bath. This was confirmed by Fukushima, as shown in FIGURE 22 [110, 111]. The level of cobalt in the deposit then fell to a plateau region that began at $1mA/cm^2$, the transition current density that heralds the start of anomalous co-deposition.

This is assumed to happen because a pH rise at the surface of the cathode allows the precipitation of zinc hydroxide and so the cobalt percentage seen in the electrodeposit is less than in the electrolyte. Increasing the deposition current density beyond the range investigated in this work, is predicted to result in a significant increase in cobalt content of the electrodeposit. (i.e. reversion to the usual type of deposition expected from the electrochemical series). This would be shown by a dramatic increase in cobalt percentage in the electrodeposit, due to a suitable rise in pH at the cathode, allowing the precipitation of cobalt hydroxide [120]. Many workers have also observed the same trend within the current density range investigated [116, 132, 137, 138, 146]. Their interpretation of the results corresponds to the Fukushima pH variation model that has been presented and discussed in this work.

Generally the appearance of the zinc-cobalt electrodeposits became shiny as the current density was increased but darker at the highest current density examined[138]. The nodular appearance of the coatings was reduced as the current density was increased. Zinc hydroxide whiskers usually visible on the specimen surface were absent with a more crystalline deposit was seen [147]. The quality of the electrodeposit decreased at current densities ≥100mA/cm^2, which may be linked to increased hydrogen production at the cathode during electroplating causing a more crazed deposit and preventing dendritic growth [133, 138, 148, 149]. Further evidence for this may be a slight drop in cathode efficiency observed for the system at higher current densities, indicating that more hydrogen may be being passed into the metal substrate under these conditions. However, Knodler believed that hydrogen evolution at the cathode may produce an inhibiting effect that causes orientated growth of zinc electrodeposits, which is contrary to findings of the current study [136].

HYDROGEN EMBRITTLEMENT TESTING

Control Specimens

Cadmium, the standard industrial electroplated coating, was tested with zinc electroplated specimens and unplated specimens, in the baked and unbaked conditions. These were used as control specimens with which to compare all the other electroplated specimens and the mean time to failure data values are given in TABLE 24.

Cadmium electroplated specimens were shown to be embrittled and had a time to failure of 4.2 hours compared to the unplated specimens time to failure of 18.9 hours. Cadmium electroplated specimens baked under standard conditions regained their mechanical properties and showed a time to failure comparable to unplated specimens, as illustrated in FIGURE 61 in Chapter 3.

The zinc electroplated specimens tested showed a longer time to failure than cadmium electroplated specimens but they were still obviously embrittled having a time to failure of 5.6 hours, the standard baking treatment only produced 87% recovery, as shown in FIGURE 62 in Chapter 3. This could be due to a low diffusivity of hydrogen through zinc electroplate or less hydrogen being absorbed in the zinc electroplating process [97].

TABLE 24: Weibull Data for Control Specimens

Specimen	Unbaked TTF (Hours)	Baked TTF (Hours)
Cadmium	4.2	18.9
Zinc	5.6	16.4
Unplated	18.7	18.9

Standard Zinc-Cobalt Electroplated Specimens

Tensile specimens electroplated with the standard zinc-cobalt electrolyte showed a reduction in embrittlement compared to both cadmium and zinc control specimens. An average time to failure of 7.0 hours was seen for the unbaked specimens. This was a recovery on standard baking treatment of 89% compared to unplated control specimens (and 91% for 48 hours baking treatment), shown in FIGURE 66 in Chapter 3. The recovery of the failure time was probably aided by the general non-uniform, porous nature of the electrodeposits that allowed the diffusible hydrogen a clear evolution pathway. However, the incomplete recovery may have been due to a relatively hydrogen impervious initial layer that did not allow easy escape of hydrogen to the atmosphere during baking. This could have been cobalt or zinc rich in nature. If some hydrogen was to remain trapped in the coating after baking treatment, it may cause failure when stress is subsequently applied to the material.

Electrodeposited zinc has been shown to increase its quantity of retained hydrogen with storage time [136]. Knodler believed hydrogen in electrodeposits could be contained in supersaturated solution, trapped in voids and also formed by chemical reaction from occlusion of zinc hydroxide. He determined, by a series of extraction experiments, that the final suggestion was the most probable cause of the increased hydrogen levels in zinc electrodeposits. Due to the presence of zinc hydroxide in anomalous co-deposited binary coatings, the effect of a time delay after electroplating and before baking, on the embrittlement performance on zinc-cobalt electroplating, was investigated.

A delay of 24 hours before standard baking decreased the time to failure for the specimens to 16.1 hours compared to those that had immediate baking with an average

time to failure of 16.6 hours. These results may be explained by the findings of Sharp. He states that release of hydrogen from low energy traps during baking may cause mobile hydrogen to become available to combine with higher energy traps, which under load facilitate rapid failure [31]. The time delay also may allow the chemical reaction proposed by Knodler to increase the level of retained hydrogen in the specimens, accounting for the decreased failure time.

However, a delay of 12 hours improved the time to failure for the specimens to 20.3 hours, shown in FIGURE 67 in Chapter 3. This may have been due to hydrogen diffusing out of the specimen or moving to irreversible traps where it was no longer able to affect the embrittlement of the specimen [58]. The time delay may not have been sufficient before baking to allow the chemical reaction with occluded zinc hydroxide in the coating to release hydrogen to lower the failure time. Indeed Knodler does report an incubation time required for the effect to occur, but is vague about on set of a visible response at these duration times. These results are summarised in TABLE 25.

TABLE 25: Weibull Data for Standard Zinc-Cobalt Specimens

Specimen	Unbaked TTF (Hours)	Baked TTF (Hours)
Zinc	5.6	16.4
Zinc-cobalt	7.0	16.6
Zinc-cobalt 48 hour bake	-	17.2
Zinc-cobalt 12 hour delay	-	20.3
Zinc-cobalt 24 hour delay	-	16.1

Modification of the Standard Zinc-Cobalt Electrolyte

Investigations were undertaken to determine how the increase in time to failure from 5.6 hours for zinc specimens to 7.0 hours for zinc-cobalt specimens was possible with an average cobalt composition of <1% (by EDAX). It was suspected that the enriched cobalt interlayer shown to be present by the parameter and electrodeposit experiments was the reason for these findings. If the cobalt enrichment at the interface of the

specimen was manipulated to increase or reduce this layer, the subsequent effect could be used to show its influence on the uptake of hydrogen into the specimens during electroplating. Pure nickel is known to be a barrier to hydrogen because it has a low diffusion coefficient, about $8x10^{-10}$ cm^2s^{-1} [18]. We postulated that the cobalt interlayer could act in a similar way as a barrier to hydrogen. This information could be used to determine a way of maximising the performance of zinc-cobalt electroplating by improving its embrittlement index in the baked and unbaked condition.

Change in pH of Standard Electrolyte

The pH of the electrolyte was shown to be an important factor on the cobalt composition of the electrodeposit, so pH variation of the electrolyte was assessed for the tensile specimens. The pH of a standard zinc-cobalt electrolyte, (nominally pH4.2), was both increased and decreased for the pH examinations and the results are given in FIGURE 68 of Chapter 3. An alkaline pH of 5 was found to be detrimental to the embrittlement performance and it reduced the average time to failure for the specimens to 4.5 hours, more embrittled than the average pure zinc electroplated specimens. However, a more acidic pH3 electrolyte also showed no improvement and reduced the time to failure to 6.3 hours. Rather surprisingly pH1 produced the only improvement, increasing the time to failure to 7.2 hours. The pH results are summarised in TABLE 26.

The electrolyte that was pH1, produced an increase in cobalt composition of the electrodeposit, as shown by the parameter variation investigations. As the EDAX technique could only give an average compositional measurement it suggested that the interlayer formed at this pH was either initially much richer in cobalt composition or a slightly enriched cobalt layer was being deposited for a longer period giving a 'thicker' interlayer. The parameter variation data, hydrogen embrittlement testing at different pH values and depth profile information combined, provides evidence that there was detectable cobalt enrichment at the interface from a pH1 electrolyte. This enrichment showed a significant embrittlement reduction compared to standard pH zinc-cobalt electrolytes. A similar result has been reported for zinc-nickel electrodeposits produced at pH2 [18].

TABLE 26: Weibull Data for Change in Electrolyte pH

Specimen	Unbaked TTF (Hours)	Baked TTF (Hours)
Zinc	5.6	16.4
Zinc-cobalt pH4.2	7.0	16.6
Zinc-cobalt pH5	4.5	-
Zinc-cobalt pH3	6.3	-
Zinc-cobalt pH1	7.2	-

Compositionally Modulated Multi-Layer Deposits

To further investigate the effect of the interlayer, it was decided to use the CMM technique where electroplated layers are used to produce a coating with superior performance. While this has been used extensively for corrosion resistance [15, 125], this work examined the effect on embrittlement performance and the results are summarised in TABLE 27.

TABLE 27: Weibull Data for Cobalt Interlayer Specimens

Specimen	Standard TTF (Hours)	Cobalt Interlayer TTF (Hours)
Zinc	5.6	7.5
Zinc-cobalt	7.0	7.2
Zinc-cobalt pH1	7.2	-
Zinc-cobalt baked	16.6	19.7

Initially a 0.5μm layer of cobalt was deposited on the tensile specimen and then an electroplated zinc layer was deposited over this. The effect, as shown in FIGURE 70 Chapter 3, was to increase the time to failure for the 2-layer system to 7.5 hours, which was not only an improvement on pure zinc electroplating, but also for zinc-cobalt specimens electroplated at pH1. The cobalt interlayer was assumed to be responsible for the observed partial reduction in embrittlement effects for zinc electroplating. A thicker cobalt layer would therefore presumably further reduce the quantity of hydrogen

absorbed and the observed embrittlement. This was shown by the pH1 specimens already mentioned, that had the thickest cobalt interlayer and correspondingly the longest time to failure.

A similar effect was also seen with specimens that had been plated with 0.5μm of cobalt followed by standard zinc-cobalt electroplating over the top, shown in FIGURE 71 Chapter 3. There was an improvement in embrittlement performance giving a time to failure for the specimens of 7.2 hours, equalling the zinc-cobalt specimens electroplated at pH1. Both these methods produced specimens that had very narrow standard deviation bands [99].

When specimens electroplated in this way were baked using standard conditions, they appeared to completely recover their mechanical properties having an average time to failure of 19.7 hours, shown in FIGURE 73 Chapter 3. These results confirm the theory that the initial layer to form on the substrate is of particular significance to the hydrogen uptake and loss during baking treatment. The cobalt interlayer in the DBT (dual bath technique) specimen acted as a barrier to hydrogen so that during baking the hydrogen escaped to the atmosphere rather than diffusing into the steel substrate.

The experimental results for these specimens had a much larger standard deviation than the unbaked specimens. However, as more procedures were required to be performed on each specimen it was likely there would be a greater standard deviation. (A residual austenite microstructure has been shown to act as a hydrogen reservoir, however, the specimens are very unlikely to contain austenite due to the series of heat treatments that were undergone [150]). Hydrogen in the coating of these specimens was more efficiently removed by the recommended standard baking treatment, due to the cobalt interlayer, which is why they had regained their mechanical properties.

The effect of altering the noble element in the electrolyte to nickel or addition of another element to the zinc-cobalt electrolyte was also examined and the results will be discussed later in this Chapter.

Ultimate Tensile Strength

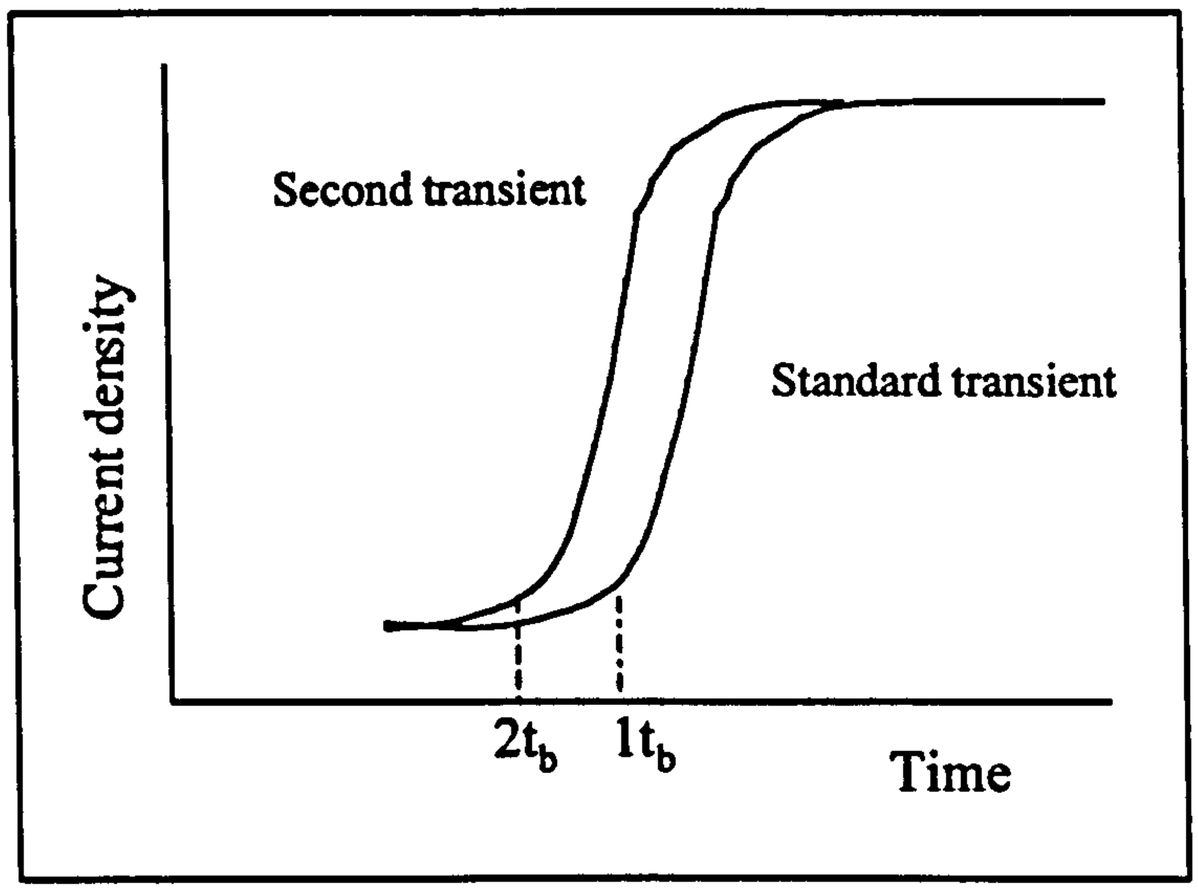
When slow strain rate fracture stress values are close or equal to the original tensile strength of the sample, it generally indicates that there is no or very little hydrogen embrittlement. FIGURE 56 demonstrates that the baked electroplated zinc-cobalt specimens did not have an altered UTS, despite exhibiting embrittled behaviour by not regaining 100% time to failure values. FIGURE 57 shows that zinc-cobalt electroplated specimens, formed under various conditions but not baked, resulted in embrittlement seen by shorter time to failure and also corresponding lower tensile strength values.

PERMEATION TESTING

Electrochemical measurements were used to assess the hydrogen uptake and permeation that was responsible for the observed embrittlement effects. As with all permeation testing the shape of the transient that is produced is indicative of the behavior of the charging hydrogen that is passing through a metal specimen and the interaction that might occur during the measurement period. For unplated steel which is cathodically charged there are several situations that may alter the shape of the curve that is seen.

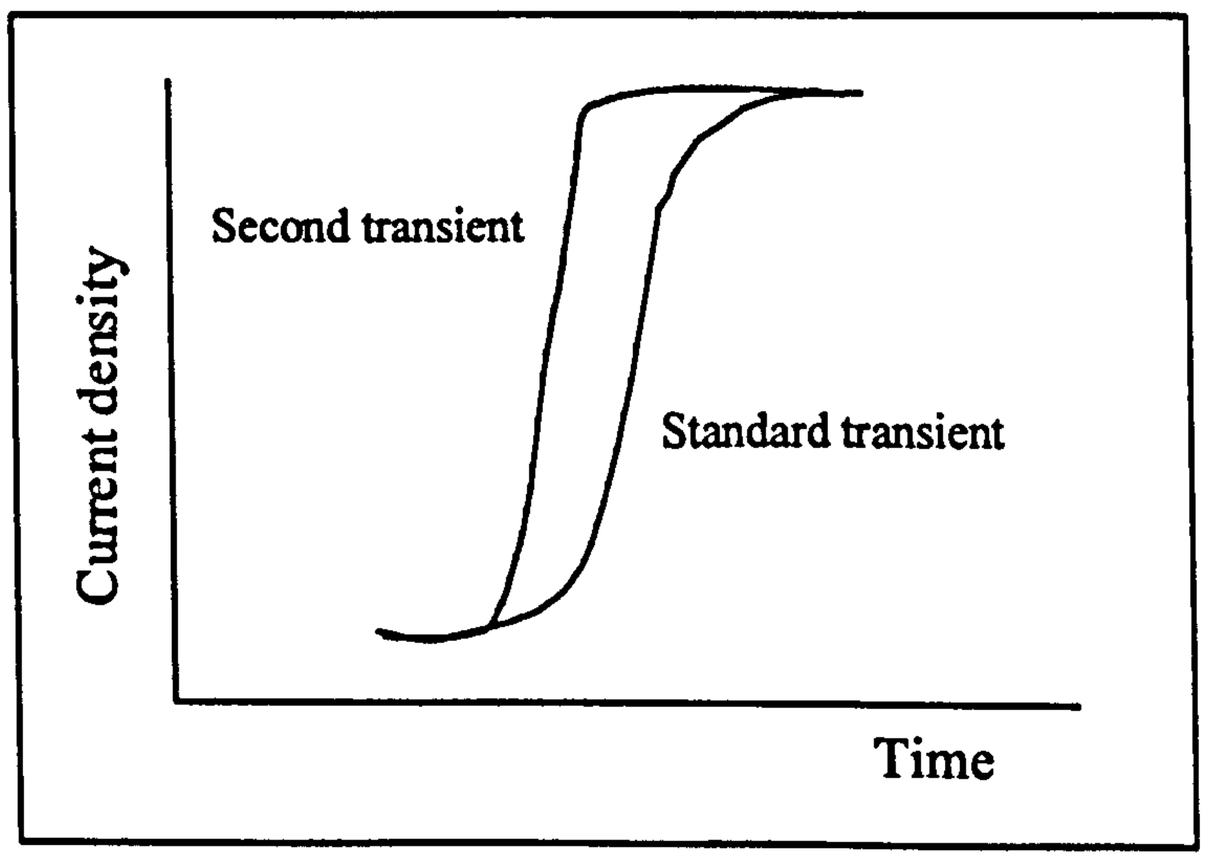
As hydrogen passes into a bare metal specimen that is being charged, traps within the microstructure of that specimen are filled with hydrogen in a number of ways. Turnbull illustrated that if a specimen is charged with hydrogen and then recharged after a suitable decay time, to allow the diffusible hydrogen to escape, the breakthrough time of the second transient is shorter than that of the first, as illustrated in FIGURE 105 [58]. This is due to the irreversible traps in the microstructure being filled during the first charging experiment and so the hydrogen that is passed through the metal in the second experiment no longer has these areas to fill.

FIGURE 105: Breakthrough Time and Position of Curve



Another visible phenomenon associated with the filling of traps is seen in the shape of the rising portion of the permeation transient. Traps in a metal are filled with charging hydrogen as it permeates into the specimen. If a specimen is charged for a second time, the slope of the rising transient becomes earlier and steeper, resulting in a reduction in the rise time of the curve, as illustrated in FIGURE 106.

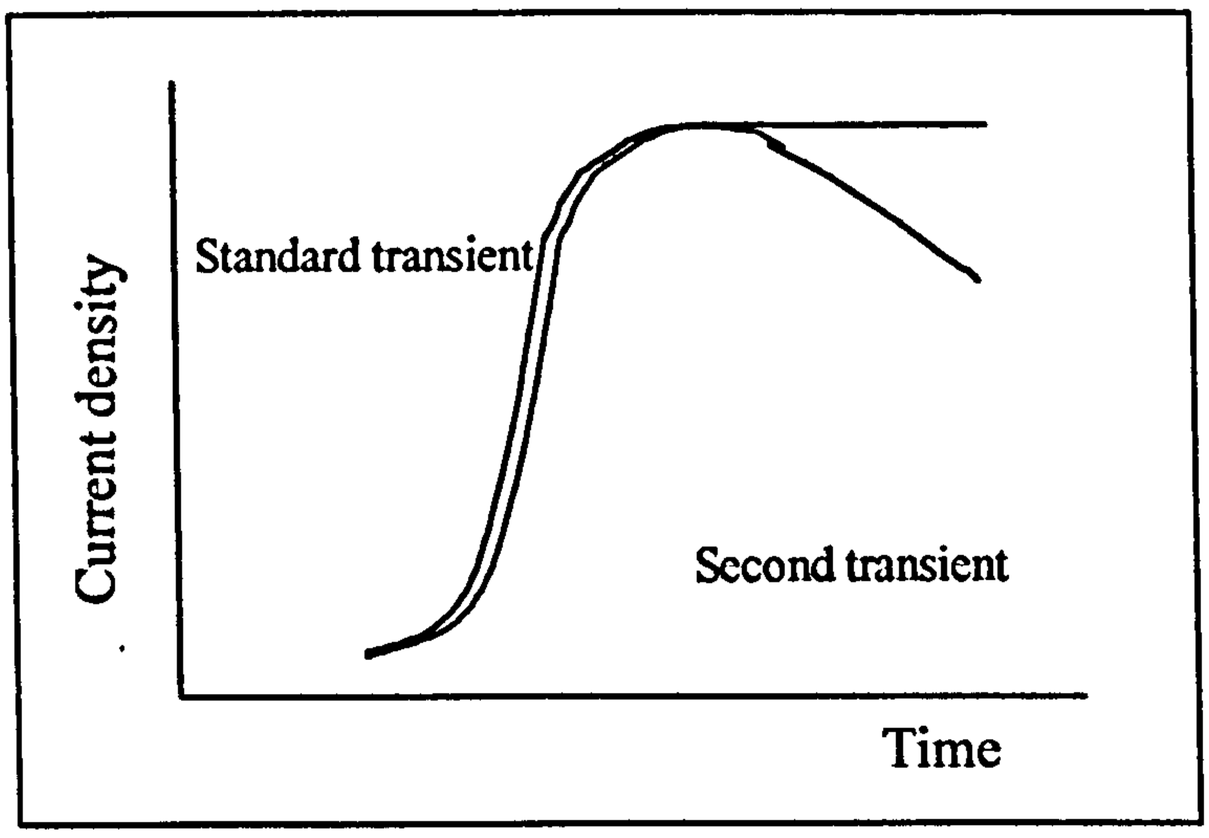
FIGURE 106: Rise Time and Shape of Curve



The other area of the permeation transient that can be affected by changes is the steady state section of the curve. This section can become misshapen and the level can drop causing a decrease in height of the transient, as the result of voids forming in the microstructure, as shown in FIGURE 107. Voids in the metals microstructure can collect

hydrogen and hence reduce the quantity that is detected in the exit side of the cell over time. These voids can be accompanied by blistering in metal specimens and surface damage, if the current being used is great enough.

FIGURE 107: Amount of Hydrogen Permeated and Decay of the Transient

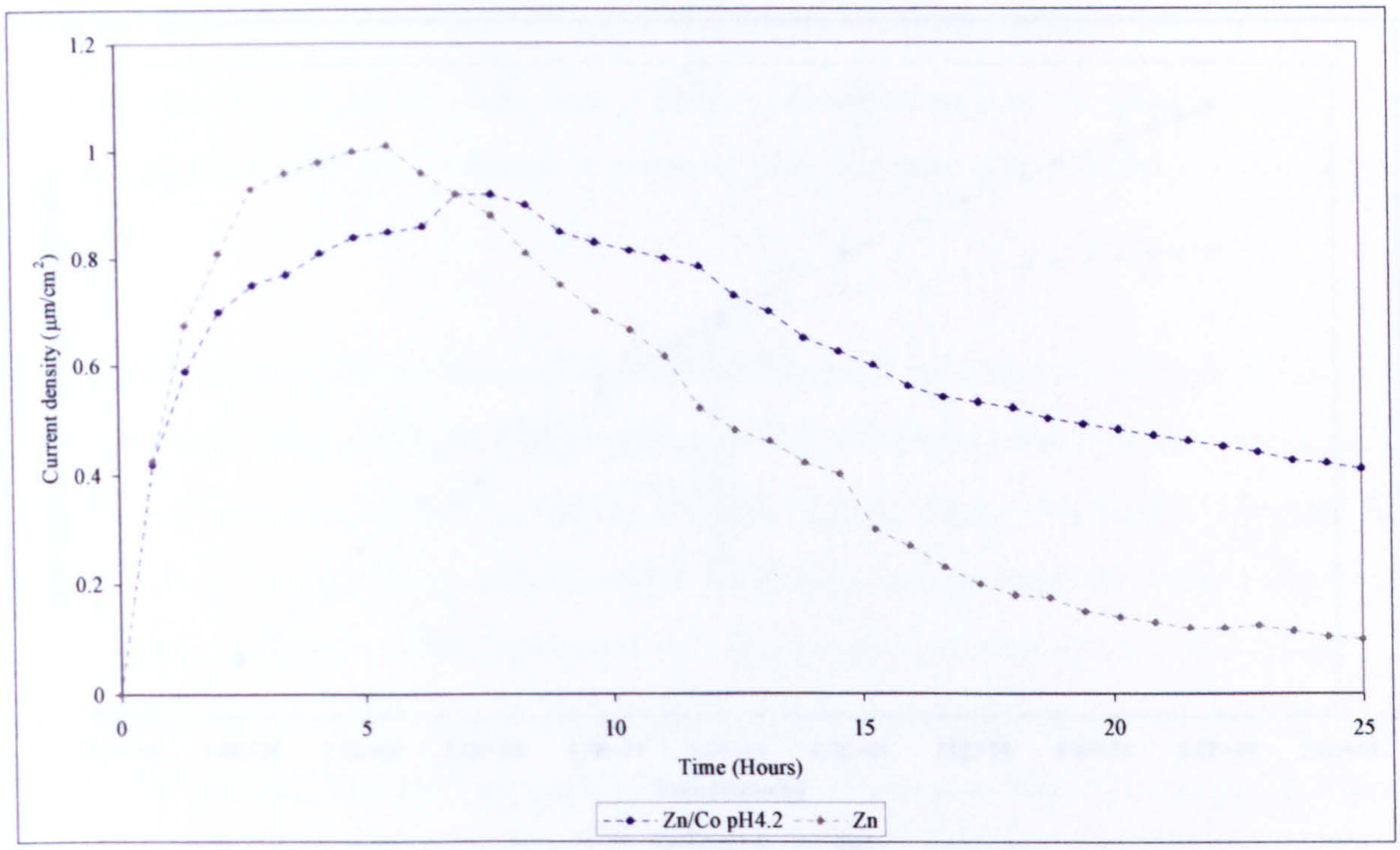


Type of Electroplating

The permeation testing was used to relate the amount of hydrogen permeated by each type of electroplating with the effect that was seen by the embrittlement observations. During electroplating only a small amount of hydrogen permeated the shim, but after plating, (unlike hydrogen charging experiments), the hydrogen permeation current continued to rise for a considerable time before slowly reaching a maximum and finally beginning to decay. This indicates that hydrogen was diffusing from the electrodeposit (the coating was becoming depleted in hydrogen), into the steel after the electroplating process had stopped. In the case of zinc-cobalt electroplating there was still significant hydrogen permeation after 25 hours, as shown in FIGURE 108 (peak at 8 hours), indicating that any de-embrittlement treatment should be carried out immediately to minimise the quantity of hydrogen entering the steel.

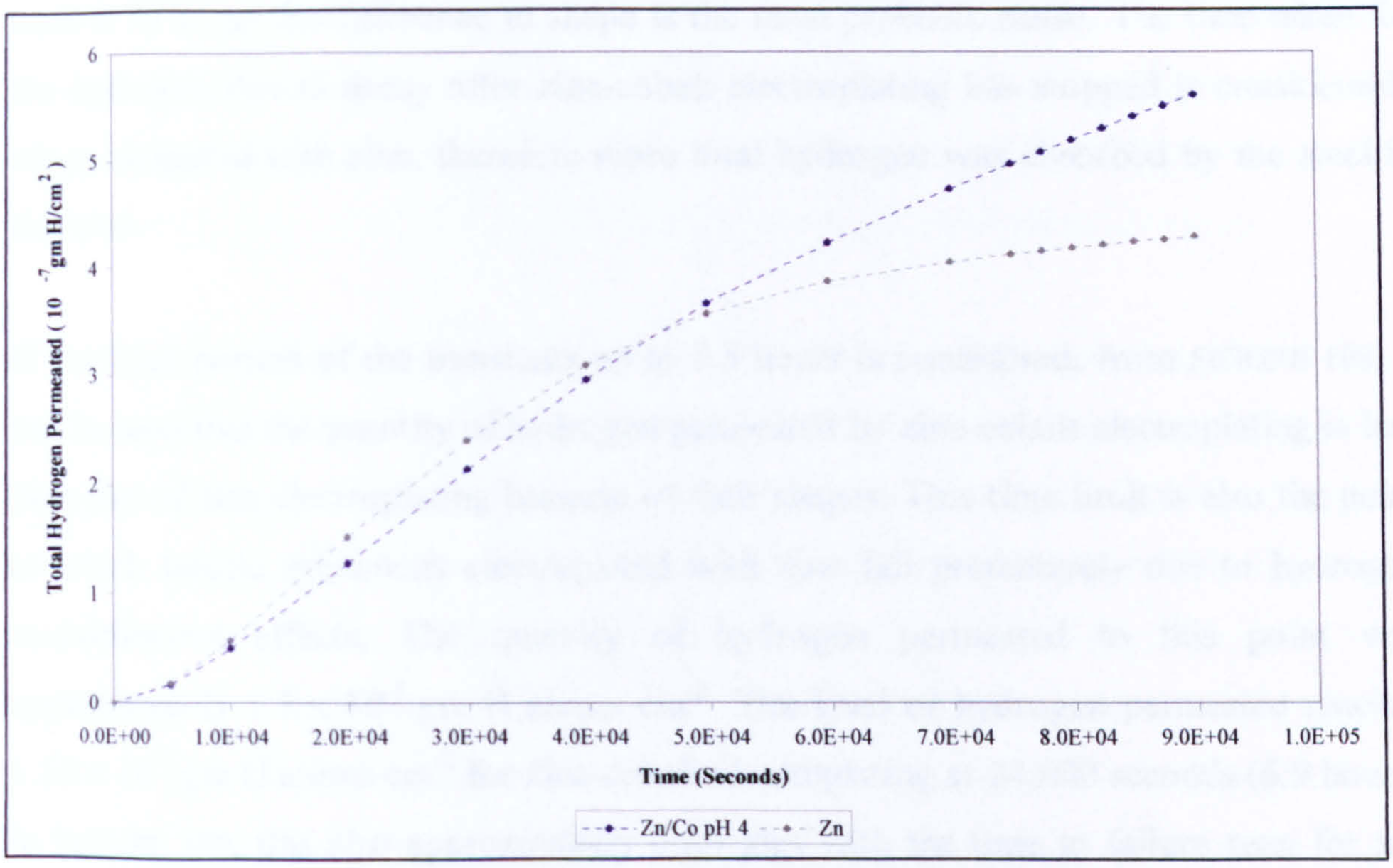
FIGURE 108 demonstrates the shape of a typical hydrogen permeation transient produced for zinc and zinc-cobalt electroplating.

FIGURE 108: Permeation Transients for Zinc and Zinc-Cobalt Electroplating



The rise of the zinc transient shown in FIGURE 108 is much quicker than that seen for standard zinc-cobalt electroplating. However, despite the steeper rise and greater height of the transient, the fall of the zinc transient is much more rapid and complete than is seen for zinc-cobalt electroplating. The effect that is seen in zinc-cobalt electroplating is probably due to the cobalt interlayer that has been shown by Auger depth profiling to form, as mentioned earlier in the discussion.

FIGURE 109: Amount of Hydrogen Permeated by the Type of Electroplates



Integration of the zinc and zinc-cobalt transients, as shown in FIGURE 109, provides the amount of hydrogen that is permeated during the test. These figures can be compared with the embrittlement results to show the effect that the permeated hydrogen has on the specimen. Zinc electroplated tensile specimens have a shorter time to failure than zinc-cobalt electroplated specimens but the total amount of hydrogen permeated in the failure time for zinc and zinc-cobalt specimens are relatively similar, as shown in TABLE 28.

TABLE 28: Comparison of Zinc and Zinc-Cobalt Electroplating

Electrodeposit	TTF(Hours)	H Permeated in Failure Time (10^{-7} gm H atoms cm^{-2})
Zinc	5.6	1.5
Zinc-cobalt	7.0	1.8

Thomasson reported that a hydrogen content of 1 ppm (1 x 10^{-6} H gms/gm Fe) may be responsible for hydrogen embrittlement seen in 4340 steel with a UTS of 1780MPa [91]. The levels suggested by other workers are as low as 0.15ppm, comparable with the values listed in TABLE 28 [151]. Temperature effects cannot be used to account for the

differences observed in the amount of hydrogen permeated, as both the electrolytes are used at 50°C, so the difference in shape is the most probable cause. The time taken for the hydrogen flux to decay after zinc-cobalt electroplating has stopped is considerable when compared with zinc, therefore more total hydrogen was absorbed by the steel in this case.

If the front portion of the transients up to 5.5 hours is considered, from FIGURE 108, it can be seen that the quantity of hydrogen permeated by zinc-cobalt electroplating is less than that of zinc electroplating because of their shapes. This time limit is also the point at which tensile specimens electroplated with zinc fail prematurely due to hydrogen embrittlement effects. The quantity of hydrogen permeated to this point was approximately 1.5×10^{-7} gm H atoms cm^{-2}. The level of hydrogen permeated reaches 1.52×10^{-7} gm H atoms cm^{-2} for zinc-cobalt electroplating at 24,000 seconds (6.9 hours) in FIGURE 109, this also approximately coincides with the time to failure seen for the tensile specimens. These findings illustrate the importance of using several techniques in conjunction with each other to explain the behaviour of experimental specimens.

Temperature of Experiment

The rate of hydrogen diffusion is a temperature dependant variable, being faster at higher temperatures [39, 87, 95, 151, 152, 153, 154.]. The electrolytes in this work were used at different operating temperatures, 25°C, 43°C and 50°C, so it was important to assess the effect this had on the transients that were produced for the different electrolyte types. Due to the experimental difficulties with heating the electrolytes used to different experimental temperatures, (causing alteration in conductivity and convection of the electrolyte ions), it was decided to assess this effect by charging a clean fresh unplated steel membrane in sodium hydroxide solution [87, 95].

It was important to consider the traps that were present in the steel membrane when the temperature charging experiments were undertaken to assess the amount of permeated hydrogen. If specimens were reused, then the latter transients produced from the membrane might yield shorter breakthrough and rise times (due to traps being filled in the earlier charging) causing confusion and yet greater difficulty in measuring the

already short time scales. For this reason the permeation transients that are shown in FIGURE 77 Chapter 3, are for fresh specimens that were prepared identically for each experiment. The permeation transients produced for the charging experiments were standard in shape with the latter part of the transient being a flat line. An increase in temperature produced an increase in hydrogen flux for the transients observed.

According to Arrhenius, EQUATION 19, change in experimental temperature should have a log scale effect on the amount of hydrogen that is permeated through a specimen in a given period of time. This is related to the heat of activation that is required for hydrogen diffusion to occur. Bockris experimentally determined the effect that temperature had on the diffusion coefficient, D, and developed EQUATION 23 to relate the changes that would be seen for a steel [87]. When the results were plotted as $\log_{10}D$ versus temperature (Kelvin), an Arrhenius plot, a linear relationship was clearly visible.

EQUATION 23: Diffusion Coefficient as a Function of Temperature

$$D = 4.47 \times 10^{-2} e^{-92220/RT} \text{ cm}^2/\text{s}$$

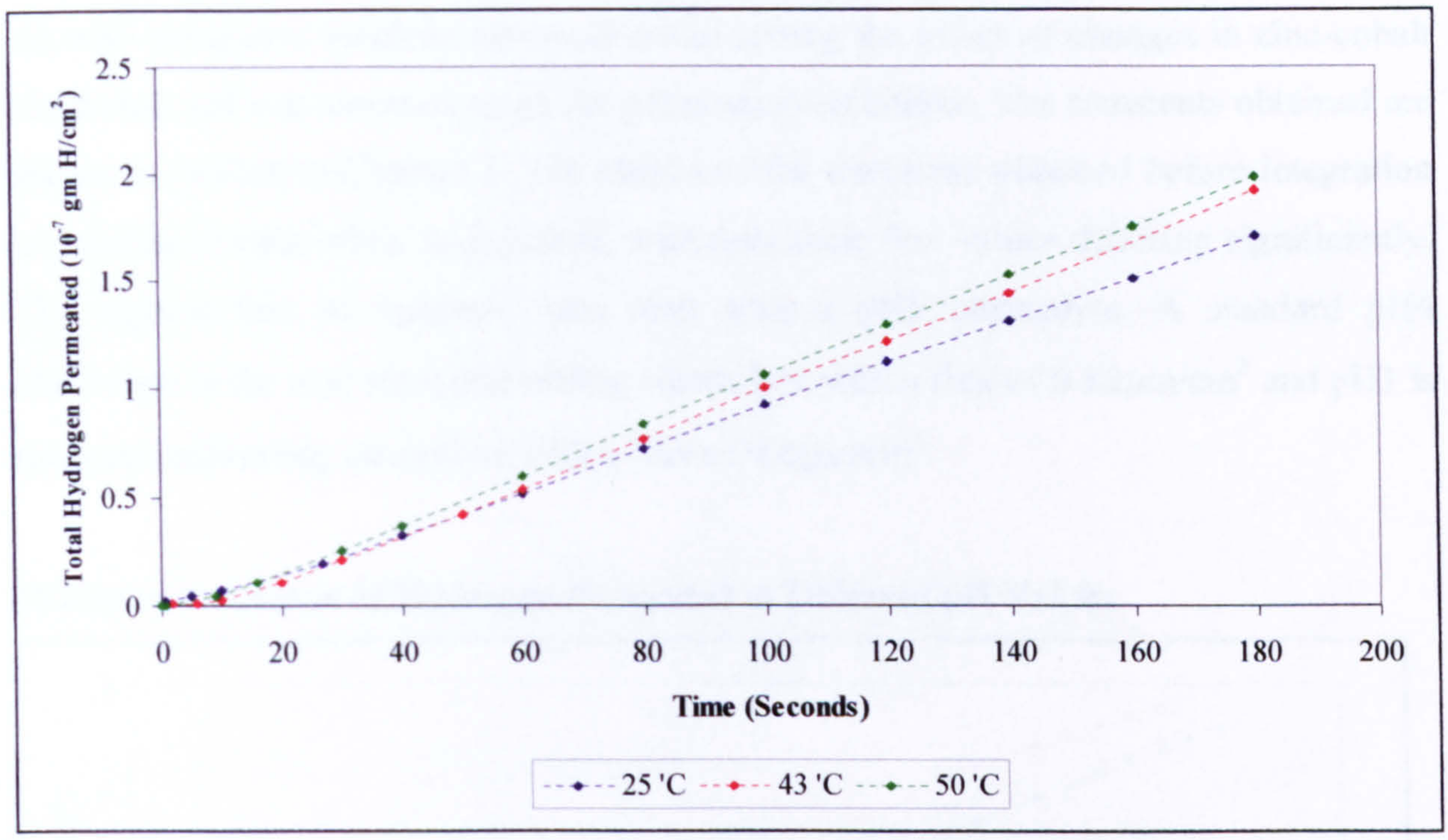
Where: R = universal gas constant

T = temperature (Kelvin)

The effect that performing zinc-cobalt electroplating at 25°C or 43°C instead of 50°C would have on the amount of hydrogen permeated into the steel substrate can be estimated using these transients. If it is assumed that the observed change in flux for the experiments is solely due to temperature differences and that C_0 is a constant, then it can be concluded that the D (diffusion coefficient) and t_b (break through time) change.

The amount of hydrogen permeated did not increase in the expected logarithmic fashion with an increase in temperature. The short break through time, which required measurement, combined with the thin shim and possible variations in its surface condition, may have resulted in experimental error of significant magnitude to mask the expected relationship.

FIGURE 110: Amount of Hydrogen Permeated for Different Temperatures



Integration of the curves in FIGURE 77 Chapter 3, gives the amount of permeated hydrogen as a function of time as shown in FIGURE 110. From FIGURE 110, it can be seen that the total amount of hydrogen atoms permeated varied little with temperature. TABLE 29 illustrates that a transient formed at 50°C was 1.2 times larger than the one formed at 25°C and a transient formed at 43°C was 1.1 times larger than the one formed at 25°C. Normalising the zinc-cobalt transient to either 25 or 43°C would reduced the peak height of the transient. However, the shape of the transient seen is still a critical consideration for the embrittlement seen for the specimen, as is the pH of the electrolyte being used.

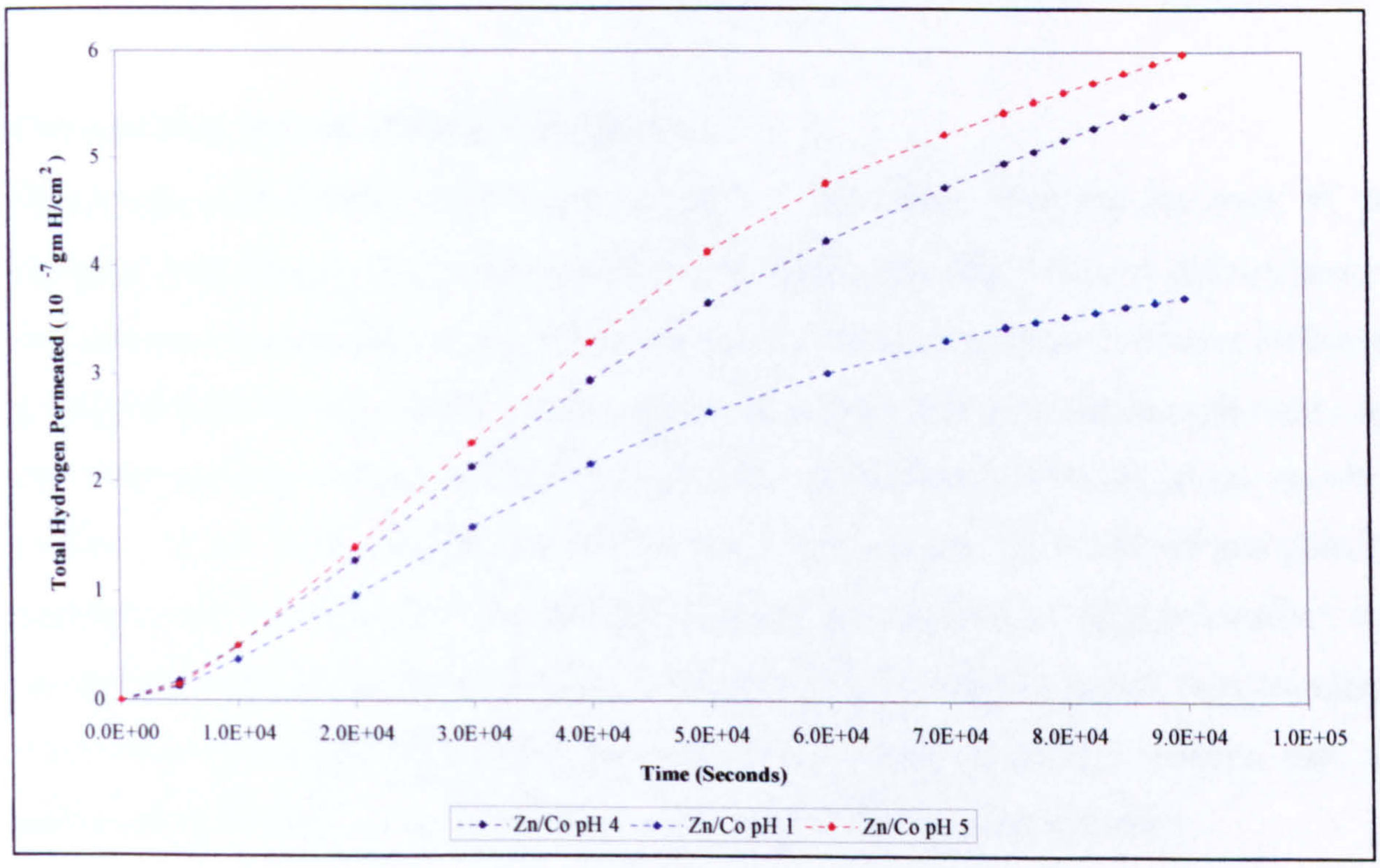
TABLE 29: Hydrogen Permeated as a Function of Temperature

Temperature (°C)	Total Hydrogen Permeated (10^{-7} gm H atoms cm^{-2})	H permeated at Temperature / H permeated at 25°C
50	2.0	1.2
43	1.85	1.1
25	1.7	1

pH of Electrolyte

As with parameter variation and mechanical testing the effect of changes in zinc-cobalt electrolyte pH was assessed using the permeation technique. The transients obtained are shown in FIGURE 75 Chapter 3. The shapes of the transients obtained before integration are similar to each other, as expected, with only their flux values differing significantly. The highest flux of 1μm/cm^2 was seen with a pH5 electrolyte. A standard pH4 electrolyte is the next most embrittling electrolyte with a flux of 0.82μm/cm^2 and pH1 is the least embrittling electrolyte with a flux of 0.6μm/cm^2.

FIGURE 111: Amount of Hydrogen Permeated at Different pH Values



Integration of the transients, shown in FIGURE 111, yields the total quantity of hydrogen that was permeated at the various pH values, the results mirror the flux order as shown in TABLE 30. The ranking is also duplicated by the embrittlement testing results, showing that until a critical value is reached, the lower the quantity of permeated hydrogen, the longer the time to failure observed. As with the zinc specimens the failure time and the total quantity of hydrogen permeated corresponded well and these results are given in TABLE 30. The longer time to failure seen with pH1 zinc-cobalt electroplated specimens was presumed to be due to the cobalt enriched initial layer that

had been shown to exist by the Auger depth profile results. This confirmed that the amount of cobalt at the interlayer was crucial to the embrittlement performance.

TABLE 30: Comparison of Zinc-Cobalt Electrolyte pH

Zinc-Cobalt Specimen pH	TTF (Hours)	Flux (μm/cm^2)	Hydrogen Permeated in Failure Time (10^{-7} gm H atoms cm^{-2})
1	7.2	0.6	1.3
4.2	7.0	0.8	1.8
5	4.5	1.0	1.0

Current Density and Diffusion Coefficient

Specimens electroplated with 8 μm of pure cobalt were prepared for each of the charging experiments that were undertaken to assess the effect current density had on the amount of permeated hydrogen. If specimens were reused then the latter transients produced from the membrane might produce data with shorter breakthrough times and rise times causing confusion. For this reason the permeation transients that are shown in FIGURE 112 are for specimens that had been not been reused. This allayed any possible problems with a change in breakthrough time and provided an undamaged surface that would not yield results incorporating bare steel effects with the cobalt measurements. As well as providing information on the effect change in current density had, the diffusion coefficient for cobalt was also estimated from these experiments.

FIGURE 112 shows the direct relationship between the charging current density and the height of the observed permeation transient. As expected an increase in charging current density increased the quantity of hydrogen that was permeated. The observed effect was much greater than that seen for either temperature or pH variation studies. Similar results were obtained for extraction transients obtained at different charging current densities in 0.2M sodium hydroxide solution by Berman et al [154]. They observed that if the charging current density was doubled the resulting peak ionisation current density of the extraction transient was also doubled.

FIGURE 112: Effect of Charging Current Density

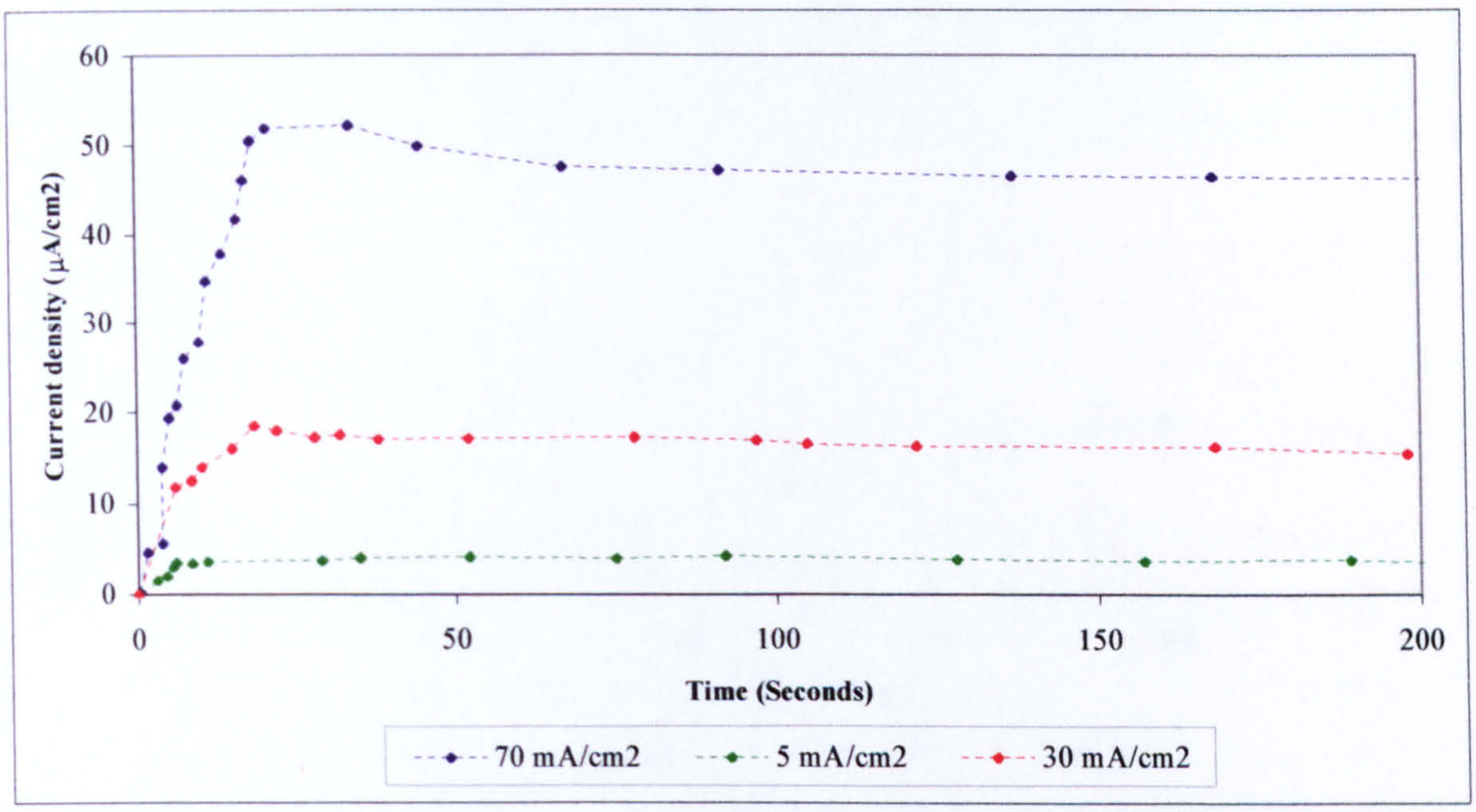
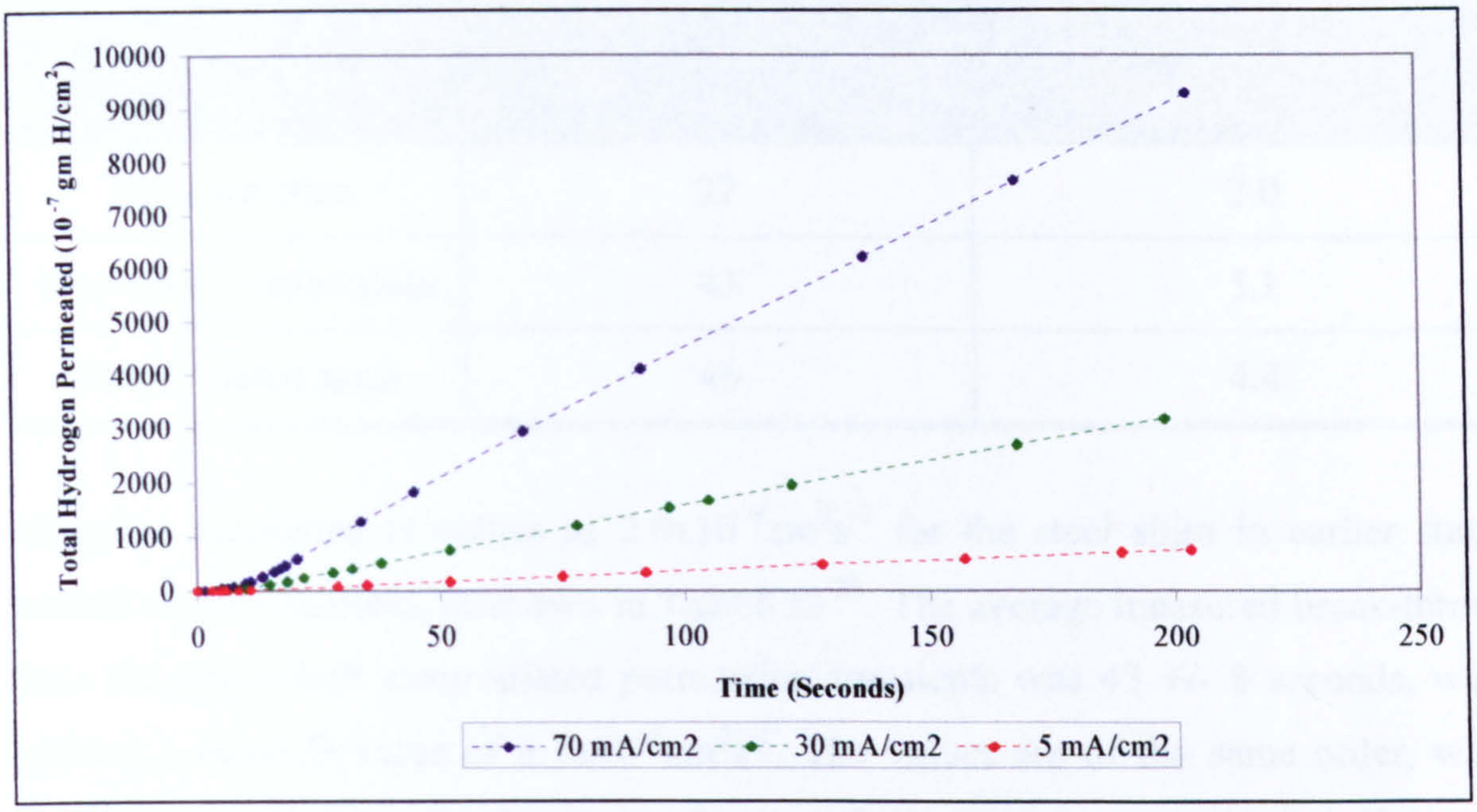


TABLE 31 illustrates that increasing the charging current density on the cobalt electroplated steel shim in this work by 6, from 5 to 30mA/cm^2, resulted in an increased peak transient current density of 5.4. An increase in charging current density of 14, from 5 to 70mA/cm^2, caused an increase in peak transient current density of 15.3.

TABLE 31: Hydrogen Flux as a Function of Current Density

Charging Current Density (cm^2s^{-1})	Flux ($\mu m/cm^2$)	Charging Current Density/ $5cm^2s^{-1}$
70	52	15
30	18.5	5
5	3.4	1

FIGURE 113: Integration of the Current Density Transients



Integration of the transients produced at different current densities shows the quantity of hydrogen that had been permeated for each current density, as shown in FIGURE 113. The increase in total quantity of hydrogen permeated from 5mA/cm^2 to 30mA/cm^2 was 4, while the increase from 5mA/cm^2 to 70mA/cm^2 was 12, as shown in TABLE 32.

TABLE 32: Total Hydrogen Permeated as a Function of Current Density

Charging Current Density (cm^2s^{-1})	Total Hydrogen Permeated (10^{-7} gm H atoms cm^{-2})	Charging Current Density/ $5cm^2s^{-1}$
70	9280	12
30	3162	4
5	763	1

As mentioned in Chapter 1, the diffusion coefficient for a membrane will change as the thickness of an electroplated layer increases [39, 87, 95]. For the current density investigations, the membrane thickness was fixed at 58μm as the cobalt layer was electrodeposited before charging commenced. TABLE 33 shows the break through times and diffusion coefficients found during this work.

TABLE 33: Comparison of D Values and Break Through Times Used in This Work

Specimen	Break Through Time (s)	Diffusion Coefficient ($10^{-8}cm^2s^{-1}$)
Unplated shim	32	2.0
Zinc-cobalt plated shim	43	5.1
Cobalt plated shim	46	4.4

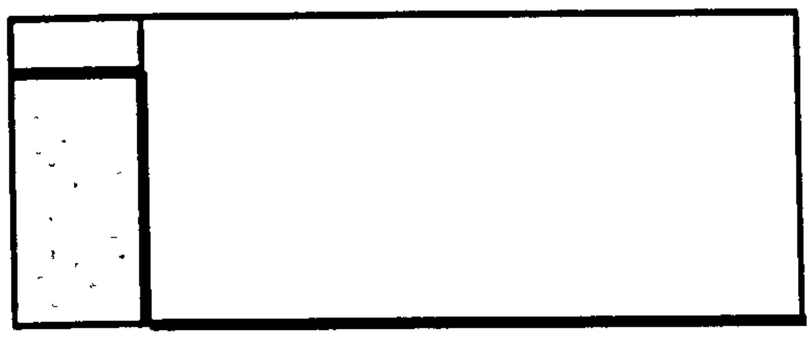
Kilgallon calculated D values of $2.0x10^{-8}cm^2s^{-1}$ for the steel shim in earlier studies carried out at Cranfield, as shown in TABLE 33 [28]. The average measured break-through time for zinc-cobalt electroplated permeation transients was 43 +/- 8 seconds, which yielded a mean D value of $5.1x10^{-8}cm^2s^{-1}$. The values are of the same order, which indicates that steel has the dominant effect on the hydrogen permeation coefficient for the combined system. However, it must be remembered that the zinc-cobalt electroplating calculations used a shim thickness of 58μm and a temperature of 50°C, rather than 50μm and the room temperature of the unplated experiments. These differences will alter the diffusion coefficient and break through time values in accordance with EQUATION 10 in Chapter 1.

The calculated D value for an electrodeposited cobalt layer is $4.4x10^{-8}cm^2s^{-1}$, again indicating that the steel has the most influence on the system. From these experiments it would appear that the diffusion coefficient for cobalt is small. However, cobalt has been shown by hydrogen embrittlement testing, to provide a less effective barrier to hydrogen ingress into a steel substrate than nickel, which is known to have a very small D value. The thickness of an electroplated cobalt layer that would retard hydrogen uptake and prevent hydrogen embrittlement of a steel substrate would therefore be great and may render it inadequate as a coating for fasteners, i.e. thicker than 8μm.

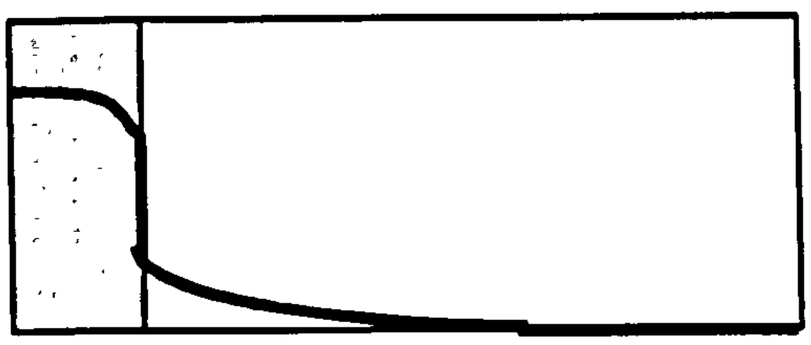
An actual D for cobalt cannot be calculated from the information obtained because an accurate representation of the situation occurring in the composite material is unknown. There are effectively 2 interfaces in the composite material due to the layers (cobalt, cobalt/steel) and each has different properties and D values. At each of the interfaces

there are a number of possible scenarios with experimental duration, as shown in FIGURE 114.

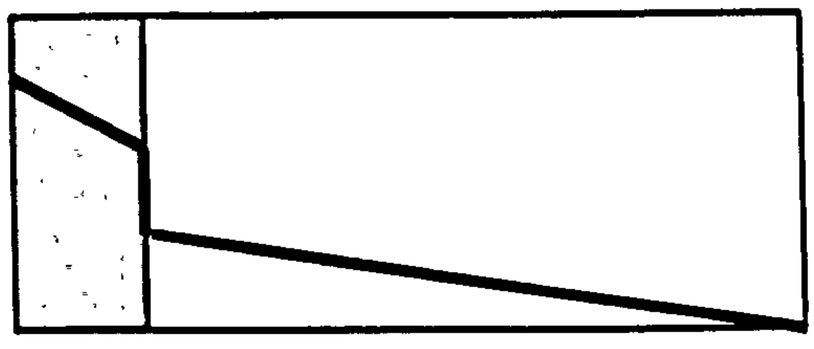
FIGURE 114: Predicted Hydrogen Diffusion Profiles during Permeation Experiments



Initially all the charging hydrogen is contained in the cobalt layer.



The hydrogen concentration is higher in the cobalt due to differences in hydrogen solubility. Hydrogen begins to diffuse into the steel and the permeation is determined by the diffusion through the steel.



The concentration gradient in the cobalt differs from the steel and the hydrogen concentration on each side of the interface reflects the different diffusivity to hydrogen of the layers.

The state of the profile across the 2 interfaces is unknown at any given time in all the electrodeposited coatings examined in this study. However, the increasing coating thickness during electroplating as well as the non-uniformity of the binary and ternary alloy composition further complicates the situation. The detailed levels of each of the steps shown depend on the relative D values for the two materials. The transient conditions in the early part of the sequence will not give gradients with straight lines, due to non-steady state conditions. The gradients will become more like those shown in FIGURE 114, after an extended period (probably > break through time).

The permeation experiments illustrate that the electrodeposit acts as a reservoir for hydrogen due to the observed continuing release of hydrogen after electroplating has ceased. Initially the concentration of hydrogen in the electrodeposited layer is higher than the substrate and the transfer of that hydrogen to the substrate is slow. Further complications of an increasing surface thickness have been removed as the cobalt/steel composite layers are of known thickness, and are being charged in situ by a known quantity. However, the concentration gradient that is present in the electrodeposited cobalt at any particular time cannot be estimated accurately, so D for cobalt cannot be determined with any confidence.

HYDROGEN DETECTION

Coated specimens

The hydrogen mapping technique was proved to be of use when determining if there was detectable hydrogen present in a coated specimen. Initial experiments were carried out to resolve the concerns expressed by Yao and Cahoon who observed a reaction with emulsion and more reactive elements in uncharged specimens[155]. This did not occur in the current work and a chemical reaction was not observed between baked electroplated zinc-cobalt or cobalt layers and the emulsion treatment, FIGURES 79-82, Chapter 3. However, limited use could be made of electroplated specimens because of the significant response that was observed compared with that of the steel substrate. Work by Perez and Overjero Garcia in 1982, stated that the resolution of the technique was only 0.3μm [156]. Therefore, for both of these reasons, unplated charged specimens were preferentially used in the present work to determine the extent of hydrogen penetration into a specimen.

Interestingly it was observed that if a delay was introduced before the emulsion treatment but after specimen preparation, a reduced response was seen for the coated specimens. A clear boundary could be distinguished in the dual bath technique specimens and differences in the hydrogen detected could be determined in the two layers, shown in FIGURE 82 Chapter 3. This could have been due to hydrogen diffusion from the surface lowering the response or a build up of a surface oxide film that prevented a stronger response. Yao and Cahoon believed that maintenance of a perfect

oxidation film was necessary on the metal surface to provide reliable results [155]. However, in this work it was decided that the specimens were only to be used as comparisons to one another and so a delay was not incorporated into the experimental regime.

Unplated specimens

The unplated specimens that were charged at 120mA/cm^2 for various lengths of time, in a solution of 10% sulphuric acid doped with a small quantity of thiourea, allowed different amounts of hydrogen to diffuse into the steel lattice. In order to assess how much and how far the hydrogen had penetrated, theoretical plots were calculated using EQUATION 20, and shown in FIGURE 84 Chapter 3. Comparisons were then made between these theoretical values and the experimentally observed responses such as FIGURE 83.

The results in TABLE 21 Chapter 3, show that the mean experimentally determined values for the distance that hydrogen had diffused in the charged unplated specimens was approximately 79% of that which had been calculated theoretically. Deviation in the values obtained can be explained in a number of ways. Firstly, differences between the specimens, due to differences in the trap type and microstructure that were present (see Chapter 1), could cause variation in hydrogen diffusion values under the same experimental conditions. The choice of the D value used in EQUATION 10, is also a source of disparity, as steady state conditions are not necessarily reached during the testing period. The values obtained at longer charging times are in better agreement than those obtained for shorter charging times. This was also seen in similar work previously carried out at Cranfield [85]. While reducing the temperature of the specimen in liquid nitrogen slowed any loss of hydrogen from the surface that could have occurred during preparation, this source of discrepancy may not have been eliminated completely.

As hydrogen diffuses into the steel specimen, it eventually builds up until a uniform hydrogen concentration is reached across the specimen. Break through time (initial hydrogen penetration across the specimen) can be calculated using the steady state expression in EQUATION 10. If a charging time of greater than or equal to the break through time is used (if the detection limits are good), then the silver emulsion should

be detected over the whole of the surface of the specimen as hydrogen should be present throughout. However, an estimated hydrogen diffusion coefficient for the steel must be substituted into the expression to determine the break through time.

Analysis of data for 6.5 hours charging

The specimen charged for 6.5 hours showed a response to the emulsion treatment over its whole cross sectional area. If an initial D value of $2.5x10^{-7}$ cm^2/s^{-1} (suggested by Trembath and used for the theory calculations) was used, with the specimen half width of 0.3 cm, the t_b value of 23,529 seconds (6.5 hours) was calculated [85].

$$t_b = (0.3)^2 / [(15.3*2.5x10^{-7})]$$
$$= 23,529 \text{ seconds}$$

However, if another D value of $4x10^{-7}$ cm^2/s^{-1}, determined by deLuccia for similar steel, was used a t_b of 14,706 seconds (4 hours) was obtained [92].

$$t_b = (0.3)^2 / [(15.3*4x10^{-7})]$$
$$= 14,706 \text{ seconds}$$

These calculations suggest that a full response was expected for a charging time of 6.5 hours, with both the D values used. Therefore further calculations must be carried out to determine which of the values is most appropriate.

Analysis of data for 4 hours charging

Result analysis of the specimen charged for 4 hours show that there was incomplete hydrogen penetration of the specimen cross sectional area. This agreed with the predicted penetration value, that suggested a D value of $2.5x10^{-7}$ cm^2/s^{-1}. Therefore, the D estimate was reasonably precise, if the detection limits of the technique are assumed to be accurate. Using EQUATION 10, the experimental D value can be determined from the mean observed penetration values, if they are substituted for the specimen thickness.

$$D = (0.22)^2/[(15.3*14400)]$$
$$= 2.2x10^{-7} cm^2/s^{-1}$$

Analysis of data for 2 hours charging

The penetration results obtained experimentally for 2 hours charging time were greater than the predicted theoretical value. Trembath also reported this phenomenon for shorter

charging times used in her work, but the effect we observed was not as great [85]. Using EQUATION 10, the experimental D value was estimated from the observed hydrogen penetration value.

$$D = (0.18)^2/[(15.3*7200)]$$
$$= 2.9x10^{-7}\ cm^2/s^{-1}$$

The calculated D value was larger than the theoretical value used, due to the observed penetration depth being greater than predicted. This implied that the D value changed with time due to the non-steady state conditions that are seen at shorter charging times. The original equation used to calculate the theoretical diffusion profiles was based on a slab. The cylindrical specimens used in this work, allowed hydrogen to diffuse more quickly towards the centre of the specimen. The hydrogen effectively became more concentrated as the specimen internal cross sectional area decreased with depth. This also had a significant effect on the variation of the calculated D from the predicted value.

The theoretical hydrogen penetration will be smaller than the actual observation if the diffusion coefficient chosen is too small as indicated by the 2 hour charging time data. The sensitivity of the HMT technique also plays an important role in these findings, and can be defined as 'the minimum difference that is observed between hydrogen fluxes from different sources in the same sample' [86].

This definition leads to the conclusion that the sensitivity of the technique is dependent on the efficiency of the emulsion. The efficiency of the emulsion is dependent on the manufacturing process and is equivalent to the ratio of the number of silver grains seen by the SEM compared to the number of hydrogen atoms crossing a given area of emulsion. This is a fixed value and cannot be altered by improved methodology during actual experiments. Resolution is refined by using a grain size of 140nm but a 120nm grain size was used in this work in order to obtain optimised data. However, application of the emulsion in monogranular layers (to prevent a higher number of silver grains being detected than are present), is known to leave about 15% of the surface uncovered and therefore unable to interact with all the hydrogen that is present [85].

Analysis of data for 30 minutes charging

The results obtained for 30 minutes charging times were used to determine the minimum level of hydrogen that was required for the technique to detect a response. As can be seen by the data in TABLE 21 Chapter 3, there was a minimal response for this charging time. These results confirm that quantitative use of this technique is not possible, especially at short plating times, as the number of silver particles formed is not directly equivalent to the hydrogen concentration. The technique does not account for the absorbed hydrogen that recombines to form hydrogen molecules, the described 15% error margin, non-steady state conditions and experimental preparation of the specimens allowing hydrogen diffusion from the specimens.

The accurate level of hydrogen needed to detect a response is also difficult to define, but with careful and fast specimen preparation it is reasonably sensitive to low levels of hydrogen. Variations in specimen surface condition can cause large variation in observed response. A surface oxide layer may significantly reduce the emulsion response, as it may retard hydrogen absorption into the specimen. Random imperfections or inclusions that favour hydrogen absorption may enhance response. These effects cannot be assessed by this methodology. The drawbacks of this technique suggest that while the HMT decoration is useful in pinpointing the hydrogen present in specimens, other techniques like the permeation experiments are of more quantitative value.

CORROSION MEASUREMENTS

Electrochemical testing

The polarisation and LPR measurement results provided comparable information on the coating that was being tested. It was important to maintain a steady temperature throughout the electrochemical testing as the potential measured varies with experimental temperature [138]. This effect may account for the slight variation that was seen in the E_{corr} measurements for the polarisation and LPR specimens for each coating type. These can be corrected by using the Nernst equation. A more significant effect may be due to altered aeration or specimen surface state.

Both techniques were used to measure detectable changes in the specimen coating after the set immersion time. The polarisation results revealed that immersion for 3 months slowed the corrosion rate for the unplated steel specimens, cadmium, zinc and zinc-cobalt electroplated specimens. In addition to this there was no zinc coating left after the 3 month immersion period, which was clearly demonstrated by the shift in E_{corr} value to that of unplated steel. The LPR experiments showed that the polarisation resistance for the control steel and cadmium increased for the 3 month immersion specimens compared to the initial values that had been obtained for the specimen types. Zinc and zinc-cobalt electroplated specimens however, that had been immersed for 3 months had lower polarisation resistance. Closer inspection of the coupons confirmed that there was no electrodeposited coating remaining on these specimens.

Each technique showed that there was a significant decrease in the corrosion rate as the immersion time was increased as expected. This was attributed to a change in the surface state of the specimens either from corrosion layer formation, enoblement or coating removal. It is believed that a shorter immersion period, or testing performed at more frequent intervals would have shown more easily the corrosion trends of the coatings. All the results obtained are given in TABLE 22, Chapter 3.

Weight loss

The weight loss for the specimens reflected a similar pattern to that which had been shown by the electrochemical testing. There was a decrease in weight loss with an increase in immersion time. The results shown in TABLE 23, illustrate that of the control specimens unplated steel lost most weight and cadmium lost least weight (and therefore coating) over both the immersion periods. All the alloying additions to zinc that were investigated improved its corrosion performance [157].

Zinc-cobalt electroplated specimens seemed to perform better, (lost less weight), if the coating was unbaked before immersion. This was contrary to both zinc and cadmium electroplated coatings but in agreement with the trend that was observed for unplated steel coupons. In general it is expected that a baked coating will lose more weight

during immersion testing than an unbaked specimen, as a result of blisters or loss of coating adhesion caused by the heating treatment [157].

TABLE 34: Summary of Corrosion Data for Steel, Cadmium, Zinc and Zinc-Cobalt

Specimen	E_{corr} (mV)		Electrochemical Corrosion Rate (mdd)	Weight Loss Corrosion Rate(mdd)	
	Polarisation Scans	LPR		Baked	Unbaked
Steel (initial)	600	601	194	92	88
Steel	580	584	86	83	67
Cadmium(initial)	820	815	22	10	13
Cadmium	720	710	1	10	19
Zinc(initial)	1020	1014	69	46	62
Zinc	600	607	226	46	66
Zinc-Cobalt(initial)	1014	1004	26	59	49
Zinc-Cobalt	648	618	181	43	43

Zinc Summary

Corrosion rates quoted by the Zinc Development Association for zinc in flowing seawater are from 50 to 220mdd under total immersion [17]. The lower end of this range compares well with the results obtained by weight loss for initial zinc specimens and those immersed for 6 months, of 56mmd. The initial rate calculated from polarisation data is also comparable to this value at 69mdd. However, polarisation data obtained for specimens that had been immersed for 3 months gave a much higher value of

226mdd, due to removal of the protective coating. This calculated corrosion rate is in agreement with the rate found for initial steel coupons. The potential of –1020mV, seen for an undamaged zinc coating is also in agreement with values found by Baldwin [7]. The initial corrosion current density of 10.6μA/cm^{-2}, found by Baldwin, is of the same order of magnitude as our value of 23μA/cm^{-2}.

Cadmium Summary

The potential of –816mV, seen for an initial unpassivated cadmium coating is in agreement with values found by Baldwin and Cramer of –800mV [7, 24]. The values became less negative as the immersion time was increased. Baldwin's value rose to -750mV, while the recorded value for this work was –710mV. The later corrosion current density of 0.13μA/cm^{-2}, found by Baldwin, is of the same order of magnitude as our 3 month value of 0.27μA/cm^{-2}.

Zinc-cobalt Summary

The corrosion potential of –1004mV, seen for an initial zinc-cobalt coating is similar to values found by Baldwin of –1020mV and Cramer who presented values of –1000mV [7, 24]. The initial corrosion current density of 3.17μA/cm^{-2}, found by Baldwin, is of the same order of magnitude as our value of 8.98μA/cm^{-2}. As with zinc, the coating was removed after 3 months immersion so the later values gained for these tests refer to the steel substrate rather than the coating. The rate of corrosion recorded for initial specimens was 29μA/cm^{-2}, which was in agreement with values obtained by Short and Dennis on similar coatings tested by LPR measurement [19].

The corrosion rate of the initial zinc-cobalt specimens was comparable (weight loss) or better than (electrochemical methods) that of pure zinc, but was not more corrosion resistant than cadmium. It is assumed that if more frequent electrochemical monitoring during the immersion period were undertaken, enoblement would be seen for the zinc-cobalt specimens before eventual loss of the coating. During the extended testing period for the weight loss specimens, it was seen that zinc-cobalt provided better protection for the steel substrate, yielding a lower weight loss. Therefore the specimens that were electroplated with zinc-cobalt would be protected for longer in

the same conditions than if they had been electroplated with zinc alone. However, cadmium electroplated specimens would still have superior coating protection performance.

The improved corrosion performance for zinc-cobalt specimens is thought to be due to the cobalt in the coating providing a protective layer that prevents zinc dissolution through its pores. The embrittlement findings suggest a thicker cobalt layer is responsible for a lowering of the risk of embrittlement. It may be that a thicker cobalt layer would result in a further improvement in corrosion resistance. However, the effect of varying the thickness of the cobalt layer on the system corrosion resistance was not investigated in this work. Voltammetric stripping experiments by Kirilova have shown that coatings of zinc and cobalt have potentials that are less negative than zinc but more negative than cobalt as we have shown for the zinc-cobalt alloy coatings tested in our study. The researchers also suggest that the cobalt layer retards coating dissolution in the manner that has been described [125].

DISCUSSION ZINC-NICKEL

PARAMETER VARIATION

Compositional change of zinc-nickel electrodeposits was examined by varying the electroplating parameters used to deposit them in order that the mode by which they were formed would be ascertained. The deposition model once established was used as a standard binary deposit model, which could be compared to the zinc-cobalt electrodeposit findings.

Time

Zinc-nickel electrodeposits followed a similar compositional trend to zinc-cobalt electrodeposits with the deposit thickness increasing with time and the quantity of nickel in the electrodeposit decreasing. FIGURE 38 shows that the initial electroplated layer to be produced appeared to be rich in nickel; 16% compared to the average 12% usual in the standard 15 minute electrodeposit. The nickel composition fell from 16% to 8% over the electroplating time range investigated, (30 seconds to 30 minutes), which is much less than the ten-fold drop seen for either of the zinc-cobalt electrodeposits investigated. This may be due to the different nature of the type of electroplating baths. The zinc-nickel bath contains a much higher composition of noble metal ion than the corresponding zinc-cobalt electroplating bath. This is a well known factor in the influence of electrodeposit composition [17, 116]. As the noble metal content of the bath is increased its content in the electrodeposit also increases [117, 119, 120, 145, 149]. The higher initial bath level combined with a different pH, temperature and no buffering effects from bath additions may account for the greater content and the lesser drop that was seen for the zinc-nickel electrodeposits.

The quality and morphology of the electrodeposits was largely unaffected by the change in electroplating time and showed a similar trend to that which was observed for the zinc-cobalt electroplating. The zinc-nickel specimens showed the presence of zinc hydroxide whiskers on their electroplated surface when examined on the SEM. These were less easily distinguished from the rest of the coated surface at longer electroplating times, as Baldwin and Kudryavtsev had also observed [120, 148]. The cathode efficiency remained constant after an initial increase from 69% up to 90% after 2 minutes. The

lower cathode efficiency at the start of the series can be attributed to the higher nickel composition of the initial layer and to a possibly higher cathode hydrogen production rate.

PARAMETER VARIATION

Temperature

The results shown in FIGURE 39 demonstrate that the temperature of the zinc-nickel electrolyte had a direct effect on the composition of its electrodeposits. As the temperature increased, the level of nickel in the electrodeposit remained constant from 25 to 45°C then it increased gradually until after 55°C where it began to rise rapidly. Kamitani reported a smaller zinc-nickel electrolyte temperature range, from 33 to 37°C, which produced a constant nickel content in the electrodeposits [117]. Baldwin states that increase in electrolyte temperature increases the nickel content of the deposit and raises the transition current density of the system. He warns that this effect coupled with an increase in bath acidity could lead to reduced scope for the occurrence of anomalous co-deposition [120].

In his review, Hall is much more conservative about the effect of temperature on zinc-nickel electrodeposit composition. He claims that the effect of temperature on electrodeposit composition is unpredictable. While an increase in temperature reduces polarisation of nickel enabling, it also counteracts the diffusion limitations of zinc, enabling both to deposit more readily [119]. His observation may serve to explain the optimum range for anomalous co-deposition, where the composition of the electrodeposit is largely unaffected by the increase in temperature, due to competing bath effects. The faster increase in nickel composition past 55°C is however in agreement with literature predictions, as is the general trend for the nickel content to increase over the temperature range investigated [119, 120,145, 149].

The appearance of the coatings did not alter greatly as all were smooth and even on visual inspection. Those produced at higher temperatures were brighter and finer grained on inspection under the SEM. However, small cracks were visible at the highest temperatures used, which maybe due to the evolution of hydrogen impeding dendritic

grain growth and enhancing nucleus generation causing a fine grain structure[149]. Hydrogen adsorption may be sufficient under these conditions (and at high temperature) to interfere with lattice planes. This disruption and resulting stress may cause visible cracks to form [149]. The 10% drop in cathode efficiency for the zinc-nickel electrolyte over the temperature range investigated from 94% would seem to agree with the increased production of hydrogen at the cathode [145, 149]. The drop in efficiency that was seen is governed mainly by the cathode efficiency of nickel deposition, as the effect on efficiency of zinc deposition is minimal with increase in temperature [147]. However, the efficiency of the zinc-nickel system is generally much better than the equivalent zinc-cobalt process.

PARAMETER VARIATION

pH

Hall states that electrolyte pH change has little effect on the composition of electrodeposits that are formed from baths containing uncomplexed metal ions [119]. However, the sulphate ions present in our bath had a buffering effect from pH2 to pH4.5, as shown in FIGURE 40, where the nickel content remained relatively constant; supporting a similar finding by Fukushima [145]. Outside the plateau region observed in this work, the nickel content of the electrodeposit was higher at more acidic pH values and lower at more alkaline pH values. The plateau pH range observed by Kamitani and co-workers for their chloride based system was much smaller, from pH5.5 – 5.8 [117], which may have been due to the different deposition current density used rather than the chloride based electrolyte.

These findings were unlike zinc-cobalt, which at levels greater than pH5 showed a rise in the cobalt content of the electrodeposit but were similar to those observed by El Rehim and co-workers for a zinc-nickel system [149]. A localised surface pH value of 5.25 allows precipitation of zinc hydroxide that is more easily attained at alkaline pH values. Zinc hydroxide inevitably suppresses nickel deposition and so accounts for the lower the nickel content in the electrodeposit. At pH1 zinc hydroxide is not formed easily due to the acid conditions and the deposition mechanism undergone is the normal type which is why the electrodeposit contains much higher levels of nickel [147].

The morphology of the electrodeposit is largely unaffected by the change in pH. The electrodeposits formed at more acidic pH values showed a slightly finer nodular appearance to those formed at more alkaline pH values. The presence of zinc hydroxide whiskers was also more easily determined at more alkaline pH values. The cathode efficiency of the zinc-nickel electrolyte rose from pH1 to a maximum value of 94% at pH3 then gradually fell again towards pH5.5. The lowest cathode efficiency value was seen for the most acidic conditions and the highest nickel content in the electrodeposit. These observations are confirmed in the available literature [149]. Baldwin states that the magnitude of the transition current density is an associated effect with changes in pH [120]. He found that acidity of an electrolyte can reduce the current range over which anomalous co-deposition is obtained. He also observed that more acid electrolytes show lower cathode efficiency. Both these findings are confirmed by this work. The gradual decline in cathode efficiency seen at pH3 and over can be explained by the change in composition of the electrodeposit that is present.

PARAMETER VARIATION

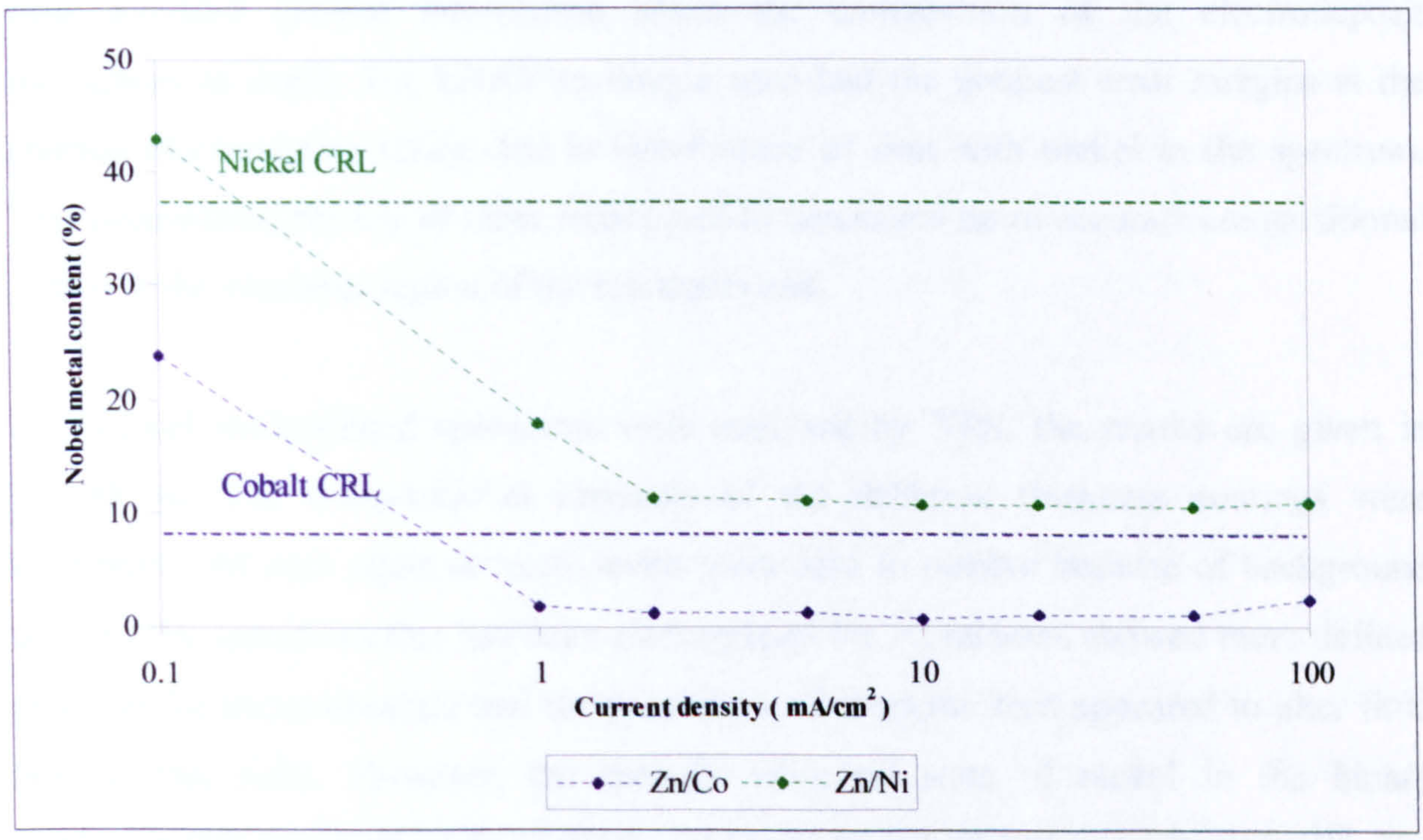
Current density

FIGURE 41 shows that an increased current density led to the expected increase in deposited material [137]. As predicted the specimens electroplated at a current density of 0.1mA/cm^2 showed a higher nickel content than the specimens produced in the rest of the current density range investigated (1mA/cm^2 to 100mA/cm^2). The 0.1mA/cm^2 specimens confirmed the findings from the time parameter investigations for the shortest electroplating times. After this current density there was a relatively constant level of nickel in the electrodeposits that were formed. The high level of nickel at low current density was due to the normal deposition mechanism occurring. As the current density was increased the anomalous co-deposition mechanism became responsible for electrodeposition [111, 116, 119, 145].

FIGURE 22 in Chapter 1 based on work by Fukushima clearly demonstrates, with the use of a composition reference line (CRL), the same distinction between normal and anomalous co-deposition for binary electrodeposits. Adding a CRL to the results obtained for zinc-nickel and zinc-cobalt electrodeposits with variation in deposition

current density, the same pattern is clearly shown as illustrated in FIGURE 115. There was a slight rise at the end of the current density range investigated for the zinc-cobalt electrolyte, which was not seen for zinc-nickel, however it may have been seen if the current density had been raised higher still. Fukushima states that the current density for transition back to normal deposition from anomalous co-deposition maybe as high as 100mA/cm^2 for certain zinc-nickel electrolytes [145]. These results validated the deposition mechanism that was alleged for zinc-cobalt electrolytes that has already been discussed.

FIGURE 115: Compositional Variation of Binary Electrodeposits with Current Density



The electrodeposits appeared to be smooth and even on examination, their quality only visually deteriorated past 50mA/cm^2 where they became more uneven and darker in appearance. On closer inspection on the SEM, the electrodeposits in the anomalous co-deposition range were largely unaffected by a change in current density. The dendritic nature of the deposition seemed to be retarded at the higher end of the range of current densities investigated, as observed for zinc-cobalt electrodeposits. The decrease in quality of the electrodeposit at the highest current density also corresponded to a fall in the cathode efficiency, which may indicate more hydrogen being passed in to the metal substrate [133]. The lowest cathode efficiency at a current density of 0.1mA/cm^2 can be explained by the change in deposition mechanism to the normal type and the rise in nickel composition of the electrodeposit under those conditions. The greatest cathode

efficiency of 95% was seen at 2mA/cm^2, it then gradually fell to 86% at 100mA/cm^2. The mean efficiency found by Carr under standard deposition parameters was also 80-90% [18]. The observed trend was predicted from literature observations for electrolytes over the same range in current densities [145].

ELECTRODEPOSIT EXAMINATION

XPS analysis

The parameter variation investigations proved that zinc-cobalt and zinc-nickel electrodeposits showed the same variation trend with time. Alteration in electroplating time provided general information about the composition of the electrodeposit throughout its depth. The EDAX technique used had the greatest error margins at the shortest electroplating times, due to interference of iron with nickel in the spectrum. This necessitated the use of other techniques to determine more accurate compositional values at the interlayer region of the electrodeposit.

Zinc-nickel electroplated specimens were analysed by XPS, the results are given in FIGURE 46. The compositional elements of the different thickness coatings were confirmed, but once again accurate levels were hard to resolve because of background scatter. The specimens that had been electroplated for >2 minutes showed more defined peaks in the traces obtained and the proportion of elements seen appeared to alter little beyond this point. However, the metallic chemical state of nickel in the binary electrodeposit, proposed by Fukushima, could not be established unequivocally [110]. The specimens that had been baked after electroplating and prior to examination showed signs of oxides due to higher levels of oxygen on the upper surface of the specimen. However, all the zinc-nickel specimens clearly showed a high level of oxygen through out their thickness, which has been credited to the presence of hydroxides in the electrodeposit. This evidence helps to support the anomalous co-deposition model that is being presented for the electrodeposition of both the zinc-binary alloys.

Auger Depth Profile

XPS analysis established the elements that were present in the electrodeposits tested but did not confirm their proportion or chemical state. Depth profiles of 0.2μm thick

unbaked electrodeposits were examined by progressive Argon beam etching. FIGURE 49 shows clear evidence that the standard pH zinc-nickel electrolyte produced nickel enrichment at the surface of the specimen. This supported similar findings by Carr using the same electrolyte [18], and Barcelo who studied zinc-nickel chloride electrolytes [158]. This information combined with the other electrodeposit examination shows that the anomalous co-deposition mechanism was the method by which both zinc-cobalt and zinc-nickel are deposited.

HYDROGEN EMBRITTLEMENT TESTING

Standard Zinc-Nickel Electroplated Specimens

Specimens that were electroplated with the standard zinc-nickel electrolyte showed an average failure time of 18.0 hours, shown in FIGURE 63 Chapter 3. This indicates a lower level of embrittlement compared to cadmium, zinc and zinc-cobalt electroplated specimens. Pure nickel is known to be a barrier to hydrogen because it has a low diffusion coefficient, 10^{-12} - 10^{-10} cm^2s^{-1}, and it was suspected that the nickel enrichment in the initial layer was responsible for the findings [18].

Standard baking treatment further improved the time to failure for the specimens to 20.4 hours shown in FIGURE 63 Chapter 3. The porous nature of the zinc-nickel coating allows hydrogen absorbed during the electroplating process to diffuse out during the baking treatment [159]. Both the times seen for the baked or unbaked zinc-nickel electroplated specimens were comparable with the 18.9 hours seen for the average time to failure for the unplated control specimens, and were shown by student T-test to be part of the same distribution population. These specimens are considered to be non-embrittled and this effect has been reported before for certain slow strain rate testing on 4340 steel specimens electroplated with zinc-nickel [159]. The Weibull data for zinc-nickel electroplated specimens compared to unplated controls are given in TABLE 35.

TABLE 35: Weibull Data for Zinc-Nickel

Specimen	Unbaked TTF (Hours)	Baked TTF (Hours)
Zinc-nickel	18.0	20.4
Unplated	18.7	18.9

Investigations were undertaken to determine how the observed effect on time to failure for the specimens was possible with a nickel composition of 12% compared to pure zinc. Nickel enrichment had been seen in the parameter variation and electrodeposit investigations, as cobalt enrichment had been for the zinc-cobalt specimens. A comparison of the noble metal enriched layers was attempted to show their influence on the uptake of hydrogen into the specimens during electroplating.

Compositionally Modulated Multi-Layer Coatings

To compare the effects of nickel and cobalt enrichment in the interlayer, the CMM technique[3, 15, 125] was used to produce nickel based coatings that could be directly compared to their cobalt alternatives. All the results are summarised in TABLE 36 and discussed in the following section.

TABLE 36: Weibull Data for Nickel Interlayer Coatings

Specimen	Standard TTF (Hours)	Cobalt Interlayer TTF (Hours)	Nickel Interlayer TTF (Hours)
Zinc	5.6	7.5	8.9
Zinc-cobalt	7.0	7.2	17.8
Zinc-cobalt baked	16.6	19.7	19.6
Zinc-nickel	18.0	7.2	21.1

Initially 0.5μm of nickel was deposited on the tensile specimen and then an electroplated zinc layer was deposited over the top of this. The effect, illustrated in FIGURE 70, was to increase the time to failure for the 2-layer system to 8.9 hours, which was not only an improvement on pure zinc electroplating, but also for cobalt/zinc layered specimens. A similar result was seen when a 0.5μm cobalt layer was deposited and a layer of zinc-nickel was electroplated over the top. FIGURE 71 showed that the time to failure seen for the specimens was 7.2 hours. These results show that the initial electroplated layer is of most significance to the embrittlement that is seen for the specimens rather than the remainder of the coating. Nickel provided a much better barrier to hydrogen than cobalt.

A 0.5μm nickel layer followed by an overlaid zinc-nickel coating, shown in FIGURE 72, gave a time to failure of 21.1 hours. Finally specimens that had been electroplated with 0.5μm of nickel followed by standard zinc-cobalt electroplating over the top showed an improved embrittlement performance. FIGURE 71 demonstrated the failure time for these specimens rose to 17.8 hours, which was over 2 times longer than the zinc-cobalt specimens electroplated at pH1. The nickel/zinc-cobalt layered coating provided the zinc-cobalt coating with the minimum risk of hydrogen embrittlement and demonstrated that nickel was an excellent barrier to hydrogen. The comparable time to failure of these specimens with binary zinc-nickel specimens proved that a nickel rich layer is formed during electroplating as suggested in previous work [17, 18]. The nickel rich layer forms initially during electroplating by a 'normal deposition' process, as nickel is more electrochemically noble than zinc. When the cathode pH has risen to pH5.25 whiskers of zinc hydroxide are formed, which suppress nickel deposition and allow zinc to be reduced and deposited via the 'anomalous co-deposition' mechanism [17].

When specimens electroplated in this way were baked using standard conditions, they appeared to completely recover their mechanical properties having an average time to failure of 19.7 hours for cobalt with zinc-cobalt over the top and 19.6 hours for nickel with zinc-cobalt over the top. However, the results seen in FIGURE 73, had a much wider standard deviation than the unbaked specimens. This was possibly due to the greater number of procedures that had been carried out on them causing a larger experimental result standard deviation. As baking the standard zinc-cobalt electroplated specimens did not produce full recovery, the presence of a 0.5μm layer of cobalt has been shown to have a significant effect in the layered coatings. The cobalt interlayer in the DBT specimen provides a barrier to hydrogen that causes its escape to the atmosphere rather than diffusion into the steel.

PERMEATION TESTING

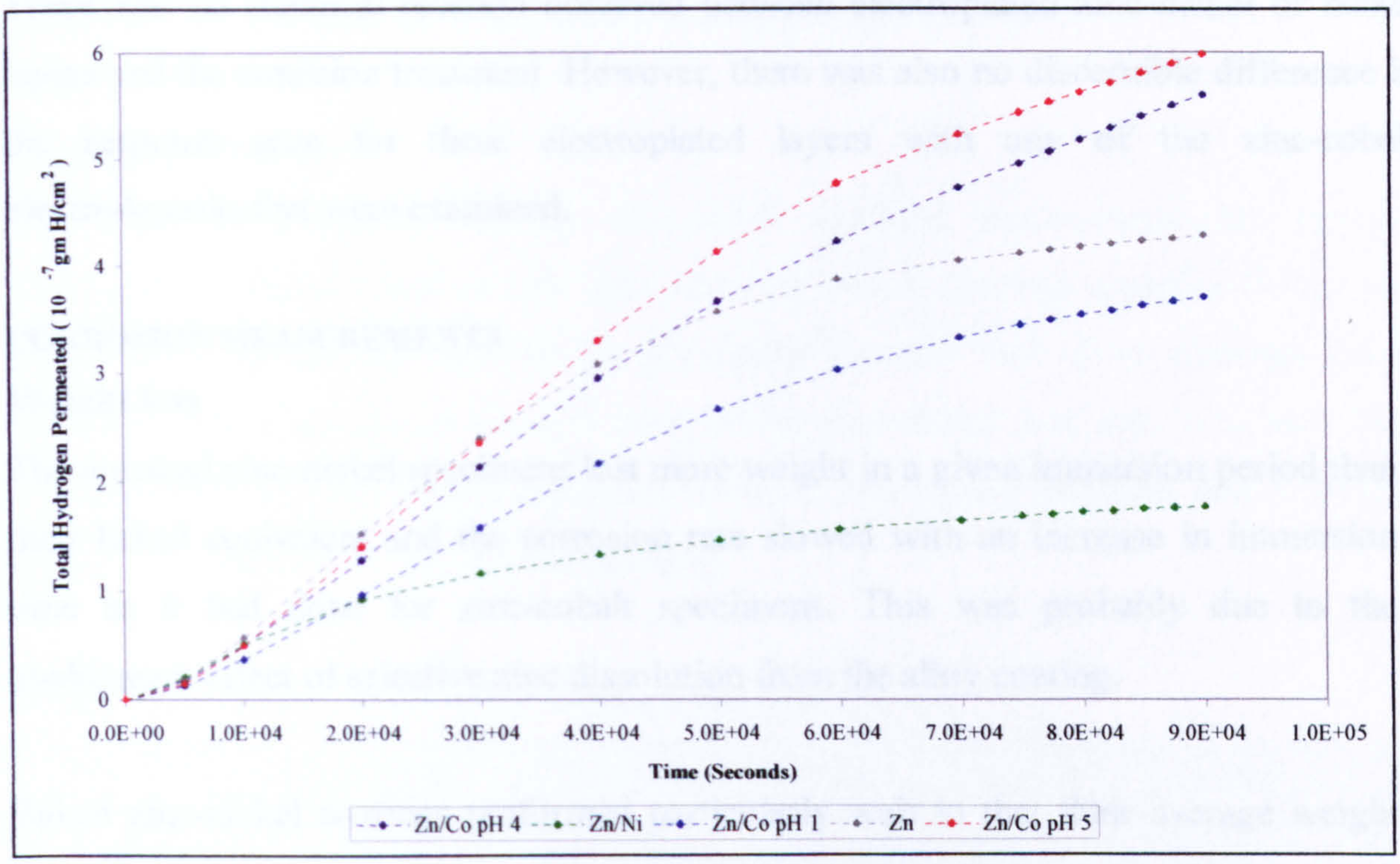
FIGURE 76 demonstrates that the observed flux of the zinc-nickel permeation transient was in the region of 0.6μA/cm^2. This value is in agreement with the work of Carr who found the same result working with the identical electrolyte. The figure is much lower than both zinc and pH5 zinc-cobalt permeation transients, that both had a flux of

approximately 1μA/cm^2. The pH4.2 zinc-cobalt permeation transient had a flux of 0.8μA/cm^2. This was a lower value than the zinc and pH5 zinc-cobalt flux values but higher than the zinc-nickel flux, it was also maintained for much longer. The pH1 zinc-cobalt permeation transient had the most similar flux value to zinc-nickel, of about 0.6μA/cm^2. Howęver, the flattened shape of the curve that was observed was again maintained for a longer period.

When comparing the permeation transient flux values for zinc-nickel it must be remembered that both zinc and zinc-cobalt electroplating are performed at 50°C. From previous calculations, in the Zinc-cobalt Discussion, it can be seen that an additional factor of 1.2 must be used to correct for the temperature difference. This is because zinc-nickel electroplating was performed at 25°C.

A more significant factor is that the electroplating deposition current density used for zinc-nickel electroplating is 20mA/cm^2, twice that of zinc-cobalt, leading to a predicted reduction of half. All these observations lead to the conclusion that zinc-cobalt electroplating provides a less effective barrier to hydrogen than zinc-nickel. The corrected flux of 0.36μA/cm^2 would yield an even lower corrected total amount of hydrogen permeated for zinc-nickel than is shown in the uncorrected integrated transients shown in FIGURE 116.

FIGURE 116: Total Amount of Uncorrected Hydrogen Permeated



The total amount of hydrogen permeated for zinc-nickel electroplating is less than that of zinc or zinc-cobalt electroplating. When the level of hydrogen permeated reaches 1.6 x 10^{-7} gm H atoms cm^{-2} for zinc-nickel electroplating at 66,000 seconds (18.3 hours) in FIGURE 116, it is also the approximate time to failure seen for the tensile specimens. This permeated hydrogen level also corresponds to the level that is responsible for zinc and zinc-cobalt electroplated tensile specimen failure at various pH values as shown in TABLE 37.

TABLE 37: Comparison of Zinc-Nickel Electroplating

Electrodeposit	TTF (Hours)	Hydrogen Flux ($\mu A/cm^2$)	H Permeated(10^{-7} gm H atoms cm^{-2})
Zinc	5.6	1	1.5
Zinc-cobalt (pH4.2)	7.0	0.8	1.8
Zinc-nickel	18.0	0.6	1.6

HYDROGEN DETECTION

There was no chemical reaction observed between electroplated zinc-nickel or nickel layers and the emulsion treatment. However, there was also no discernible difference in the response seen for these electroplated layers with any of the zinc-cobalt electrodeposits that were examined.

CORROSION MEASUREMENTS

Weight loss

The unbaked zinc-nickel specimens lost more weight in a given immersion period than their baked equivalent and the corrosion rate slowed with an increase in immersion time as it had done for zinc-cobalt specimens. This was probably due to the enoblement effect of selective zinc dissolution from the alloy coating.

Baked zinc-nickel coatings performed particularly well in that their average weight loss for the immersion tests was 36mdd. This was an improvement on the zinc-cobalt average of 51mdd and the pure zinc average of 46mdd. However, the mean weight loss for cadmium was only 10mdd. The unbaked specimens provided a slightly different corrosion rate order. While cadmium coated specimens had the lowest rate of 16mdd, and zinc the highest of the coated specimens of 64mdd, zinc-cobalt average rate was 46mdd and zinc-nickel was 47mdd. These results highlight the importance of oxide film formation and also the effect coating enoblement has in reducing the corrosion rate of coatings.

Electrochemical

The corrosion potential of –975mV, seen for an initial zinc-nickel coating is lower than values found by Baldwin of –950mV, for a zinc-14%nickel coating[7]. The initial corrosion current density of 2.10μA/cm^{-2}, found by Baldwin, is also lower than the 19.01μA/cm^{-2} found in this study. The difference in the results is probably due to the lower nickel level in the zinc-11%nickel coatings produced in this work. Unlike the zinc or zinc-cobalt coatings, the coating was not removed after 3 months immersion and the corrosion current density remained relatively constant, being 17.71μA/cm^{-2} after 3 months immersion. The potential of the alloy coating also became more noble,

rising to –727mV after 3 months immersion. The zinc-nickel coating in Baldwin's study rose to a potential of –750mV after a shorter immersion time.

Zinc-nickel Summary

The corrosion protection of the zinc-nickel coatings electrochemically tested, displayed an improvement on the zinc and zinc-cobalt coatings (despite the lower initial corrosion rate for zinc-cobalt), principally because both these coatings were removed after 3 months immersion time, while zinc-nickel was not. However, the cadmium coating had a slower corrosion rate than zinc-nickel, showing that it would protect for longer under the same conditions.

TABLE 38: Summary of Corrosion Data for Zinc-Nickel

Specimen	E_{corr} (mV)		Electrochemical Corrosion Rate(mdd)	Weight Loss Corrosion Rate(mdd)	
	Polarisation Scans	LPR		Baked	Unbaked
Steel (initial)	-600	-601	194	92	88
Steel	-580	-584	86	83	67
Zinc-Nickel (initial)	-979	-976	55	43	53
Zinc-Nickel	-720	-726	51	28	41

DISCUSSION ZINC-COBALT-IRON

The effect of doping a modified zinc-cobalt electrolyte with iron was investigated due to increasing reports in the literature that this type of electrolyte has beneficial effects [103, 119, 133, 160]. A zinc-iron-cobalt acid based electrolyte was chosen for easy comparisons with the acid zinc-cobalt electrolyte under study. It was hoped to help further elucidate the role cobalt plays in preventing or retarding hydrogen uptake from the acid electroplating performed in this work [103].

PARAMETER INVESTIGATIONS

Time

FIGURE 38 shows the thickness of the zinc-cobalt-iron electrodeposit increased with time, but the compositional noble metal trend was the reverse of that observed for both binary electrolytes. There was a slight overall increase in the iron group metal percentage in the coating. After 2 minutes plating time the percentage of cobalt in the coating increased and a maximum of 12% was reached at about 20 minutes. This suggests a different deposition mechanism in the 3-element system, as the anomalous co-deposition mechanism described by Brenner and seen in the zinc-alloy 2-element systems, yields higher noble metal content at lower plating times which decreases with longer plating times [17, 18, 108]. The cobalt level in the ternary coating was higher than in the binary zinc-cobalt electrodeposits because the compositions of the electrolytes differ. The increased ion content of the bath which affects a corresponding increase in the cobalt content of the electrodeposit is a well documented fact [103, 111, 116, 119, 132, 144]. The quantity of iron in the coating initially decreased to 1.5% and became fairly constant after about 10 minutes plating time.

The morphology of all the ternary electrodeposits deviated little from that, which was obtained for the zinc-cobalt or zinc-nickel electrodeposits, under similar experimental conditions. This was contrary to findings for zinc-nickel studies that have shown the addition of iron, to form ternary zinc-nickel-iron electrodeposits, results in a finer grained and harder deposited coating. These effects become more pronounced with increasing iron concentration [103]. The iron is believed to adsorb on the active plane or high energy sites, inhibiting crystal growth in that area, altering the usual crystal

growth. This crystal disruption leads to a finer grained deposit that could be responsible for improved corrosion protection, as it may reduce the porous and microcracked structure inherent in zinc-nickel electrodeposits [159].

The quality of the electrodeposit seemed to vary little with a variation in electroplating time. The initial cathode efficiency increased with time until a relatively constant value of 73% was reached after 2 minutes plating time.

PARAMETER VARIATION

Temperature

FIGURE 39 shows that the percentage of cobalt in the electrodeposits increased at higher temperatures, a phenomenon also seen for the binary zinc-cobalt coatings[116]. As the level of cobalt increased in the deposited coating, the iron level decreased slightly over the temperature range examined. The level of noble metal content increased beyond 35°C, and was close to the electrolyte cobalt content indicating a change towards the normal deposition mechanism, until 55°C where it reached a maximum and then began to decrease again.

Electroplating at higher temperatures increased the brightness and smoothness of the ternary coatings, contrary to Shukla's findings for nickel-cobalt-zinc ternary electrodeposits [118]. The amount of electrodeposited material and the cathode current efficiency remained relatively constant at about 73%. There was a slight decrease with a rise in temperature and cobalt content of the deposit, which is similar to results obtained for the binary electrodeposits.

PARAMETER VARIATION

pH

Like the binary zinc-cobalt coatings the cobalt content of the zinc-cobalt-iron coatings increased at more alkaline pH values, and the iron composition of the deposit fell correspondingly over the range investigated, as shown in FIGURE 40. As the pH of the electrolyte was lowered from pH3 to pH4, the percentage of noble metal component in the coating increased sharply. This phenomenon has already been illustrated by

experiments carried out in the embrittlement testing described for the zinc-cobalt electroplating and has also been observed in work investigating zinc-nickel plating at slightly more acidic pHs [18]. Under low pH conditions a noble metal inter-layer can be formed by normal deposition which reduces ingress of hydrogen to the metal surface and zinc deposition at higher pH values is significantly more difficult from a reactivity stand point. Both these effects could significantly alter the overall percentage of the noble metal seen in the deposit.

There was little change in the specimen appearance with a change in pH value but the cathode current efficiency decreased from 77% to 68% with a corresponding increase in alkalinity and cobalt content in the coating.

PARAMETER VARIATION

Current density

An increase in current density resulted in a direct increase in deposited material, as shown in FIGURE 41. A current density of 0.1mA/cm^2 gave the highest iron content, which decreased with an increase in current density to 1mA/cm^2, beyond which it remained relatively at a relatively constant level of 1-2%. The cobalt content of the electroplated coating fell at 1mA/cm^2 and then gradually rose above the bath composition at current densities of ≥2mA/cm^2 to 100mA/cm^2. As the cobalt level in the coating increased with current density the iron content decreased correspondingly. In terms of electrochemical reduction potentials a higher current density should produce an electrodeposit rich in the less noble bath component (zinc), which is what was observed[15]. Therefore, increasing the current density seemed to result in the normal deposition type demonstrated by a high total noble metal percentage in the deposit[111]. At the lowest current densities, iron and cobalt deposition are electrochemically favoured to zinc deposition, and the reverse behaviour was observed to the binary zinc-alloys investigated.

The visual appearance of the coatings was smooth and even over the range investigated. However, the coating became noticeably brighter at current densities >50mA/cm^2, under closer examination with the SEM they appeared to be more nodular. This point

also corresponded to a slight drop in cathode efficiency, which may indicate more hydrogen being passed into the metal substrate during electroplating [139]. Wang and O'Keefe (using pure and doped zinc-cobalt electrolytes) produced some interesting similarities in morphology (shape and type) and compositional trends with parameter variation to ternary electrodeposits produced in this work [133]. Addition of iron in this work improved the general appearance and uniformity of the electrodeposits by decreasing the dendritic nature of the structure in a similar manner that germanium has been shown to act [133].

Younan believed that the grain size refinement phenomenon could be explained by Fe atom surface adsorbtion, which inhibits the usual crystal growth [103]. The variation in deposition potentials at the surface that promoted a different preferred orientation also resulted in deposition of a different noble metal phase. The phase of cobalt that is deposited has been shown to be important in influencing the embrittlement performance, and at the higher ternary cobalt compositions, this could help explain the reduced effect that was observed and that will be discussed later in this section [140, 142].

The cathode efficiency trends observed for the zinc-cobalt-iron parameters were the same as those seen for zinc-cobalt and zinc-nickel plating. The efficiency followed the compositional findings, a lower efficiency was seen with higher cobalt content in the deposit formed. The cathode current efficiency was a minimum at a current density of 0.1 mA/cm^2, a maximum at 5mA/cm^2 from where it gradually fell.

ELECTRODEPOSIT EXAMINATION

XPS analysis

Zinc-cobalt-iron electroplated specimens were analysed by XPS and the results are given in FIGURE 47. The proportions of the constitutional elements of the different thickness coatings were not accurately resolved because of background scatter. However, the levels appeared to alter little. All specimens showed a high level of oxygen throughout their thickness that has been attributed to the presence of hydroxides in the electrodeposit. The baked specimens showed signs of higher oxygen levels on their upper surface probably due to oxide presence. Mossbauer studies of zinc-cobalt-

chromium alloys indicate that the cobalt atoms contained in these deposits are present as isolated atoms in the zinc matrix and not aggregated groups [146]. This may also be true for the iron or cobalt in the ternary electrodeposit, but no firm conclusions could be drawn, as the cobalt chemical state was not determined [103].

Depth Profile Data

XPS analysis established the elements that were present in the electrodeposits tested but did not confirm their proportion or chemical state. Depth profiles of 0.2μm thick unbaked electrodeposits were examined by progressive Argon beam etching. FIGURE 50 shows relatively constant levels of cobalt throughout the specimen thickness and no evidence of cobalt enrichment at the surface of the specimen. This information combined with the other electrodeposit examination shows that the zinc-cobalt-iron electrodeposits were probably not formed by anomalous co-deposition mechanism, unlike zinc-cobalt and zinc-nickel electrodeposits.

HYDROGEN EMBRITTLEMENT TESTING

Addition of Iron to a Modified Acid Zinc-Cobalt Electrolyte

FIGURE 69 shows the initial zinc-cobalt-iron electrolyte examined gave an improved mean time to failure of 11.2 hours compared to the more embrittled zinc and zinc-cobalt electrodeposits. (This coating had a cobalt composition of 12%, which was examined in more detail by the parameter variation investigations). The high cobalt content of this coating led to the quantity of cobalt in the electrodeposit being reduced to 10%, which resulted in the mean specimen time to failure being shortened to 10.7 hours. Addition of cobalt to a modified zinc electroplating bath to yield an electrodeposit containing <1% cobalt and >99% zinc, only increased the time to failure of the specimens to an average 7.0 hours compared to pure zinc electroplated specimens which failed in 5.6 hours. Therefore, Weibull specimen analysis showed that the time to failure is increased with an increase in cobalt composition of the electrodeposit, as shown in TABLE 39.

TABLE 39: Weibull Data for Zinc-Cobalt-Iron

Specimen	Unbaked TTF (Hours)	Baked TTF (Hours)
Zinc-cobalt	7.0	16.6
Zinc-nickel	18.0	20.4
Zinc-cobalt-iron (10%)	10.7	21.0
Zinc-cobalt-iron (12%)	11.2	-

Both the types of ternary electroplated specimens failed in a greater time than the binary zinc-cobalt specimens. However, the ternary specimens that contained a comparable quantity of cobalt to the zinc-nickel specimens failed in a shorter time than the nickel containing specimens. Baking the 10% ternary electroplated specimens led to complete recovery in their time to failure to 21.0 hours, which was a significant improvement on the baking recovery for the zinc-cobalt binary specimens, as shown in TABLE 39.

Embrittlement indices

The average embrittlement indices, were calculated from reduction in area measurements using EQUATION 24. (Larger diameter specimens would need to absorb more hydrogen to affect failure times). A high number represents a small chance of embrittlement and a longer time to failure for a specimen.

EQUATION 24: Embrittlement Index from Reduction in Area Calculations

$$EI = RA'/RA \times 100\%$$

Where: RA' = Reduction in area for specimen

RA = Reduction in area for unplated specimen

The reductions in area results, shown in TABLE 40, illustrate that there is an improvement in embrittlement performance for the zinc-cobalt specimens, over zinc alone. These findings are borne out in work by Cramer, who found an approximate 10% improved performance for zinc-cobalt compared to specimens similarly treated zinc coatings [24]. Specimens that exhibited a high percentage area reduction showed

significant amounts of necking along with ductile, cup and cone fracture surfaces. Specimens, which showed a low percentage reduction in area exhibited little necking and had angled, brittle, fracture surfaces. These results confirmed similar findings by Cramer using similar zinc-alloy coatings[24].

All the zinc based coating systems tested produce less severely embrittled specimens than those specimens that had been electroplated with 8μm of cadmium. The embrittlement of a zinc-cobalt coating could be manipulated with electrolyte pH variation, to increase the cobalt enrichment of the interlayer, and further reduce the embrittlement seen. Weibull analysis illustrated that the addition of a third metal, iron into the electrolyte to produce a ternary alloy, increased the time to failure and further reduced the observed embrittlement of the specimens. The significant percentage increase of cobalt in the both types of ternary electrodeposit, to either 10 or 12% was probably due to a complex deposition mechanism involving iron, which is also electrodeposited to a significant level in the initial electrodeposit examined.

If more cobalt were deposited in the interlayer region, either because of a higher bath concentration (ternary electrolyte), or because of the deposition mechanism (pH effects in binary anomalous co-deposition), a significantly improved embrittlement performance to zinc or cadmium electroplating was observed. Further work would need to be carried out in this area to investigate the deposition mechanism of the ternary metal bath and to help establish a reason for these findings, other than higher cobalt bath composition. However, all the cobalt based plating baths used in this work, still give a more embrittled specimen than those specimens plated using the zinc-nickel electroplating system. These results combined with the previous findings illustrate that a cobalt interlayer is not as an effective barrier to hydrogen as a nickel interlayer.

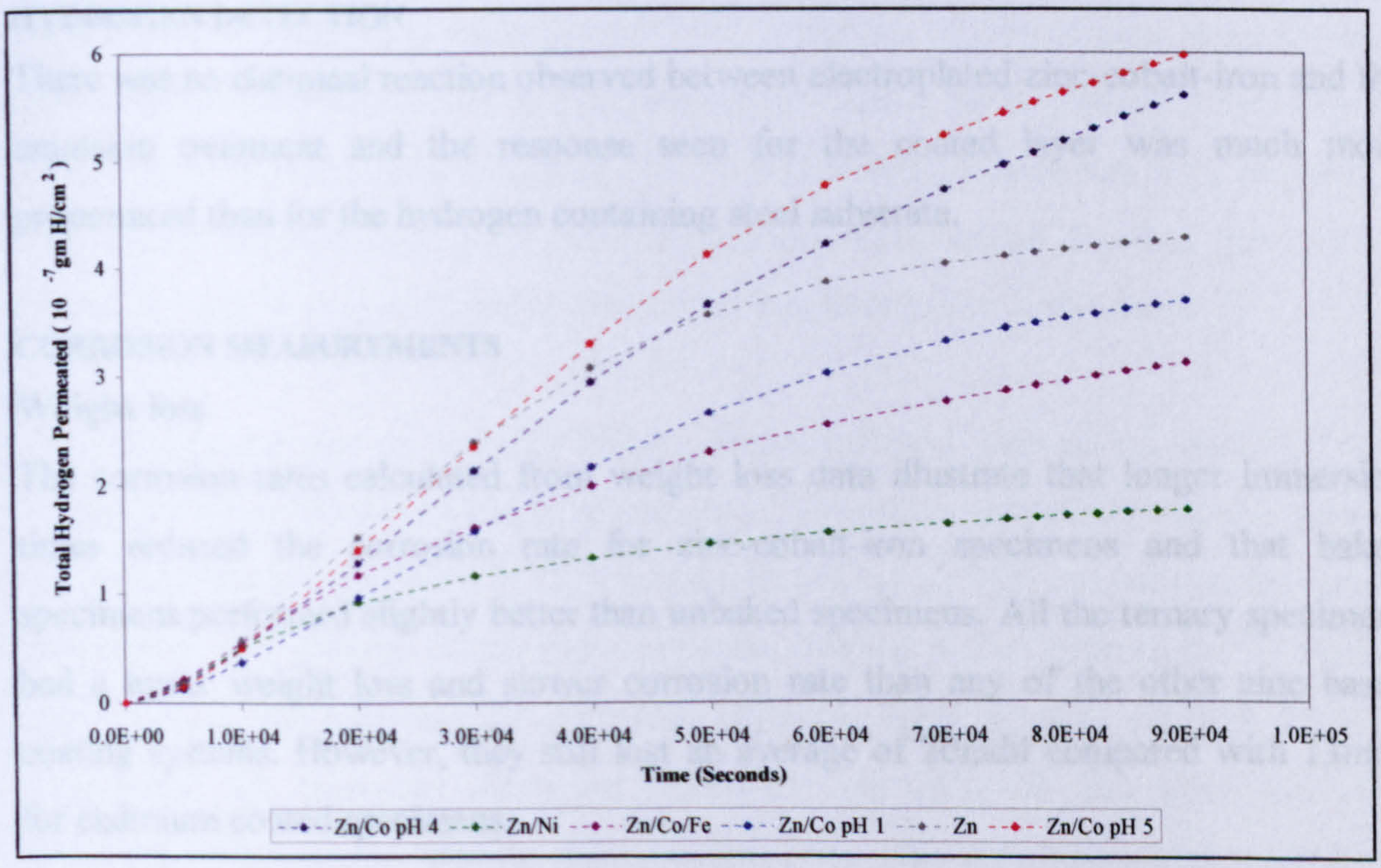
TABLE 40: Embrittlement Index for the Plated Specimen Types

Specimen Type	Reduction In Area(%)	Embrittlement Index
Control	25.4	100
Cadmium	0.50	2.00
Cadmium Baked	25.2	98.9
Zinc	1.10	4.33
Zinc Baked	2.28	8.97
Zinc-Cobalt	5.29	20.8
Zinc-Cobalt Baked	18.1	71.1
Zinc-Cobalt-Iron	8.36	32.9
Zinc-Cobalt-Iron Baked	24.7	97.0
Zinc-Nickel	20.4	80.2
Zinc-Nickel Baked	24.0	94.4
Cobalt/Zinc	1.65	6.49
Nickel/Zinc	2.41	9.48
Cobalt/Zinc-Nickel	2.87	11.3
Nickel/Zinc-Nickel	25.3	99.4
Cobalt/Zinc-Cobalt	1.99	7.83
Nickel/Zinc-Cobalt	19.6	77.15
Cobalt/Zinc-Cobalt Baked	25.7	101
Nickel/Zinc-Cobalt Baked	25.7	101

PERMEATION

FIGURE 76 demonstrates that the observed flux of the zinc-cobalt-iron permeation transient was in the region of 0.7μA/cm^2. This value is much lower than the flux of approximately 1μA/cm^2 obtained for both zinc and pH5 zinc-cobalt permeation transients. The standard pH4.2 zinc-cobalt permeation transient had a flux of 0.82μA/cm^2, which was maintained for longer as it decayed more slowly. The lower flux value of 0.6μA/cm^2 for a pH1 zinc-cobalt permeation transient was similar to the zinc-nickel flux value. The ternary transient decay was intermediate to zinc-cobalt and zinc-nickel and integration of all the transients shown in FIGURE 117 yields the total amount of hydrogen permeated in 25 hours.

FIGURE 117: Total Amount of Hydrogen Permeated by the Type of Electroplating



The total amount of hydrogen permeated for zinc-cobalt-iron electroplating is less than that of zinc or zinc-cobalt electroplating, but more than zinc-nickel electroplating. It can been seen from FIGURE 117 that at the zinc-cobalt-iron time to failure of 10.7 hours (40,000 seconds), 1.9 x 10^{-7} gm H atoms cm^{-2} of hydrogen had been permeated into the steel substrate. This value is in good agreement with the hydrogen permeated in the failure time for the other coatings examined, which had a hydrogen failure value of between 1.4 x 10^{-7} gm H atoms cm^{-2} and 1.6 x 10^{-7} gm H atoms cm^{-2}.

TABLE 41: Comparison of Zinc-Cobalt-Iron Electroplating

Electrodeposit	TTF (Hours)	Hydrogen Flux ($\mu A/cm^2$)	H Permeated (10^{-7} gm H atoms cm^{-2})
Zinc	5.6	1	1.5
Zinc-cobalt (pH1)	7.2	0.6	1.3
Zinc-cobalt (pH4.2)	7.0	0.8	1.8
Zinc-cobalt (pH5)	4.5	1.0	1.0
Zinc-nickel	18.0	0.6	1.6
Zinc-cobalt-iron	10.7	0.7	1.9

HYDROGEN DETECTION

There was no chemical reaction observed between electroplated zinc-cobalt-iron and the emulsion treatment and the response seen for the coated layer was much more pronounced than for the hydrogen containing steel substrate.

CORROSION MEASUREMENTS

Weight loss

The corrosion rates calculated from weight loss data illustrate that longer immersion times reduced the corrosion rate for zinc-cobalt-iron specimens and that baked specimens performed slightly better than unbaked specimens. All the ternary specimens had a lower weight loss and slower corrosion rate than any of the other zinc based coating systems. However, they still lost an average of 20mdd compared with 13mdd for cadmium coated specimens.

Electrochemical

The initial corrosion potential of –990mV, seen for a zinc-cobalt-iron coating, rose to –742mV after 3 months immersion. The initial corrosion current density of 25.65$\mu A/cm^{-2}$, fell to 4.33$\mu A/cm^{-2}$ after 3 months immersion. However, unlike the zinc and zinc-cobalt coatings, the ternary coating was not removed in the immersion time. The zinc-cobalt iron coating performed better than all the zinc based coatings

with a rate of 11mdd, but not as well as cadmium, which had a corrosion rate of only 1mdd after 3 months immersion.

Zinc-Cobalt-Iron Summary

These findings confirm initial studies by the Garteur programme, which showed encouraging corrosion resistance results in both exposure trials and salt spray tests for zinc-cobalt-iron electroplated panels [161]. The zinc-cobalt-iron electrodeposits may hold answers to why other ternary electrodeposits such as the zinc-nickel-iron systems appear to be so effective at corrosion protection. The poor corrosion resistance of zinc-nickel electrodeposits in certain conditions (alkaline pH) can be attributed to micro-cracks that are present in its structure [159, 162]. However, cracked and porous electrodeposits do provide a short circuit pathway for hydrogen to travel when de-embrittlement treatment is under gone [137, 159]. Additions of iron to zinc electrodeposits aids corrosion resistance but the improvement cannot be explained solely by the formation of a more uniform deposit [137, 163]. While iron addition has been reported as reducing the electrodeposit grain size and hardness in zinc-nickel deposits, there was no real effect seen in iron additions to zinc-cobalt electrodeposits in this work [103].

The enoblement that is seen in binary zinc-cobalt and zinc-nickel coatings is of undoubted benefit to the corrosion resistance of the system, this effect was also seen for the ternary coating studied [7, 19, 137]. It is thought that cobalt aids corrosion resistance by influencing the surface oxide film properties during active corrosion [133]. Paatsch showed that 1% additions of transition elements such as; Co, Ni and Fe were responsible for improved corrosion resistance. He believed that good corrosion protection was expected when transition metals (d-metals) were zinc alloying additions. When the d-metal is strongly segregated, immobile and homogeneously distributed in the ZnO passive layer it can reduce corrosion significantly. The ZnO matrix is effectively doped by the d-metal, which causes an increased valence electron charge density at the zinc atoms. Once the dopant is captured at a zinc vacancy, it can interfere with the corrosion current by scavenging a mobile cation vacancy. If the d-metal exhibits a strong positive charge compared to zinc then this segregation effect is great[163].

The way in which ternary coatings are formed, could influence their eventual corrosion resistance. Ananth studied ternary nickel-molybdenum-iron electrodeposit nucleation under different parameters. He concluded that increased current density caused phase segregation. An increase in the Mo content increased heterogeneity in the electrodeposited phase and improved corrosion performance. The pH was found to affect the composition and alters the nature of the cathode diffusion layer [164]. A multinucleated crystal structure was observed in samples electrodeposited at near neutral pH levels.

Differences in nucleation can be explained by the variation in deposition potentials spread over the substrate surface. Mo rich phases occur where the deposition potential is high. Variation in the operating parameters can lead to Mo rich clusters or more blended monophase structures that appear to be more porous under the SEM. A fine grain size and evenly distributed pores also appear to correspond to more evenly spread Mo. Ananth stated that highly cracked coatings had high rates of corrosion.

Wang and O'Keefe determined that additions to a zinc-cobalt bath (tin, lead and antimony) improved the density and morphology of an electrodeposit and possibly resulted in a higher cobalt percentage in the electrodeposit [133]. This may also be the case for additions of iron to a modified zinc-cobalt bath to produce the ternary electrodeposit that is described in this work. The improved corrosion resistance may be attributable to the uniform, non-cracked electrodeposits that are formed, in conjunction with the noble metal content of the alloy.

TABLE 42: Summary of Corrosion Data for Zinc-Cobalt-Iron

Specimen	E_{corr} (mV)		Electrochemical Corrosion Rate(mdd)	Weight Loss Corrosion Rate(mdd)	
	Polarisation Scans	LPR		Baked	Unbaked
Steel (initial)	-600	-601	194	92	88
Steel	-580	-584	86	83	67
Zinc-Cobalt-Iron (initial)	-983	-986	68	22	22
Zinc-Cobalt-Iron	-732	-743	11	15	20

SUMMARY

LIMITING HYDROGEN EMBRITTLEMENT

Electroplating provides many types of coatings that can be modified for the required situation, but embrittlement remains a problem. Despite practical improvements reducing the initial risk of embrittlement heat treatment is usually required. Gabe states that hydrogen embrittlement of electroplated specimens can be influenced in several ways based on the hydrogen evolution and entry process as discussed in Chapter 1[139].

Elimination of water, can prevent ensuing embrittlement [139]. Some groups also claim that surface preparation of specimens before electroplating can reduce or even eliminate the embrittlement of those specimens [117, 159].

Increasing the cathode current efficiency to nearly 100% will minimise the electrochemical source of hydrogen and so decrease the risk of embrittlement[139].

The physical structure of a coating is an important property that can be altered to reduce embrittlement. This can be achieved in a number of ways. High porosity of a coating will allow hydrogen to desorb, while a low porosity of underlayers will prevent initial adsorption [159].

Solute ions in an electrolyte such as cyanide and organic additives can affect the hydrogen evolution process by poisoning effects during hydrogen evolution and so promote absorption [95]. Nitrates and oxidants depolarise hydrogen evolution thereby removing hydrogen prior to its possible absorption.

Noble metals such as platinum and palladium catalyse the hydrogen atom recombination step and so promote evolution, reducing the tendency for hydrogen absorption in the substrate [95].

Underlayers such as nickel and copper act as a barrier to hydrogen adsorption in steel substrates. This can be shown by their hydrogen diffusion coefficient measured by permeation techniques [18, 151].

As can be seen by the previous points, for the benefit of a corrosion coating that prolongs the service life of a component, many factors must be addressed to ensure that the coating does not precipitate another equally deleterious problem. The statements listed provide a useful understanding of the processes and factors that affect embrittlement but their significance varies considerably for each particular application.

Pure noble metals are a non-renewable resource and are expensive to produce, so the cost of their extensive use may out weigh the benefits seen. However, the zinc-alloys examined in this work, which provide improved corrosion performance with relatively low noble metal composition have additional benefits from their embrittlement performance under certain pH conditions.

The zinc-nickel electrolyte tested in this study has a consistently higher cathode current efficiency than the zinc-cobalt electrolyte and the zinc-nickel specimens are less embrittled. While cathode current efficiency can provide a good indication of system performance, small amounts of hydrogen, as low as 0.15 ppm, have been shown to have dramatic effects on the embrittlement performance of a specimen [151]. It has been shown in this study that the interlayer that is formed in zinc-cobalt and zinc-nickel binary electroplating is of primary importance to the observed embrittlement. The hydrogen permeability of this barrier layer determines the extent of the specimen embrittlement that occurs due to the permeation of the small quantity of hydrogen that is absorbed by the coating. Porosity of the electroplated coating may also be advantageous allowing a readily available path for hydrogen removal by baking [159]. Variation of electrolyte properties can produce a superior type of coating performance e.g. zinc-cobalt electroplating performed at pH1 is less embrittling than the standard pH4.2, but it must be remembered, that each system can only be improved within limits.

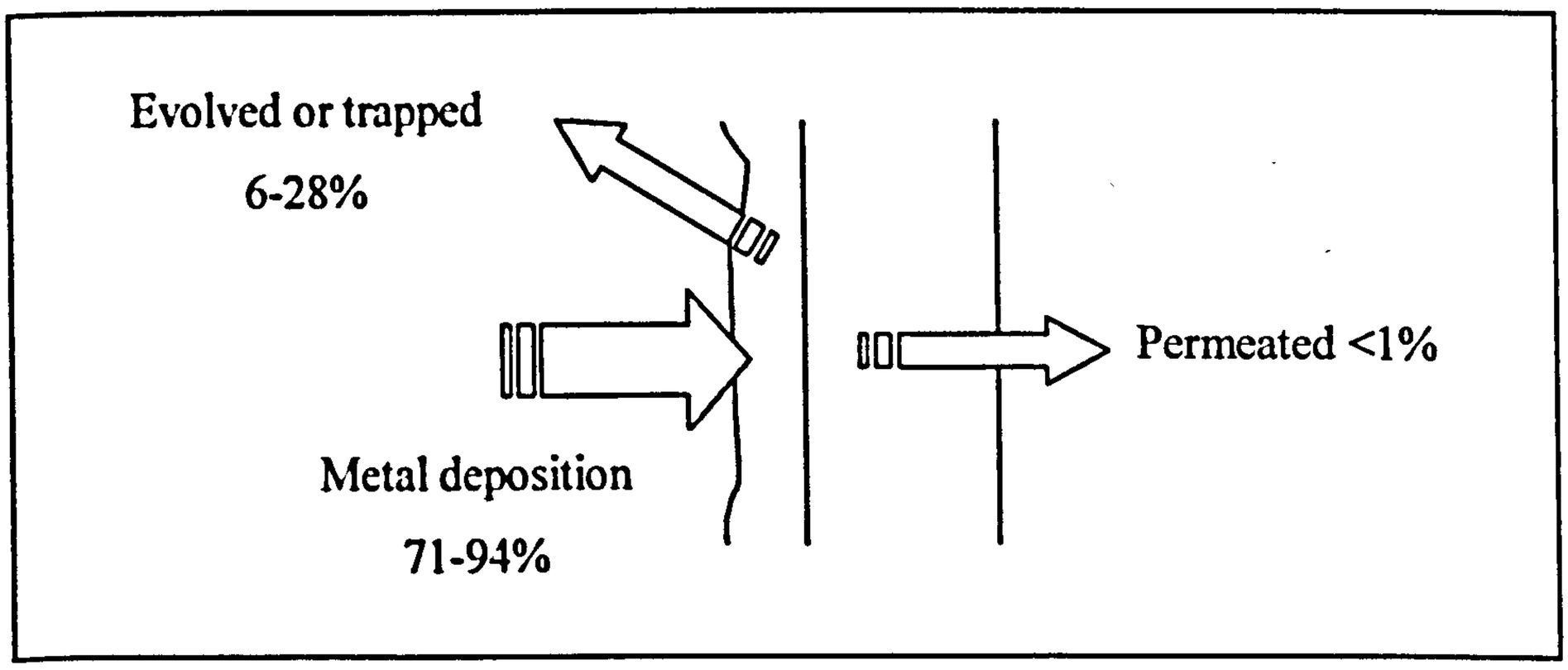
As with all coating processes, electroplating must be impurity free, as certain ions such as S^{2-} and As^{5+}, poison hydrogen recombination and promote hydrogen uptake. The environmental effects of certain substances like cadmium, is now an important world-wide issue and so must also be considered at all the process stages. To complicate matters further, certain solute ions do not always produce beneficial electroplated

specimen properties e.g. zinc is embrittling, and these must also be contemplated in process development.

WHERE THE HYDROGEN GOES

The current efficiencies of the electroplating processes were calculated from the weights of the electrodeposited material produced and the values ranged from 71 to 94%. The remaining charge, not accounted for by electrodeposit formation, was responsible for generating hydrogen. The majority of this was either evolved from the surface as bubbles or became trapped in the coating. The distribution of hydrogen during electroplating is illustrated in FIGURE 118 and TABLE 43.

FIGURE 118: Hydrogen Distribution during Electroplating



The permeation experiments showed that the steel only absorbed a relatively small amount of hydrogen from the total charge passed over the 25 hour period measured, as shown in FIGURE 118. This hydrogen was responsible for the embrittlement seen in the slow strain rate specimens. The zinc-nickel and zinc-cobalt-iron electroplated specimens caused the least embrittlement and had the lowest quantity of permeated hydrogen. Their low embrittlement levels are attributable to the formation of a hydrogen barrier at the coating/substrate interface. However, their current efficiencies varied considerably despite the majority of the remaining hydrogen being evolved or trapped.

TABLE 43: Where the Hydrogen Goes

Coating	Hydrogen % Forming the Coating	Hydrogen % Trapped or Evolved	Hydrogen % Permeated
Zinc	94	5.5	0.46
Zinc-cobalt (pH1)	71	29	0.41
Zinc-cobalt (pH4)	72	27	0.59
Zinc-cobalt (pH5)	71	28	0.64
Zinc-cobalt-iron	73	27	0.16
Zinc-nickel	90	10	0.09

CONCLUSIONS

All the aims of the project were achieved and a series of conclusions can be drawn from the results obtained.

1. Zinc-cobalt electroplating of AISI 4340 high strength steel caused serious hydrogen embrittlement. However, the embrittlement was less severe than that caused by cadmium or zinc electroplating, demonstrated by the corresponding embrittlement indices (Cd 2, Zn 4 and Zn-Co 21).

2. The embrittlement observed for zinc-cobalt electrodeposits was pH dependent. Specimens that were electroplated at pH1 showed least embrittlement, which was attributed to the cobalt rich interlayer, detected by Auger depth profiles, at the coating/substrate interface. The greatest embrittlement was seen for pH5 specimens that did not form a detectable cobalt rich interlayer at the substrate interface. These pH effects can be explained by the deposition mechanism occurring during the binary zinc-cobalt alloy electroplating.

3. The mechanical properties of zinc-cobalt electroplated specimens were not fully regained by standard baking treatments. Increasing the baking period to 48 hours from 24 hours only increased the recovery from 89 to 91%.

4. The embrittlement susceptibility of baked zinc-cobalt specimens was greater than unbaked zinc-nickel electroplated specimens.

5. Using a dual bath technique to deposit a 0.5μm cobalt layer before the standard zinc-cobalt electroplating was applied, produced a coating that allowed the specimen to regain nearly 100% of its mechanical properties after standard baking treatment. The cobalt layer was shown to provide a sufficient barrier to hydrogen so that baking removed the hydrogen in the coating rather than allowing diffusion into the substrate.

6. The zinc-nickel coating showed the least embrittlement of the single layer coatings tested (EI 80). The finding was attributed to the formation of an enriched nickel layer at the coating/substrate interface that had a low diffusion coefficient to hydrogen. The porous nature of the electrodeposit also aided diffusion of hydrogen during the baking treatment.

7. The embrittlement of zinc-cobalt electrodeposits can be reduced to the same level as zinc-nickel electroplating, by using a 0.5μm thick layer of nickel before zinc-cobalt electrodeposition.

8. The addition of a third element, iron, to a modified zinc-cobalt electrolyte to produce a ternary coating, reduced the observed embrittlement compared to standard binary zinc-cobalt electroplated specimens.

9. There was a clear relationship between the quantity of permeated hydrogen and the observed extent of hydrogen embrittlement seen for the slow strain rate specimens.

10. An average value of 1.5×10^{-7} gm H atoms cm^{-2} of hydrogen, absorbed from the coating by the substrate, was required to cause embrittlement failure. This value was independent of coating type.

11. The embrittlement effect was due to a small proportion of hydrogen, between 0.1 to 0.6% of the total charge passed during electroplating. The majority of the hydrogen generated during electroplating was either evolved or trapped in the porous coating.

12. A silver decoration technique was used successfully to detect hydrogen in electroplated coatings and charged unplated steel specimens. Specimens that had been charged for 50% or over of their estimated break through time showed excellent agreement with theoretical predictions.

13. The electrodeposits that were formed all showed good adhesion to their metal substrate. They appeared to have a uniform distribution and even morphology when electroplated under the optimum conditions determined during this work.

14. The ternary electrodeposits exhibited excellent corrosion performance in both polarisation and weight loss experiments. Zinc-nickel and zinc-cobalt-iron electrodeposits also exhibited enoblement behaviour with prolonged exposure. It is expected that zinc-cobalt would have behaved in a similar manner had the specimens been more regularly monitored during the testing period.

FUTURE WORK

1. Commercial zinc-cobalt electrolytes should be tested to see if full de-embrittlement could be achieved using standard baking treatments, as full recovery was not observed for the standard zinc-cobalt electroplated specimens examined in this work.

2. Further investigation of the zinc-cobalt-iron electrodeposits is warranted, as the work carried out during this research project indicated that they appear to have excellent corrosion and embrittlement performances.

3. Binary zinc-cobalt electrodeposits with higher cobalt content than those studied in this work would warrant investigation. They are expected to have an improved embrittlement performance and recovery after standard baking treatment. Modification of the bath composition by addition of cobalt or temperature variation would be adequate methods to attain a suggested cobalt value of 10%. This would provide direct comparison with zinc-nickel electrodeposits.

4. The permeation and corrosion behaviour of modulated multiple layered coatings would be an additional area of interest to pursue.

ACKNOWLEDGEMENTS

Firstly I would like to thank my supervisor Dr. M.J. Robinson for his help and support over the course of this project at Cranfield. His patience and guidance have been a valuable asset to me throughout this endeavour. I would also like to acknowledge the financial assistance that was given by my sponsors DERA, especially Dr. Chris Smith for the advice and experience that he provided in our meetings every six months.

A big thank you to the staff at Cranfield especially Paul Kilgallon, Sue Impey, Andrew Dyer and Colin Matthews for their technical support and teaching to this poor chemist who had to become a metallurgist, photographer and microscopist in a few weeks. A fluffy thank you to my friends, housemates (including Norman the cat) and colleagues at Cranfield and further a field who were prepared to drink coffee, eat chocolate and put the world to rights no matter how long it took. A beery thanks to the bar managers on campus who provided me with distraction and employment, not to mention sticky feet on Friday and Saturday nights, their monetary loss was Barclays gain and mine.

A chocolately thank you to both my new families, loved for both lending me their children to sit for (and so their cool toys to play with) and providing a quiet biscuit filled haven from my farmhouse full of boys and the inevitable football on television. A bubbly thank you to my scuba family who introduced me and my overdraft to diving and playing with the fishes. I know now that the best fun you can have at the seaside is in membrane suit with a 10 litre cylinder and a buddy like Jon, Tracey (yet to happen), Jood or Kevin.

A loving thank you, as always, to my actual family for the support and help that you always provide no matter how late I am in the mornings or grumpy I am at night. I am very lucky to have you all. Thank you for all the extra work you do, that I seem to create for you and for never bringing it up. Lastly to Gary, thank you for editing this thesis, 'You are my lobster'.

APPENDICES

EQUATION 25: Calculation of Thickness

Thickness (10^{-3} cm) = weight (10^{-3} g) / area (cm^2) * density of zinc (g / cm^2)

EQUATION 26: Chemical Equivalents [107]

$W_a = W_1 * W_2 / (f_1 W_2 + f_2 W_1)$

Where W_a = electrochemical equivalent of the alloy

W_1 and W_2 = electrochemical equivalents of the two metals

f_1 and f_2 = fractions by weight of the metals in the alloy: $f_1 + f_2 = 1$

EQUATION 27: Expected Weight Gain

Expected weight gain = $it * (RMM) / zF$

Where i = total applied current in amps

t = time during which the current is passed in seconds

RMM = relative molecular mass (see EQUATION 18)

z = ionic charge = 2

F = Faraday constant = 96487 C $mole^{-1}$

EQUATION 28: Cathode Efficiency

Cathode efficiency = weight gain (g) / expected weight gain (g)* 100%

[1] B. Fitzsimons, 'Thermally sprayed metal coatings for corrosion protection'. PCE March, (1996), 24-32.

[2] Airco Temescal, 'Physical vapour deposition'. Airco Incorporated, (1976), USA.

[3] A. Sachian, M. Blidarium, E. Roman and C. Raducanu, 'Functional composite zinc electrodeposition'. Transactions of the Institute of Metal Finishing, 75, (6), (1997), 213-215. C.T. Dervos, C. Kollia, S. Psarrou, P. Vassiliou and N. Spyrellis, 'Electrical properties of nickel composite electrocoatings'. Transactions of the Institute of metal finishing, 76 (4), (1998), 127-130.

[4] M. Siluvai Michael, M. Pushpavanam and K. Balakrishnan, 'Conversion coatings for zinc-cobalt alloy electrodeposits'. Bulletin of Electrochemistry, 12, (1-2), (1996), 80-82.

[5] http:/www.d-n-a.net/users/dnetGOjg/Disasters.htm, www.airdisasters.co.uk, (22/5/00).

[6] Defence Standard 03-4/2, 'The Pre-Treatment and Protection of Steel Parts of Specified Maximum Tensile Strength Exceeding 1450 Nmm^{2}, (1977). 'Dembrittle for not less than 24 hours at 190-230°C' Bae specification ABP1-4041 method 7, (1993). ' 24 hours at 190°C time quoted is a minimum and maybe exceeded if convenient' Draft Dowty specification PS 131 Cadmium plating of UHTS.

[7] K.R.Baldwin and C.J.E. Smith, 'Advances in replacements for cadmium plating in aerospace applications'. Transactions of the Institute of Metal Finishing, 74 (6), (1996), 202-209.

[8] M.J. Nelson and E.C. Groshart, 'Cadmium plating replacements'. Aerospace Environmental Technical Conference, Huntsville, Alabama, August 10-11, (1994). NASA Conference publication number 3298, (1995), 277-284. P. Decker and K. Cramer, 'Development of alternate material selection system for cadmium electroplating'. Triservice conference on corrosion, Wrightsville beach, North Caroline, USA, (1997), 17-21 November, 9.1-9.15. G. Vaessen, F. Andrews, C. Brindle, E. Hultgren, E. Kock, D. Marchandise, W. t'Hart and C.J.E. Smith, 'Cadmium substitution on aircraft'. 83 rd meeting of the AGARD SMP, 'Environmentally compliant surface treatments for materials for aerospace applications', Florence, Italy, (1996), 4-5 September.

[9] D.Smart and S.J.Wake, 'Zinc-cobalt alloy plating from an alkaline electrolyte'. W. Canning Materials Ltd, Birmingham.

[10] V.S. Vasantha, M. Pushpavanam and V.S. Muralidharan, 'Hydrogen in electrodeposited tin-zinc alloy'. Plating and Surface Finishing, 82, (6), (1995), 81-83.

[11] O.A. Ashira and J. Shirokoff, 'Electrodeposition and characterisation of tin-zinc alloy coatings'. Applied Surface Science, 103, (2), (1996), 159-169.

[12] E. Budman and D. Stevens, 'Tin-zinc electroplating'. Anti-Corrosion Methods and Materials, 45, (5), (1998), 327-332.

[13] T. Hara, M. Sagiyama, T. Urakawa, T. Adaniya, Y. Fukuda and Y. Tsuchiya, 'Properties of zinc-manganese alloy electroplated steel'. Nippon Technical Report, Overseas number 48, (1987), 29-37.

[14] M. Eyraud, A. Garnier, F. Mazeron and J. Crosier, 'Morphology and composition of electrodeposited zinc-manganese alloys'. Plating and Surface Finishing, 82, (1), (1995), 63-70.

[15] G. Chawa, G.D. Wilcox and D.R. Gabe, 'Compositionally modulated zinc alloy coatings for corrosion protection'. Transactions of the Institute of Metal Finishing, 76, (3), (1998), 117-120.

[16] J. O'Grady, 'Zinc- cobalt coatings in the motor industry'. Galvanotechnik, 49(10), (1995), 780-782.

[17] K. Baldwin, ' The corrosion of zinc-nickel alloys'. PhD Thesis, Cranfield University, (1992).

[18] M.J.Carr, 'Effect of Zinc Alloy Electroplating on the Hydrogen Embrittlement of High Strength Steels'. PhD Thesis, Cranfield University, (1995).

[19] A.Abibsi, N.Short and K.Denis, 'Corrosion resistance of zinc alloy coatings'. Transactions of the Institute of Metal Finishing, 67, (1991), 73-77.

[20] D. Crotty, ' Zinc alloy plating for the automotive industry'. Metal Finishing, 94 (9), (1996), 54-58.

[21] W. Seigert and J. O'Grady, 'Zinc-cobalt, zinc-nickel or zinc-iron'. Metalloberflache, 47(8), (1993), 378-381.

[22] M.E. Roper and J. O'Grady, 'Zinc alloy coatings–a European perspective'. Transactions of the Institute of Metal Finishing, 74 (4), (1996), 3-5.

[23] Personal communication, C.J.E. Smith, Defense Evaluation and Research Agency.

[24] K.Cramer, I.C. Handsy and J.P. Ault, 'Performance of zinc and zinc alloy plating on grade 8 fasteners'. Society of Automotive Engineers Transactions Journal Materials Manufacturing, 105 (5), 1996, 762-771.

[25] J.M.Evans and M.J.Robinson, 'The Effect of Electroplating and Post-Plating Heat-Treatment on the Hydrogen Embrittlement of High Strength Steels'. Final Report MOD Extramural Research Agreement 2028/0173/XR/MA, (1986-1989).

[26] R.A. Oriani, ' Hydrogen - the versatile embrittler'. Corrosion- NACE 43(7), (1987), 390-397.

[27] A.R. Troiano, 'General keynote lecture: in hydrogen in metals'. Editors M. Bernstein and A. Thompson, American Society of Metals, Metals Park, (1973), 3-15.

[28] P.J. Kilgallon, 'The effect of sulphate reducing bacteria on the hydrogen absorption of cathodically protected high strength low alloy steels'. Ph.D. Thesis, Cranfield University, (1994).

[29] A.R. Troiano, 'The role of hydrogen and other interstitials in mechanical behaviour of metals'. Transactions ASM, 52, (1960), 54-80.

[30] R.P.M. Proctor, 'Detrimental effects of cathodic protection: Embrittlement and cracking phenomena'. Cathodic protection: theory and practise. Editors V. Ashworth and C.J.L. Booker, Ellis Horwood, (1986), 293-313.

[31] M.J. Robinson and P.J. Kilgallon, 'A review of the effects of microstructure on the hydrogen embrittlement of high strength offshore steels'. HSE, Offshore Technology Report, OTO 1999056, Cranfield University, (1999).

[32] I. M. Berstein and A.W. Thompson, 'Effect of metallurgical variables on environmental fracture of steels'. International Metals Review, 212, (1976), 269-287.

[33] A. Ciszewski, T. Radomski and M. Smialowski. Corrosion, NACE, Houston, Texas, (1986), 671-679.

[34] C.A. Zapffe and C.E. Sims, 'Hydrogen embrittlement, internal stress and defects in steel'. Transactions AIME 145, (1941), 225-261.

[35] R.D.McCright, 'Effects of environmental species and metallurgical structure on the hydrogen entry into steel', Stress corrosion cracking and hydrogen embrittlement of iron based alloys. Editors R.W. Staehle, J. Hochmann and R.D. McCright. Conference Proceedings, Unieux-Firminy, 12-16 June. 1973. NACE, 5, (1977), 306-325.

[36] J. O'M. Bockris and D.F.A. Koch, Journal Physical Chemistry, 64, (1961), 1941.

[37] R.N. Iyer, H.W. Pickering and M. Zammanzadeh, 'The mechanistic analysis of hydrogen entry into metals during cathodic hydrogen charging'. Scripta Metallurgica, 22, (1988), 911-916.

[38] W. Beck and P. Fischer, 'The hydrogen evolution reaction on iron corroded in dilute and very dilute solutions of sulphuric acid'. Corrosion Science, 15, (1975), 757-766.

[39] M.A.V. Devanathan and Z. Stachurski, 'The adsorption and diffusion of electrolytic hydrogen in palladium'. Proceedings of the Royal Society, A270, (1962), 90-102.

[40] B.W. Allcock, 'Hydrogen concentration measurements using a gel-filled electrochemical probe'. Ph.D. Thesis, Cranfield University, (1993).

[41] P.H. Pumphrey, 'The role of sulphide inclusions in hydrogen entry during exposure of steels to acids'. Corrosion, 36, (10), (1980), 537-543.

[42] M.D. Archer and N.C. Grant, 'Achievable boundary conditions in potentiostatic and galvanostatic hydrogen permeation through palladium and nickel foils'. Proceedings of the Royal Society (London), 395, (A), (1984), 165-183.

[43] R.N. Iyer, I.Takeuchi, M. Zamanzadeh and H.W. Pickering, 'Hydrogen sulphide effect on hydrogen entry into iron - a mechanistic study'. Corrosion, 46(6), (1990), 460-467.

[44] J.L. Lee and J.Y. Lee, 'Hydrogen trapping in AISI 4340 steel'. Metals Science, 17, (1983), 426-432.

[45] A. McNabb and P.K. Foster, ' A new analysis for the diffusion of hydrogen in iron and ferritic steels'. Transactions AIME, 227, (1963), 618-627.

[46] R.A. Oriani, 'The diffusion and trapping of hydrogen in steel'. Acta Metallurgica, 18, (1970), 147-157.

[47] M. Koiwa, 'Trapping effect in diffusion of interstitial impurity atoms in BCC lattices'. Acta Metallurgica, 22, (1974), 1259-1268.

[48] M.I Luppo and J. Ovejero-Garcia, 'The influence of microstructure on the trapping and diffusion of hydrogen in a low carbon steel'. Corrosion Science, 32 (10), (1991), 1132 – 1136.

[49] H.G. Von Ellerbrook, G. Vibrans and H.P. Stuwe, 'Diffusion of hydrogen in iron with cavities'. Acta Metallurgica, 20, (1972), 53-60.

[50] A.J. Kumnick and H.H. Johnson, 'Hydrogen transport through annealed and deformed Armco iron'. Metallurgical Transactions, 5, (1974), 1199-1206.

[51] A.H. Cottrell and B.A. Bilby, Proceedings of the Physics Society, 62(A), (1949), 49.

[52] A.W. Cochardt, G. Schoek and H. Wiedersich, 'Interaction between dislocations and interstitial atoms in BCC metals'. Acta Metallurgica, 3, (1955), 533-537.

[53] H.H. Podgurski and R.A. Oriani, 'Nitrogenation of Fe-Al alloys. III. Absorption of hydrogen in nitrogenated Fe-Al alloys'. Metallurgical Transactions, 3, (1972), 2055-2063.

[54] O.D. Gonzales, 'The measurement of hydrogen permeation in alpha-iron: an analysis of the experiments'. Transcations AIME, 245, (1969), 607-612.

[55] J.A. Donovan, 'Accelerated evolution of hydrogen from metals during plastic deformation'. Metallurgical Transactions, 7, (A), (1975), 1677-1683.

[56] M. Iino, 'Evaluation of hydrogen-trap binding enthalpy I'. Metallurgical Transactions, 18(A), (1987), 1559-1564.

[57] J.P. Hirth, ' Effects of hydrogen on the properties of iron and steel'. Metallurgical Transactions 11(A), (1980), 861 - 890.

[58] A. Turnbull, M.W. Carroll and D.H. Ferriss, 'Analysis of hydrogen diffusion and trapping in a 13% chromium martensitic stainless steel'. Acta Metallurgica, 37, 7, (1989), 2039-2046.

[59] H.K. Birnbaum, 'Environmental-induced cracking of metals'. Editors R.P. Gangloff and M.B. Ives, NACE, Houston, (1990), 21-30.

[60] M.R. Louthan, G.R. Caskey, J.A. Donovan and D.E. Rawl, 'Hydrogen embrittlement of metals'. Materials Science and Engineering, 10, (1972), 289-300.

[61] H.H. Johnson and J.P. Hirth, ' Internal hydrogen supersaturation produced by dislocation transport'. Metallurgical Transactions A, 7 (A), (1976), 1543-1548.

[62] D.G. Westlake, 'A generalised model for hydrogen embrittlement'. Transactions ASM, 62, (1969), 1000-1006.

[63] J.J. Gilman, 'The role of surface hydrides in stress corrosion cracking'. Stress corrosion cracking and hydrogen embrittlement of iron based alloys. Editors R.W. Staehle, J. Hochmann, R.D. McCright and J.E. Slater. Conference Proceedings, Unieux-Firminy, 12-16 June. 1973. NACE, 5, (1977), 326-331.

[64] J.P. Hirth and B. Carnahan, 'Hydrogen adsorption at dislocations and cracks in iron'. Acta Metallurgica, 26, (1971), 1795-1803.

[65] R. Thompson, 'Brittle fracture in a ductile material with application to hydrogen embrittlement'. Journal Materials Science, 13, (1978), 128-142.

[66] C.D Beachem, 'New model for hydrogen assisted cracking (hydrogen embrittlement)'. Metallurgical Transactions, 3, (1972), 437-451.

[67] S.P. Lynch, 'Mechanisms for hydrogen assisted cracking'. Metals Forum, 2, (1979), 189-200.

[68] S.P. Lynch, 'A comparative study of stress-corrosion cracking, hydrogen-assisted cracking and liquid metal embrittlement in Al, Ni, Ti, and Fe-based alloys'. Hydrogen effects in Metals. Editors I.M. Bernstein and A.W. Thompson, (1981), 863-871.

[69] S.P. Lynch, 'Herringbone patterns on fracture surfaces'. Scripta Metallurgica, 20, (1986), 1067-1072.

[70] S.P. Lynch, 'Environmentally assisted cracking at high velocities'. Scripta Metallurgica, 21, (1987), 157-162.

[71] H.K. Birnbaum, 'Mechanisms of hydrogen related fracture of metals'. Hydrogen effects on Material Behaviour. Editors N.R. Moody and A.W. Thompson, (1990), 639-660.

[72] D. Shih, I.M. Robertson and H.K. Birnbaum, 'Hydrogen embrittlement of α-titanium, in situ TEM studies'. Acta Metallurgica, 36, (1988), 111-124.

[73] H.C. Rogers, ' Hydrogen embrittlement in engineering materials'. Materials Protection, April, (1962), 26-33.

[74] T. Zakroczymski, 'The effect of straining on the transport of hydrogen in iron, nickel and stainless steel'. Corrosion (NACE), 41, (1985), 485-489.

[75] R.A. Oriani, 'Environmental-induced cracking of metals'. Editors R.P Gangloff and M.B. Ives, NACE, Houston, (1990), 439-448.

[76] L.B. Pfeil, 'Effect of occluded hydrogen on the tensile strength of iron'. Proceedings of the Royal Society, London, 122, (A), (1926), 182-195.

[77] P. Lacombe, M. Aucouturier, J.P. Laurent and G. Lapasset, 'Tritium autoradiography and hydrogen embrittlement'. Stress corrosion cracking and hydrogen embrittlement of iron based alloys. Editors R.W. Staehle, J. Hochmann, R.D. McCright and J.E. Slater, Conference Proceedings, Unieux-Firminy, 12-16 June. 1973. NACE 5, (1977), 423-431.

[78] R.A.Oriani, ' A decohesion theory for hydrogen induced crack propagation'. Stress corrosion cracking and hydrogen embrittlement of iron based alloys. Editors R.W. Staehle, J. Hochmann, R.D. McCright and J.E. Slater, Conference Proceedings, Unieux-Firminy, 12-16 June. 1973. NACE 5, (1977), 351-358.

[79] H. Vehoff and W. Rothe, 'Gaseous hydrogen embrittlement in FeSi- and Ni single crystals'. Acta Metallurgica, 31, (1983), 1781-1793.

[80] A.J. Griffiths, R.B. Hutchings and A. Turnbull, 'Validation of the role of bulk charging of hydrogen in the corrosion fatigue cracking of a low alloy steel'. Progress in the understanding and prevention of corrosion, 1627-1632.

[81] N.J. Petch and P.Stables, 'Delayed fracture of metals under static load'. Nature, 169, (1952), 842-843.

[82] E.N. Pugh, 'A post conference evaluation of our understanding of the failure mechanism'. Stress corrosion cracking and hydrogen embrittlement of iron based alloys. Ed R.W. Staehle, J. Hochmann, R.D. McCright and J.E. Slater, NACE-5, NACE, Houston, (1977), 39-51.

[83] H.H. Uhlig, 'Stress sorption cracking and the critical potential'. Stress corrosion cracking and hydrogen embrittlement of iron based alloys. Editors R.W. Staehle, J. Hochmann, R.D. McCright and J.E. Slater, Conference Proceedings, Unieux-Firminy, 12-16 June 1973. NACE-5, (1977), 174-179.

[84] G.G. Hancock and H.H. Johnson, 'Hydrogen, oxygen and sub-critical crack growth in a high strength steel'. Transactions TMS-AIME, 236, (1966), 513-516.

[85] V.J. Trembath, 'Microprinting to detect hydrogen in steels.' MSc Thesis, Cranfield University, (1993).

[86]J. Ovejero-Garcia, 'Hydrogen microprint technique in the study of hydrogen in steels'. Journal Metal Science, 20, (1985), 2623-2629.

[87] W.Beck, J. O'M. Bockris, J. McBreen and L. Nanis, 'Hydrogen permeation in metals as a function of stress, temperature and dissolved hydrogen concentration'. Proceedings of the Royal Society, 290 (A), (1966), 220-235.

[88] T. Boellinghaus, H. Hoffmeister and A. Dangeleit, 'A scatterband for hydrogen diffusion coefficients in micro-alloyed and low carbon structural steels'. Welding in the World, 35 (2), (1995), 83-96.

[89] D. Noel, C.P. Vijayan and J.J. Hechler, Surface and Coatings Technology, 28, (1986), 25-237.

[90] M. J. Robinson, C.H.J. Parker, and K.J. Seal, 'The influence of sulphate reducing bacteria on hydrogen absorption by cathodically protected steel in the marine environment'. Proceedings Conference, UK Corrosion, Manchester, 2, (1991), 22-24.

[91] W.H. Thomasson, ' Quantative measurement of hydrogen charging rates into steel surfaces exposed to seawater under varying cathodic protection levels'. Materials Performance, July, (1988), 63-69.

[92] J.J. deLuccia and D.A. Berman, 'An electrochemical technique to measure diffusible hydrogen in metals (Barnacle electrode)'. Electrochemical Corrosion Testing, ASTM STD 727, (1981), 256-273.

[93] S.S. Chatterjee, B.G. Ateya and H.W. Pickering, 'Effect of electrodeposited metals on the permeation of hydrogen through iron membranes'. Metallurgical Transactions, 9(A), (1978), 389-395.

[94] R. H. Song and S. Pyun, 'Hydrogen permeation through a bilayer of Fe/Electrodeposited Ni'. Journal of Electrochemical Society, 137 (4), (1990), 1051-1056.

[95] A-M. Brass and J. Collet-Lacoste, 'The effect of surface on measurement of hydrogen transport in iron with the electrochemical permeation technique'. Hydrogen effects in Materials. The Minerals, Metals and Materials Society. (1996) 189-203. Editors A.W. Thompson and N.R. Moody.

[96] M.O. Speidel and M.V. Hyatt, 'Stress corrosion cracking of high strength aluminium alloys'. Advances in Corrosion Science and Technology, Chapter 3, 2, (1972), 132-157. Editors M. G. Fontana and R. W. Staehle. Plenum Press, London.

[97] K.A. Lucas and M.J. Robinson, 'The influence of lattice hydrogen content on the hydrogen assisted cracking of high strength steel'. Corrosion Science, 26(9), (1986), 705-717.

[98] J.A. Beavers and G.H. Koch, 'Limitations of the slow strain rate test for stress corrosion cracking testing'. Corrosion, March, (1992), 256-264.

[99] W. J. Pollock, 'Statistical treatment of slow strain rate data for assessment of hydrogen embrittlement in high strength 4340 steel'. Corrosion Science, 33(7), (1992), 1105-1119.

[100] H.H Uhlig and R.W. Revie, 'Corrosion and corrosion control'. J. Wiley and Sons, New York, Third Edition, (1985).

[101] M. Pourbaix, Atlas of electrochemical equilibria in aqueous solutions. (1966), Pergamont Press, Oxford.

[102] J.C. Scully, 'The fundamentals of corrosion'. Pergamon press, Oxford, Second Edition, (1975).

[103] M.M. Younan, R. Ichino and T. Oki, 'Crystal orientation and microhardness of electrodeposited Zn-Ni-Fe alloys'. Metal Finishing, 94, (4), (1996), 40-43.

[104] V. Ivanova, G. Raichevski, V. Krastev and S. Vitkova, 'Anodic behaviour of electrodeposited Zn-Sn alloys'. Transactions of the Institute of Metal Finishing, 76, (6), (1998), 219-223.

[105] M. Simmonds, G.D. Wilcox and C.J.E. Smith, 'Electrodeposited composite coatings- an alternative to cadmium'. Paper given at 40th Corrosion Science Symposium, U.M.I.S.T., 7th –9th September 1999.

[106] A.M. Beccaria, 'Zinc layer characterization on galvanized steel by chemical methods'. Corrosion Science, 46 (11), (1990), 906-912.

[107] F.A. Lowenheim, 'Electroplating'. Published by McGraw-Hill, 1978.

[108] A.Brenner, 'Electrodeposition of Alloys- principles and practise'. Volume 1, Academic Press, New York, 1963, 75.

[109] S. Glasstone, 'Studies of electrolytic polarisation. Part VI- Electrodeposition potentials of alloys of zinc with iron, cobalt and nickel'. Journal of the Chemical Society, (1927), 130, 641-647.

[110] K.Higashi, H.Fukushima, T.Urakawa, T.Adaniya and K.Matsudo, 'Mechanism of the electrodeposition of zinc alloys containing a small amount of cobalt'. Journal of the Electrochemical Society, 128(10), (1981), 2081-2085.

[111] H.Fukushima, T.Akiyama, J.Lee, M.Yamaguchi and K.Higashi, 'Mechanism of the electrodeposition of zinc with iron group metals from sulphate baths'. Transactions Japanese Institute of Metals, 24(3), (1983), 125-131.

[112] B. Lustman, Transactions of the Electrochemistry Society, (1943), 84, 363-375.

[113] H. Dahms, 'The influence of hydrolysis on the deposition of iron group metals (Fe, Co, Ni) at the dropping mercury electrode'. Journal of Electrochemical Society, (1964), 8, 5-12.

[114] H. Dahms and I.M. Croll, 'The anomalous co-deposition of iron-nickel alloys'. Journal of Electrochemical Society, (1965), 112(8), 771-775.

[115] E. Raub, 'Theoretical and practical aspects of alloy plating'. Plating and Surface Finishing, (1976), 2, 29-37.

[116] W.M.J.C.Verberne, 'Zinc-cobalt alloy electrodeposition'. Transactions of Institute of Metal Finishing, 64(1), (1986), 30-32.

[117] M.Kamitani, T.Koga and H.Tsuji, 'Electrodeposition of bright zinc-nickel alloys'. Surface Finishing 85, 72 Annual Technical Conference Proceedings, Detroit 15-18 July 1985.

[118] R.K.Shukla, S.K.Jha and S.C.Srivastava, 'Studies of the effects of addition agents on the electrodeposition of Ni-Co-Zn alloys from a borate bath'. Surface Technology 17, (1982), 157-164. R.K Shukla, S.K. Jha and S.C. Srivastava, 'Electrodeposition of Ni-Co-Zn alloys from a borate bath'. Surface Technology, (1981), 697-701.

[119] D.E.Hall, 'Electrodeposited zinc-nickel alloy coatings- a review'. Plating and Surface Finishing, (1983), 59-65.

[120] K.R.Baldwin, M.J.Robinson and C.J.E.Smith, 'A study into the electrodeposition mechanism of Zn/Ni alloys from an acid sulphate bath'. Royal Aerospace Establishment, Technical Report 91019 (RAE), (1991).

[121] W. Canning Limited, 'The Canning handbook on electroplating'. Twenty second edition, (1978), Published by W. Canning Limited, Birmingham.

[122] A.G. Hopkins, 'Surface analysis'. Corrosion tests and standards, application and interpretation, Edited by R. Baboian, ASTM, (1995).

[123] G.A.Ottewill, B.A.Plunkett and F.C.Walsh, 'The analysis of metal ions on solution'. Transactions of the Institute of Metal Finishing, 71(4), (1993), 166-170.

[124] 'Inductively coupled plasma spectrometry'. Methods for the examination of waters and associated materials, HMSO, (1996).

[125] I. Kirilova, I.Ivanov, St. Rashkov, 'Anodic behaviour of composition modulated zinc-cobalt multi-layers electrodeposited from single and dual baths'. Journal of Applied Electrochemistry, 28, (1998), 1359-1363.

[126] BAE specification, 'Cadmium plating of steels, titanium and copper alloys'. ABP1-4041, PS 131, (1993).

[127] E.A. Steigerwald, F.W. Schaller and A.R. Troiano, 'The role of stress in hydrogen induced delayed fracture'. Transactions of Metal Society AIME, (1960), (218), 832-841.

[128] J.Evans, 'The effect of nickel plating on the hydrogen embrittlement of high strength steel'. PhD Thesis Cranfield University, (1992).

[129] S.E. Melas,' Microprinting to detect hydrogen damage in steels.' MSc Thesis, Cranfield University, (1994).

[130] J. Crank, 'The mathematics of diffusion'. Second Edition, (1975). Clarendon Press, Oxford.

[131] Defence Standard 032/1, 'Cleaning and preparation of metal surfaces'. Directorate of Standardisation, Procurement Executive, MoD, Glasgow, UK.

[132] J.S. Zhang, Z.L. Yang, M.Z. An, W.L. Li and Z.M. Tu, 'Electrodeposition of zinc-cobalt alloys from a chloride bath'. Plating and Surface Finishing, 82, (5), (1995), 135-137.

[133] H.M. Wang and T.J. O'Keefe, 'Effect of additives on anomalous deposition in zinc-cobalt alloy electrogalvanizing'. Journal of applied electrochemistry, 24(9), (1994), 900-905.

[134] J.M. Keen and J.G.P. Farr, 'The growth of electrodeposits'. Journal of the Electrochemical Society, 109 (8), (1962), 668-678.

[135] T.E. Sharples, 'Zinc-cobalt: fighting corrosion in the 1990's'. Products Finishing, 54(6), (1990), 38-44.

[136] E. Raub and A. Knodler, 'Hydrogen in electrodeposited zinc'. Transactions of the Institute of Metal Finishing, 38, (1961), 131-136.

[137] D. Crotty and R. Griffin, 'Performance characteristics of zinc alloys'. Plating and Surface Finishing, 84, (4), (1997), 57-61.

[138] A.M.Abd El-Halim, M.H. Fawzy and M.A. Mahmoud, 'Influence of bath compositions and some operating conditions on the electroplating of cobalt from aqueous sulphate baths'. Transactions of the Institute of Metal Finishing, 71, (2), (1993), 48-51.

[139] D.R. Gabe, 'The role of hydrogen in metal electrodeposition processes'. Journal of Applied Electrochemistry, 27, (1997), 908-915.

[140] J. Downes, 'Structure and morphology of electrodeposited zinc/zinc-cobalt alloy coatings'. PhD Thesis Nottingham University, (1994).

[141] H.Comert and J.N.Pratt, 'The thermodynamic properties of solid cobalt-zinc alloys'. Thermochimica Acta, 59, (1982), 267-285.

[142] J. Dille, J. Charlier and R. Winand, ' The structure and mechanical properties of thick cobalt electrodeposits'. Journal of Materials Science, 32, (1997), 2637-2646.

[143] R. Fratesi, G. Roventi, G. Giuliani and C.R. Tomachuk, 'Zinc-cobalt alloy electrodeposition from chloride baths'. Journal of Applied Electrochemistry, 27 (9), (1997), 1088-1094.

[144] V. Narasimhamurthy and B.S. Sheshadri, 'Electrodeposition of zinc-cobalt alloys from an alkaline sulphate bath containing triethanolamine and gelatine'. Metal Finishing, 96, (4), (1998), 24-27.

[145] H.Fukushima, T. Akiyama, K. Hagashi, R. Kammel and M. Karimkhani, 'Electrodeposition behaviour of zinc-nickel alloys from sulphate baths over a wide range of current density'. Metalloberflache, Mar., 42, (1988), 242-247.

[146] H. Leidheiser Jr., A. Vertes and M.L. Varsanyi, 'Mossbauer spectroscopic study of the chemical state of cobalt in an electrodeposited zinc-cobalt alloy'. Journal of Electrochemical Society, (1981), 128(7), 1456-1459.

[147] K.R. Baldwin, C.J.E. Smith and M.J. Robinson, 'A study into the electrodeposition mechanisms of zinc-nickel alloys from an acid-sulphate bath'. Transactions of the Institute of Metal Finishing, 72, (2), (1994), 79-88.

[148] V.N. Kudryavtsev, K.S. Pedan and V.I. Anufrieva, 'Throwing power of a weakly acidic electrolyte for depositing bright zinc-cobalt coatings'. Protection of Metals, 27, (3), (1992), 385-386.

[149] S.S. Abd El Rehim, E.E. Faoud, S.M. Abd El Wahab and Hamdy. H. Hassan, 'Electroplating of zinc-nickel binary alloys from acetate baths'. Electrochimica Acta, 41, (9), (1996), 1413-1418.

[150] C. Andreone and A. Murut, 'Influence of the austenite retained in the hydrogen embrittlement in AISI 4340'. Scripta Metallurgica et Materialia, 24, (1990), 1453-1458.

[151] H.C. Davis and J.A. Gray, 'Hydrogen permeation measurements on some electrodeposited protective coatings for high strength steels'. Transactions of the Institute of Metal Finishing, 46, (1968), 12-19.

[152] J.M. Chen and J.K. Wu, 'Hydrogen diffusion through copper-plated AISI 4140 steels'. Corrosion Science, 33, (5), (1992), 657-666.

[153] J. O'M. Bockris, 'On hydrogen damage and the electrical properties of interfaces'. Stress corrosion cracking and hydrogen embrittlement of iron based alloys. Editors R.W. Staehle, J. Hochmann, R.D. McCright and J.E. Slater, Conference Proceedings, Unieux-Firminy, 12-16 June. 1973. NACE 5, (1977), 286-305.

[154] D.A. Berman, W. Beck and J.J. DeLucia, 'The determination of hydrogen in high strength steel structures by an electrochemical technique'. Hydrogen in metals, 595-607.

[155] J. Yao and J.R. Cahoon, 'The use of silver decoration technique in the study of hydrogen transport in metallic materials'. Metallurgica Transactions, 21(A), (3), (1990), 603-608.

[156] T.E. Perez and J. Ovejero Garcia, 'Direct observation of hydrogen evolution in the electron microscope scale'. Scripta Metallurgica, 16, (1982), 161-164.

[157] W. Sha, C.J. Murphy and J.Quinn, 'Corrosion and hydrogen penetration properties of electro- and electroless depositions'. Journal of Alloys and Compounds, 287, (1999), L7-L9.

[158] G.Barcelo, E.Garcia, M.Sarret, C. Muller and J. Pregonas, 'Characterization of zinc-nickel alloys obtained from an industrial chloride bath'. Journal of Electrochemistry, 28, (1998), 1113-1120.

[159] N. Gage, D.A. Wright and B.A. Wilson, 'Testing hydrogen embrittlement properties of zinc/nickel electroplated coatings on high strength steels'. Asia Pacific Interfinish 1994, conference, Melbourne, Victoria, Australia, October 2-4, (1994). Taken from Australisian Institute of Metal Finishing, 2, (1994), 36.1 –36.13.

[160] F. Simon, 'Alternatives for nickel in electroplating processes'. Transactions of the Institute of Metal Finishing, 75, (3), (1997), B53-B56.

[161] G. Vaessen, F. Andrews, C. Brindle, E. Hultgren, E. Koch, D. Marchandise, W. t'Hart and C.J.E. Smith, 'Cadmium substitution in aircraft'. 83rd Meeting of the AGARD SMP on 'Environmentally compliant surface treatments of materials for aerospace applications'. Florence, Italy, 4-5 September, (1996), R-816, 15.1-15.5.

[162] N.R. Short, S. Zhou and J.K. Dennis, 'Electrochemical studies on the corrosion of a range of zinc alloy coated steel in alkaline solutions'. Surface and Coatings Technology, 79, (1996), 218-224.

[163] W. Paatsch, W. Kautek and M. Sahre, 'Corrosion behaviour and mechanical properties of plated zinc-alloys'. Transactions of Institute of Metal Finishing, 75 (6), (1997), 216-218.

[164] M.V. Ananth and N.V. Parthasaradhy, 'Electron microscope observations on electrolytic Ni-Mo-Fe coatings'. Transactions of the Institute of Metal Finishing, 76, (1), (1998), 35-38.